Generation and control of super-octave-spanning spectra

This dissertation is submitted to the University of Hamburg for the degree of

Doctor rerum naturalium

eingereicht an der Fakultät für Mathematik, Informatik und Naturwissenschaften

Fachbereich Physik

Universität Hamburg

Submitted by

Shih-Hsuan Chia

B.S., Physics, National Taiwan University, 2007

M.S., Photonics and Optoelectronics, National Taiwan University, 2009

Hamburg, November 2015

Date of Oral defense: 12 July, 2016

The following evaluators recommend the admission of the dissertation:

Herr Jun.-Prof. Ludwig Mathey

Herr Prof. Dr. Franz Xaver Kärtner

Herr Prof. Dr. Henry N. Chapman

Herr Dr. Andrea Cavalleri

Herr Prof. Dr. Wilfried Wurth

Declaration

I hereby declare that I have written the present dissertation by my own and have not used other than the acknowledged resources.

Shih-Hsuan Chia
Hamburg, November 2015

Acknowledgements

First and foremost, I am truly grateful for the generous support from my thesis supervisor, Prof. Dr. Franz X. Kärtner. During my PhD studies, he always shows his passion and confidence toward research and life. Franz is an ideal advisor, who gives a lot of freedom in research while providing sufficient guidance. It is fruitful to discuss with him, who loves to share his wide research experience and deep physical insight. In addition, I would like to thank Prof. Dr. Henry Chapman about his support on the SONICC project. I also would also like to thank my doctoral committee members for their helpful feedback.

I wish to express my gratitude to Dr. Guoqing (Noah) Chang for being a wonderful mentor and friend. Without Noah, I wouldn't have the opportunity to investigate fiber-laser-based microscope systems. I enjoy having all kinds of conversation with Noah that makes my life really joyful. Dr. Oliver D. Mücke is also such a great colleague and friend. He helps me a lot for broadening my vision about ultrafast technology. He is so resourceful and kind whenever I was bothered by any problem.

Under the synergistic environment in CFEL and the close collaboration with the MIT side, I have been given the chance to fulfill intellectual curiosity and explore own research interest. I especially thank Dr. Li-Jin Chen for passing his knowledge in laser dynamics and coating designs to me. I also thank Dr. Qing Zhang for the help to build up the Ti:Sapphire oscillators. With regards to the Ti:sapphire parametric synthesizer, I would like to acknowledge Cirmi Giovanni, Shaobo Fang, Giulio M. Rossi, and Roland Mainz for the experimental support and discussions. In the nonlinear light microscope project, I want to thank the great help from Hsiang-Yu Chung, as well as Gengji Zhou and Chen Li for prototyping the required fiber laser source. Besides, I am also grateful for enjoyable discussions with the other group members and colleagues, especially for thesis proofreading from Anne-Laure Calendron. Furthermore, I deeply appreciate the friendship from Yi-Jen Chen, Hong Ye, Xiaojun Wu, Wei Liu, Yudong Yang, Jhih-An You, and Qian Cao, as well as Zheng Li, Bin Li, and Yuan-Pin Chang.

I also would like to thank the secretary Christine Berber for her assistance and support in the administrative things, as well as IMPRS coordinators, Anja Bleidorn, Sonia Utermann, and Julia Quante.

At last, I gratefully thank my parents, my brother, and friends who provide their unconditional support and whole-hearted encouragement during my PhD life. This dissertation is dedicated to my most beloved ones.

"無論什麼事，得知於人者太多，出之於己者太少。因為需要感謝的人太多了，就感謝天罷"

謝天，陳之藩

Publication List

Patent

1. F. X. Kärtner and ***S.-H. Chia***, "Chirped dichroic mirror and a source for broadband light pulses," European patent application EP14155053 (February13, 2014).

Refereed Journal Publications

1. ***S.-H. Chia***, L.-J. Chen, and F. X. Kärtner, "Spatiotemporal dynamics of few-cycle Ti:sapphire lasers," manuscript in preparation.
2. ***S.-H. Chia***, G. Cirmi, S. Fang, G. M. Rossi, O. D. Mücke, and F. X. Kärtner, "Chirped mirrors for broadband dispersion management: principles and limitations," manuscript in preparation.
3. H. Çankaya, A.-L. Calendron, C. Zhou, ***S.-H. Chia***, O. D. Mücke, G. Cirmi, and F. X. Kärtner, "40-μJ Passively CEP-stable seed source for Yb-based high-energy optical waveform synthesizer," manuscript in preparation.
4. W. Liu, ***S.-H. Chia***, H.-Y. Chung, F. X. Kärtner, and G. Chang, "Energy scalable ultrafast fiber laser sources tunable in 1.03-1.2 μm for multi-photon microscopy," manuscript in preparation. ***co-first author**
5. K. Şafak, M. Xin, Q. Zhang, ***S.-H. Chia***, O. D. Mücke, and Franz X. Kärtner, "Jitter analysis of pulsed
6. timing-distribution and remote-laser synchronization systems," manuscript submitted to *Opt. Express*.
7. O. D. Mücke, S. Fang, G. Cirmi, G. M. Rossi, ***S.-H. Chia***, H. Ye, Y. Yang, R. Mainz, C. Manzoni, P. Farinello, G. Cerullo and F. X. Kärtner, "Toward Waveform Nonlinear Optics Using Multimillijoule Sub-Cycle Waveform synthesizers." *IEEE J. Sel. Top. Quant. Electron*. 21, 1-12 (2015).
8. ***S.-H. Chia***, G. Cirmi, S. Fang, G. M. Rossi, O. D. Mücke, and F. X. Kärtner, "Two-octave-spanning dispersion-controlled precision optics for sub-optical-cycle waveform synthesizers," *Optica* 1, 315-322 (2014).
9. ***S.-H. Chia***, L.-J. Chen, Q. Zhang, O. D. Mücke, G. Chang, and F. X. Kärtner, "Broadband continuum generation in mode-locked lasers with phase-matched output couplers," *Opt. Lett*. 39, 1445-1448 (2014).

Refereed Conference Proceedings

1. ***S.-H. Chia***, G. Cirmi, S. Fang, G. M. Rossi, O. D. Mücke, and F. X. Kärtner, "Dispersion Management for Two-Octave-Spanning High-Energy Sub-Optical-Cycle Parametric Waveform Synthesizers," in Technical Digest of *Advanced Solid State Lasers*, paper ATu3A.2, Shanghai, China (2014).
2. R. Mainz, G. M. Rossi, C. Manzoni, G. Cirmi, Y. Yang, ***S.-H. Chia***, S. Fang, O. D. Mücke, G. Cerullo, and F. X. Kärtner, "Timing jitter characterization of a high-energy sub-cycle optical waveform synthesizer," in Technical Digest of *Advanced Solid State Lasers*, , paper ATu5A.3 Shanghai, China (2014).
3. G. M. Rossi, G. Cirmi, S. Fang, ***S.-H. Chia***, O. D. Muecke, F. Kärtner, C. Manzoni, P. Farinello, and G. Cerullo, "Spectro-Temporal Characterization of All Channels in a Sub-Optical-Cycle Parametric Waveform Synthesizer," in Technical Digest of *CLEO/QELS*, paper SF1E.3 (2014).
4. G. Cirmi, G. Rossi, S. Fang, ***S.-H. Chia***, O. D. Mücke, C. Manzoni, P. Farinello, G. Cerullo, and F. X. Kärtner, "High-Energy Sub-Optical-Cycle Parametric Waveform Synthesizer," in Technical Digest of *19th International Conference on Ultrafast Phenomena,* paper 07.Mon.P1.55, Okinawa, Japan (2014).
5. S. Fang, H. Ye, G. Cirmi, G. Rossi, ***S.-H. Chia***, O. D. Mücke, and F. X. Kärtner, "Above-Millijoule Optical Waveforms Compressible to Sub-fs Using Induced-Phase Modulation in a Neon-Filled Hollow-Core Fiber," in Technical Digest of *19th International Conference on Ultrafast Phenomena,* paper 09.Wed.P3.60 (2014).
6. O. D. Mücke, G. Cirmi, S. Fang, G. M. Rossi, ***S.-H. Chia***, C. Manzoni, P. Farinello, G. Cerullo, and F. X. Kärtner, "Few-Cycle Parametric Amplifiers and Sub-Cycle Waveform Synthesizers," in *JSAP-OSA Joint Symposia 2014 Abstracts*, paper 17a_C4_2 (2014).

7. S. Fang, H. Ye, G. Cirmi, ***S.-H. Chia***, S. Carbajo, O. D. Mücke, and F. X. Kärtner, "High-Energy Carrier-Envelope Phase-Stable Optical Waveforms Compressible to <1 fs Using Induced-Phase Modulation in Argon-Filled Hollow-Core Fiber," in Technical Digest of *Research in Optical Sciences,* paper HW1C.2, Berlin, Germany (2014).
8. ***S.-H. Chia***, L. Chen, and F. X. Kärtner, "Broadband mode-locking with phase-matched output couplers," in Technical Digest of *CLEO/QELS*, paper CTh1H.5, San Jose, CA, USA (2013).
9. F. X. Kärtner, O. Mücke, G. Cirmi, S. Fang, ***S.-H. Chia***, C. Manzoni, P. Farinello, and G. Cerullo, "High Energy Sub-cycle Optical Waveform Synthesizer," in Technical Digest of *Advanced Solid State Lasers*, paper AW2A.1, Paris, France (2013).
10. ***S.-H. Chia***, L. Chen, and F. X. Kaertner, "Spatio-spectral phase-matching in broadband soliton mode-locked lasers," in Technical Digest of *Advanced Solid State Lasers*, paper JTh2A.35, Paris, France (2013).
11. O. D. Mücke, S. Fang, G. Cirmi, ***S.-H. Chia***, F. X. Kaertner, C. Manzoni, P. Farinello, and G. Cerullo, "Millijoule-Level Parametric Synthesizer Generating Two-Octave-Wide Optical Waveforms for Strong-Field Experiments," in Technical Digest of *CLEO/QELS,* paper CTh3H.3, San Jose, CA, USA (2013).
12. S. Fang, G. Cirmi, ***S.-H. Chia***, O. D. Mücke, F. X. Kärtner, C. Manzoni, P. Farinello, and G. Cerullo, "Multi-mJ Parametric Synthesizer Generating Two-Octave-Wide Optical Waveforms," in Technical Digest of *CLEO-PR & OECC/PS,* paper WB3_1, Kyoto, Japan (2013).
13. G. Cirmi, S. Fang, ***S.-H. Chia***, O. D. Mücke, F. X. Kärtner, C. Manzoni, P. Farinello, and G. Cerullo, "High-energy pulse synthesis of optical parametric amplifiers," in Technical Digest of *CLEO/QELS,* paper CG_4_6, San Jose, CA, USA (2013).
14. ***S.-H. Chia***, L.-J. Chen, and F. X. Kärtner, "Spatiotemporal Pulse Dynamics of Passively Mode-locked Few-cycle Ti:sapphire Lasers," in *5th EPS-QEOD Europhoton Conference on Solid-state Fibre and Waveguide Coherent Light Sources*, paper ThP.5, Stockholm, Sweden (2012).

Abstract

Continued progress in photon science demands advances in light source technology. For this purpose, this dissertation presents the generation and control of super-octave-spanning optical pulses based on dielectric chirped mirrors.

The generation of isolated attosecond XUV pulses and exploration of attosecond physics would strongly benefit from the availability of intense phase-stable optical waveforms custom-sculpted on the time scale of the light period. The pulse energy and bandwidth scalability of the driving optical waveforms depend on the precise dispersion control. In this work, various dispersion compensation techniques are introduced, and an unprecedented chirped mirror system with smooth dispersion control over 2-octave bandwidth is demonstrated based on an analytical analysis of dual-adiabatic-matching (DAM) structures. These mirrors are used in a sub-cycle optical waveform synthesizer supporting <2-fs multi-mJ-level optical waveforms over a super-octave bandwidth of 0.49 μm - 2.3 μm. The proposed designs benefit the development of advanced high-intensity sub-cycle parametric synthesizers and other ultrabroadband applications.

On the other hand, optical pulse trains from femtosecond mode-locked oscillators can be used as optical flywheels providing a very precise timing reference, opening up several interesting research areas in optical frequency metrology, such as optical clocks and ultra-low noise RF-sources. Few-cycle Ti:sapphire oscillators, featuring low quantum noise, are capable of generating octave-spanning spectra with ~1 nJ of pulse energy, enabling direct carrier-envelope-phase stabilization via f-2f self-referencing. In Chapter 4, the detailed spatiotemporal dynamics of few-cycle Ti:sapphire oscillators is studied by numerical analysis. Based on the spatiotemporal modeling, the laser cavity can act as an enhancement cavity to shape the spectral components via intracavity phase matching.

The phase-matching concept is also demonstrated experimentally, providing a >10 dB enhancement at the spectral wings while maintaining excellent beam quality, which is of great importance to improve the stabilization of optical flywheels and to seed ytterbium-based amplifiers for pumping high-power optical parametric (chirped-pulse) amplifiers. Furthermore, the developed spatiotemporal model can be implemented not only for studying octave-spanning oscillator dynamics but also for optimizing advanced ultrafast sources.

During my doctoral studies, a nonlinear light microscope system is also demonstrated. Nonlinear light microscopy is one of the most important applications in ultrafast photonics. For example, second-harmonic generation (SHG) microscopy is a promising candidate for detecting chiral crystals, so-called second-order nonlinear optical imaging of chiral crystals (SONICC). The feasibility of nonlinear light microscopy depends on the availability of robust femtosecond sources and reliable electronic control. We develop a nonlinear light microscope system based on femtosecond fiber lasers and high-speed electronics. With the demonstrated nonlinear light microscope, sub-μm resolution imaging at a video frame rate can be obtained with reduced excitation power compared with commercially available SONICC systems. With the developed ultrafast fiber laser technology and optimized electronic control, a custom-made nonlinear light microscope is constructed, which is capable of observing nucleation and growth kinetics of protein nanocrystals.

Zusammenfassung

Kontinuierlicher Fortschritt im Bereich der Forschung mit Licht ist eng mit der Weiterentwicklung von Laserlichtquellen verbunden. Die vorliegende Dissertation präsentiert die Erzeugung und Dispersionskontrolle von optischen Pulsen, die sich spektral über mehr als eine Oktave erstrecken, mit sogenannten doppelt durchgestimmten Spiegeln (DCMs).

Die Erzeugung von Attosekundenpulsen und Erforschung der Physik auf Attosekunden Zeitskalen würde stark von intensiven, phasenstabilen, optischen Wellenformen profitieren, die auf der Zeitskala einer Lichtperiode geformt werden können. Die Skalierbarkeit der Pulsenergie und der Bandbreite ist stark abhängig von einer präzisen Dispersionskontrolle. In der vorliegenden Arbeit werden mehrere Techniken zur Dispersionskontrolle eingeführt und ein System aus dispersionskompensierenden Spiegeln mit zuvor nicht erreichtem glatten Phasenverlauf über zwei Oktaven, durch Analyse von sogenannten Dual-Adiabatic-Matching (DAM)-Strukturen, demonstriert. Diese Spiegel finden in dem optisch parametrischen Wellenform-Synthesizer Anwendung, welcher die Erzeugung von Pulsen mit weniger als 2 Femtosekunden im Millijoulebereich über eine Bandbreite von 0,49µm bis 2,3µm ermöglicht. Das vorgelegte Design unterstützt die Entwicklung von hochenergetischen parametrischen Subzyklen-Wellenform-Synthesizern und anderen ultrabreitbandigen Anwendungen.

Andererseits bieten optische Pulszüge, welche von modengekoppelten Femtosekunden-Laseroszillatoren generiert werden, eine sehr präzise Zeitreferenz, die mehrere interessante Forschungsthemen in der optischen Frequenzmetrologie, wie optische Uhren und extrem rauscharme Radiofrequenzquellen, eröffnet. Wenigzyklen Titan:Saphir-Oszillatoren mit einem geringen Quantenrauschen ermöglichen die Erzeugung von oktavspannenden Spektren mit ~1nJ Pulsenergie und eine direkte Stabilisierung der Phase zwischen Träger und Einhüllenden (CEP) mittels f-2f Selbstreferenzierung. Im Kapitel 4 wird die raumzeitliche Dynamik von Wenigzyklen-Titan:Saphir-Oszillatoren mithilfe von numerischen Methoden simuliert. Die Simulationen zeigen ebenfalls, dass Laserresonatoren als Überhöhungsresonator wirken und Spektralkomponenten durch resonatorinterne Phasenanpassung formen können.

Das Konzept der Phasenanpassung wird ebenfalls experimentell demonstriert und liefert eine >10 dB Erhöhung der spektralen Leistung an den Rändern des Spektrums bei gleichzeitig exzellentem Strahlprofil. Dies ist von großer Bedeutung für die Erhöhung der Stabilität von optischen Taktgebern und zum Seeden von Ytterbium-basierten Verstärkern zum Pumpen von optisch parametrischen Verstärkern (für gechirpte Pulse) mit hoher Leistung.
Desweiteren kann das entwickelte raumzeitliche Modell nicht nur implementiert werden, um die Dynamik von oktavspannenden Laseroszillatoren zu verstehen, sondern auch, um hochentwickelte ultraschnelle Lichtquellen zu verbessern.

Während der Arbeit an meiner Promotion hatte ich die Gelegenheit, mich an der Entwicklung eines nichtlinearen Lichtmikroskopes zu beteiligen. Diese Mikroskope stellen eine der wichtigsten Anwendung der ultraschnellen Photonik dar. Als Beispiel sei die Mikroskopie mit der zweiten Harmonischen genannt, welche eine vielversprechende Technik zur Detektion von chiralen Kristallen darstellt, die sogenannte Second-Order Nonlinear Optical Imaging of Chiral Crystals (SONICC). Die Durchführbarkeit solch einer Mikroskopiertechnik setzt stabile Laserlichtquellen und zuverlässige Steuerelektronik voraus. Im Rahmen dieser Arbeit haben wir ein nichtlineares Mikroskop basierend auf einem Femtosekunden-Faserlaser und entsprechender Hochgeschwindigkeitselektronik aufgebaut. Mit dem aufgebauten nichtlinearen Mikroskop wurde ein bildgebendes Verfahren mit sub-µm Auflösung bei einer Bildwiderholrate im Videobereich realisiert, und dies bei einer geringerer Anregungsleistung im Vergleich zu kommerziellen SONICC-Systemen. Mit der entwickelten ultraschnellen Faserlasertechnologie und der optimierten Steuerelektronik wurde ein kompaktes nichtlineares Lichtmikroskop konstruiert, welches in der Lage ist, Keimbildung und die Wachstumskinetik von Proteinnanokristallen aufzulösen.

Contents

List of Figures

Chapter 1

Introduction

1.1 **Background**

Since the invention of mode-locked lasers, the advance in generation of ultrafast optical sources has led to tremendous successes towards broader spectral bandwidths, higher pulse energies, and more stable operations, as well as shorter pulse durations and better phase control. The pursuit in ultrafast laser technology is strongly driven by the explorations of the research/industry frontiers, such as precision metrology [1.1-3], ultrafast dynamics [1.4-6], and microscopic applications [1.7, 8]. For example, the feasibility of generating short optical pulses (*e.g.*, <1 ps) has enabled ultrafast pump-probe experiments to reveal the electronic and molecular dynamics, which offer new horizons to a better understanding of condensed matter [1.4], chemical [1.5] and biological [1.6] processes. Optical frequency combs, along with precise phase control between microwave and optical frequency, have revolutionized optical frequency metrology [1.2], optical atomic clocks [1.3], and high-precision spectroscopy [1.9, 10].

The frontier studies of strong-field light-matter interactions, such as laser plasma interaction [1.11], high harmonic generation (HHG) [1.12], and strong-field ionization [1.13] strongly rely on the availability of intense optical bursts and precise optical waveform control. The development of carrier-envelope-phase-(CEP)-controlled few-cycle optical waveforms with high pulse energies has already led to the generation of isolated attosecond pulses in the EUV regime [1.14, 15] via HHG process. Moreover, the exploration of waveform nonlinear optics expands ultrafast spectroscopy to attosecond resolution [1.16, 17]. Furthermore, the realization of the energy and bandwidth scalability of ultrashort optical transients provides a new enabling technology for the demonstration of bright coherent tabletop high-harmonic sources, especially in the water-window and keV X-ray region [1.18].

Few-cycle mode-locking dynamics

The development of mode-locking techniques and the discovery of broadband laser gain medium paved the way for advancing ultrafast lasers [1.19]. In order to generate short optical bursts in a laser oscillator, several longitudinal modes should be excited in the cavity and their relative phase should be carefully controlled. However, laser oscillation normally supports just a few resonator modes where the saturated gain meets cavity loss due to the non-uniform gain/loss feature in the cavity. As a result, additional efforts must be considered in the oscillator cavity in order to overcome the gain filtering effect and to lock the phase coherence of a large number of lasing modes. The ways to enable these have been termed mode locking, and the main goal is to offer an environment favoring pulse-train generation instead of continuous-wave operation. Since the mid-1960s, ways to achieve laser mode locking in both active [1.20-22] and passive [1.23-27] fashions have been introduced, successfully reducing the achievable pulse duration from the sub-nanosecond to subpicosecond regime. For the two following decades, dye lasers played an important role in ultrashort pulse generation, due to their broadband emission with colliding-pulse mode-locking (CPM) [1.28]. However, the toxicity and handling issue of the laser dye limit its possible applications. To date, ultrafast dye lasers have been revolutionized by solid-state lasers, such as Ti:Sapphire lasers, based on the Kerr-lens mode-locking (KLM) technique [1.29].

In order to achieve passive mode locking and femtosecond operation, a saturable absorber has to be employed inside the cavity introducing less loss on the high intensity beam than on the continuous wave [1.27]. In KLM oscillators [1.29], the pulses building-up in a laser cavity experience an intensity-dependent self-focusing via optical Kerr effect, resulting in intensity-dependent cavity spatial mode. By inserting a slit (*i.e.*, hard-aperture KLM) or matching the pump beam with the higher-intensity laser beam (*i.e.*, soft-aperture KLM), the intracavity pulses experience an intensity-dependent loss called self-amplitude modulation (SAM) acting as a saturable absorber. KLM provides almost instantaneous SAM, and hence it sets no lower bound to the achievable pulse duration. Since the first demonstration in 1991 [1.29], Ti:Sapphire oscillators, which are commercially available even for <5 fs pulse generation, have become the main workhorses in ultrafast applications.

The physics behind KLM is quite complicated and interesting: both spatial and temporal effects are coupled in a KLM Ti:Sapphire oscillator due to the interplay between optical Kerr nonlinearity, cavity dispersion, and diffraction, as well as gain-saturation and gain-guiding. Various spatial or temporal analyses have been developed for explaining the physics behind the operation of KLM oscillators [1.30-38]. For example, by modeling Kerr-lens effect as an intensity-dependent lens and performing the self-consistent ABCD analysis of the laser cavity, the strength of the SAM action can be characterized from the spatial variation of the beam width [1.30, 31]. In the time domain, dispersion-managed soliton mode-locking is proposed [1.37]: dispersion-managed self-phase modulation (SPM) via Kerr nonlinearity associated with dispersive elements inside the cavity is balanced, supporting stable few-cycle pulses between round-trip evolutions. Due to the coupling between these effects, especially strong for few-cycle pulse generation, a reliable analysis for cavity optimization becomes extremely challenging. In addition, the nonlinear coupling between spatial and temporal effects is linked by optical Kerr nonlinearity via self-focusing and SPM. As a result, full understanding of the spatio-temporal behaviors requires a complicating three-dimensional modeling to explain the few-cycle laser dynamics, such as the wavelength-dependence of the laser beam profile. More importantly, further improvement of these few-cycle lasers requires a more accurate theory that can deal with the full spatio-temporal mode-locking dynamics in the laser.

Dispersion management for sub-optical-cycle waveform synthesizers

The generation of intense few/sub-cycle bursts remains great technical and experimental challenges. The technology widely applied for the implementation of stable and energetic femtosecond sources have been relies on broadband stimulated emission, such as Ti:Sapphire oscillators and amplifiers. However, the possible spectral bandwidth is limited by the emission cross section of the gain medium, leading to gain narrowing during the amplification process: the light around the center region of the emission cross section experiences a higher gain than the spectral wings. As a result, in order to explore the achievable spectral bandwidth, ways for nonlinear spectral broadening (*e.g.*, SPM in hollow core fibers (HCFs) [1.39-42] or optical parametric generation in nonlinear crystals [1.43-47]) have been widely implemented and investigated. Optical few-cycle waveform via

supercontinuum generation based on gas-filled HCF compressors has become a standard technology [1.39-42], and sub-cycle ~300-μJ optical pulses (covering 260–1100 nm) have been demonstrated for attosecond science experiments [1.41, 48]; however, the available pulse energy and obtainable bandwidth seem to be limited by multiphoton ionization, which induces ionization losses and detrimental nonlinearities [1.42, 49]. Moreover, HCF-based technique is not capable of varying the center wavelength: the center wavelength of the generated supercontinuum is directly linked with the driving sources (*e.g.,* ~800 nm using a Ti:Sapphire amplifier).

The advances in laser technology have led to the introduction of ultrafast optical parametric amplifiers (OPAs) as practical sources for femtosecond pulses tunable across the visible, near and far infrared spectral ranges [1.43-47]. Comparing with HCF compressors, the ultrafast OPA setups allow scalabilities of both pulse energy and operating wavelength regimes by increasing the number of amplification stages and varying the phase-matching conditions, respectively. As a result, a super-octave-wide optical waveform with a high pulse energy (*i.e.,* at the millijoule (mJ) level) can be obtained by synthesizing multiple channels of femtosecond OPAs operating at different wavelength regimes. Moreover, mid-IR few cycle pulses can be generated with proper phase-matching geometry via optical parametric process for precise mid-IR spectroscopy, and one can realize of bright coherent tabletop HHG sources in the water-window and even further in the keV X-ray region [1.18, 50].

Dispersion management, the way to stretch and compress optical bursts, plays an essential role in the ultrafast laser technology. In a laser oscillator, the feasibility of broadband mode-locking depends not only on the choices of laser gain medium, but also on the ability of intracavity dispersion compensation. Moreover, by stretching the seed pulse to reduce its peak intensity, chirped pulse amplification (CPA) [1.51] has been widely employed nowadays as the gold standard technique to amplify ultrashort pulses. Furthermore, in optical parametric amplifiers (OPAs), dispersion optimizations between the pump and seed beam improve the conversion efficiency and spectral bandwidth [1.52]. Since the invention of pulsed lasers, several approaches have been proposed for dispersion compensation, including passive methods using prism pairs [1.53], grating pairs [1.54], and chirped mirrors (CMs) [1.55-62], as well as programmable techniques based on liquid-crystal modulators [1.40, 63], acousto-optic modulators [1.64], and mechanically deformable mirrors [1.44, 65].

For example, prism pairs [1.53] are intensively employed in a laser oscillator due to the negligible insertion loss, and grating pairs [1.54] are usually used as external pulse compressor/stretcher because they can provide large negative/positive dispersion. Considering the scalability of handling bandwidth, spatial light modulators with >1-octave bandwidths have been demonstrated [1.40, 63]. However, they are hampered by the use of the gratings in 4-*f* systems.

The generation of isolated attosecond XUV pulses and exploration of attosecond physics would strongly benefit from the availability of intense phase-stable optical waveforms custom-sculpted on the time scale of the light period [1.16, 18, 41]. Although synthesizing multiple channels of femtosecond OPAs paves a way to obtain high-energy super-octave-wide optical waveform [1.66, 67], the generation of intense sub-cycle pulses from broadband synthesizers requires precise dispersion management and pulse compression. Comparing with the other techniques, the employment of CMs, although not adaptable, has the advantage of supporting potentially multi-octave-spanning high-intensity sources with high throughputs [1.55-61]. ~1.5-octave-spanning chirped mirror has been demonstrated [1.61, 62]. The further exploration of CM technology is required to synthesis extremely intense sub-optical-cycle waveform: the feasibility of energy scalability depends on not only the capability of increasing amplification stages, but also the way to achieve dispersion management over the whole super-octave-wide bandwidth. Furthermore, temporal optimization in each amplification stage in terms of bandwidth and conversion efficiency demands on delicate dispersion distribution. As a result, the further investigations of both chirped mirror technology and dispersion-management schemes are strongly required for constructing a millijoule-level sub-cycle waveform synthesizer.

Nonlinear light microscopy

During my doctoral studies, a nonlinear light microscope is also demonstrated based on an ultrafast fiber laser system. Nonlinear light microscopy is one of the most important applications in ultrafast photonics. Optical nonlinear processes offer great opportunities to explore the field of molecular imaging. For example, two-photon fluorescence (2PF) imaging provides intrinsic optical sectioning capability (*i.e.,* lateral resolution) without the use of pinholes in confocal microscopes [1.7]. Thanks to the advance on ultrashort laser technology,

ultrashort pulse trains from mode-locked lasers feature intense peak intensity with low average power: detectable nonlinear light signals are generated due to the high peak intensity, while the possible damage from thermal heating is reduced with the low average power. Furthermore, near-infrared excitation pulses are employed to reach a deeper penetration [1.68] with less light scattering comparing with conventional microscopes using visible light. Based on different nonlinear processes, sample fingerprints can be captured via various imaging contrast agents (for example, multiphoton fluorescence excited by labeled fluorophores [1.7, 68-70], optical harmonics followed by the sample morphology [1.71-76], and Raman scattering signals sensitive to the molecule vibration modes [1.77-79]). As a result, nonlinear light microscopy, featuring deep penetration depth and intrinsic optical sectioning capability, reveals different sample characteristics, opening up several promising possibilities for biological and medical applications. Moreover, super-resolution imaging with typically sub-100-nm far field resolution can be obtained by shaping the point spread function of the fluorescence generated via stimulated emission [1.80, 81]; this method was awarded the Nobel Prize in Chemistry in 2014.

For example, second harmonic generation (SHG) microscopy is a powerful tool for the preliminary observation of chiral crystals, so called second-order nonlinear optical imaging of chiral crystals (SONICC) [1.75, 76]. Proteins perform various functions in bio-activities, which can be disclosed by its structure and ligand binding locations. Protein crystallization is typically demanded for the structural analysis via X-ray diffraction. Crystallizing proteins, however, is often extremely difficult and requires carefully screening and monitoring the trial processes. Imaging approaches to characterize crystallization processes are thus required. Coherent SHG signals only arise from noncentrosymmetric structures, and it can be enhanced with certain classes of ordered systems. Therefore, the SHG imaging contrast via SONICC can be only found in certain crystal classes, and the presence of protein crystals can be visualized with a good sensitivity and background suppression [1.75, 76].

The technical feasibility using nonlinear light microscope strongly depends on the availability of robust and easily-operated sources. Ultrafast fiber lasers are regarded as promising candidates due to the potential of compact size, simple maintenance, and relatively inexpensive cost [1.82]. Moreover, the advance on nonlinear light microscope

demands on high speed electronics. On one hand, the development of high frame rate is driven by the desire of real-time observations of fast biological/chemical dynamics, requiring above-MHz level of data acquisition rate. On the other hand, modulated signals along with lock-in detection allow signal subtraction from its background. Based on femtosecond fiber lasers and high speed electronics, the construction of nonlinear light microscope systems is an interesting topic requiring further investigation, which is promising for the observation of nucleation and growth kinetics of the crystals from high resolution SONICC imaging.

1.2 **Scope of the thesis**

This thesis aims for the generation and control of super-octave-spanning sources and a microscopic application based on ultrafast fiber lasers. Parts of Chapters 2 and 3, including text and figures, are reproduced from own published journal papers [1.67, 83], as well as some parts of Chapters 4 and 5 from Ref. [1.84, 85]. The thesis structure, as well as the emphasis on personal contributions, is provided as follows:

Chapter 2 describes the dispersion management techniques, which set the foundation in the development of ultrafast laser technology. An introduction to optical dispersion is provided and the developed dispersion control technique is detailed. For super-octave-wide dispersion control, I investigated the capabilities of dielectric chirped mirror design. >2-octave-spanning chirped dichroic mirrors and high-reflection chirped mirrors are demonstrated based on an analytical analysis of dual-adiabatic-matching (DAM) structure. A further evaluation regarding the potential of chirped mirrors is provided in terms of feasibility of even-broader design bandwidth, limitations on damage threshold, trade-off between design bandwidth and dispersion-compensating amount.

In Chapter 3, I propose a two-octave-spanning dispersion-controlled scheme based on dispersive mirror systems, providing a new enabling technology for pulse-energy and bandwidth scaling of sub-cycle optical waveform synthesizers. The experimental demonstrations are contributed from Dr. Giovanni Cirmi, Dr. Shaobo Fang, Dr. Oliver D. Mücke, Giulio M. Rossi, and Roland Mainz [1.67]. The energy and bandwidth scalabilities of ultrashort optical transients, which are ultimately limited by the used optics, are the necessary prerequisite especially for the realization of bright coherent table-top high-

harmonic sources. We implemented the chirped dichroic mirror described in Chapter 2 to efficiently optimize the beam combining from different spectra, and a double-chirped mirror pair to avoid unwanted nonlinearity during beam propagation. These novel designs provide custom-tailored dispersion and reflectivity over more than two octaves of bandwidth ranging from 0.49 μm - 2.3 μm, supporting 1.9-fs-short sub-optical-cycle pulses. In addition, since the material dispersion features distinct behaviors in different channels operated in different wavelength regimes, I provide a preliminary analysis, as a guideline for experimental constructions, on the delicate dispersion distribution in order to optimize the 3-channel 3-stage optical waveform synthesizer.

In Chapter 4 and Chapter 5, the full spatiotemporal features of few-cycle Ti:sapphire oscillators are analyzed, in order to have a better understanding of the laser dynamics for future optimization and applications. The spatiotemporal cavity modeling is initiated by Dr. Li-Jin Chen with some preliminary results as well as the experimental demonstration of 2 GHz Ti:sapphire oscillators [1.85], and I completed the whole analysis and made further optimizations in this thesis. In order to characterize different mechanisms, the modeling methods are introduced, including the optical Kerr nonlinearity, dispersion, diffraction, gain features of Ti:sapphire oscillators (*i.e.*, gain profile, gain saturation, and the geometry of the pump beam), and multiphoton ionization processes. The starting point of the laser dynamics is the mechanism of few-cycle mode-locking. Different laser conditions are examined and analyzed numerically, in order to describe the working points of octave-spanning oscillators experimentally achievable by means of fine-tuning cavity dispersion, cavity geometry, and pump power. In addition, although the use of chirped mirror pairs has led to the success of demonstrating octave-spanning oscillators [1.58], the residual dispersion errors of the chirped mirrors influence the laser performances in terms of available bandwidth, sub-structures on the generated spectra, and beam profile. By considering the residual phases and the output coupling as the perturbation to dispersion-managed soliton mode-locking, the detailed features of the experimental demonstrations can be explained, which opens the possibility for further optimizations. The advanced studies are focused on the intracavity spatiotemporal phase-matching based on the perturbation of dispersion-managed solitons. The laser cavity can not only be employed to produce the simulated emission from the gain medium, but also acts as an enhancement cavity to shape the spectrum mainly generated by self-phase modulation. With a proper intracavity phase-matching, the wavelength

components in the spectral wings (*e.g.*, ~1140 nm for the direct stabilization of carrier-and-envelope phase and ~1030 nm for seeding of Yb-based amplifiers) can be greatly enhanced while maintaining a fundamental beam shape. In Chapter 5, the phase-matching concept is demonstrated experimentally in a linear-cavity Ti:sapphire oscillator, providing a >10 dB enhancement around 1140 nm with a good beam quality. The future improvement requires a more precise intracavity dispersion control: a phase-optimized end-mirror is designed and fabricated to compensate the residual dispersion errors in the cavity. With precise intracavity dispersion control and use of different output coupling window, the octave-spanning spectra can be optimized and well-controlled for different applications.

Chapter 6 describes our approach to set up a nonlinear light microscope system based on femtosecond fiber lasers and high speed electronics, in collaboration with Hsiang-Yu Chung. The ultrafast fiber laser system including a nonlinear-polarization-evolution mode-locked Yb:fiber oscillator and an amplifier is constructed to deliver ~110-fs pulses with ~3 nJ of pulse energy. The construction of the fiber laser source is assisted by Gengji Zhou and Chen Li. I proposed the schemes of electronic control and microscope systems. With the demonstrated nonlinear light microscope, sub-μm resolution imaging at a video imaging rate can be obtained with a reduced excitation power compared with the commercial systems. Possible routes for further implementations are also suggested.

References

[1.1] M. Hentschel, R. Kienberger, C. Spielmann, G. A. Reider, N. Milosevic, T. Brabec*, et al.*, "Attosecond metrology," *Nature,* vol. 414, pp. 509-513, 2001.

[1.2] T. Udem, R. Holzwarth, and T. W. Hänsch, "Optical frequency metrology," *Nature,* vol. 416, pp. 233-237, 2002.

[1.3] T. Rosenband, D. Hume, P. Schmidt, C. Chou, A. Brusch, L. Lorini*, et al.*, "Frequency ratio of Al+ and Hg+ single-ion optical clocks; metrology at the 17th decimal place," *Science,* vol. 319, pp. 1808-1812, 2008.

[1.4] C. V. Shank, "Investigation of ultrafast phenomena in the femtosecond time domain," *Science,* vol. 233, pp. 1276-1280, 1986.

[1.5] A. H. Zewail, *Femtochemistry: ultrafast dynamics of the chemical bond* vol. 1: World Scientific, 1994.

[1.6] V. Sundström, "Femtobiology," *Annu. Rev. Phys. Chem.,* vol. 59, pp. 53-77, 2008.

[1.7] W. Denk, J. H. Strickler, and W. W. Webb, "Two-photon laser scanning fluorescence microscopy," *Science,* vol. 248, pp. 73-76, 1990.

[1.8] W. R. Zipfel, R. M. Williams, and W. W. Webb, "Nonlinear magic: multiphoton microscopy in the biosciences," *Nature biotechnology,* vol. 21, pp. 1369-1377, 2003.

[1.9] R. Holzwarth, T. Udem, T. W. Hänsch, J. Knight, W. Wadsworth, and P. S. J. Russell, "Optical frequency synthesizer for precision spectroscopy," *Physical Review Letters,* vol. 85, p. 2264, 2000.

[1.10] D. J. Jones, S. A. Diddams, J. K. Ranka, A. Stentz, R. S. Windeler, J. L. Hall*, et al.*, "Carrier-envelope phase control of femtosecond mode-locked lasers and direct optical frequency synthesis," *Science,* vol. 288, pp. 635-639, 2000.

[1.11] A. Buck, M. Nicolai, K. Schmid, C. M. Sears, A. Sävert, J. M. Mikhailova*, et al.*, "Real-time observation of laser-driven electron acceleration," *Nature Physics,* vol. 7, pp. 543-548, 2011.

[1.12] P. B. Corkum, "Plasma perspective on strong field multiphoton ionization," *Physical Review Letters,* vol. 71, p. 1994, 1993.

[1.13] L. Keldysh, "Ionization in the field of a strong electromagnetic wave," *Sov. Phys. JETP,* vol. 20, pp. 1307-1314, 1965.

[1.14] E. J. Takahashi, P. Lan, O. D. Mücke, Y. Nabekawa, and K. Midorikawa, "Attosecond nonlinear optics using gigawatt-scale isolated attosecond pulses," *Nature communications,* vol. 4, 2013.

[1.15] L. Veisz, D. Rivas, G. Marcus, X. Gu, D. Cardenas, J. Mikhailova*, et al.*, "Generation and applications of sub-5-fs multi- 10-TW light pulses," in *2013 Conference on Lasers and Electro-Optics Pacific Rim*, Kyoto, 2013, p. TuD2_3.

[1.16] F. Krausz and M. Ivanov, "Attosecond physics," *Reviews of Modern Physics,* vol. 81, p. 163, 2009.

[1.17] M. Schultze, M. Fieß, N. Karpowicz, J. Gagnon, M. Korbman, M. Hofstetter*, et al.*, "Delay in photoemission," *Science,* vol. 328, pp. 1658-1662, 2010.

[1.18] T. Popmintchev, M.-C. Chen, D. Popmintchev, P. Arpin, S. Brown, S. Ališauskas*, et al.*, "Bright coherent ultrahigh harmonics in the keV X-ray regime from mid-infrared femtosecond lasers," *science,* vol. 336, pp. 1287-1291, 2012.

[1.19] H. A. Haus, "Mode-locking of lasers," *IEEE Journal of Selected Topics in Quantum Electronics,* vol. 6, pp. 1173-1185, 2000.

[1.20] L. Hargrove, R. Fork, and M. Pollack, "Locking of He–Ne laser modes induced by synchronous intracavity modulation," *Applied Physics Letters,* vol. 5, pp. 4-5, 1964.
[1.21] D. J. Kuizenga and A. Siegman, "FM and AM mode locking of the homogeneous laser-Part I: Theory," *Quantum Electronics, IEEE Journal of,* vol. 6, pp. 694-708, 1970.
[1.22] D. J. Kuizenga and A. Siegman, "FM and AM mode locking of the homogeneous laser-part II: experimental results in a Nd: YAG laser with internal FM modulation," *Quantum Electronics, IEEE Journal of,* vol. 6, pp. 709-715, 1970.
[1.23] A. DeMaria, D. Stetser, and H. Heynau, "SELF MODE-LOCKING OF LASERS WITH SATURABLE ABSORBERS," *Applied Physics Letters,* vol. 8, pp. 174-176, 1966.
[1.24] E. Ippen, C. Shank, and A. Dienes, "Passive mode locking of the cw dye laser," *Applied Physics Letters,* vol. 21, pp. 348-350, 1972.
[1.25] H. A. Haus, "Theory of mode locking with a fast saturable absorber," *Journal of Applied Physics,* vol. 46, pp. 3049-3058, 1975.
[1.26] K. Sala, M. C. Richardson, and N. Isenor, "Passive mode locking of lasers with the optical Kerr effect modulator," *Quantum Electronics, IEEE Journal of,* vol. 13, pp. 915-924, 1977.
[1.27] H. A. Haus, J. G. Fujimoto, and E. P. Ippen, "Structures for additive pulse mode locking," *JOSA B,* vol. 8, pp. 2068-2076, 1991.
[1.28] R. Fork, B. Greene, and C. Shank, "Generation of optical pulses shorter than 0.1 psec by colliding pulse mode locking," *Applied Physics Letters,* vol. 38, pp. 671-672, 1981.
[1.29] D. E. Spence, P. N. Kean, and W. Sibbett, "60-fsec pulse generation from a self-mode-locked Ti: sapphire laser," *Optics letters,* vol. 16, pp. 42-44, 1991.
[1.30] G. Cerullo, S. De Silvestri, V. Magni, and L. Pallaro, "Resonators for Kerr-lens mode-locked femtosecond Ti:sapphire lasers," *Optics Letters,* vol. 19, pp. 807-809, 1994.
[1.31] J. Herrmann, "Theory of Kerr-lens mode locking: role of self-focusing and radially varying gain," *JOSA B,* vol. 11, pp. 498-512, 1994.
[1.32] I. P. Christov, H. C. Kapteyn, M. M. Murnane, C.-P. Huang, and J. Zhou, "Space–time focusing of femtosecond pulses in a Ti: sapphire laser," *Optics letters,* vol. 20, pp. 309-311, 1995.
[1.33] I. P. Christov, M. M. Murnane, H. C. Kapteyn, and V. D. Stoev, "Mode locking with a compensated space–time astigmatism," *Optics letters,* vol. 20, pp. 2111-2113, 1995.
[1.34] I. P. Christov and V. D. Stoev, "Kerr-lens mode-locked laser model: role of space time effects," *JOSA B,* vol. 15, pp. 1960-1966, 1998.
[1.35] I. P. Christov, V. D. Stoev, M. M. Murnane, and H. C. Kapteyn, "Absorber-assisted Kerr-lens mode locking," *JOSA B,* vol. 15, pp. 2631-2633, 1998.
[1.36] V. Kalosha, M. Müller, J. Herrmann, and S. Gatz, "Spatiotemporal model of femtosecond pulse generation in Kerr-lens mode-locked solid-state lasers," *JOSA B,* vol. 15, pp. 535-550, 1998.
[1.37] Y. Chen, F. Kärtner, U. Morgner, S. Cho, H. Haus, E. Ippen*, et al.*, "Dispersion-managed mode locking," *JOSA B,* vol. 16, 1999.
[1.38] M. Y. Sander, J. Birge, A. Benedick, H. M. Crespo, and F. X. Kärtner, "Dynamics of dispersion managed octave-spanning titanium: sapphire lasers," *JOSA B,* vol. 26, pp. 743-749, 2009.
[1.39] M. Nisoli, S. De Silvestri, O. Svelto, R. Szipöcs, K. Ferencz, C. Spielmann*, et al.*, "Compression of high-energy laser pulses below 5 fs," *Optics Letters,* vol. 22, pp. 522-524, 1997/04/15 1997.

[1.40] E. Matsubara, K. Yamane, T. Sekikawa, and M. Yamashita, "Generation of 2.6 fs optical pulses using induced-phase modulation in a gas-filled hollow fiber," *JOSA B,* vol. 24, pp. 985-989, 2007.
[1.41] A. Wirth, M. T. Hassan, I. Grguraš, J. Gagnon, A. Moulet, T. T. Luu*, et al.*, "Synthesized light transients," *Science,* vol. 334, pp. 195-200, 2011.
[1.42] S. Bohman, A. Suda, T. Kanai, S. Yamaguchi, and K. Midorikawa, "Generation of 5.0 fs, 5.0 mJ pulses at 1 kHz using hollow-fiber pulse compression," *Optics Letters,* vol. 35, pp. 1887-1889, 2010/06/01 2010.
[1.43] G. Cerullo, M. Nisoli, S. Stagira, and S. De Silvestri, "Sub-8-fs pulses from an ultrabroadband optical parametric amplifier in the visible," *Optics letters,* vol. 23, pp. 1283-1285, 1998.
[1.44] A. Baltuška, T. Fuji, and T. Kobayashi, "Visible pulse compression to 4 fs by optical parametric amplification and programmable dispersion control," *Optics letters,* vol. 27, pp. 306-308, 2002.
[1.45] G. Cerullo and S. De Silvestri, "Ultrafast optical parametric amplifiers," *Review of scientific instruments,* vol. 74, pp. 1-18, 2003.
[1.46] A. Siddiqui, G. Cirmi, D. Brida, F. Kärtner, and G. Cerullo, "Generation of< 7 fs pulses at 800 nm from a blue-pumped optical parametric amplifier at degeneracy," *Optics letters,* vol. 34, pp. 3592-3594, 2009.
[1.47] D. Brida, G. Cirmi, C. Manzoni, S. Bonora, P. Villoresi, S. De Silvestri*, et al.*, "Sub-two-cycle light pulses at 1.6 μm from an optical parametric amplifier," *Optics letters,* vol. 33, pp. 741-743, 2008.
[1.48] T. T. Luu, M. T. Hassan, A. Moulet, O. Razskazovskaya, N. Kaprowicz, V. Pervak*, et al.*, "Isolated optical attosecond pulses," in *CLEO: QELS_Fundamental Science*, 2013, p. QF1C. 6.
[1.49] M. Nisoli, S. Stagira, S. De Silvestri, O. Svelto, S. Sartania, Z. Cheng*, et al.*, "Toward a terawatt-scale sub-10-fs laser technology," *Selected Topics in Quantum Electronics, IEEE Journal of,* vol. 4, pp. 414-420, 1998.
[1.50] M. Ebrahim-Zadeh and I. T. Sorokina, *Mid-infrared coherent sources and applications*: Springer Science & Business Media, 2008.
[1.51] D. Strickland and G. Mourou, "Compression of amplified chirped optical pulses," *Optics communications,* vol. 55, pp. 447-449, 1985.
[1.52] J. Moses, C. Manzoni, S.-W. Huang, G. Cerullo, and F. X. Kaertner, "Temporal optimization of ultrabroadband high-energy OPCPA," *Optics express,* vol. 17, pp. 5540-5555, 2009.
[1.53] R. Fork, O. Martinez, and J. Gordon, "Negative dispersion using pairs of prisms," *Optics letters,* vol. 9, pp. 150-152, 1984.
[1.54] E. Treacy, "Optical pulse compression with diffraction gratings," *Quantum Electronics, IEEE Journal of,* vol. 5, pp. 454-458, 1969.
[1.55] R. Szipöcs, C. Spielmann, F. Krausz, and K. Ferencz, "Chirped multilayer coatings for broadband dispersion control in femtosecond lasers," *Optics Letters,* vol. 19, pp. 201-203, 1994.
[1.56] F. Kärtner, N. Matuschek, T. Schibli, U. Keller, H. Haus, C. Heine*, et al.*, "Design and fabrication of double-chirped mirrors," *Optics letters,* vol. 22, pp. 831-833, 1997.
[1.57] N. Matuschek, L. Gallmann, D. Sutter, G. Steinmeyer, and U. Keller, "Back-side-coated chirped mirrors with ultra-smooth broadband dispersion characteristics," *Applied Physics B,* vol. 71, pp. 509-522, 2000.

[1.58] F. Kärtner, U. Morgner, R. Ell, T. Schibli, J. Fujimoto, E. Ippen*, et al.*, "Ultrabroadband double-chirped mirror pairs for generation of octave spectra," *JOSA B,* vol. 18, pp. 882-885, 2001.
[1.59] G. Tempea, V. Yakovlev, B. Bacovic, F. Krausz, and K. Ferencz, "Tilted-front-interface chirped mirrors," *JOSA B,* vol. 18, pp. 1747-1750, 2001.
[1.60] G. Steinmeyer, "Brewster-angled chirped mirrors for high-fidelity dispersion compensation and bandwidths exceeding one optical octave," *Optics express,* vol. 11, pp. 2385-2396, 2003.
[1.61] V. Pervak, A. Tikhonravov, M. Trubetskov, S. Naumov, F. Krausz, and A. Apolonski, "1.5-octave chirped mirror for pulse compression down to sub-3 fs," *Applied Physics B,* vol. 87, pp. 5-12, 2007.
[1.62] V. Pervak, F. Krausz, and A. Apolonski, "Dispersion control over the ultraviolet-visible-near-infrared spectral range with HfO_2/SiO_2-chirped dielectric multilayers," *Optics letters,* vol. 32, pp. 1183-1185, 2007.
[1.63] T. Tanigawa, Y. Sakakibara, S. Fang, T. Sekikawa, and M. Yamashita, "Spatial light modulator of 648 pixels with liquid crystal transparent from ultraviolet to near-infrared and its chirp compensation application," *Optics letters,* vol. 34, pp. 1696-1698, 2009.
[1.64] P. Tournois, "Acousto-optic programmable dispersive filter for adaptive compensation of group delay time dispersion in laser systems," *Optics communications,* vol. 140, pp. 245-249, 1997.
[1.65] E. Zeek, K. Maginnis, S. Backus, U. Russek, M. Murnane, G. Mourou*, et al.*, "Pulse compression by use of deformable mirrors," *Optics Letters,* vol. 24, pp. 493-495, 1999.
[1.66] S.-W. Huang, G. Cirmi, J. Moses, K.-H. Hong, S. Bhardwaj, J. R. Birge*, et al.*, "High-energy pulse synthesis with sub-cycle waveform control for strong-field physics," *Nature photonics,* vol. 5, pp. 475-479, 2011.
[1.67] O. Mucke, S. Fang, G. Cirmi, G. Rossi, S.-H. Chia, H. Ye*, et al.*, "Toward Waveform Nonlinear Optics Using Multimillijoule Sub-Cycle Waveform Synthesizers," *Selected Topics in Quantum Electronics, IEEE Journal of,* vol. 21, pp. 1-12, 2015.
[1.68] N. G. Horton, K. Wang, D. Kobat, C. G. Clark, F. W. Wise, C. B. Schaffer*, et al.*, "In vivo three-photon microscopy of subcortical structures within an intact mouse brain," *Nature photonics,* vol. 7, pp. 205-209, 2013.
[1.69] C. Xu, W. Zipfel, J. B. Shear, R. M. Williams, and W. W. Webb, "Multiphoton fluorescence excitation: new spectral windows for biological nonlinear microscopy," *Proceedings of the National Academy of Sciences,* vol. 93, pp. 10763-10768, 1996.
[1.70] D. R. Larson, W. R. Zipfel, R. M. Williams, S. W. Clark, M. P. Bruchez, F. W. Wise*, et al.*, "Water-soluble quantum dots for multiphoton fluorescence imaging in vivo," *Science,* vol. 300, pp. 1434-1436, 2003.
[1.71] Y. Barad, H. Eisenberg, M. Horowitz, and Y. Silberberg, "Nonlinear scanning laser microscopy by third harmonic generation," *Applied Physics Letters,* vol. 70, pp. 922-924, 1997.
[1.72] E. Brown, T. McKee, A. Pluen, B. Seed, Y. Boucher, and R. K. Jain, "Dynamic imaging of collagen and its modulation in tumors in vivo using second-harmonic generation," *Nature medicine,* vol. 9, pp. 796-800, 2003.
[1.73] S.-W. Chu, S.-Y. Chen, T.-H. Tsai, T.-M. Liu, C.-Y. Lin, H.-J. Tsai*, et al.*, "In vivo developmental biology study using noninvasive multi-harmonic generation microscopy," *Optics Express,* vol. 11, pp. 3093-3099, 2003.

[1.74] D. Débarre, W. Supatto, A.-M. Pena, A. Fabre, T. Tordjmann, L. Combettes*, et al.*, "Imaging lipid bodies in cells and tissues using third-harmonic generation microscopy," *Nature methods,* vol. 3, pp. 47-53, 2006.
[1.75] R. D. Wampler, D. J. Kissick, C. J. Dehen, E. J. Gualtieri, J. L. Grey, H.-F. Wang*, et al.*, "Selective detection of protein crystals by second harmonic microscopy," *Journal of the American Chemical Society,* vol. 130, pp. 14076-14077, 2008.
[1.76] D. J. Kissick, D. Wanapun, and G. J. Simpson, "Second-order nonlinear optical imaging of chiral crystals," *Annual review of analytical chemistry (Palo Alto, Calif.),* vol. 4, p. 419, 2011.
[1.77] A. Zumbusch, G. R. Holtom, and X. S. Xie, "Three-dimensional vibrational imaging by coherent anti-Stokes Raman scattering," *Physical Review Letters,* vol. 82, p. 4142, 1999.
[1.78] C. L. Evans, E. O. Potma, M. Puoris' haag, D. Côté, C. P. Lin, and X. S. Xie, "Chemical imaging of tissue in vivo with video-rate coherent anti-Stokes Raman scattering microscopy," *Proceedings of the National Academy of Sciences of the United States of America,* vol. 102, pp. 16807-16812, 2005.
[1.79] C. W. Freudiger, W. Min, B. G. Saar, S. Lu, G. R. Holtom, C. He*, et al.*, "Label-free biomedical imaging with high sensitivity by stimulated Raman scattering microscopy," *Science,* vol. 322, pp. 1857-1861, 2008.
[1.80] S. W. Hell and J. Wichmann, "Breaking the diffraction resolution limit by stimulated emission: stimulated-emission-depletion fluorescence microscopy," *Optics letters,* vol. 19, pp. 780-782, 1994.
[1.81] S. W. Hell, "Far-field optical nanoscopy," *science,* vol. 316, pp. 1153-1158, 2007.
[1.82] M. E. Fermann and I. Hartl, "Ultrafast fibre lasers," *Nature photonics,* vol. 7, pp. 868-874, 2013.
[1.83] S.-H. Chia, G. Cirmi, S. Fang, G. M. Rossi, O. D. Mücke, and F. X. Kärtner, "Two-octave-spanning dispersion-controlled precision optics for sub-optical-cycle waveform synthesizers," *Optica,* vol. 1, pp. 315-322, 2014/11/20 2014.
[1.84] S.-H. Chia, L.-J. Chen, Q. Zhang, O. D. Mücke, G. Chang, and F. X. Kärtner, "Broadband continuum generation in mode-locked lasers with phase-matched output couplers," *Optics Letters,* vol. 39, pp. 1445-1448, 2014/03/15 2014.
[1.85] L.-J. Chen, "Design, optimization, and applications of few-cycle Ti: Sapphire lasers," Massachusetts Institute of Technology, 2012.

Chapter 2

Multi-octave dispersion control by dispersive dielectric mirrors

2.1 Introduction to dispersion management

2.1.1 Introduction to optical dispersion

Nowadays, ultrashort pulses supporting coherent bandwidths over several hundred nanometers have been routinely obtained and widely applied in many research fields. However, when propagating through a linear optical system, broadband pulses are reshaped due to dispersion: the waves of different optical frequencies have different phase velocities (*i.e.*, material dispersions) or different optical paths (*i.e.*, the dispersions introduced by *e.g.* grating pairs [2.1], prism pairs [2.2], and dispersive mirrors [2.3]). The effect of the dispersion has always to be seriously considered during ultrashort pulse propagation to the purposes of source development and precise waveform control. For example, the advance in ultrafast sources has relied extensively on the developments of ways to characterize and manipulate dispersion: the generated spectral bandwidth, pulse duration, and pulse energy are often limited by the dispersive properties of the optical elements in the source. Furthermore, studies of ultrafast dynamics and strong-field physics strongly depends on the capability of pulse-shape manipulation and dispersion management which limits the duration of the burst that can be generated or delivered effectively to the target.

Ways to characterize dispersion have been well developed. After passing through a dispersive optical element, the pulse suffers not only from a distortion of the group delay but also of the pulse-shape. The group delay (T_g) is specified as the phase ($\emptyset$) derivative on frequency ($\partial\emptyset/\partial\omega$). The pulse-shape distortion is usually characterized by the Taylor coefficients of the group delay with respect to frequency ω (*e.g.* group delay dispersion

(GDD): $\partial T_g/\partial\omega$, and third-order dispersion (TOD): $\partial^2 T_g/\partial\omega^2$) at the center frequency of the pulse. For a positively (resp. negatively) chirped pulse (*i.e.* with positive (resp. negative) GDD), the higher frequency components are lagging behind (resp. going ahead) the lower ones; unlike GDD, net TOD leads to an asymmetric pulse broadening with side lobes and other detrimental structures. However, when propagating an ultrabroadband (*e.g.* octave-spanning) optical burst, the Taylor series of the group delay at a center frequency may not be sufficient to describe its dispersive behavior; Taylor expansion is a local approximation of a mathematical function, but an octave-spanning spectrum goes over the validity range of this approximation. Therefore, instead of using the coefficients of higher-order dispersion at a center wavelength, the group delay of each wavelength in the whole operating range is characterized and applied to octave-spanning pulses in the following chapters.

Light-propagating media are the most common sources of optical dispersion. Therefore, the material dispersion should be precisely modeled and measured before considering dispersion compensation. In transparent material, the material dispersion is typically described by the Sellmeier equations in the following form:

$$n^2(\lambda) = 1 + \frac{B_1\lambda^2}{\lambda^2 - C_1} + \frac{B_2\lambda^2}{\lambda^2 - C_2} + \frac{B_3\lambda^2}{\lambda^2 - C_3}, \tag{2.1}$$

where n is the refractive index, and λ is the wavelength. $B_{1,2,3}$ and $C_{1,2,3}$ are the experimentally determined Sellmeier coefficients. These coefficients are usually quoted for λ in micrometer in vacuum. Some examples are provided in Table 2.1, as well as the corresponding dispersion plotted in Fig. 2.1. In the visible and near infrared regimes, the materials typically provide positive (or normal) dispersion. Therefore, the main goal of dispersion compensation in ultrafast sources is typically to offer negative dispersion.

	B_1	B_2	B_3	C_1	C_2	C_3
Ti:sapphire	1.023798	1.058264	5.280792	0.0037758	0.012254	321.3616
Air	0.0002463	0.000299	-	0.0082250	0.003637	-
BaF_2	0.643356	0.506762	3.8261	0.0033396	0.012029	2151.698
Fused silica	0.68374	0.42032	0.58503	0.0046035	0.013397	64.493

Table 2.1. The Sellmeier coefficients of the commonly-used materials for dispersion compensation [2.4]. The coefficients for air are for NTP condition.

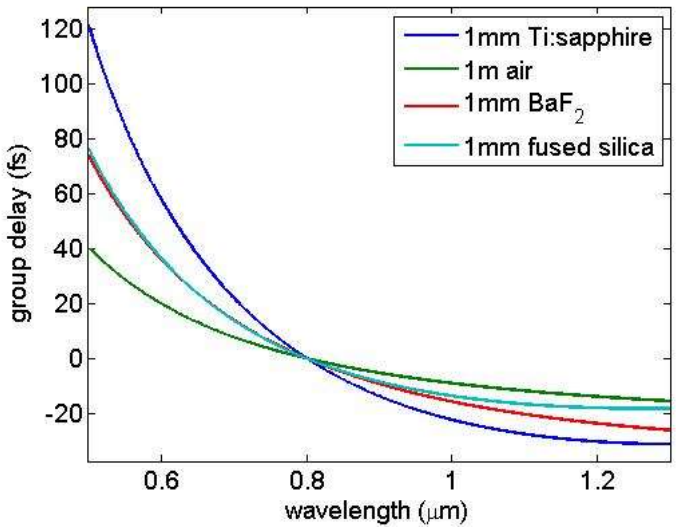

Fig. 2.1. Material dispersion: wavelength-dependent group delays of the materials listed in Table 2.1.

2.1.2 **Dispersion compensation techniques**

Several dispersion-compensating methods have been demonstrated. One has to consider the characteristics of different methods, such as the operating bandwidth, overall throughput, and maximum pulse-energy handling, when applied in various ultrafast laser applications.

The use of diffraction grating pairs is the first way to achieve tunable negative GDD [2.1], demonstrated in 1969. Fork *et al*. also obtained negative GDD with pairs of Brewster-angled prisms in 1984 [2.2]. The origin of the adjustable dispersion is the angular dispersion arising from diffraction and refraction in grating and prism pairs, respectively. Compared to prism pairs, grating pairs typically offer a larger amount of GDD but with a higher loss. Therefore, prism pairs have been widely used inside laser oscillators, and grating pairs usually employed as external pulse compressors/stretchers. For instance, using only fused silica prisms, <10-fs of optical pulses have been obtained directly from an oscillator in 1994 [2.5]. However, either using grating or prism pairs, the offered negative GDD is associated with a significant amount of higher-order dispersion which limits the capability of the compensating bandwidth. Thus, a combination of both prism and grating pairs with opposite-sign TOD is capable of the generation of <5-fs pulses with an external compression

[2.6]. Nonetheless, such combinations cannot be applied for few-optical-cycle pulse generation either in laser oscillators due to the losses of the gratings, or in external compressors at high power level due to the onset of unwanted nonlinearities in prisms. Moreover, the operating bandwidth about ~1 octave is also hampered by the use of gratings: one has to avoid the angular overlapping between different diffraction orders.

Active dispersion control (*i.e.,* adaptive dispersion provided with a feedback loop) can be realized based on liquid-crystal modulators [2.7, 8], acousto-optic modulators [2.9], and mechanically deformable mirrors [2.10, 11]. With prisms or gratings to provide a spatial distribution of the different frequencies, the relative phase between different frequencies can be independently adjusted by the elements of liquid-crystal modulators or deformable mirrors. 2.6-fs pulses can be obtained based on liquid-crystal modulators and 4-*f* grating systems [2.7]. The total throughput is also limited by the efficiency of gratings.

Without gratings and prisms, pulse shapers based on acousto-optic modulators provide a compact solution with nearly no angular deformation [2.9]. However, the acoustic time length, optical self-focusing effect, higher-order dispersion of the acousto-optic birefringent crystal and compensation of the own dispersion of the device limit the operating repetition rate, maximum handling peak power, working bandwidth, and shaping capability, respectively. Although devices approaching one octave in bandwidth are possible, the total throughput is quite low, typically 10-50%, depending on the bandwidth of the device.

In general, dispersion management with <1 octave in bandwidth is well developed via the above-mentioned methods. Grating-based techniques, which can also be applied as pulse stretchers, typically provide a large amount of dispersion from diffraction but the overall throughput is also limited by diffraction. The maximum pulse-energy handling limits the use of prism-based pulse shapers in high power amplifiers due to the unwanted nonlinearities in the bulk material of the prisms. As a result, a robust and low-loss solution is in great demand to tailor the dispersion of intense optical bursts with multi-octave bandwidth.

2.2 Introduction to dispersive dielectric mirror designs

Chirped mirrors, composed of alternating high and low index layers, provide a high reflection window with well-controlled dispersion by designing the coating thickness of alternating layers. Chirped mirrors are typically grown by ion-beam sputtering, which allows low absorption losses (<100 ppm) [2.12]. Therefore, these mirrors have been widely used for broadband intracavity dispersion compensation. In addition, the use of chirped mirrors is promising for the compression of high-energy pulses because the desired dispersion is provided with little material (*i.e.* less than a few micrometers) in the beam path, thus avoiding nonlinear effects in the compressor.

In chirped mirrors, the dispersion is designed and provided by varying the optical path between different wavelengths via Bragg reflection [2.3]. A positive/negative chirp can be provided by decreasing/increasing the layer thickness from the ambient medium to the mirror substrate. The designed bandwidth depends on both the total layer number and the Fresnel reflection bandwidth. Fresnel bandwidth is defined as the high reflection bandwidth of a standard dielectric Bragg-mirror, which is determined by the Fresnel reflectivity between the alternating high and low index materials. Therefore, larger index contrast between the two materials provides larger reflection bandwidth. As a result, TiO_2 or Nb_2O_5 are typically used as the high index material, and SiO_2 as the low one in broadband chirped mirror design. Fig. 2.2(a) shows the simple-chirped structure with TiO_2/SiO_2 layer pairs, where the Bragg wavelength is monotonically increased with each quarter-wave layer pair to provide negative dispersion, as well as a broader high-reflection bandwidth than the Fresnel reflection bandwidth of a fixed layer pair [2.3]. The high reflectivity range of the chirped structure can be easily extended to >1 octave by simply chirping slowly enough and using a sufficient number of layer pairs. However, pronounced GD ripples are usually observed as the lower blue curve shown in Fig. 2.3. In fact, high reflection chirped mirrors act as Gires-Tournois interferometers. These GD ripples are due to the impedance mismatch between the free space and the multi-layer grating. Since the period of the oscillations in the spectral domain determines the position of a satellite in the time domain, the suppression of the adverse GD ripples by achieving impedance matching to avoid internal resonances is of great importance especially in few-optical-cycle pulse generation.

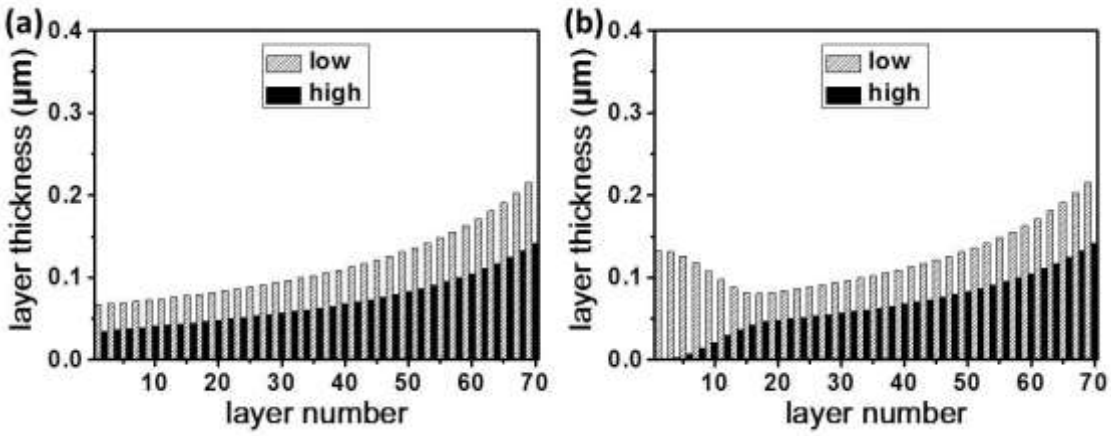

Fig. 2.2. Design structures of different chirped mirrors, (a) simple chirped structure and (b) double chirped structure. Light enters from the first layer, and the last layer is directly deposited on the fused silica substrate.

Several CM structures were proposed to smooth the GD ripples: double-chirped mirrors (DCMs) [2.13, 14], Brewster-angle CMs [2.15], back-side-coated CMs [2.16], tilted-front-interface CMs [2.17]. The double-chirped structure [2.13], as shown in Fig. 2.2(b), has been proposed to achieve impedance matching by adiabatically tapering the impedance in the front layer pairs, which is shown to be equivalent to an adiabatic chirp in the thickness of the high index layer in addition to the chirp of the center wavelength of the Bragg mirror. The smoother GD from double chirped structure comparing with the simple chirped one is plotted as the lower red curve in Fig. 2.3. DCMs are typically matched to the low index material of the mirror due to the less impedance mismatch with the ambient air. Ideally, the matching can be extended to any other ambient medium by a properly designed AR-coating in the front layers.

In reality, the quality of the required AR-coating for impedance matching is demanding (*e.g.*, <0.1% in reflectivity) in order to suppress the adverse GD ripples especially for broadband dispersion control. To relax the quality of the required AR-coating, the Back-side-coated CM [2.16] and tilted-front-interface designs [2.17] were thus proposed to direct out the residual reflection from the main beam path. For example, in tilted-front-interface designs [2.17], the AR-coating is deposited on the front of the slightly wedged substrate, so that the residual reflection has a different reflection angle than the main beam: the dispersion properties of the main beam aren't affected by the residual reflection. Although these designs are good enough for some applications, the Fresnel reflection loss along with

relaxed AR-coating (*e.g.*, at least 1% of loss) still hampers low-loss applications, such as intracavity dispersion control for octave-spanning Ti:sapphire oscillators.

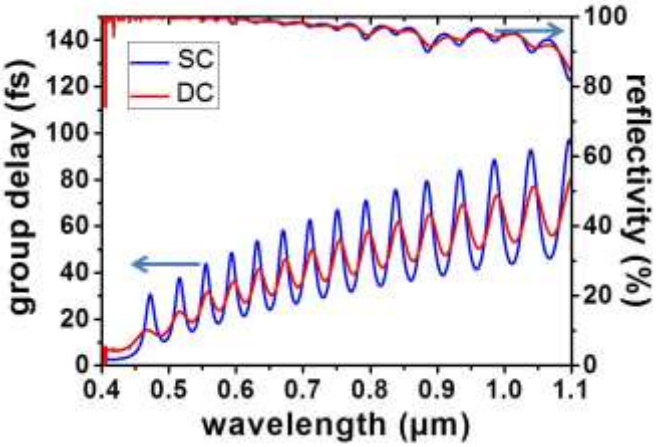

Fig. 2.3. Reflectivities and GDs of different structures shown in Fig. 2.2. SC: simple chirped structure (*i.e.*, Fig. 2.2(a)); DC: double chirped structure (*i.e.*, Fig. 2.2(b)).

DCMs under Brewster-angle incidence [2.15] can be the solution for the Fresnel reflection loss issue. In this case, the impedance of the low index layer is automatically matched to the ambient air. 1.5-octave in bandwidth has been demonstrated with Brewster-angle CMs. However, under p-polarized incidence the index contrast or Fresnel reflectivity of a layer pair is reduced as discussed in Subsection 2.5.1. Moreover, more layer pairs are necessary to achieve high reflectivity, which increases the fabrication difficulty. Furthermore, Brewster-angle-incidence mirrors are hardly implemented as curved mirrors, which are the key elements inside a laser oscillator.

Complementary pair designs are thus proposed [2.14, 18] to extend the operating bandwidth while maintaining the high reflectivity. One can design a complementary coating to compensate for the GD ripples from a single chirped mirror, for example, with an additional phase shift of π (*i.e.*, placing a layer with quarter-wavelength thickness) between the AR-coating and the back-mirror [2.14]. The first-order GTI-effect is thus canceled with a complementary pair, which constitutes a tremendous improvement since the required reflectivity of the front AR-coating is less demanding. <5fs pulse can be directly obtained in an octave-spanning Ti:sapphire oscillators using DCM pairs as intracavity mirrors [2.14]. As external pulse compressors, 1.5-octave-wide dispersion compensations were achieved with average reflectivity of >95% in the range of 0.4 μm - 1.2 μm [2.19], as well as in UV-VIS-NIR

range of 0.3 μm – 0.9 μm [2.20]. These mirror pairs make it possible to compress pulses down to sub-3 fs. The discussions on limitations of compensating bandwidth and amount are provided in Section 2.4.

2.3 **Chirped dichroic mirrors**

2.3.1 **Dual-adiabatic-matching structures**

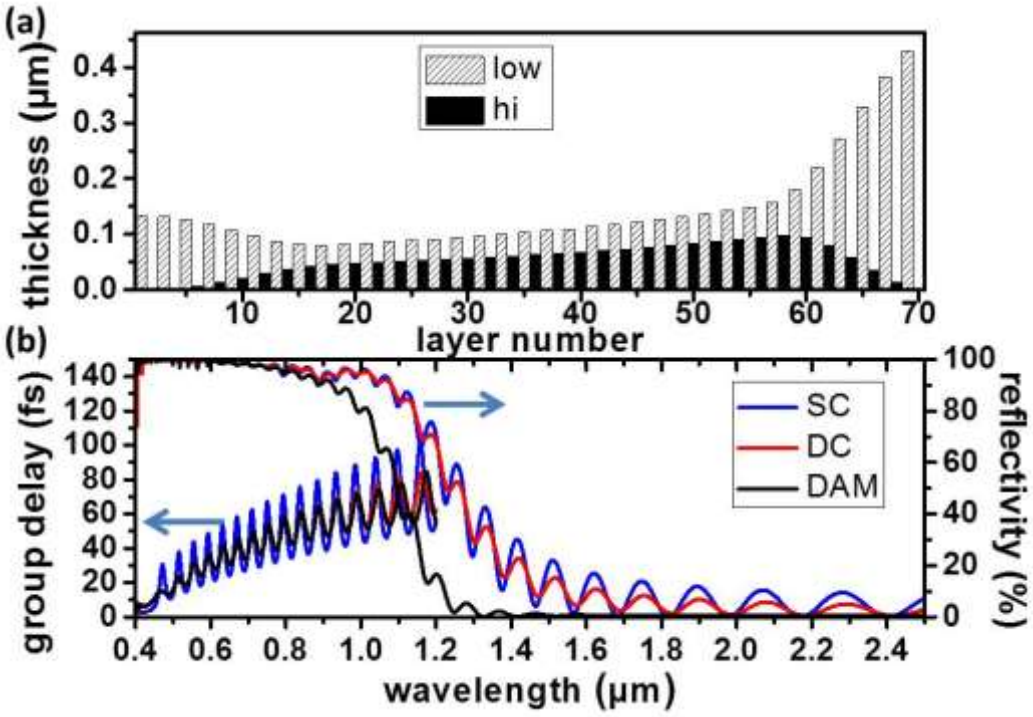

Fig. 2.4. (a) Dual adiabatic matching (DAM) structure and (b) the corresponding reflectivity and group delay, as well as the ones of simple-chirped and double-chirped structures. SC: simple chirped structure (*i.e.*, Fig. 2.2(a)); DC: double chirped structure (*i.e.*, Fig. 2.2(b)).

Multilayer mirror designs covering more than 2 octaves in bandwidth require multi-octave impedance matching, and have not been achieved so far. Analytic designs of coating structures should be further exploited. Here, we introduce a dual-adiabatic-matching (DAM) structure [2.21], as shown in Fig. 2.4(a). Based on a double-chirped design, the DAM structure introduces another double chirp in the back section of the mirror approaching the substrate, adiabatically tapering the impedance again to provide high transmission for long wavelengths. Reflectivities and dispersion behaviors of different designs (*i.e.,* simple chirped, double chirped, and DAM structure) are also plotted in Fig. 2.4(b). The front and back

chirped high-index layers perform dual adiabatic impedance matching, providing (1) high reflectivity and smooth GD over the high reflectivity range of the mirror and (2) high transmission with side-lobe suppression outside the high-reflectivity range, respectively.

Based on the above-mentioned characteristics of the DAM structure, the proposed structure can be used as an ultrabroadband chirped dichroic mirror (CDM), which is a dichroic mirror with a well-controlled chirp over the reflection window. To realize the idea, the analytical DAM structure is employed as an initial design, which provides a high-reflection window for the spectral range of 0.45 μm – 1 μm and transmission in the range of 1.1 μm - 2.5 μm for p-polarized laser beams with an incident angle of 45^{o}. The design procedure optimizes the thicknesses and number of layers, as well as the compensating thickness of the dispersive material (*e.g.,* fused silica), using a fast algorithm [2.22, 23]. The numerical optimized result is shown in Fig. 2.5. With an AR coating in the initial few layers, the following structure preserves the DAM structure. The GD in reflection is optimized to compensate 0.52 mm optical path in fused silica over the spectral range from 0.45 μm - 1.3 μm, which is even broader than the high-reflectivity range of 0.45 μm - 1.1 μm as shown in Fig. 2.6.

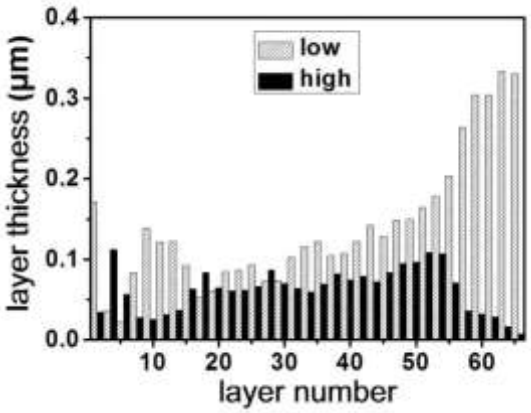

Fig. 2.5. The perturbed DAM structure to optimize the reflectivity and group delay behaviors using the initial DAM structure, as well as a AR coating section in the initial few layers to provide impedance matching from air to the low index material.

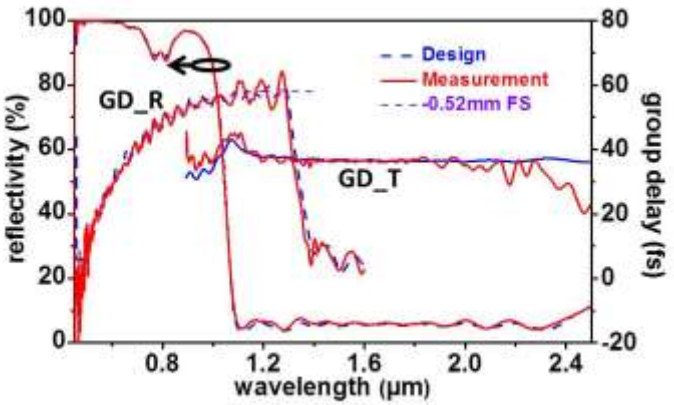

Fig. 2.6. Reflectivity and group delay in both reflection and transmission of the optimized DAM mirror [2.24], which can be used as a CDM with a high reflectivity band in the range 0.45 μm - 1 μm and a high transmission band 1.1 μm – 2.4 μm. The group delay in reflection from 0.45 μm – 1.3 μm is designed to compensate the dispersion of 0.52mm optical path in fused silica, as shown by the purple dashed curve. GD_R, designed/measured GD in reflection; GD_T, the transmitted designed/measured GD; FS, fused silica.

2.3.2 **Kramer-Kronig relation in mirror designs**

Coherent synthesis of pulses with different spectra provides a route towards generation of multi-octave spanning optical waveform. In addition to the bandwidth scalability, the synthesized waveform can be customary tailored by controlling the phase offset between different channels. In order to combine coherent spectra with a spectral overlap, the simultaneous dispersion management in both reflection and transmission, especially around the edge of the high-reflection band, is very important. However, the GD oscillations in the margin of the high reflection window are usually rather large due to the strong resonant interferences originating from internal Fabry–Pérot effects. The backside impedance-matching section in the DAM structure in Fig. 2.4(a) smooths the transmittance and reduces these typically observed GD oscillations, as shown in Fig. 2.4(b): since the reflection from the back impedance-matching region is suppressed, the etalon resonance is reduced between the quarter-wave Bragg stacks and the back impedance-matching section. On the other hand, the GD in the transmission port is subject to the Kramers-Kronig relation [2.25]:

$$\emptyset_t = \frac{-1}{\pi} \boldsymbol{P} \int_{-\infty}^{\infty} \frac{ln|T(\omega')|}{\omega - \omega'} d\omega' \qquad (2.1)$$

where $\emptyset_t$ and $T(\omega')$ are the transmission phase and transmittance, respectively. By taking the derivatives on both sides and integrating by parts on the right-hand side, one can obtain:

$$\boldsymbol{GD} = \frac{\boldsymbol{d\emptyset_t}}{\boldsymbol{d\omega}} = \frac{1}{\pi}\boldsymbol{P}\int_{-\infty}^{\infty}\frac{\boldsymbol{T'}}{\boldsymbol{\omega-\omega'}}d\omega', \text{ where } T' \equiv \frac{dT(\omega')/d\omega'}{T(\omega')} \tag{2.2}$$

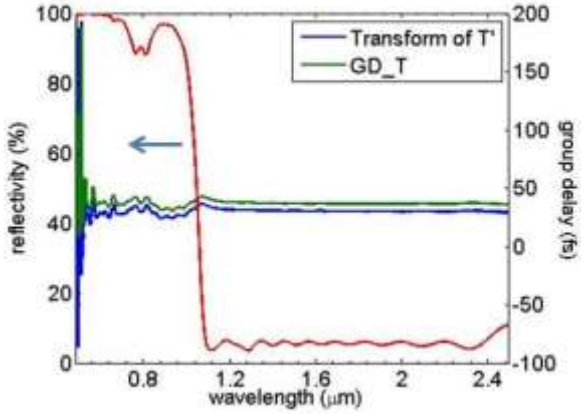

Fig. 2.7. Transmission and GD of the designed CDM, as well as the GD derived from Eq. 2.2. The Hilbert transform of T' is in a great agreement with the calculated GD with an artificial GD offset. GD_T, the transmitted designed GD.

Therefore, the GD in transmission is the Hilbert transform of *T'*, which is mathematically analogous to the relation between absorption and reflection coefficients in electron spectroscopy [2.26, 27]. As a result, the variations of GD in transmission (*i.e.*, group-delay dispersion (GDD)) are related to the changes of the transmittance curves especially in the spectral range close to the edge of the high-reflection band: If the transmittance of the CDM is slowly varying in the transition region, the corresponding GD curve is also slowly varying. In Fig. 2.7, with the transmittance of the designed CDM, the Hilbert transform from Eq. 2.2 is in a great agreement with the GD obtained from the analytic computation [2.22]. With the designed CDM, the variation of the transmission GD in the transition range between high-transmission band and high-reflection band, 1.0 μm -1.1 μm, is <10 fs. The nature of Hilbert transform in Eq. 2.2 suggests that even lower GD variation is possible based on a mirror with a smoother transmittance curve and a wider transition region. As an example, Fig. 2.8(a) shows the designed transmittances with different slopes. The lower transmission slopes provide lower GD variations in Fig. 2.8(b).

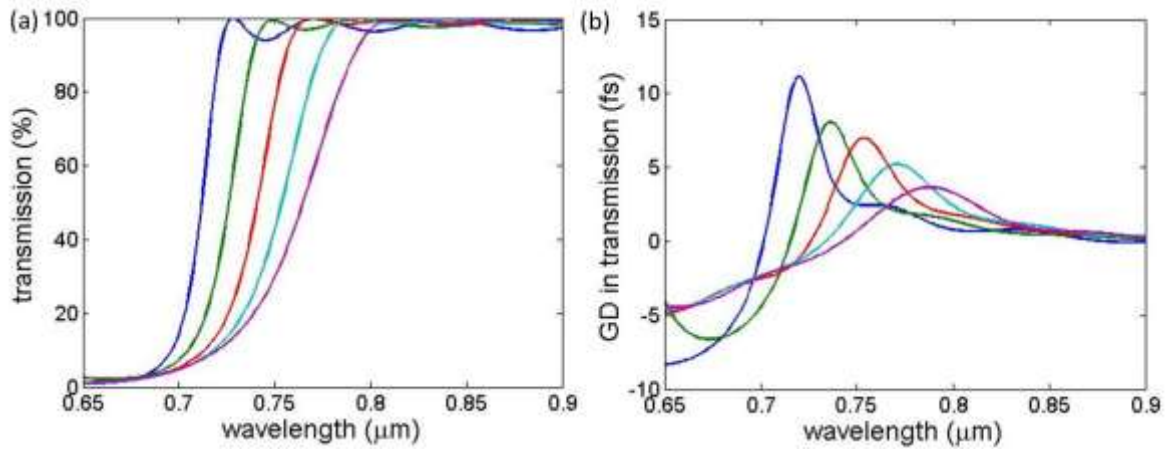

Fig. 2.8. (a) Dichroic mirrors designed with slope-varying transmittances and (b) the corresponding GD in transmission specified with the same color in (a).

2.4 **>2-octave-spanning chirped mirror design**

The dual adiabatic matching (DAM) structure lends itself to the design of an ultrabroadband DCM pair. Ultrabroadband DCM pairs are designed as the final compression unit, which is key enabling technology to realize >2-octaves multi-mJ sub-cycle waveforms, which is discussed in Chapter 3, without running into *B*-integral problems distorting the pulse quality. The proposed structure, which is a proper impedance matching section to reduce the Gires-Tournois effect in the chirped mirror design, reflects the light below its Bragg wavelength and provides a smooth transmittance for the longer wavelengths. As a result, cascading the DAM structure in the front layers, as an ultrabroadband impedance matching section, makes it possible to achieve >2-octave bandwidth DCMs, as shown in Fig. 2.9, designed for a 3-degree incident angle in p-polarization.

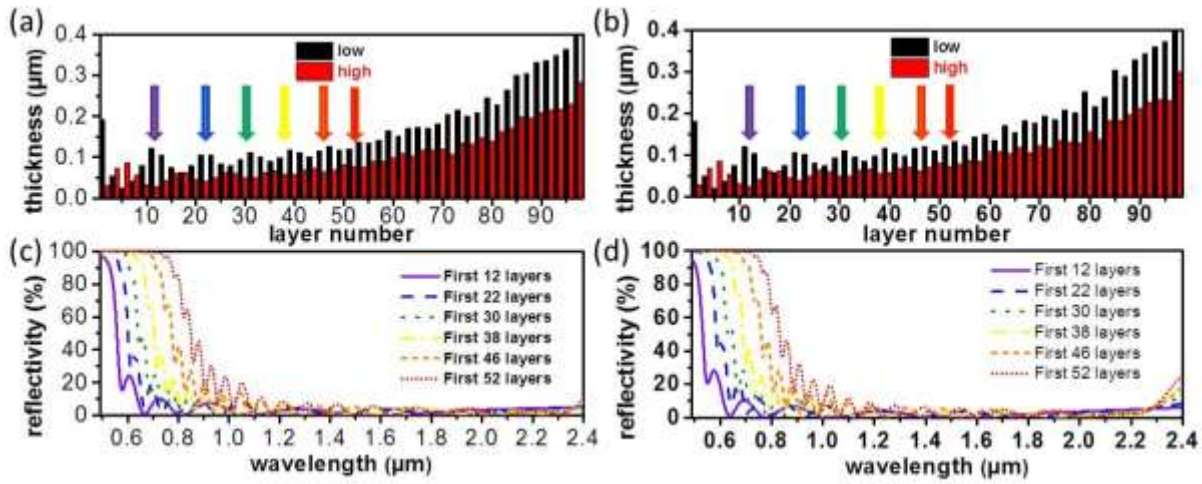

Fig. 2.9. (a) and (b) Structures of the optimized DAM DCM pair [2.24]. (c) and (d) AR behaviors for the longer wavelengths in the cascaded DAM sections indicated by the arrows in the mirror structure in (a) and (b), respectively; low, low-index material, SiO_2; high, high-index material, TiO_2.

For the use in the parametric synthesizer as discussed in Chapter 3, the ultrabroadband DCM pair is designed, and the compensating thickness of dispersive materials is numerically optimized for 1.44 mm optical path in fused silica in the spectral range from 0.49 μm - 1.05 μm, and 0.32 mm optical path in ZnSe in the range of 1.05 μm - 2.3 μm. For >1-octave-wide chirped mirrors, mirrors providing negative chirp are advantageous, because short wavelength light is reflected by the top layers, whereas long wavelength light penetrates deeper and mostly sees an average index of the thinner top layers. In order to demonstrate the broadband impedance matching of the cascaded-DAM-like structures, Fig. 2.9(c-d) shows the reflectivity of the structures from the ambient air to the specific layers pointed by the arrows in Fig. 2.9(a-b), respectively. As the number of front layers increases, starting from the air, the high-reflectivity band expands to longer wavelengths, which is determined by the Bragg wavelength of the layer pairs. The arrows in Fig. 2.9(a-b) point to the end layer of each DAM-like structure, providing broadband AR coating (impedance matching) with <5% reflection to the design wavelength of 2.3 μm. The designed/measured reflectivity and GD of the pair are shown in Fig. 2.10. The average reflectivity of each mirror in the ultrabroadband DCM pair is >90% and the calculated peak-to-peak values of the averaged residual GD ripples are controlled to <5 fs over >2-octave bandwidth. In such super-octave chirped mirrors, the light with short wavelength can be reflected not only by the front quarter-wave-thick layers, but also from the two/three-times thick back layers. As a result, notches in reflectivity around 0.8 μm result from small resonances inside the mirror structure: short-wavelength light should be well-controlled,

depending on the design criteria, and mostly reflected by the front layers, otherwise strong internal resonances occurs for the short wavelengths and leads to deep notches in reflectivity, as well as strong spikes in GD. In Fig. 2.10, the dispersion and reflectivity measurements using a home-built white-light interferometer and a photospectrometer, respectively, show excellent agreement with the design targets.

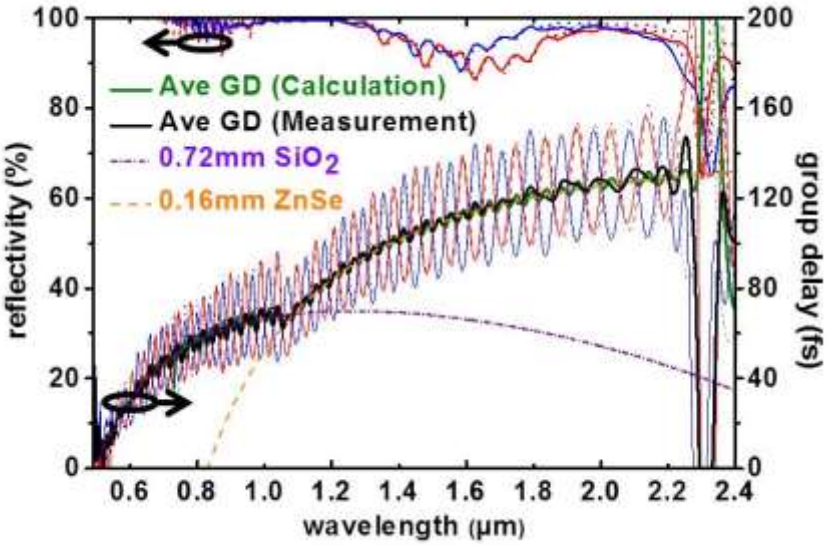

Fig. 2.10. Reflectivity and averaged GD of the ultrabroadband DCM pair [2.24]: the calculation is shown by the blue/red dashed lines and the solid lines show the measurement results. The dispersion of a DCM pair (*i.e.*, twice the average GD) compensates a 1.44-mm optical path in fused silica and a 0.32-mm optical path in ZnSe for ranges of 0.49–1.05 μm and 1.05–2.3 μm, respectively.

2.5 Limitations on current chirped mirror designs

Even broader design bandwidth of DCM pairs could be possible but limited by the required reflectivity and dispersion management, depending on the applications and the capability of precise fabrication control. For example, it is difficult to design chirped mirrors with >99.5% reflection over >2-octave-wide bandwidth to be used as intracavity mirrors for precise dispersion compensation in a broadband laser oscillator.

2.5.1 **Bandwidth scaling with different incident angles**

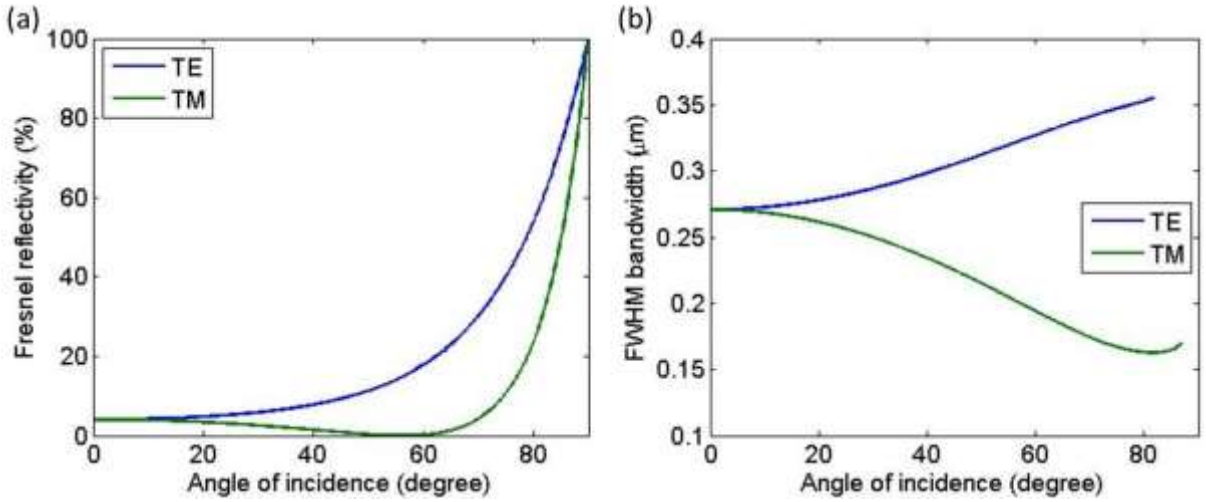

Fig. 2.11. (a) The Fresnel reflectivity and (b) FWHM reflection bandwidth of TiO_2/SiO_2 layer pairs with a Bragg wavelength of 0.8 μm at different incident angles and polarizations. In (b), the bandwidth with a fundamental quarter-wave thickness at 0.8 μm are shown as the blue and green curve with s- and p-polarization, respectively. TE, s-polarization; TM, p-polarization.

In order to achieve even broader bandwidth designs, one has to increase the total layer numbers or increase the Fresnel reflection bandwidth. Although the fabrication tolerance can be improved by experience and feedback monitoring, complicated designs with more layers are harder to be controlled in terms of the reflectivity and GD behavior when growing the coatings, easier leading to cumulative fabrication-errors of mirror characteristics. <100 of the total layer number are typically employed when designing mirrors. In order to further scale the dealing bandwidth, one may try to increase the Fresnel reflection bandwidth by changing the incident angle. As an illustration In a simplified case, if the index difference between the materials is much smaller than its refractive index, Fresnel bandwidth Δf can be expressed as the following forms:

$$\Delta f = \left(\frac{n_H - n_L}{n_H + n_L}\right) f_c cos\theta \quad \text{(in p-polarization)} \tag{2.3}$$

$$\Delta f = \left(\frac{n_H - n_L}{n_H + n_L}\right) f_c sec\theta \quad \text{(in s-polarization)} \tag{2.4}$$

where n_H and n_L are the refractive indices of the high and low index materials, respectively. f_c is the center frequency, and ϑ is the light incident angle between high/low index layers. Fig. 2.11 shows the Fresnel reflectivity and FWHM reflection bandwidth of TiO_2/SiO_2 layer pairs, designed with a Bragg wavelength of 0.8μm at different incident angles and polarizations. As a result, larger/narrower bandwidth can be obtained with a larger angle of incidence in s-

polarization/p-polarization, respectively; however, larger Fresnel reflectivity also implies larger impedance mismatch from ambient medium (*i.e.*, air) to the coating materials, resulting in more pronounced GD oscillations in chirped mirror designs.

In order to explore the bandwidth capabilities with respect to different incident angles and polarizations, different designs optimized for different incident conditions (60° TM, 30° TM, 30° TE, and 60° TE) are investigated and compared with the close-to-normal-incidence case (3° TM) described in Section 2.4. For a fair comparison, the mirror pairs, with a fixed total layer number (~100 layers), are designed and optimized for compensating a piece of fused silica in the spectral range from 0.49 μm - 1.05 μm, and ZnSe in the range of 1.05 μm - 2.3 μm. The GD goals of different pair designs are set to be optimized, complementary to some to-be-determined path lengths of both fused silica and ZnSe, as listed in Table 2.2. >90% reflectivity and <1-rad phase distortion are specified when evaluating the bandwidth capability. Fig. 2.12 shows the reflectivity and average GDs of the designed mirror pairs. Similar to the Bragg mirrors, the design bandwidth is increased from the larger incident angle in p-polarization to the normal incidence, and then further increased in the case with larger incident angle in s-polarization. An extremely broad bandwidth expanding from 0.49 μm to 2.9 μm can be obtained by the 60° TE design. However, more pronounced average GD oscillations due to larger impedance mismatch are observed even in the optimized complimentary pair design.

Even highly pronounced with 25fs fluctuations in the 60° TE design, the fast GD oscillation causes only minor effect in residual phase error, which is still controlled within 1 rad over the whole bandwidth. In order to evaluate the pulse distortion, an ideal design, which has front layers providing perfect impedance-matching/AR-coating, is optimized under the same incident condition. The perfect AR-coating is numerically performed by assuming that the incident light onto the mirror is propagating in a medium with the same index as the low index material. The impedance-matched design preserves the slow-varying residual GD with the greatly-reduced GD oscillation. If required, the fast oscillation could also be reduced by employing pairs of mirror-pair designs to cancel higher-order Gires-Tournois-interfeometer resonances. The much smoother average GD and the reflectivity with the impedance-matched design are shown as the green curves in Fig. 2.13, as well as the practical 60° TE cases in blue. A square spectrum with a uniform power spectral density

in wavelength from 0.49 μm to 2.9 μm is used to examine the pulse distortions between the two cases in Fig. 2.13. After a pair of the designed mirrors and the corresponding compensating materials, the pulses would be distorted by the residual GDs of the mirror pairs. The slightly-distorted pulse intensity is compared with the transform-limited one, as shown in Fig. 2.14. As a result, the FWHM pulse durations on both cases are 1.7 fs, as well as the undistorted one (*i.e.*, transform-limited pulse). Therefore, fast GD oscillation might be negligible when considering sub-cycle pulse compressions.

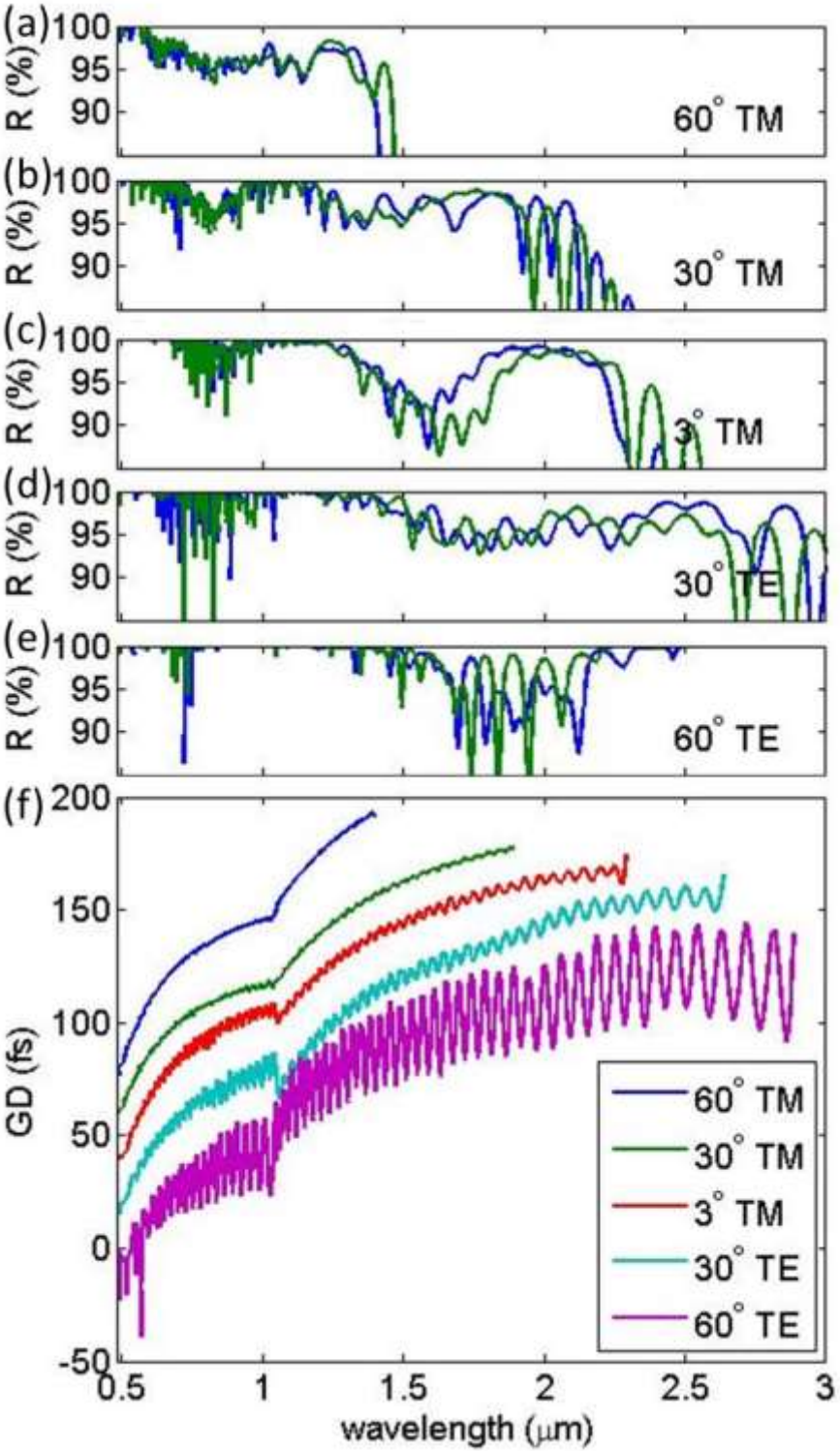

Fig. 2.12. (a)-(e) The reflectivity of DAM DCM pairs designed with specified incident angles and polarizations; (f) the corresponding average GDs of the designed mirror pairs. The possible design bandwidths with different incident conditions: 60° TM: 0.49 μm – 1.4 μm; 30° TM: 0.49 μm – 1.9 μm; 3° TM: 0.49 μm – 2.3 μm; 30° TE: 0.49 μm – 2.65 μm; 60° TE:0.49 μm – 2.9 μm. The average GD differences over the whole design bandwidths of different designs are almost the same, ~130 fs.

Design / Materials	60° TM	30° TM	3° TM	30° TE	60° TE
SiO_2 (in mm)	1.42	1.20	1.45	1.30	1.00
ZnSe (in mm)	0.35	0.32	0.32	0.40	0.30

Table 2.2 Compensating dispersion, with listed optical paths of SiO_2 and ZnSe, of a pair of designs with different incidence angles. SiO_2 is employed in the short spectral range of 0.49 μm - 1.05 μm, as ZnSe above 1.05 μm.

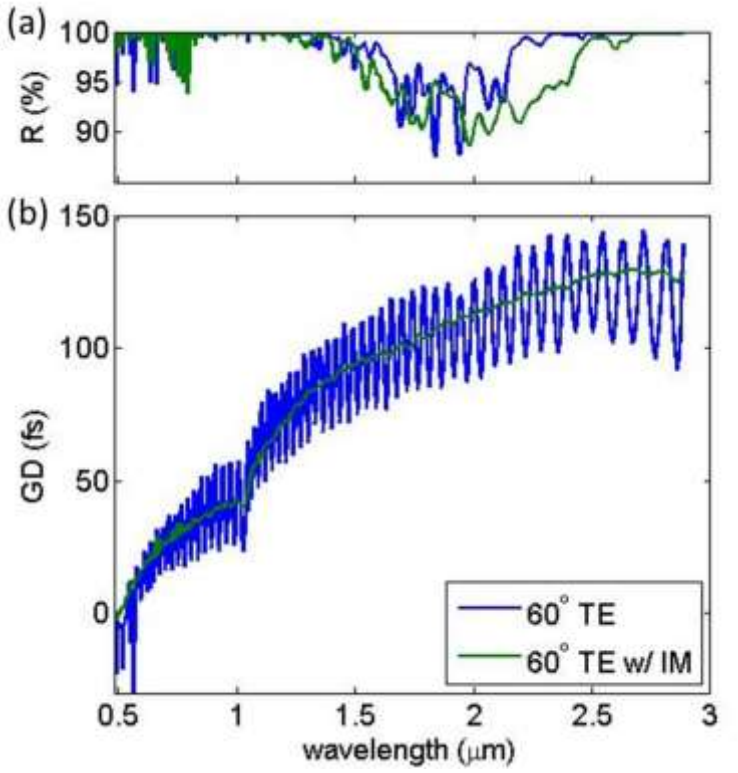

Fig. 2.13. (a) The reflectivity and (b) average GDs of two mirror pairs, which are designed with the incidence from air (blue) and from an impedance matching medium (green), with 60° of incident angle in s-polarization. In (b), strong Fresnel reflection (~20%) from air to the mirror structures leads to strong GD oscillations (blue) as Gires-Tournois interferometers.

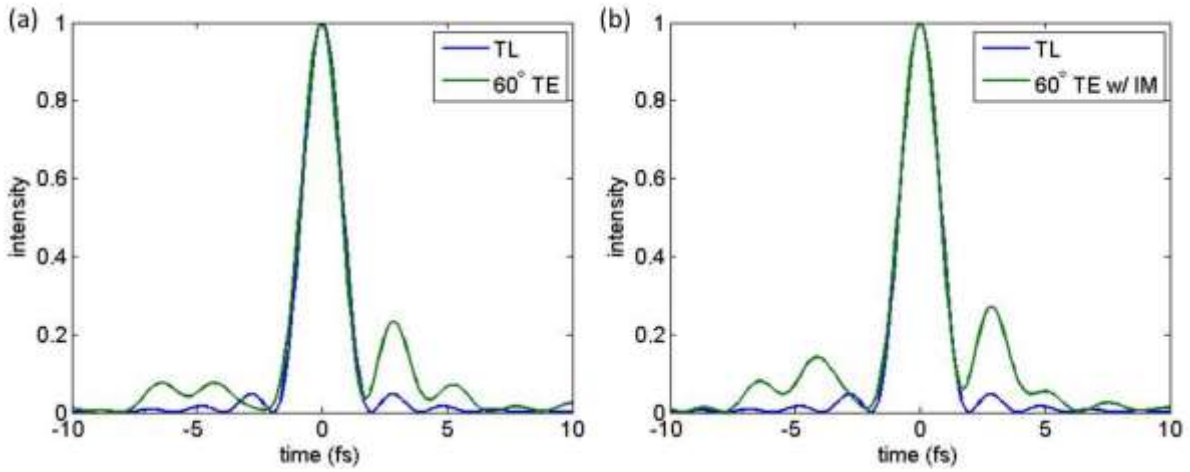

Fig. 2.14. The pulse characteristics in time domain after bouncing of (a) a 60° TE mirror pair and (b) an impedance-matched 60° TE mirror pair. Blue pulses in (a) and (b) shows the transform-limited intensity of an input test spectrum with an uniform power spectral density from 0.49 μm to 2.9 μm. Green curves shows the output pulses from mirror pairs after compensating the designed amount of dispersion from fused silica and ZnSe. All the pulses in (a) and (b) have the same FWHM pulse widths, 1.7 fs. TL: the transform-limited pulse.

2.5.2 **Increasing the compensating dispersion**

Although the dealing bandwidth can be up to >2 octave, the total GD differences provided by chirped mirrors (*e.g.*, ~130 fs with the designs as shown in Fig. 2.12(f)) are limited by the optical path differences between different wavelengths inside the mirror. Therefore, instead of using chirped quarter-wave Bragg stacks, two/three-time-thick stacks with the same total layer number could be also employed to design chirped mirrors in order to provide a larger amount of dispersion. However, the reflection bandwidth of Bragg stacks is approximately inversely proportional to the order of Bragg reflection. Fig. 2.15 shows the FWHM reflection bandwidths of TiO_2/SiO_2 layer pairs, with a quarter-wave and three-quarter-wave thicknesses at 0.8 μm for different incident angles and polarizations: the three-time-thick stacks provide only one-third of the bandwidth obtained in the case of quarter-wave Bragg stacks. As a result, with a fixed total layer number, the design bandwidth is compromised when one tries to increase the amount of compensated dispersion.

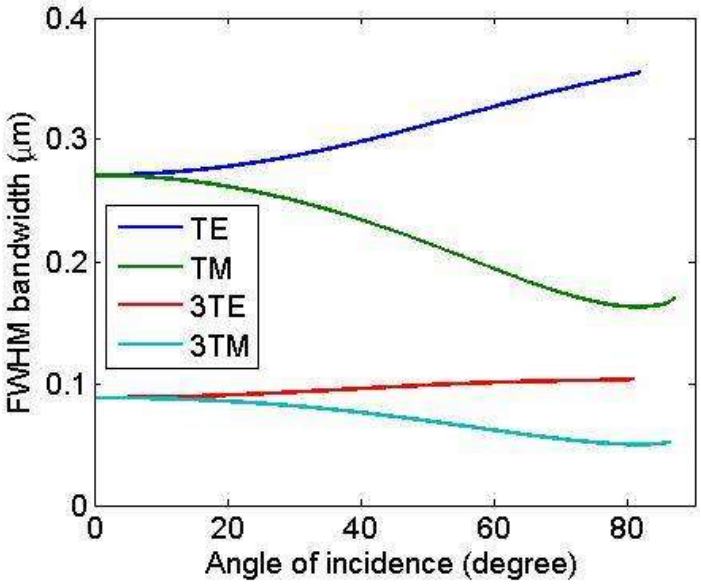

Fig. 2.15. FWHM reflection bandwidths of TiO_2/SiO_2 layer pairs with a quarter-wave and three-quarter-wave Bragg stacks at 0.8 μm in different incident angles and polarizations. TE, quarter-wave-thick layers in s-polarization; TM, quarter-wave-thick layers in p-polarization; 3TE, three-quarter-wave-thick layers in s-polarization; 3TM, three-quarter-wave-thick layers in p-polarization.

2.5.3 **Energy and intensity scalability**

The maximum pulse energy and peak intensity sustainable by the chirped mirrors are limited by the laser-induced damage threshold (LIDT) and accumulation of nonlinear phase inside the coating material. LIDT of the lower band-gap dielectric coating material (TiO_2 in our case) would hamper the energy scalability of the ultrabroadband source based on DCMs. Nonlinear effects in the mirror would lead to additional absorption loss [2.28] or index changes of the coating materials due to optical Kerr effect. Regarding LIDT, the threshold fluence of ion-beam sputtering (IBS) TiO_2 films was measured to be >0.1 J/cm^2 using a 25-fs Ti:sapphire amplifier [2.29]. Although the repetition rate [2.30], pulse duration, and center wavelength of the optical source, as well as the coating structures of the DCMs would also affect the breakdown fluence, sub-cycle optical pulses supporting up to several tens of mJ of pulse energy with a >1 cm^2 flat-top beam size should be possible based on the multilayer chirped mirrors. On the other hand, the effect of mirror nonlinearity can be evaluated by calculating the induced nonlinear phase shift. The nonlinear refractive indices of TiO_2 and SiO_2 are ~0.02 cm^2/TW and ~0.0003 cm^2/TW, respectively, at 1.064 μm of optical wavelength [2.31]. With a typical <10 μm of total coating thickness, <1 TW/cm^2 of the peak

intensity should be tolerable with <1 rad of nonlinear phase shift (*i.e.*, B-integral). Furthermore, in order to further reduce the mirror nonlinearity, one may employ less high refractive index materials especially in the front layers, where the pulse would be almost compressed to the highest peak intensity.

2.6 **Summary**

Various dispersion compensation methods are introduced. Chirped mirrors are capable of super-octave-wide dispersion compensation, which cannot be obtained by other pulse compression techniques so far. In this chapter, a chirped dichroic mirror and high-reflection chirped mirror pair with >2-octave-spanning bandwidth are demonstrated based on analytically analyzing a novel mirror design, dual-adiabatic-matching (DAM) structures. The design limitations, in terms of the handling bandwidth, the magnitude of dispersion, and the damage threshold, are discussed: (1) the bandwidth capabilities of dielectric chirped mirrors depend on different incident angles and polarizations. With a larger angle of incidence in s-polarization, a larger covering bandwidth can be obtained with a more pronounced residual GD variations. (2) A trade-off is found between the amount of compensating dispersion and the design bandwidth. With a fixed total layer number, the design bandwidth is compromised when one trying to increase the amount of compensating dispersion. (3) Although the repetition rate, pulse duration, and center wavelength of the optical source, as well as the coating structures of the DCMs would also affect the breakdown fluence, sub-cycle optical pulses supporting up to several tens of mJ pulse energy with a >1 cm^2 beam size should be possible based on the multilayer chirped mirrors. With a typical <10 μm of total coating thickness, <1 TW/cm^2 of the peak intensity should be tolerable with <1 rad of nonlinear phase shift (*i.e.*, B-integral).

References

[2.1] E. Treacy, "Optical pulse compression with diffraction gratings," *Quantum Electronics, IEEE Journal of,* vol. 5, pp. 454-458, 1969.

[2.2] R. Fork, O. Martinez, and J. Gordon, "Negative dispersion using pairs of prisms," *Optics letters,* vol. 9, pp. 150-152, 1984.

[2.3] R. Szipöcs, C. Spielmann, F. Krausz, and K. Ferencz, "Chirped multilayer coatings for broadband dispersion control in femtosecond lasers," *Optics Letters,* vol. 19, pp. 201-203, 1994.

[2.4] L.-J. Chen, "Design, optimization, and applications of few-cycle Ti: Sapphire lasers," Massachusetts Institute of Technology, 2012.

[2.5] J. Zhou, I. P. Christov, G. Taft, C.-P. Huang, M. M. Murnane, and H. C. Kapteyn, "Pulse evolution in a broad-bandwidth Ti: sapphire laser," *Optics letters,* vol. 19, pp. 1149-1151, 1994.

[2.6] A. Baltuska, Z. Wei, M. S. Pshenichnikov, and D. A. Wiersma, "Optical pulse compression to 5 fs at a 1-MHz repetition rate," *Optics letters,* vol. 22, pp. 102-104, 1997.

[2.7] E. Matsubara, K. Yamane, T. Sekikawa, and M. Yamashita, "Generation of 2.6 fs optical pulses using induced-phase modulation in a gas-filled hollow fiber," *JOSA B,* vol. 24, pp. 985-989, 2007.

[2.8] T. Tanigawa, Y. Sakakibara, S. Fang, T. Sekikawa, and M. Yamashita, "Spatial light modulator of 648 pixels with liquid crystal transparent from ultraviolet to near-infrared and its chirp compensation application," *Optics letters,* vol. 34, pp. 1696-1698, 2009.

[2.9] P. Tournois, "Acousto-optic programmable dispersive filter for adaptive compensation of group delay time dispersion in laser systems," *Optics communications,* vol. 140, pp. 245-249, 1997.

[2.10] E. Zeek, K. Maginnis, S. Backus, U. Russek, M. Murnane, G. Mourou, *et al.*, "Pulse compression by use of deformable mirrors," *Optics Letters,* vol. 24, pp. 493-495, 1999.

[2.11] A. Baltuška, T. Fuji, and T. Kobayashi, "Visible pulse compression to 4 fs by optical parametric amplification and programmable dispersion control," *Optics letters,* vol. 27, pp. 306-308, 2002.

[2.12] http://lo.de/?Coating_Guide:Prod._Methods:Ion_Beam_Sputtering

[2.13] F. Kärtner, N. Matuschek, T. Schibli, U. Keller, H. Haus, C. Heine, *et al.*, "Design and fabrication of double-chirped mirrors," *Optics letters,* vol. 22, pp. 831-833, 1997.

[2.14] F. Kärtner, U. Morgner, R. Ell, T. Schibli, J. Fujimoto, E. Ippen, *et al.*, "Ultrabroadband double-chirped mirror pairs for generation of octave spectra," *JOSA B,* vol. 18, pp. 882-885, 2001.

[2.15] G. Steinmeyer, "Brewster-angled chirped mirrors for high-fidelity dispersion compensation and bandwidths exceeding one optical octave," *Optics express,* vol. 11, pp. 2385-2396, 2003.

[2.16] N. Matuschek, L. Gallmann, D. Sutter, G. Steinmeyer, and U. Keller, "Back-side-coated chirped mirrors with ultra-smooth broadband dispersion characteristics," *Applied Physics B,* vol. 71, pp. 509-522, 2000.

[2.17] G. Tempea, V. Yakovlev, B. Bacovic, F. Krausz, and K. Ferencz, "Tilted-front-interface chirped mirrors," *JOSA B,* vol. 18, pp. 1747-1750, 2001.

[2.18] V. Pervak, I. Ahmad, M. Trubetskov, A. Tikhonravov, and F. Krausz, "Double-angle multilayer mirrors with smooth dispersion characteristics," *Optics express,* vol. 17, pp. 7943-7951, 2009.

[2.19] V. Pervak, A. Tikhonravov, M. Trubetskov, S. Naumov, F. Krausz, and A. Apolonski, "1.5-octave chirped mirror for pulse compression down to sub-3 fs," *Applied Physics B,* vol. 87, pp. 5-12, 2007.
[2.20] V. Pervak, F. Krausz, and A. Apolonski, "Dispersion control over the ultraviolet-visible-near-infrared spectral range with HfO_2/SiO_2-chirped dielectric multilayers," *Optics letters,* vol. 32, pp. 1183-1185, 2007.
[2.21] F. Kärtner and S.-H. Chia, "Chirped dichroic mirror and a source for broadband light pulses," ed: Google Patents, 2015.
[2.22] J. R. Birge and F. X. Kärtner, "Efficient analytic computation of dispersion from multilayer structures," *Applied Optics,* vol. 45, pp. 1478-1483, 2006/03/01 2006.
[2.23] J. R. Birge and F. X. Kärtner, "Efficient optimization of multilayer coatings for ultrafast optics using analytic gradients of dispersion," *Applied optics,* vol. 46, pp. 2656-2662, 2007.
[2.24] S.-H. Chia, G. Cirmi, S. Fang, G. M. Rossi, O. D. Mücke, and F. X. Kärtner, "Two-octave-spanning dispersion-controlled precision optics for sub-optical-cycle waveform synthesizers," *Optica,* vol. 1, pp. 315-322, 2014/11/20 2014.
[2.25] R. H. Kop, P. de Vries, R. Sprik, and A. Lagendijk, "Kramers-Kronig relations for an interferometer," *Optics communications,* vol. 138, pp. 118-126, 1997.
[2.26] A. Damascelli, Z. Hussain, and Z.-X. Shen, "Angle-resolved photoemission studies of the cuprate superconductors," *Reviews of modern physics,* vol. 75, p. 473, 2003.
[2.27] R. Egerton, *Electron energy-loss spectroscopy in the electron microscope*: Springer Science & Business Media, 2011.
[2.28] O. Razskazovskaya, T. T. Luu, M. Trubetskov, E. Goulielmakis, and V. Pervak, "Nonlinear absorbance in dielectric multilayers," *Optica,* vol. 2, pp. 803-811, 2015/09/20 2015.
[2.29] M. Mero, J. Liu, W. Rudolph, D. Ristau, and K. Starke, "Scaling laws of femtosecond laser pulse induced breakdown in oxide films," *Physical Review B,* vol. 71, p. 115109, 2005.
[2.30] M. Mero, B. Clapp, J. C. Jasapara, W. Rudolph, D. Ristau, K. Starke*, et al.*, "On the damage behavior of dielectric films when illuminated with multiple femtosecond laser pulses," *Optical Engineering,* vol. 44, pp. 051107-051107-7, 2005.
[2.31] M. J. Weber, *Handbook of optical materials* vol. 19: CRC press, 2002.

Chapter 3

High energy sub-cycle parametric waveform synthesizer

3.1 Introduction

Generation of extremely short and ultrabroadband optical waveforms, which are custom-tailored within a single cycle of light, opens up unprecedented opportunities for the emerging field of Waveform Nonlinear Optics, which is of primary importance, *e.g.*, for the generation of intense isolated attosecond XUV pulses [3.1, 2], launching valence-electron wavepacket dynamics in atoms and molecules [3.3-5], relativistic laser-plasma interactions and laser-driven electron acceleration [3.6, 7], and control of sub-cycle electron transport in solids [3.8]. However, the feasibility to study nonlinear interactions of matter with intense sub-cycle waveforms critically depends on the availability of high-energy multi-octave-spanning carrier-envelope phase (CEP)-controlled optical pulses. In addition, the realization of the energy and bandwidth scalability of ultrashort optical transients provides a new enabling technology for the demonstration of bright coherent tabletop high-harmonic sources, especially in the water-window and keV X-ray region [3.9]. Therefore, the generation and precise dispersion control of ever broader optical bandwidth is in high demand, in order to tailor the shortest light bursts in the time domain.

Recent developments in broadband waveform generation have produced coherent optical spectra with >1-octave bandwidth by sub-cycle waveform synthesis [3.10] and supercontinuum generation [3.3, 5]. In addition, to realize the energy scalability of ultrabroadband synthesizers for the realization of bright coherent tabletop high-harmonic sources in the water-window and keV X-ray region [3.9], multi-channel parametric waveform synthesizers with several amplification stages are required [3.10, 11], which calls for

temporal optimization in each amplification stage to maximize both conversion efficiency and bandwidth, as well as to simultaneously suppress the superfluorescence background [3.12]. The dispersion management for the generation of intense sub-optical-cycle sources is extremely delicate and challenging, especially requiring ultrabroadband and highly precise laser optics with high damage threshold. As described in Chapter 2, active compression systems based on spatial light modulators with >1-octave bandwidths have been demonstrated [3.13, 14], but they are hampered by the bandwidth and diffraction efficiency of the gratings used in 4-*f* pulse shapers. Therefore, they have not directly been applied to multi-octave-spanning high-intensity sources. Multilayer dielectric coatings such as the ones used for chirped mirrors [3.15, 16] and complementary mirror pairs [3.17-20], though not adaptable, have the advantages of supporting potentially multi-octave bandwidth with high reflectivity. Therefore, multilayer mirror designs are widely employed as robust solutions as discussed in Chapter 2: 1.5-octave-wide chirped mirror pairs [3.18, 19] for pulse compression have been developed, and optical synthesizers based on hollow-core-fiber compressors with up to four channels have been realized with separate chirped mirror designs [3.3-5]. In the previous works, the pulses covering different spectral ranges are split and individually compressed before pulse recombination. While hollow-core-fiber compressors are limited in the trade-off between pulse energy and operating bandwidth, a super-octave-spanning pulse synthesizer based on parametric amplifiers can further scale the energy to the multi-mJ range [3.21, 22]. Then, with a reasonable beam size, the maximum pulse energy reachable is ultimately limited by the peak power of the combined intense ultrashort pulse, which induces detrimental nonlinearities (*i.e.*, *B*-integral) in the following optical beam path and particularly in the beam combiner optics and the window to vacuum-chambers housing the experiment (*e.g.,* high harmonic generation). In addition, the dispersion of the beam combiner around the edge of the high-reflection band is difficult to control, as discussed in Subsection 2.3.2. As a result, synthesized electric-field transients without spectral gaps are hard to achieve with dichroic mirrors as discussed in Subsection 2.3.2: spectral gaps cannot be avoided in between the channels [3.3-5]. Therefore, to efficiently synthesize ultrabroadband optical waveforms with precise spectral-phase matching between the transmission and reflection ports of the beam combiner is required: broadband dichroic mirrors (DM) with exquisite dispersion control are necessary but not available so far. In Chapter 2, novel mirror designs with >2-octave-spanning bandwidth have been

demonstrated and discussed. In this chapter, super-octave-wide waveform synthesizers delivering multi-mJ pulse energy are introduced based on the advanced chirped mirror technology: a 3-channel parametric synthesizer with 3 amplification stages is discussed.

3.2 **3-channel parametric synthesizer**

3.2.1 **Introduction to femtosecond optical parametric amplification**

The femtosecond technology widely applied for the implementation of stable and energetic sources relies on broadband stimulated emission, such as Ti:Sapphire oscillators and amplifiers. However, the frequency tunability, as well as the obtainable spectral bandwidth, is limited by the emission bandwidth of the gain medium, leading to gain narrowing during amplification process. Optical parametric generation, along with proper nonlinear crystal and geometry, is a promising technology to realize tunable femtosecond pulses across the visible, near and far infrared spectral ranges [3.24-29].

In a transparent crystalline crystal materials with strong $\chi^{(2)}$ nonlinearity, an intense higher-frequency beam (*i.e.*, the pump beam) at frequency ω_p, amplifies a weak lower-frequency beam (*i.e.*, the signal/seed beam), at frequency ω_s. The signal beam is amplified along with an idler beam, at frequency ω_i [3.23]. Parametric interaction often occurs and then energy conservation has to be followed, which enforces

$$\omega_p = \omega_s + \omega_i \tag{3.1}$$

Meanwhile, momentum conservation is also allowed in order to efficiently process parametric generation (*i.e.*, achieving phase-matching):

$$\vec{k}_p = \vec{k}_s + \vec{k}_i \tag{3.2}$$

As a result, optical parametric processes can be employed for parametric amplification with a weak seed beam by an intense pump. With the advance on nonlinear optics and ultrafast technology, femtosecond OPAs has been regarded as powerful tools for the efficient generation of tunable, few-cycle light pulses [3.24-29]. Broadband gain in an OPA can be achieved when the group velocities of signal and idler are matched [3.26] with two kinds of geometry: (1) Degenerated OPA (DOPA): OPA employs type I phase matching at degeneracy

(*i.e.*, $\omega_s = \omega_i$) in a collinear fashion; (2) non-collinear OPA (NOPA): the group velocity of the idler pulses projected along the signal propagation direction is matched to the signal group velocity. As a result, the broadband gain from femtosecond OPAs offers the capability of amplifying broadband pulses sustaining shorter duration than the pump pulses. As an example, a pumping scheme based on Ti:sapphire laser technology can be realized either at the fundamental wavelength at 800 nm or at the second harmonic (SH) at 400 nm or higher harmonics. Regarding the generation of few-cycle pulses based on ß-Barium Borate (BBO) crystals, visible sub-10 fs pulses (500 - 700 nm) can be obtained by the SH-pumped NOPA [3.30], and sub-7 fs pulses in the near-infrared range of 650 - 950 nm is delivered by the SH-pumped DOPA [3.28]. Mid-infrared pulses (1200 - 2200 nm) are generated with the 800nm-pumped DOPA [3.27]. Most importantly, a coherent synthesis of all the above three channels are discussed in this chapter, in order to generate two-octave-spanning waveform from 500 – 2200 nm.

3.2.2 **3-channel parametric waveform synthesizer based on Ti:sapphire amplifiers**

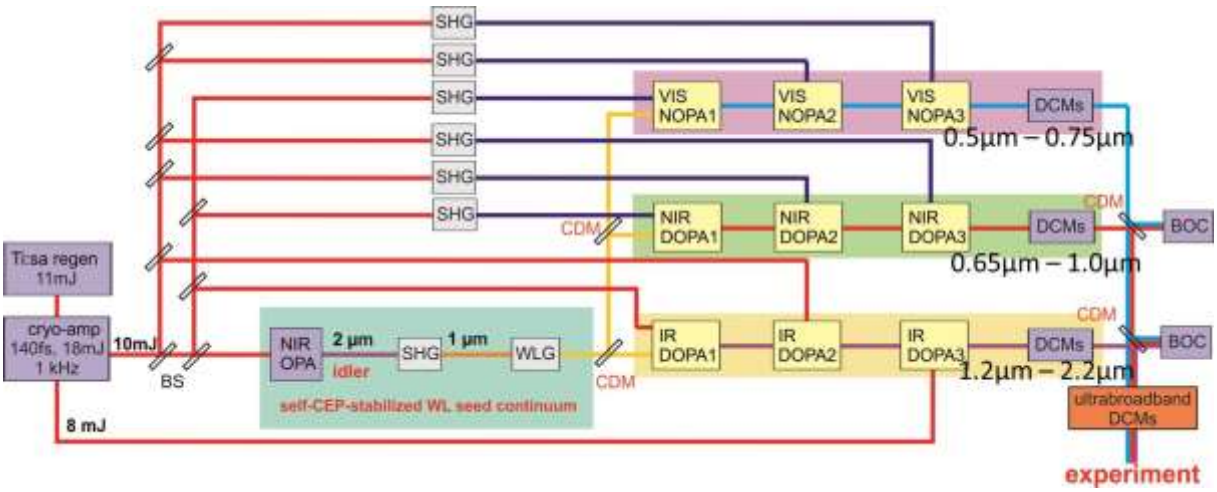

Fig. 3.1. Detailed scheme of the >2-octave-wide multi-mJ parametric waveform synthesizer [3.22]. BS, beam splitter; SHG, second-harmonic generation; WLG, whitelight generation; DBS, dichroic beam splitter; NOPA, non-collinear OPA; DOPA, degenerate OPA; DCMs, double-chirped mirrors; BOC, balanced optical cross-correlator.

For the construction of the >2-octave-spanning mJ-level parametric synthesizer, a cryogenically cooled Ti:sapphire chirped-pulse amplifier (140 fs, 18 mJ, 0.8 µm, 1 kHz) is employed as a starting source (see Fig. 3.1). A robust seed generation is required from supercontinuum generation, which eventually impacts the coherence and phase stability of

the amplified pulses. For generation of a supercontinuum seed, the stabilization of carrier-envelope phase (CEP) is crucial to determine the electric field of sub-cycle waveforms, providing the feasibility to study nonlinear interactions of matter with intense waveforms, as well as optical frequency metrology. The CEP stabilization can be achieved using either active or passive methods. In our case, a few-μJ-level, CEP-stable supercontinuum (0.5-2.5 μm, see Fig. 3.2) is generated by white-light generation in a 3-mm-thick YAG crystal pumped by the second harmonic (1.06 μm) of the self-CEP-stabilized idler [3.31] of a NIR OPA (OPerA Solo, Coherent). Without using an active electronic feed-back control, passive schemes preserve phase stability by difference frequency generation at a parametrically detuned frequency: in this process the phases of the two pulses (*i.e.*, pump and signal) sharing the same unlocked CEP add up with opposite signs, resulting in cancellation of the shot-to-shot CEP fluctuations.

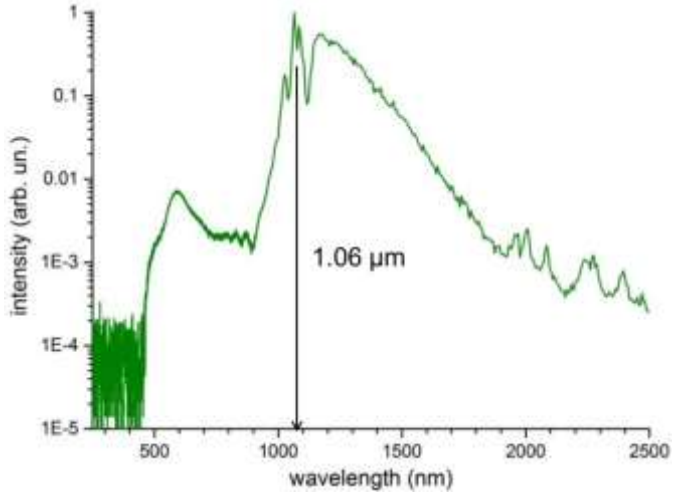

Fig. 3.2. Passively CEP-stabilized white-light seed continuum generated in a 3-mm-thick YAG crystal pumped by the second harmonic (1.06 μm) of the CEP-stable idler of the NIR OPA [3.22].

The continuum is split with chirped dichroic mirrors for seeding three OPA channels, a VIS NOPA and a NIR DOPA, pumped by 0.4 μm pulses using the SH generation from Ti:sapphire amplifiers, and an IR DOPA channel, pumped directly by the pulses at 0.8 μm, as shown in Fig. 3.1. 3-stage amplification in each channel is employed in order to boost up the synthesized pulse energy up to multi-mJ-level. Type-I BBO crystals are applied in all the three channels (the phase-matching angle is 31°, 29°, and 20° for the VIS NOPA, NIR DOPA and IR DOPA, respectively). In each stage of three OPA channels, the pulse dispersion is precisely managed based on custom-tailored double chirped mirrors (DCMs), as discussed in Section 3.3. In addition, the possible timing drifts between different channels should be also carefully controlled in order to synthesize the ultrabroadband waveform from the three OPA

channels [3.10]. Balanced optical cross-correlators (BOCs) [3.32] will be employed to detect relative timing of the pulses. The locking method based on BOCs and a feed-back active control is capable of achieving sub-cycle parametric synthesis with <30-as rms timing jitter [3.10, 31]. The passive timing jitter between the MIR DOPA and the VIS NOPA is characterized and discussed based on BOCs in Subsection 3.4.2.

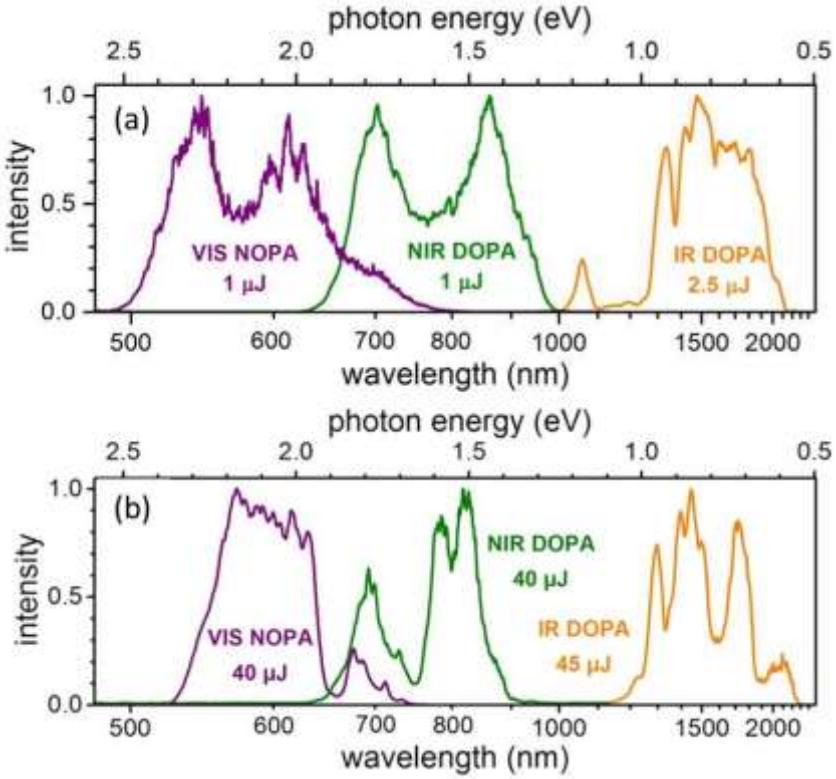

Fig. 3.3. Output spectra and corresponding energies from the (a) first and (b) second OPA stages [3.22].

Fig. 3.3 shows the measured output spectra from the first and second amplification stages, respectively. Comparing the first and second stage spectra, the VIS NOPA and NIR DOPA ones are narrower after the second stage amplification, and the IR DOPA one amplified more on the two sides instead of the center wavelength regime around 1.6 μm. It could be qualitatively explained by considering the role of dispersion between pump and seed, which is provided in Section 3.3. Even in this case, the second stage output spectra pumping by 0.4-μm pulses continuously cover the spectral range from 0.52 μm to 0.96 μm, and the IR DOPA spectrum is spanned from 1.13 μm to 2.29 μm. The FWHM TL pulse duration from the perfect synthesis of these three spectra with a 0-CEP offset (assuming the intensity weighting, 1:1.3:1, in order to obtain a better suppression of the pulse side lobes) is

1.9 fs FWHM, corresponding to 0.7 optical cycles at 785 nm center wavelength, as shown in Fig. 3.4.

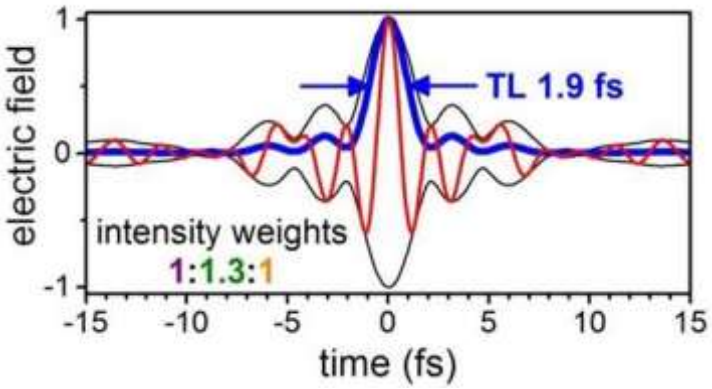

Fig. 3.4. Numerical synthesized waveform obtaining from the measured second-stage spectra (see Fig. 3.4(b)). The weighting between different channels is 1:1.3:1 assuming dispersion-free pulses with a 0 CEP offset [3.22].

As a preliminary test, the energy can be further boosted up to the multi-mJ level after the third amplification stages (see Fig. 3.5). First, the energy of the IR DOPA can be reached up to 1.7 mJ in a third IR DOPA stage employing a 4-mm-thick BBO crystal with a 7.7 mJ of pump pulses, resulting in the pump-signal conversion efficiency as high as 22%. On the other hand, using 2-mm-thick BBOs and 0.4-μm pump pulses obtained from the SH generation of the Ti:sapphire source, the reachable VIS NOPA and NIR DOPA energies after the third stages are 170 μJ and 200 μJ, respectively, as well as the spectra shown in Fig. 3.5.

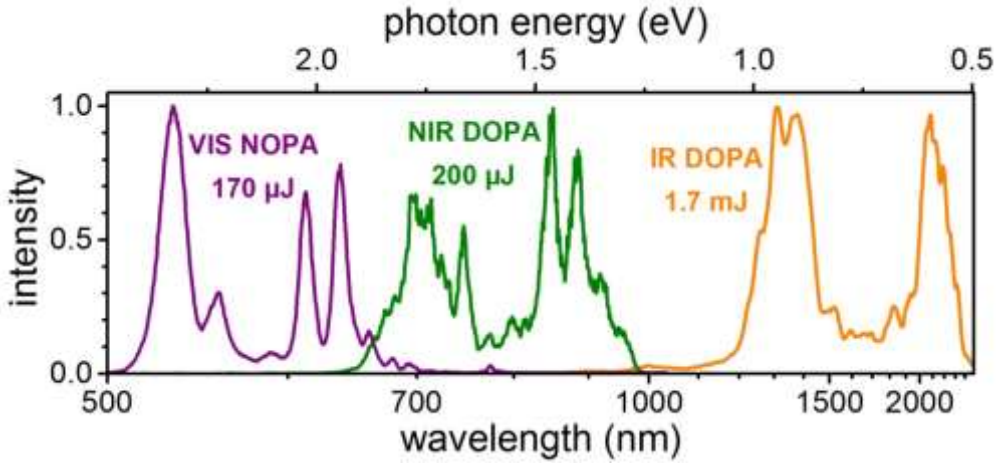

Fig. 3.5. Output spectra and corresponding energies from the third OPA stages [3.22].

3.3 Dispersion control of high energy sub-cycle synthesizers

One key technology for generating multi-mJ sub-cycle pulses and the ways to delivering them to attoscience experiments require dedicate dispersion tailoring over the whole operating bandwidth (*i.e.*, more than two octaves in our case). Comparing with hollow-fiber-based synthesizer, the fully dispersion control of multi-channel parametric synthesis with multiple amplification stages is a multifaceted challenge, which demands on several requirements: (1) temporal optimization of OPAs in each amplification stage in terms of both bandwidth and conversion efficiency, while suppressing the buildup of super-fluorescence during the amplification process, (2) reduction of the unwanted nonlinearity (*i.e.*, nonlinear phases as B-integral) due to intense burst propagation through Kerr media (*e.g.*, beam combiner substrates, entrance window of the vacuum chamber for the experiments of nonlinear waveform optics), which would destroy the pulse quality, (3) feasibility of dispersion fine-tuning for different experimental scenario, (4) final compression of the intense synthesized waveform to its Fourier limit.

3.3.1 Dispersion scheme for bandwidth and pulse-energy scalibility

In order to synthesize light transient covering different spectral range, in the previous works, separate dispersion-control units for different spectral ranges have been proposed [3.3, 5, 10, 33]. In one version, as shown in Fig. 3.6, the pulses covering different spectral ranges will be compressed before the pulse combination. Hollow-core-fiber-based optical synthesizer with up to four channels have been demonstrated using separate chirped-mirror covering different spectral regimes [3.3, 5]. However, in that case, although less demanding on dispersion-control elements, the pulse energy is harder to scale up to the multi-mJ range [3.10, 21, 22], since the combined intense ultrashort pulses induce unwanted nonlinear optical interactions which would degrade the beam quality. Thus, reducing the effect of nonlinearities can be achieved by combining the chirped pulses and then using ultrabroadband CMs as the final stage compressor: Novel mirror designs for >2-octave-spanning waveform synthesizers delivering multi-mJ pulse energy [3.21, 22] are introduced. We design and characterize the required laser optics [3.34], chirped dichroic mirrors (CDMs) for efficient splitting and coherent combining of pulses, and ultrabroadband double-chirped mirror (DCM) pairs for final compression. To avoid B-integral problems, we recombine the

still slightly chirped pulses first on the CDMs and then use an ultrabroadband DCM pair as a final compressor unit, as schematically shown in Fig. 3.7.

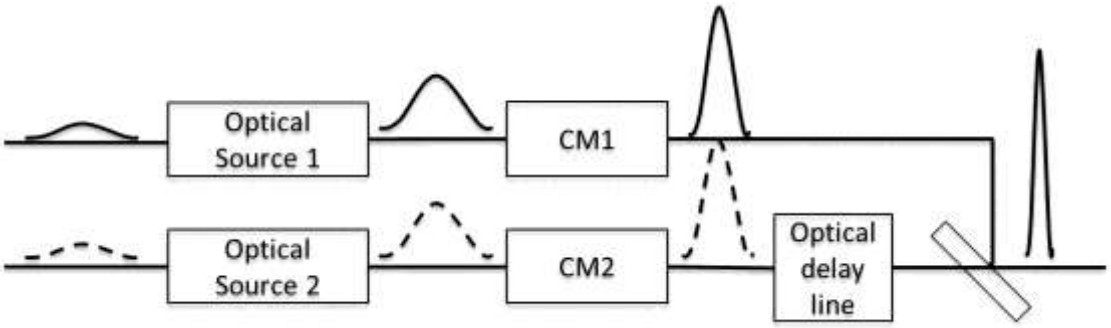

.

Fig. 3.6. Prior arts [3.3-5]of broadband few-cycle optical sources with separated chirped mirrors in different wavelength ranges. CM: chirped mirror.

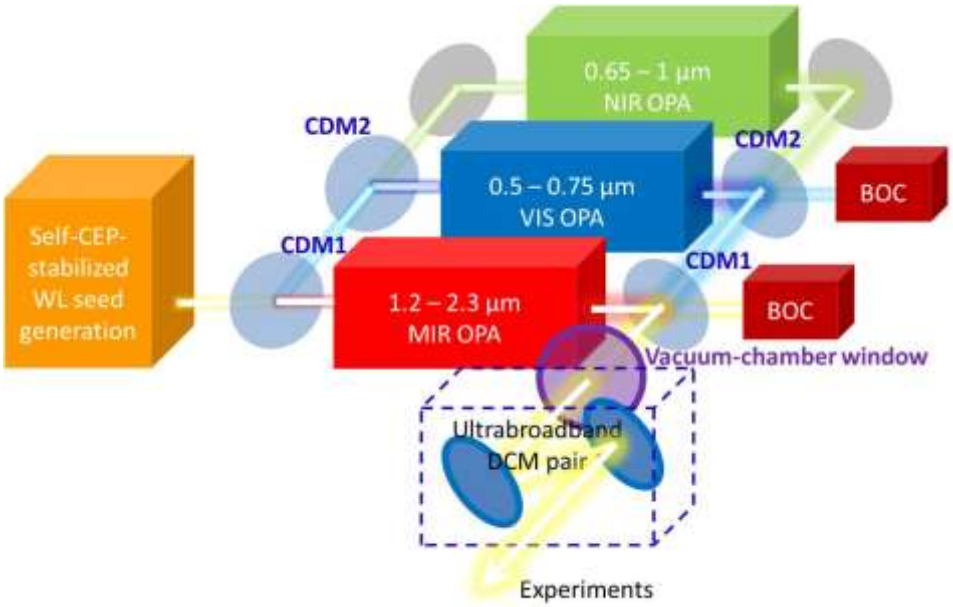

Fig. 3.7. Schematic of a >2-octave-wide 3-channel parametric synthesizer [3.21, 22, 34]. CEP, carrier-envelope phase; WL, white-light; CDM, chirped dichroic mirror; OPA, optical parametric amplifier; DCM, double-chirped mirror; BOC, balanced optical cross-correlator.

We evaluate the temporal pulse distortion introduced by the demonstrated ultrabroadband DCM pair on the waveform synthesizer output using the experimental combined second-stage OPA output spectra. As the scheme in Fig. 3.7 shows, the spectrum below 1 µm is reflected by the CDM, and the spectrum above 1.1 µm is transmitted. The combined pulse, with 1.88 fs FWHM transform-limited (TL) pulse duration, is still chirped when passing through the combiner substrate and the vacuum-chamber window to

decrease the peak intensity and thus reduce *B*-integral, and the ultrabroadband DCM pair can compensate the dispersion of the combined waveform afterwards. The pulse distortion is examined by considering the measured reflectivity and residual GD errors of the mirrors (*i.e.*, starting from the flat-phase waveform and accounting for the GD deviation of the mirrors' measured GD from the design goal, the GD of 1.44-mm/0.32-mm optical path in fused silica/ZnSe, respectively), as shown in Fig. 3.8. Fig. 3.8(b) shows the synthesized waveform after final compression by the ultrabroadband DCM pair according to the fabricated results in Section 2.4. The red dotted curve in Fig. 3.8(a) shows that the measured residual phase error of the DCM pair, is <0.1 π rad (*i.e.*, <λ/20), enabling pulse compression very close to its TL. >2-octave-bandwidth pulse compression can thus be visualized for the first time [3.34].

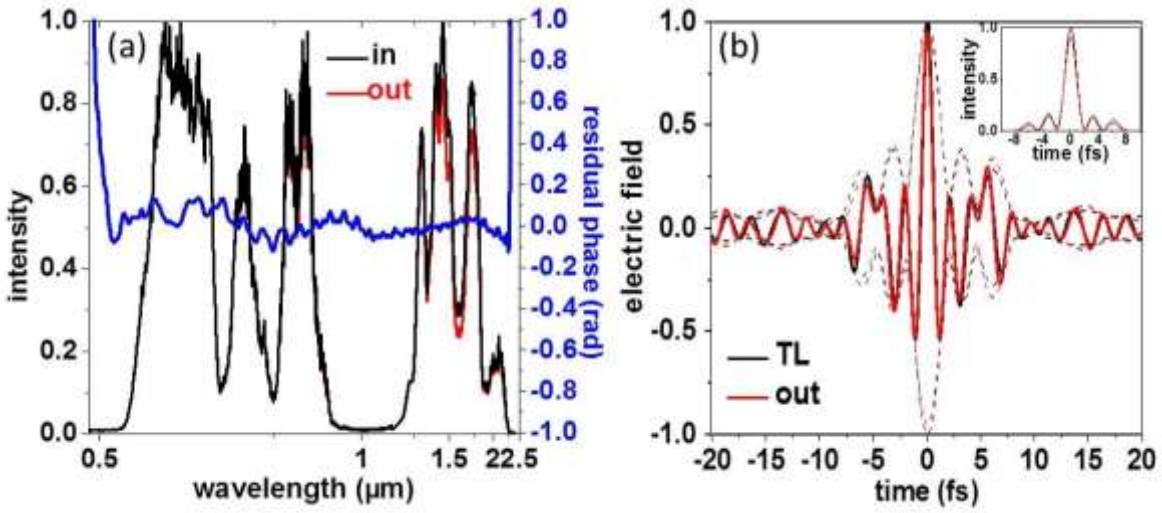

Fig. 3.8. The pulse characteristics in (a) frequency domain and (b) time domain after the ultrabroadband DCM pair. The black curve in (a) is the measured combined OPA spectra, as well as the TL electric-field waveform in (b). The red curves show the pulse after the mirror pair, as well as the residual phase shown as the blue curve in (a). The duration of the pulses depicted in the inset as the black and red lines are 1.88fs and 1.93fs, respectively. TL, transform-limited electric-field waveform.

3.3.2 **Dispersion-matched scheme for coherent beam combination**

A beam combiner's dispersion around its high-reflection band edge is difficult to control. In the previous designs, spectral gaps cannot be avoided between the channels [3.3, 5]. Therefore, to efficiently synthesize ultrabroad optical waveforms, precise spectral-phase matching between the transmission and reflection ports of the beam combiner is required.

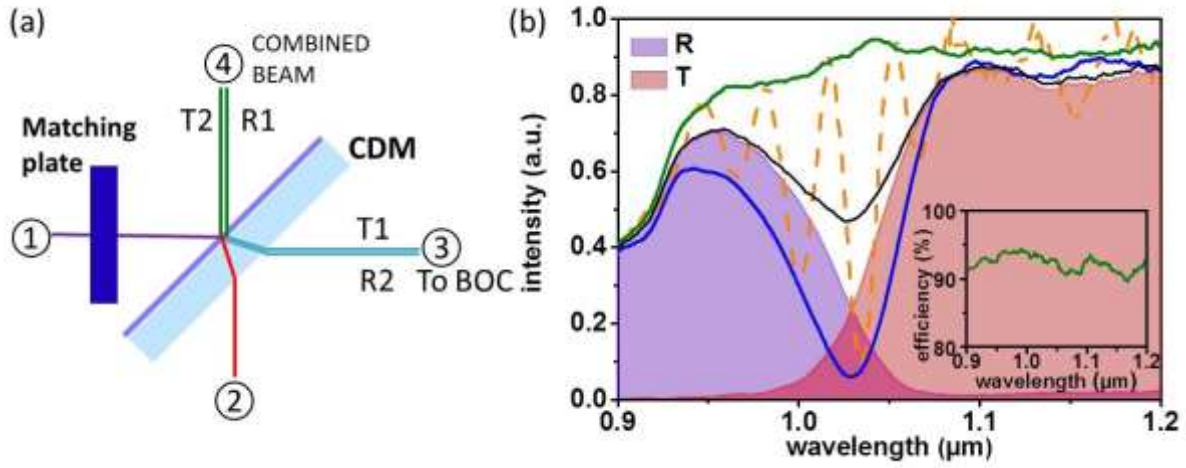

Fig. 3.9. (a) The schematic diagram of a dispersion-matched system based on the CDM [3.34]. (b) The reflection (purple), transmission (red), and the combined spectra (green, blue, and orange dashed) in port 4 with different temporal delays between port 1 and port 2 in (a), as well as the incoherently combined spectra (black). Constructive/destructive interfered spectrum over the whole transition range (1.0 μm - 1.1 μm) can be obtained as the green/blue curve. (Inset) The optimized beam combining efficiency is >90%, even including the ~8% total interface reflection losses of the matching plate in port 1.

To match the beam dispersion between reflection port and transmission port, the spectral phase in the overlapping regions should be equalized after the chirped dichroic mirror, which is similar to a previous scheme based on a dispersion-matched neutral beam splitter [3.35]. A proposed scheme with a CDM and a dielectric plate in port 1 is shown as Fig. 3.9(a). We denote the GDD of the coating between the air and the substrate interfaces with reflection R1, transmission T1, reflection R2, and transmission T2 by GDD_{R1}, GDD_{T1}, GDD_{R2}, and GDD_{T2}, respectively. Also, the GDDs for a single pass in the substrate of the chirped dichroic mirror and the dielectric plate are denoted as GDD_S and GDD_P, respectively. In the design we will match the GDD of the substrate with the GDD of the plate and GDD_{R1} (*i.e.*, $GDD_S=GDD_{R1}+GDD_P$). The GDD for each optical path is then given by:

$$\begin{aligned} &GDD(1\rightarrow 4) = GDD_P + GDD_{R1} = GDD_S, \\ &GDD(2\rightarrow 4) = GDD_S + GDD_{T2}, \\ &GDD(1\rightarrow 3) = GDD_P + GDD_{T1} + GDD_S, \\ &GDD(2\rightarrow 3) = 2GDD_S + GDD_{R2}. \end{aligned} \tag{4.1}$$

For a lossless coating without material absorption, the following relationships are generally valid [3.35, 36]: $GDD_{T1}=GDD_{T2}$ and $GDD_{R1}+GDD_{R2}=GDD_{T1}+GDD_{T2}$. Assuming the transmittance of the chirped dichroic mirror in the transition region is smooth enough, the corresponding GDD is negligible (*i.e.*, $GDD_{T1}\approx 0$). With these additional conditions via a

lossless and slowly-varying transmission coating in the transition region, the GDD from each beam path to port 4 becomes identical:

$$\begin{aligned} \mathrm{GDD}(1 \to 4) &= \mathrm{GDD_P} + \mathrm{GDD_{R1}} = \mathrm{GDD_S}, \\ \mathrm{GDD}(2 \to 4) &= \mathrm{GDD_S} + \mathrm{GDD_{T2}} = \mathrm{GDD_S}; \end{aligned} \tag{4.2}$$

The GDD from each beam path to port 3 is also identical:

$$\begin{aligned} \mathrm{GDD}(1 \to 3) &= \mathrm{GDD_P} + \mathrm{GDD_{T1}} + \mathrm{GDD_S} \\ &= \mathrm{GDD_P} + \mathrm{GDD_S}, \\ \mathrm{GDD}(2 \to 3) &= 2\mathrm{GDD_S} + \mathrm{GDD_{R2}} \\ &= \mathrm{GDD_P} + \mathrm{GDD_S}. \end{aligned} \tag{4.3}$$

Furthermore, if we additionally place an identical plate in port 4 or have a coating design that $GDD_{R1}=GDD_S$, the GDD of all input and output ports is matched. In the case discussed in Section 2.3, GDD_{R1} and GDD_S are equivalent to the GDD of -0.52 mm and 3.21 mm optical path of fused silica, respectively. Therefore, the matched optical path of the fused silica plate is 3.73 mm. In the waveform synthesizer as shown in the scheme depicted in Fig. 3.7, the combined 5% of light in port 3 will supply a balanced optical cross-correlator (BOC) for active feedback stabilization of the relative time delay of the individual pulses.

Since the dispersion is matched, the spectrum in the spectrally overlapping region in port 4 can be constructively combined with matched spectral phase over the overlapping region, which further boosts the combination efficiency. The purple/red curves in Fig. 3.9(b) show the reflected/transmitted spectra measured using a white-light source from port 1 and port 2, respectively. The combined spectra are also shown as the green, blue, orange dashed curves in Fig. 3.9(b), as well as the incoherently combined spectrum as a reference: interference fringes (orange dashed curve) are observed due to the optical delay between the beams from the two input ports. By fine-tuning the optical delay, fully constructively/destructively interfered spectra over the spectrally overlapping region can be obtained as the green/blue curves, respectively. The beam combining efficiency with the green spectrum is >90% over the transition range, even including the ~8% total interface reflection losses of the silica plate in port 1.

3.3.3 **Pulse shaping for efficient parametric amplification**

In each amplification stage, the seed pulse duration must be carefully matched to the temporal window of high parametric gain defined by the location and duration of the pump pulses in order to efficiently amplify the seed instead of the buildup of super-fluorescence background. The complete suppression of super-fluorescence background during amplification is especially crucial for obtaining clean pulses from a few-µJ-level supercontinuum to the final mJ-level waveform. In a previous study [3.12], a small compromise in the amplified bandwidth relatively to the potential full phase-matching bandwidth is obtained by choosing the appropriate seed chirp. The method not only maximizes the efficiency-bandwidth product, but also optimizes the signal-to-noise ratio. In this subsection, the dispersion characteristics of the different channels are discussed, with their impact on the optimization strategy in the different wavelength ranges.

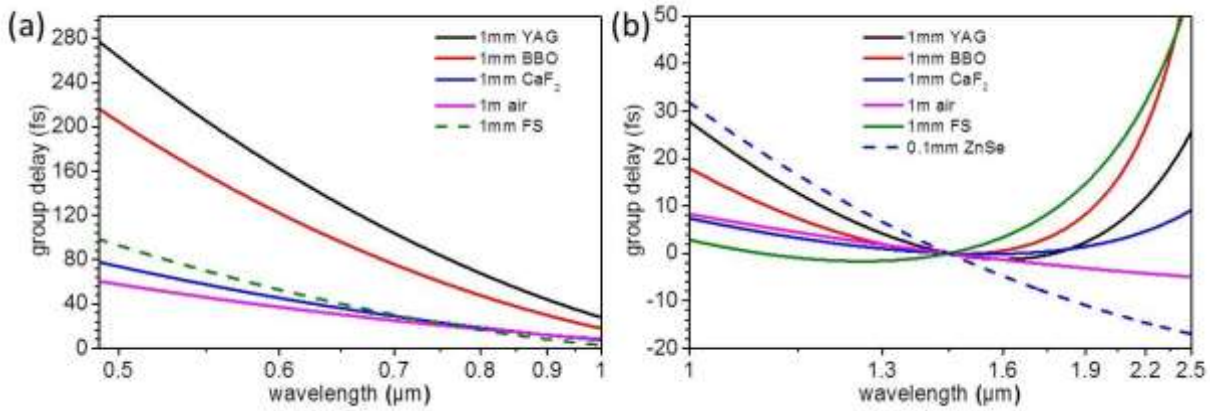

Fig. 3.10. Material dispersions (a) in VIS NOPA and NIR DOPA (0.49 µm - 1 µm), and (b) in MIR DOPA (1.2 µm – 2.5 µm). For dispersion fine-tuning in the different channels, fused silica (FS) and ZnSe are used in the spectral ranges plotted as dashed lines in (a) and (b), respectively.

Fig. 3.10 shows the dispersion characteristics of the materials used in the synthesizer, which have distinct behaviors below/above 1 µm. In NIR and VIS regimes, the used materials provide positive dispersion (*i.e.*, negative slopes of the curves in Fig. 3.10(a)). In contrast, mainly higher-order dispersion is experienced from materials in the range of 1 µm - 2.5 µm. Along with materials for dispersion fine-tuning (*e.g.*, fused silica or ZnSe) and considering the overall material dispersion in each channel, DCM pairs are custom-designed and fabricated to manage the pulse durations in different amplification stages. Fig. 3.11 shows the

reflectivity and dispersion curves (measured with a photospectrometer and a home-built white-light interferometer, respectively) for the DCM pairs, as well as the 2-octave-spanning final DCMs. The DCM pairs used in the VIS NOPA and NIR DOPA channels feature extremely smooth GD curves with negative dispersion and near-100% reflectivity over their full corresponding bandwidths. The smooth GD behavior is demanded especially in the VIS NOPA channel, since more bounces on the DCM pairs are required due to the more severe material dispersion in the short wavelength range, as shown in Fig. 3.10. In the IR DOPA channel, the DCM pair shows a non-monotonic behavior in GD to balance the higher-order dispersion from materials with a reflectivity >94% up to 2.2 µm. As discussed in Chapter 2, only negative dispersion can be provided with DCM pairs to achieve >1-octave-wide dispersion control. Unfortunately, this implies that with the present NIR DOPA DCM pairs we cannot compress the amplified spectrum within 2.2-2.5 µm (see Fig. 3.5). The black curve in Fig. 3.11 shows the DAM-structure-based ultrabroadband DCM pair [3.34] used as compression unit inside the vacuum chamber.

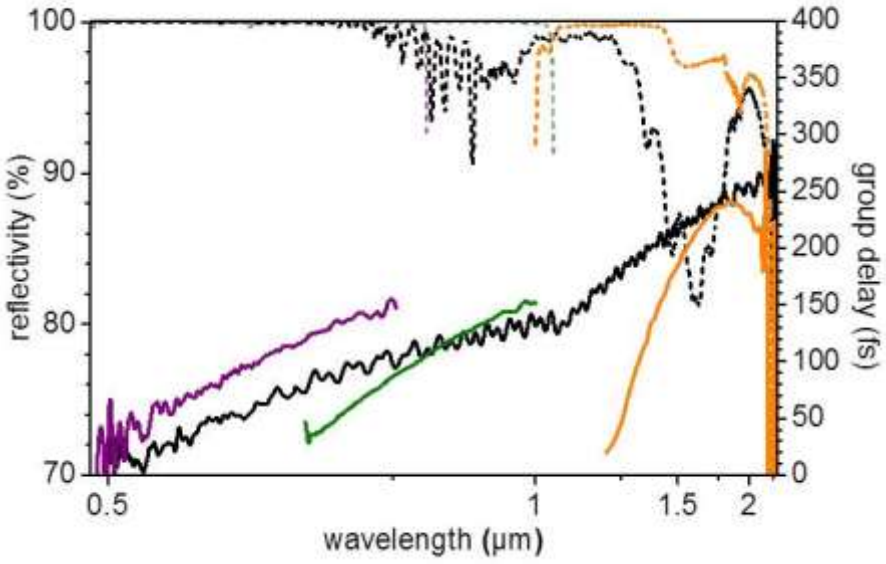

Fig. 3.11. Reflectivity and GD of all DCM pairs used for dispersion management: total reflectivity (dashed curves) and total GD (solid curves) for a DCM pair used in the VIS NOPA (purple), NIR DOPA (green), and IR DOPA (orange). The black curves show the data for the ultrabroadband DCM pair used for final compression of the combined waveform inside the vacuum chamber; it compensates a 1.44-mm optical path in fused silica and 0.32-mm optical path in ZnSe for ranges of 0.49–1.05 µm and 1.05–2.3 µm, respectively.

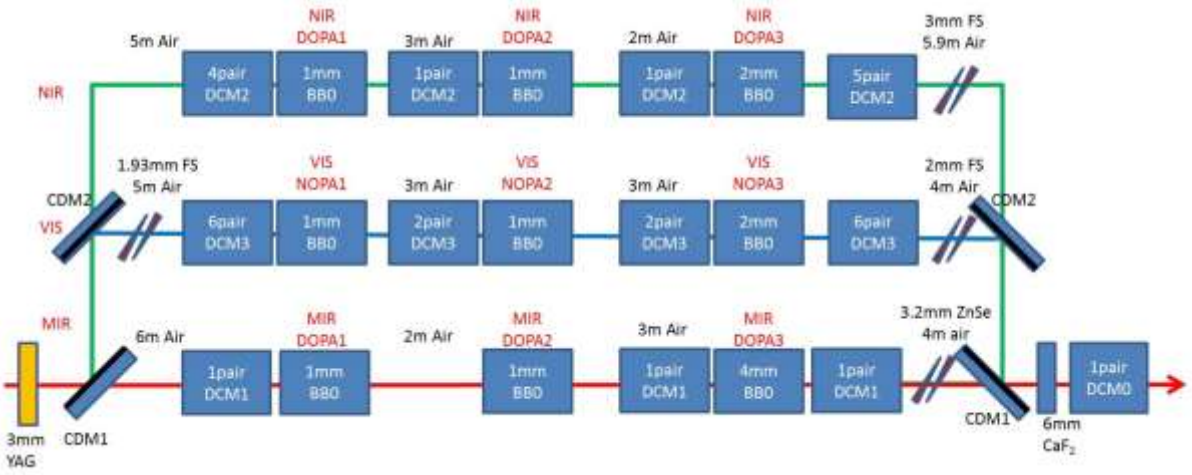

Fig. 3.12. An design of the dispersion map: 3mm YAG is used for white light seed generation. CDM1&2, chirped dichroic mirrors for splitting and combining different channels; FS, fused silica; DCM, double-chirped mirror (number of pairs as indicated). CaF_2 are employed as the window for a vacuum chamber.

The dispersion management is sketched as the dispersion map shown in Fig. 3.12. The corresponding seed evolution with respect to the pump, using the experimental second stage spectra and considering only optical dispersion and relative delays are shown in different stages of MIR DOPA, NIR DOPA, and NIR NOPA in Fig. 3.13, Fig. 3.14, and Fig. 3.15, respectively. Since the pump pulses, 140 fs for MIR DOPA at 0.8 μm and 100 fs for both NIR DOPA and VIS NOPA at 0.4 μm, are long enough, the crystal dispersion doesn't distort the pump pulse in the time domain: the width of the temporal gain window is almost fixed over the crystal, while the delay between the pump and seed are varied inside the crystal due to dispersion. In order to optimize the conversion efficiency, the pump and seed should be overlapped, and the seed pulse is matched with the temporal pump window in the center of BBO in each amplification stage.

In the MIR DOPA channel, the TOD induced by materials leads to lagging temporal side-lobes (see Fig. 3.13) from the superposition of the two lagging spectral wings. Along with the broadband phase matching of the parametric amplification, the spectral wings tend to see more gain than the center part, which is consistent with the experimental spectra shown in Fig. 3.3 and Fig. 3.5: more pronounced spectral wings are observed after amplification. On the other hand, the GDD of BBO is relatively small in the MIR range. The pump and seed can thus properly be overlapped even in the whole 4-mm-long crystal in the third stage, shown in the bottom figure of Fig. 3.13. It implies that the pump-signal conversion efficiency can be increased using a longer crystal. In reality, as high as 22% of

conversion efficiency in the third stage is realized with a 4 mm BBO, which is twice longer than the BBO crystals used in the VIS NOPA channels and NIS DOPA channels.

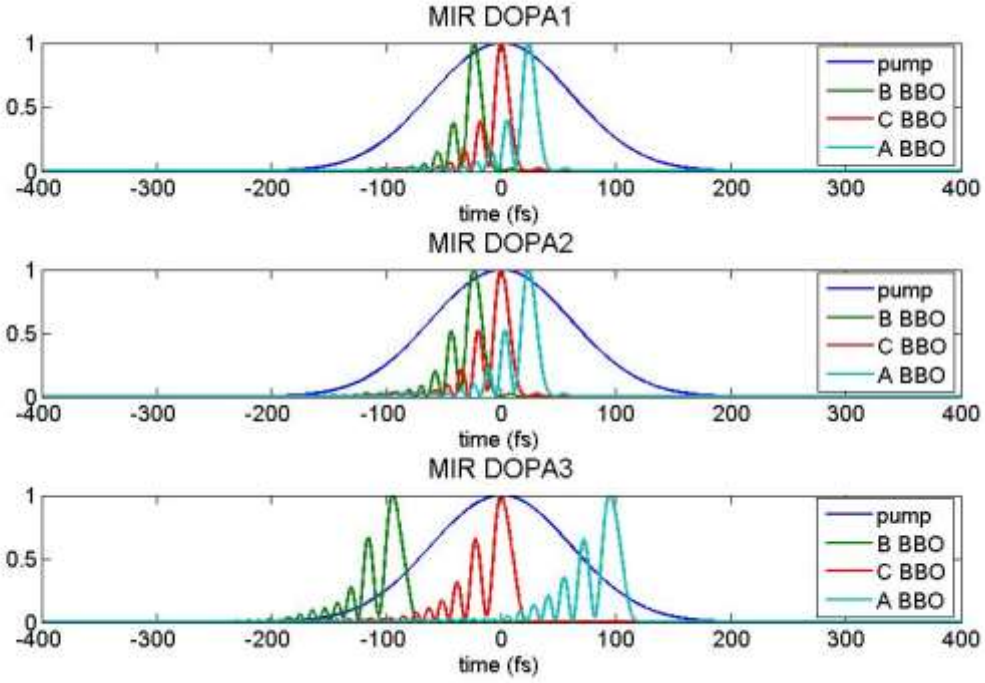

Fig. 3.13. Temporal evolution of the seed with respect to the pump in different amplification stages (upper, the first stage; middle, the second stage; bottom, the third stage) of the MIR DOPA channel. The chirp and delay of the seed are optimized to match the temporal pump window in the center of crystal, as the denoted C BBO pulses, while the BBO dispersion shapes the temporal behaviors before/after the crystal, denoted as B BBO and A BBO, respectively.

In the NIR DOPA and VIS NOPA channels, no significant temporal side-lobes are generated (see Figs. 3.14-15), and GDD is dominant in the pulse evolution. However, more severe temporal walk-off between the pump and seed inside the crystals suggests the use of shorter BBO crystal, especially in the NIR DOPA channel. Moreover, the dispersion of BBO is dramatically increased in the VIS regime; and it is harder to optimize the VIS seed pulse to match the temporal gain window. As a result, a longer pump is suggested when building VIS NOPA, or noticeable gain-narrowing would be found due to the temporal mismatch between the gain window and seed pulse.

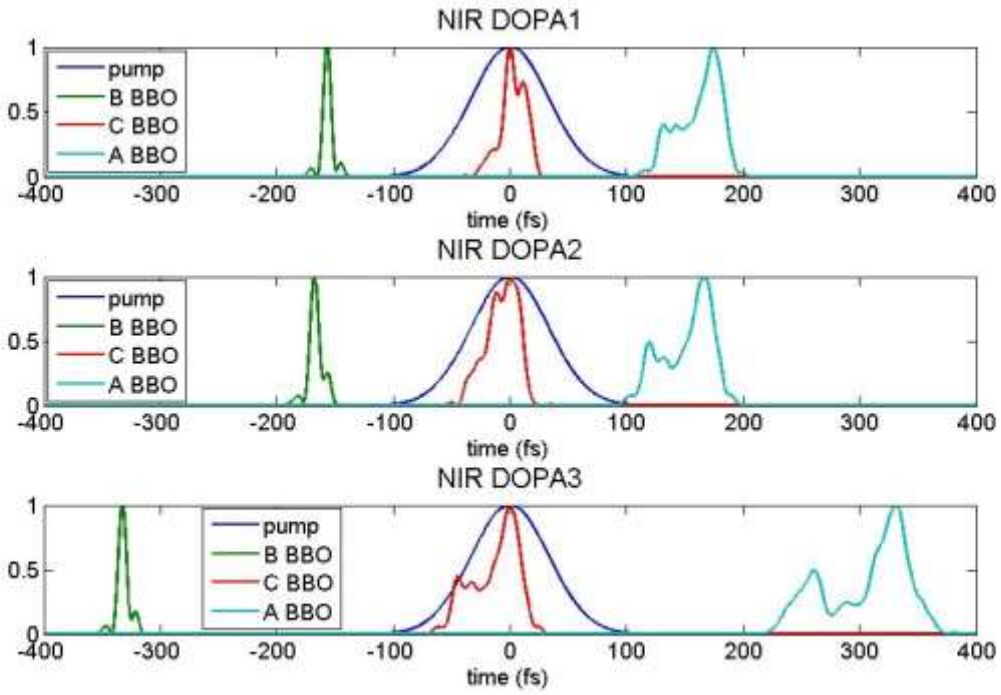

Fig. 3.14. Temporal evolution of the seed with respect to the pump in different amplification stages (upper, the first stage; middle, the second stage; bottom, the third stage) of the NIR DOPA channel. The chirp and delay of the seed are optimized to match the temporal pump window in the center of crystal, as the denoted C BBO pulses, while the BBO dispersion shapes the temporal behaviors before/after the crystal, denoted as B BBO and A BBO, respectively.

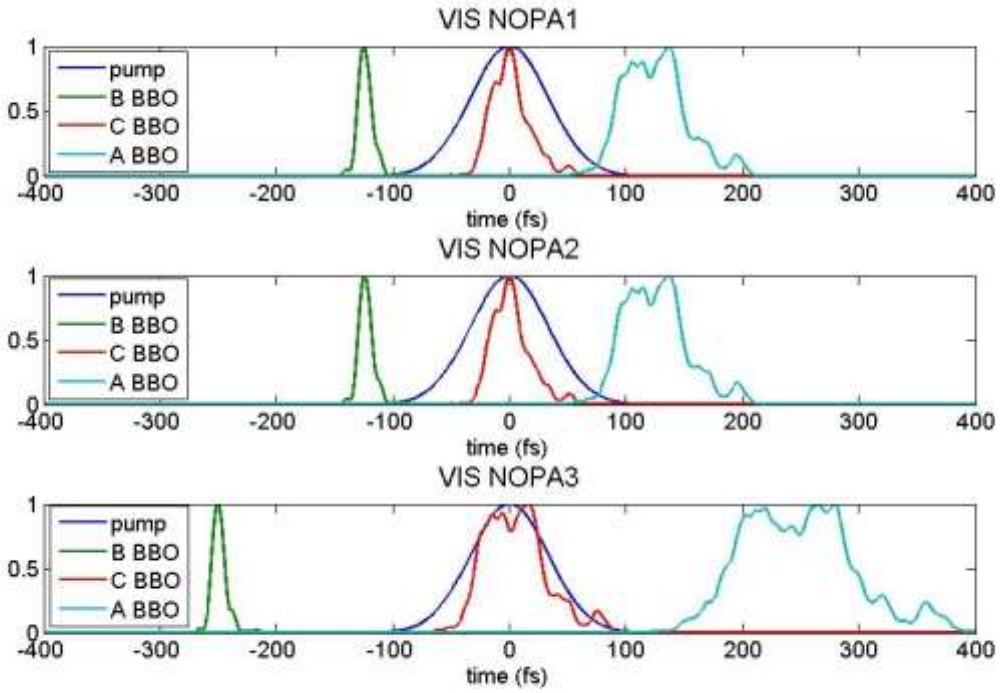

Fig. 3.15. Temporal evolution of the seed with respect to the pump in different amplification stages (upper, the first stage; middle, the second stage; bottom, the third stage) of the VIS NOPA channel. The chirp and delay of the seed are optimized to match the temporal pump window in the center of crystal, as the denoted C BBO pulses, while the BBO dispersion shapes the temporal behaviors before/after the crystal, denoted as B BBO and A BBO, respectively.

3.4 **Toward sub-cycle waveform synthesizer**

3.4.1 **Spectral-temporal pulse characterization**

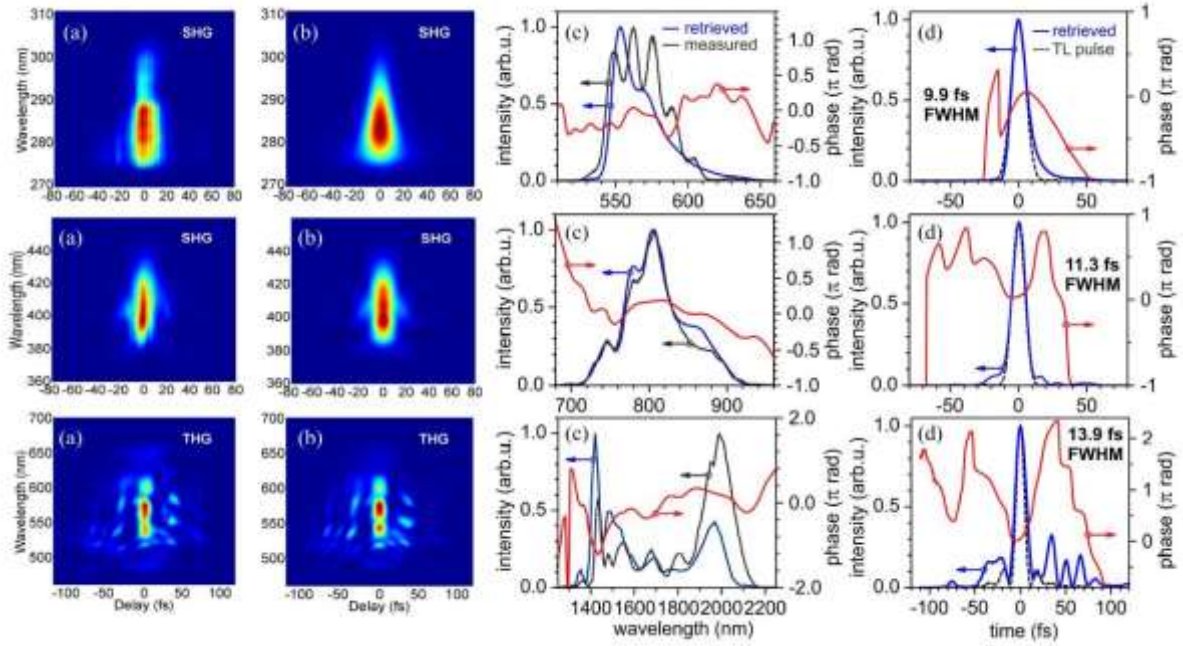

Fig. 3.16. FROG characterization of the second-stage OPA outputs from the three channels at the synthesis point [3.22]. The VIS NOPA (top) and NIR DOPA (middle) are characterized by means of SHG-FROG, and the MIR DOPA (bottom) using surface THG-FROG. (a) Measured and (b) retrieved FROG traces. (c) Retrieved spectral intensity (blue) and phases (red), as well as measured spectra (black). (d) Retrieved temporal intensity (blue) and phase profiles (red) as well as TL intensity profiles (dashed black). The retrieved FWHM pulse durations are indicated. The reconstruction of the THG-FROG (no marginal correction was applied) shows some deviations from the measured spectrum, since the surface polishing of the ZnSe wedges used for dispersion fine tuning was sub-optimum (scratches and imperfect planarity).

In order to characterize the pulse shape and to demonstrate the feasibility to recompress all three channels simultaneously close to the Fourier limit based on double chirped mirror pairs, preliminary FROG measurements of all three second-stage outputs are presented. The FROG results shown in Fig. 3.16 are measured at the actual waveform synthesis point, *i.e.*, the three pulses from different channels propagate through the complete synthesizer scheme, as plotted in Fig. 3.12, and thus experience the exact dispersion and nonlinearity. That is, the synthesis can later be performed from these pulses after locking their relative timing. The VIS NOPA and NIR DOPA were characterized by standard SHG-FROG. Because of the octave-spanning bandwidth of the MIR DOPA, a broadband technique is required without phase-matching constraints: surface third-

harmonic generation (THG) FROG is employed to characterize the MIR pulses. The FROG reconstructions show that each of the channels can be compressed close to the TL intensity profile (see dashed curves in Fig. 3.16(d)). In these measurements, we have not yet tried to compress the broadest bandwidths achieved so far (see the spectra shown in Fig. 3.3), so a further deduction of the pulse durations to <6 fs for each channel is expected with a proper optimization.

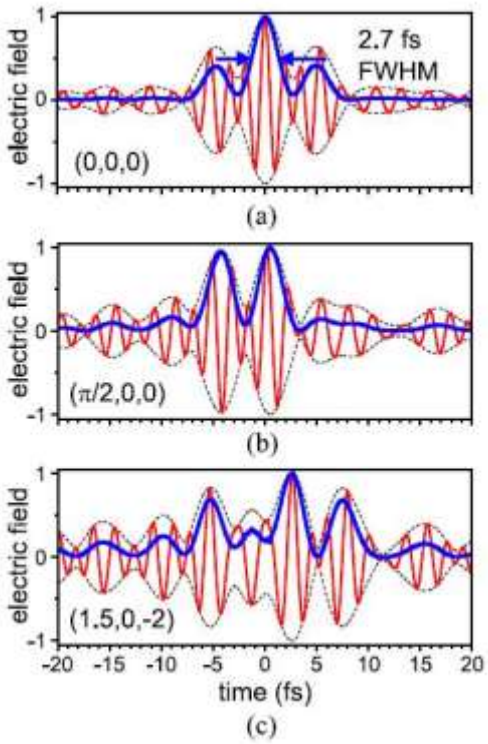

Fig. 3.17. Synthesized waveforms computed from Fig. 3.16(c), with the same field amplitudes between the 3-channel pulses. The assumed relative phases (VIS NOPA, NIR DOPA, MIR DOPA) are shown as indicated [3.22]. Red, electric field; dashed black, field envelope; blue, intensity.

The next step will be the final waveform synthesis from the three channels. A few examples (see Fig. 3.17) of synthesized waveforms for different relative phases are computed from the measured spectral amplitudes and phases in Fig. 3.16(c). Waveforms as short as 2.7 fs FWHM can be obtained. The ongoing work aims at the recompression and characterization of the full 3-channel 3-stage synthesizer.

3.4.2 **Passive timing jitter characterization**

Here we present the first study of the passive timing jitter properties of a 3-stage multi-mJ sub-cycle waveform synthesizer, which features much longer beam path (several tens of

meters), compared to those earlier synthesizers [3.3, 11]. A high passive timing stability is required between the synthesized channels, which indicate the feasibility to actually perform the coherent synthesis after establishing the active feedback stabilization. As shown in Fig. 3.1, we spatially and temporally combined the three OPA pulses after the third amplification stages (VIS NOPA3, NIR DOPA3, MIR DOPA3) on the chirped dichroic mirror. The leakage port from chirped dichroic mirrors also collinearly combines pulses from different channels, which is used to supply the BOC for relative timing comparison. We first implemented the BOC for VIS NOPA3 and MIR DOPA3. The IR pulses are employed as the reference, and we use a piezo-transducer (PZT) actuated delay stage in the VIS channel to compensate for the relative timing jitter. The timing setup is similar to the one shown in Fig. 9 in [3.33]. The BOC is composed of two identical cross-correlators to detect the sum frequency generation at 0.42 μm from the ~0.58-μm component in the VIS NOPA3 and the ~1.55-μm component in MIR DOPA3 using two 1-mm-thick type-I BBO crystals. A 3-mm-thick glass plate is placed in one of the cross-correlators to reverse the timing delay of the two pulses from different channels. The sum-frequency signals are filtered within a 10-nm optical bandwidth in front of the home-made balanced photodetector.

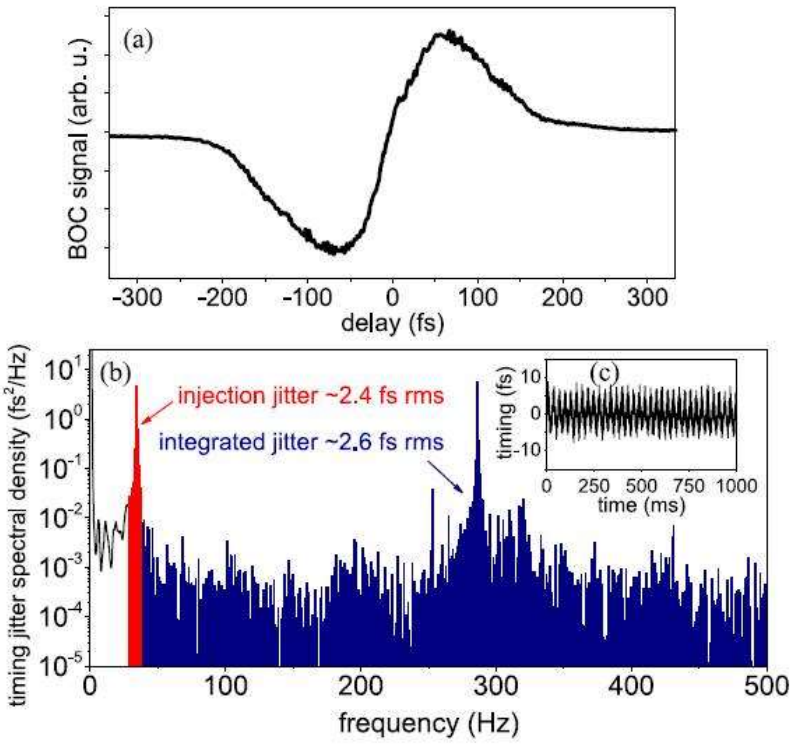

Fig. 3.18. Passive timing jitter characterization [3.22]: (a) BOC S-curve for VIS NOPA3 and MIR DOPA3, exhibiting a ~100-fs-wide linear region applicable for feedback stabilization. (b) Passive timing jitter

spectral density between the two channels measured by the same BOC, calculated from Fourier transform of the time domain measurement of the inset (c). A clear modulation from the injected 33.3-Hz test signal clearly is observed in (c). The injected sinusoidal test signal as the red area in (b) provides ~2.4-fs rms jitter at 33.3 Hz, while the blue area corresponds to the nature timing jitter without an active feedback control. By referencing the injected signal, the natural timing jitter is evaluated to be only ~2.6 fs rms.

In Fig. 3.18, we report the first characterization data of the passive timing jitter between the VIS channel and IR channel outputs after 3 stages of amplification [3.22]. The typical S-shaped BOC signal displayed in Fig. 3.18(a) features a 100-fs-wide linear region, which can be directly used for feedback stabilization of the relative timing within a 100-fs range. In order to investigate the noise properties and overall passive timing stability, we used the following experimental procedure: we injected a known sinusoidal signal at 33.3 Hz, with 1-V peak-to-peak amplitude driving the PZT used for adjusting the relative timing. From the specifications of the PZT, we calibrated the rms of this injected sinusoidal signal to be 2.4 fs. Afterwards, by comparing the red area in Fig. 3.18(b) corresponding to the reference injected noise to the blue area corresponding to the passive timing jitter, we could evaluate the overall timing jitter to be 2.6 fs rms.

Unfortunately, in this first experiment we observed that the injected 33.3-Hz signal driving the PZT excited a resonance in the PZT giving rise to a visible broad noise from 250 to 330 Hz in Fig. 3.18(b). We expect to get rid of this excessive noise by simply replacing the PZT in future experiments. With improved vibration isolation and environmental shielding of the BOC setup, we expect to achieve a sub-cycle passive timing jitter. With a common seed supplying three different channels, the timing and pulse-energy fluctuation of the seeds are automatically synchronized, eliminating the substantial timing jitter in the case with different seed sources between the synthesizer channels. [3.37] Apart from the PZT resonance issue, the observed surprisingly low 2.6-fs rms jitter seems a direct consequence of our parallel synthesizer architecture even with more than 10 meter of beam propagation.

To summarize, the passive timing jitter between parallel OPA channels in our synthesizer is already at the level of 1-2 optical cycles, which can be further improved by vibration isolations and a proper environmental shielding of the whole setup. So far we have not yet addressed the active feedback stabilization of the relative timing between the three synthesized channels with sub-cycle precision, which is a prerequisite for coherent waveform synthesis. In previous work by Leitenstorfer's group [3.38, 39], attosecond-level

passive relative timing jitter between two channels of a nJ-level waveform synthesizer based on Erbium-doped fiber technology was demonstrated. μJ-level parametric synthesis have been demonstrated in our earlier experiments [3.10, 11]. After the investigation of passive timing jitter, the low-frequency timing jitter can be easily eliminated by the PZT-based active control for the whole 3-channel OPAs, potentially enabling tight locking of the mJ-level pulses well below a tenth if not a hundredth of a cycle.

References

[3.1] E. J. Takahashi, P. Lan, O. D. Mücke, Y. Nabekawa, and K. Midorikawa, "Infrared two-color multicycle laser field synthesis for generating an intense attosecond pulse," *Physical review letters,* vol. 104, p. 233901, 2010.

[3.2] E. J. Takahashi, P. Lan, O. D. Mücke, Y. Nabekawa, and K. Midorikawa, "Attosecond nonlinear optics using gigawatt-scale isolated attosecond pulses," *Nature communications,* vol. 4, 2013.

[3.3] A. Wirth, M. T. Hassan, I. Grguraš, J. Gagnon, A. Moulet, T. T. Luu*, et al.*, "Synthesized light transients," *Science,* vol. 334, pp. 195-200, 2011.

[3.4] M. T. Hassan, A. Wirth, I. Grguraš, A. Moulet, T. T. Luu, J. Gagnon*, et al.*, "Invited Article: Attosecond photonics: Synthesis and control of light transients," *Review of scientific instruments,* vol. 83, p. 111301, 2012.

[3.5] T. T. Luu, M. T. Hassan, A. Moulet, O. Razskazovskaya, N. Kaprowicz, V. Pervak*, et al.*, "Isolated optical attosecond pulses," in *CLEO: QELS_Fundamental Science*, 2013, p. QF1C. 6.

[3.6] A. Buck, M. Nicolai, K. Schmid, C. M. Sears, A. Sävert, J. M. Mikhailova*, et al.*, "Real-time observation of laser-driven electron acceleration," *Nature Physics,* vol. 7, pp. 543-548, 2011.

[3.7] L. Veisz, D. Rivas, G. Marcus, X. Gu, D. Cardenas, J. Mikhailova*, et al.*, "Generation and applications of sub-5-fs multi-10-TW light pulses," in *Conference on Lasers and Electro-Optics/Pacific Rim*, 2013, p. TuD2_3.

[3.8] O. D. Mücke, "Isolated high-order harmonics pulse from two-color-driven Bloch oscillations in bulk semiconductors," *Physical Review B,* vol. 84, p. 081202, 2011.

[3.9] T. Popmintchev, M.-C. Chen, D. Popmintchev, P. Arpin, S. Brown, S. Ališauskas*, et al.*, "Bright coherent ultrahigh harmonics in the keV X-ray regime from mid-infrared femtosecond lasers," *science,* vol. 336, pp. 1287-1291, 2012.

[3.10] S.-W. Huang, G. Cirmi, J. Moses, K.-H. Hong, S. Bhardwaj, J. R. Birge*, et al.*, "High-energy pulse synthesis with sub-cycle waveform control for strong-field physics," *Nature photonics,* vol. 5, pp. 475-479, 2011.

[3.11] C. Manzoni, S.-W. Huang, G. Cirmi, P. Farinello, J. Moses, F. Kärtner*, et al.*, "Coherent synthesis of ultra-broadband optical parametric amplifiers," *Optics letters,* vol. 37, pp. 1880-1882, 2012.

[3.12] J. Moses, C. Manzoni, S.-W. Huang, G. Cerullo, and F. X. Kaertner, "Temporal optimization of ultrabroadband high-energy OPCPA," *Optics express,* vol. 17, pp. 5540-5555, 2009.

[3.13] E. Matsubara, K. Yamane, T. Sekikawa, and M. Yamashita, "Generation of 2.6 fs optical pulses using induced-phase modulation in a gas-filled hollow fiber," *JOSA B,* vol. 24, pp. 985-989, 2007.

[3.14] T. Tanigawa, Y. Sakakibara, S. Fang, T. Sekikawa, and M. Yamashita, "Spatial light modulator of 648 pixels with liquid crystal transparent from ultraviolet to near-infrared and its chirp compensation application," *Optics letters,* vol. 34, pp. 1696-1698, 2009.

[3.15] F. Kärtner, N. Matuschek, T. Schibli, U. Keller, H. Haus, C. Heine*, et al.*, "Design and fabrication of double-chirped mirrors," *Optics letters,* vol. 22, pp. 831-833, 1997.

[3.16] G. Steinmeyer, "Brewster-angled chirped mirrors for high-fidelity dispersion compensation and bandwidths exceeding one optical octave," *Optics express,* vol. 11, pp. 2385-2396, 2003.
[3.17] F. Kärtner, U. Morgner, R. Ell, T. Schibli, J. Fujimoto, E. Ippen*, et al.*, "Ultrabroadband double-chirped mirror pairs for generation of octave spectra," *JOSA B,* vol. 18, pp. 882-885, 2001.
[3.18] V. Pervak, F. Krausz, and A. Apolonski, "Dispersion control over the ultraviolet-visible-near-infrared spectral range with HfO_2/SiO_2-chirped dielectric multilayers," *Optics letters,* vol. 32, pp. 1183-1185, 2007.
[3.19] V. Pervak, A. Tikhonravov, M. Trubetskov, S. Naumov, F. Krausz, and A. Apolonski, "1.5-octave chirped mirror for pulse compression down to sub-3 fs," *Applied Physics B,* vol. 87, pp. 5-12, 2007.
[3.20] V. Pervak, I. Ahmad, M. Trubetskov, A. Tikhonravov, and F. Krausz, "Double-angle multilayer mirrors with smooth dispersion characteristics," *Optics express,* vol. 17, pp. 7943-7951, 2009.
[3.21] G. M. Rossi, G. Cirmi, S. Fang, S.-H. Chia, O. D. Mücke, F. Kärtner*, et al.*, "Spectro-temporal characterization of all channels in a sub-optical-cycle parametric waveform synthesizer," in *CLEO: Science and Innovations*, 2014, p. SF1E. 3.
[3.22] O. Mucke, S. Fang, G. Cirmi, G. Rossi, S.-H. Chia, H. Ye*, et al.*, "Toward Waveform Nonlinear Optics Using Multimillijoule Sub-Cycle Waveform Synthesizers," *Selected Topics in Quantum Electronics, IEEE Journal of,* vol. 21, pp. 1-12, 2015.
[3.23] Y.-R. Shen, "Principles of nonlinear optics," 1984.
[3.24] G. Cerullo, M. Nisoli, S. Stagira, and S. De Silvestri, "Sub-8-fs pulses from an ultrabroadband optical parametric amplifier in the visible," *Optics letters,* vol. 23, pp. 1283-1285, 1998.
[3.25] A. Baltuška, T. Fuji, and T. Kobayashi, "Visible pulse compression to 4 fs by optical parametric amplification and programmable dispersion control," *Optics letters,* vol. 27, pp. 306-308, 2002.
[3.26] G. Cerullo and S. De Silvestri, "Ultrafast optical parametric amplifiers," *Review of scientific instruments,* vol. 74, pp. 1-18, 2003.
[3.27] D. Brida, G. Cirmi, C. Manzoni, S. Bonora, P. Villoresi, S. De Silvestri*, et al.*, "Sub-two-cycle light pulses at 1.6 μm from an optical parametric amplifier," *Optics letters,* vol. 33, pp. 741-743, 2008.
[3.28] A. Siddiqui, G. Cirmi, D. Brida, F. Kärtner, and G. Cerullo, "Generation of< 7 fs pulses at 800 nm from a blue-pumped optical parametric amplifier at degeneracy," *Optics letters,* vol. 34, pp. 3592-3594, 2009.
[3.29] D. Brida, C. Manzoni, G. Cirmi, M. Marangoni, S. Bonora, P. Villoresi*, et al.*, "Few-optical-cycle pulses tunable from the visible to the mid-infrared by optical parametric amplifiers," *Journal of Optics,* vol. 12, p. 013001, 2010.
[3.30] A. Shirakawa, I. Sakane, and T. Kobayashi, "Pulse-front-matched optical parametric amplification for sub-10-fs pulse generation tunable in the visible and near infrared," *Optics Letters,* vol. 23, pp. 1292-1294, 1998/08/15 1998.
[3.31] G. Cerullo, A. Baltuška, O. D. Mücke, and C. Vozzi, "Few-optical-cycle light pulses with passive carrier-envelope phase stabilization," *Laser & Photonics Reviews,* vol. 5, pp. 323-351, 2011.
[3.32] T. Schibli, J. Kim, O. Kuzucu, J. Gopinath, S. Tandon, G. Petrich*, et al.*, "Attosecond active synchronization of passively mode-locked lasers by balanced cross correlation," *Optics letters,* vol. 28, pp. 947-949, 2003.

[3.33] C. Manzoni, O. D. Mücke, G. Cirmi, S. Fang, J. Moses, S. W. Huang*, et al.*, "Coherent pulse synthesis: towards sub-cycle optical waveforms," *Laser & Photonics Reviews,* vol. 9, pp. 129-171, 2015.
[3.34] S.-H. Chia, G. Cirmi, S. Fang, G. M. Rossi, O. D. Mücke, and F. X. Kärtner, "Two-octave-spanning dispersion-controlled precision optics for sub-optical-cycle waveform synthesizers," *Optica,* vol. 1, pp. 315-322, 2014/11/20 2014.
[3.35] J. Kim, J. R. Birge, V. Sharma, J. G. Fujimoto, F. Kärtner, V. Scheuer*, et al.*, "Ultrabroadband beam splitter with matched group-delay dispersion," *Optics letters,* vol. 30, pp. 1569-1571, 2005.
[3.36] H. A. Haus, "Waves and Fields in Optoelectronics (Prentice-Hall series in solid state physical electronics)," 1984.
[3.37] C. Manzoni, G. Cirmi, D. Brida, S. De Silvestri, and G. Cerullo, "Optical-parametric-generation process driven by femtosecond pulses: Timing and carrier-envelope phase properties," *Physical Review A,* vol. 79, p. 033818, 2009.
[3.38] F. Adler, A. Sell, F. Sotier, R. Huber, and A. Leitenstorfer, "Attosecond relative timing jitter and 13 fs tunable pulses from a two-branch Er: fiber laser," *Optics letters,* vol. 32, pp. 3504-3506, 2007.
[3.39] G. Krauss, S. Lohss, T. Hanke, A. Sell, S. Eggert, R. Huber*, et al.*, "Synthesis of a single cycle of light with compact erbium-doped fibre technology," *Nature Photonics,* vol. 4, pp. 33-36, 2010.

Chapter 4

Spatiotemporal dynamics of octave-spanning Ti:sapphire lasers

4.1 Introduction

Femtosecond sources with a broadband spectrum in a simple and robust fashion have paved ways for scientific explorations in many fields, such as optical metrology [4.1-3], study of ultrafast dynamics [4.4], and nonlinear light microscopy [4.5-7]. After invention of the first self-starting Ti:sapphire lasers [4.8], Kerr-lens mode-locking (KLM) offers a robust mechanism in the operation of femtosecond oscillators. With the advance in KLM solid-state lasers, few-cycle pulses can be routinely generated from a single laser oscillator with a broadband gain medium (*e.g.*, Ti:sapphire [4.9-11] and Cr-doped crystals [4.12, 13]). However, despite the great success in demonstrating few-cycle lasers, the spatiotemporal pulse dynamics has not been precisely understood from the existing numerical models. The whole laser dynamics involving optical nonlinearity is quite complicated. For example, the optical Kerr nonlinearity results in not only spectral broadening by self-phase-modulation but also intensity-dependent beam profile, which is used to differentiate between CW and pulse operation, by self-focusing.

In the early models proposed by Herrmann [4.14, 15] and Christov [4.16-19], the spatiotemporal features such as gain-guiding and space-time astigmatism have been investigated for >10fs pulses. In order to simulate sub-two-cycle or octave-spanning Ti:sapphire lasers demonstrated with dedicated dispersion compensation, a pure temporal approach was employed in our group [4.20]. In this work, all the spatial effects were modeled by an artificial saturable absorber. Therefore, although the experimental octave-spanning spectra have become numerically reproducible, physics behind many phenomena

involving spatial dynamics remains uninvestigated yet. These lasers not only show beam-size variations at different wavelengths, but the mode structure also changes across the entire spectral range [4.21, 22]. In a resonant cavity, the spatial characteristics with its dependence on cavity dispersion, as well as cavity nonlinear phase, are unanswered. As a result, both longitudinal and transverse effects inside the cavity should simultaneously be considered in order to investigate the octave-spanning laser dynamics. Comparing with the pulses applied in previous spatiotemporal models, shorter pulses with much higher intracavity intensities are evolving inside the cavity: when propagating through the gain medium, the intracavity pulses experience stronger nonlinear phase modulation. The modulation leads to coupling between longitudinal and transverse modes of the laser via Kerr nonlinearity, simultaneously from the self-phase modulation (SPM) and self-focusing (SF) effects, and further dominating the spatiotemporal dynamics of the pulse.

In this chapter, I will feature an spatiotemporal model applied to the dynamic investigation of octave-spanning Ti:sapphire oscillators. The mode-locking dynamics is explored numerically from temporal spikes to stable generation of few-cycle pulses, instead of directly jumping into a steady-state solution, which might not be sustainable and triggered from a cold cavity. Moreover, to achieve ultrabroadband operation, the beam is typically tightly focused into the gain medium and the resulting high peak intensity at the focus possibly results in multi-photon processes (ionization and absorption). In this case, multiphoton processes perturb the pulse dynamics by introducing nonlinear losses and plasma defocusing to the pulse transients, which leads to mode-locking instability. An extended three-dimensional (3-D) numerical model is discussed to capture the complete spatiotemporal features that occurs in a dispersion-managed, Kerr-lens mode-locked Ti:sapphire laser operating in few-cycle regime.

4.2 **Spatiotemporal modeling of laser dynamics**

To study the spatiotemporal dynamics of few cycle pulses circulating inside a laser cavity, we conduct a numerical analysis based on a 3-D model and then compare the results with the experimental data. The laser dynamics is determined by the nonlinear propagation through the laser crystal (*e.g.* Ti:sapphire) and the linear evolution through the passive elements such as intracavity mirrors, wedges, and air path. Due to the complicated nonlinear interactions

during the multiple round-trip propagation, the pulse evolution within one round-trip needs to be modeled and simulated in an efficient way. Subsection 4.2.1 describes the nonlinear propagation inside the Ti:sapphire crystal, and the linear pulse evolution in the optical resonator is detailed in Subsection 4.2.2. A (2+1)-D simulation is performed by assuming cylindrically symmetric beam profile to reduce the calculation complexity. We apply the numerical approach to ring cavity configurations, and demonstrate its capability to predict and analyze the full dynamics of few cycle lasers.

4.2.1 **Spatiotemporal nonlinear pulse propagation in the Ti:sapphire crystal**

The nonlinear propagation of the pulse through the crystal can be modeled by a nonlinear spatiotemporal pulse evolution equation. The equation is valid for pulses in single-cycle regime as long as the envelope and the phase of the electric field slowly vary [4.23]. The NLSTPEE equation with a complex envelope $A(r,z,\tau)$ is generally written using a retarded time τ=*t-z/*v_g as:

$$\frac{\partial A(r,z,\tau)}{\partial z} = (\boldsymbol{L}+\boldsymbol{N})A(r,z,\tau) \tag{4.1}$$

The imaginary parts of both $\boldsymbol{L}$ and $\boldsymbol{N}$ show the phase or reshaped waveform during propagation in z direction. On the other hand, the gain and loss experienced by A are indicated in the real parts of both $\boldsymbol{L}$ and $\boldsymbol{N}$. The operator $\boldsymbol{L}$ accounts for the linear effects including diffraction and dispersion through the crystal, which is given by

$$\boldsymbol{L} = \left[-T^{-1}\frac{j}{2n_0k_0}\nabla_\perp^2 - j\boldsymbol{IFT}\{k(\omega)\}\right] \tag{4.2}$$

where $\nabla_\perp^2 \equiv \partial/r\partial r + \partial^2/\partial r^2$ is the transverse Laplacian operator and the last term shows the inverse Fourier transform (***IFT***) of the propagation constant, which is an Eigenfunction in frequency. The first term in Eq. (4.2) stands for the beam diffraction, and the second term describes the dispersive pulse property. k_0 is the wavenumber in vacuum corresponding to the carrier frequency ω_0. $T \equiv (1-(j/\omega_0)\partial_\tau)$ is the operator used to correct the frequency-dependent diffraction and nonlinear effects. Thus, $\boldsymbol{L}$ can be directly operated in frequency domain. However, $\boldsymbol{N}$ should be conducted in time domain, accounting for intensity-dependent nonlinear effects including optical Kerr effect, saturated gain from the gain medium, and multiphoton ionization (MPI):

$$\boldsymbol{N} = \boldsymbol{N}_{Kerr} + \boldsymbol{N}_{gain} + \boldsymbol{N}_{MPI} \tag{4.3}$$

$$\boldsymbol{N}_{Kerr} = -jTk_0 n_2 |A|^2 \tag{4.4}$$

$$\boldsymbol{N}_{gain} = \boldsymbol{IFT}\left\{\frac{\eta_q \alpha}{2} \frac{W_p(r,z)/W_{sat}}{1+(W_l(r,z)/W_{sat})} \frac{1}{1+j(\Omega/\Delta\Omega_L)^2}\right\} \tag{4.5}$$

n_2 in Eq. 4.4 is the nonlinear refractive index of the medium. Since the right hand side of Eq. 4.4 is proportional to the spatiotemporal distribution of the beam intensity, the Kerr nonlinearity during the propagation in solid-state lasers not only contributes to the spectral broadening via SPM but also reshapes the beam profile via self-focusing. The gain effect is described as Eq. 4.5, which is an inverse Fourier transform operator regarding gain guiding from pump, intensity saturation, and wavelength-dependent gain line-shape. α is the absorption constant for the pump wavelength in the gain medium, and η_q is the quantum efficiency defined as the photon energy ratio between the pump wavelength and the laser center wavelength. $W_{sat} = \hbar\omega_0/(\sigma_L \tau_L f_{rep})$ is the saturation energy density of the gain medium associated with a cross-section σ_L and the upper-state lifetime τ_L. $f_{rep} = 1/T_R$ denotes the repetition rate of the cavity. Since the round-trip time T_R is much smaller than the upper-state lifetime, instead of implementing instantaneous intensity, the crystal experiences W_p and W_l, which are the integrated energy density (J/m^2) over one cavity round-trip time of the pump and circulating laser beam, respectively. Ω is the detuning from the carrier frequency ω_0, and $\Delta\Omega_L$ is the half-width half-maximum bandwidth of the gain line-shape. The gain line-shape is characterized as a Lorentzian function, which is quite constant with the measured gain cross section in Ti:sapphire crystals [4.24]. Along with the gain saturation, the propagating pulses encounter a Lorentzian filtering of the gain line-shape in frequency domain and a gain guiding of the pump beam profile in spatial domain. With proper cavity geometries, self-amplitude modulation (SAM), the interplay between self-focusing and the gain guiding of the pump beam, acts as a saturable absorber, which favors more gain to pulses with higher intensity. Thus, with careful dispersion management and cavity design, both saturated gain and optical Kerr effect assist in achieving stable femtosecond operation.

As the lasers operate in the few-cycle regime with much higher intracavity intensity (~1 TW/cm^2) inside the gain medium, the nonlinear effects related to MPI ought to be taken into account, given by

$$\boldsymbol{N}_{MPI} = -\frac{\beta^{(K)}}{2}|A|^{2K-2} - \frac{\sigma}{2}T(1 - j\omega_0\tau_c)\rho. \tag{4.6}$$

The first term and the second term in Eq. 4.6 correspond to multiphoton absorption (MPA) and plasma absorption/defocusing. K is the photon number required to induce band-to-band transitions of electrons in the Ti:sapphire crystal (*i.e.* K = mod(U_i/E_p), U_i: the material bandgap; E_P: the photon energy of the laser). $\beta^{(K)} = K\hbar\omega_0\sigma_K\rho_{at}$ corresponds to the MPA coefficient proportional to a cross-section σ_K derive from the Keldysh's model. σ is the inverse Bremsstrahlung cross-section that is computed with the reduced electron mass m_e^* in the medium. τ_c represents an average electron collision time. ρ is the plasma density with an upper limit of background atom density ρ_{at}. As a result, plasma generation is characterized via MPI, avalanche ionization, and the recombination process with a characteristic time τ_{rec}, which is given by:

$$\frac{\partial\rho}{\partial t} = \sigma_K|A|^{2K}(\rho_{at} - \rho) + \frac{\sigma}{n^2U_i}|A|^2\rho - \frac{\rho}{\tau_{rec}} \tag{4.7}$$

For a 5-photon process in our case, the importance of MPA and plasma effects increases with intensity to the power of 4 and 5, correspondingly, while the Kerr effect is only linearly proportional to the intensity. Based on literature [4.25-27], the value of abovementioned parameters for the Ti:sapphire crystal are listed in Table 4.1. In order to estimate the influence of MPI effects, Fig. 4.1(a) shows the peak plasma density inside the Ti:sapphire crystal generated via different peak intensities from 0.1 to 10 TW/cm^2 with a 10 fs pulse. Fig. 4.1(b) compares the nonlinear coefficients for Kerr effect (= $n_0k_0n_2I$), MPA (=$\beta^{(5)}I^4/2$), and plasma effects (=$\sigma I^5\rho/2$). As a rule of thumb, when the intensity approaches 1 TW/cm^2, the contribution from higher-order nonlinearity could be no longer negligible.

Parameter	Value (@ 0.8 μm)	
n_0	1.76	-
n_2	$3x10^{-20}$	m^2/W
ω_0	$2.3562\ x10^{15}$	rad/s
η_q	0.6650	-
α	450	m^{-1}
σ_L	$3x10^{-23}$	m^2
τ_L	$3\ x10^{-4}$	s
U_i	7.3	eV
E_P	1.55	eV
K	5	-
ρ_{at}	$11.6\ x10^{28}$	m^{-3}
σ_K	$3.45\ x10^{-73}$	$s^{-1}m^{19}W^{-5}$
$\beta^{(K)}$	$4.97\ x10^{-62}$	m^7W^{-4}
σ	$1.9\ x10^{-21}$	m^2
m_e^*	0.35	m_e
τ_c	$1\ x10^{-15}$	s
τ_{rec}	$1.5x10^{-13}$	s
$\Delta\Omega_L$	$3.24\ x10^{14}$	rad/s

Table 4.1. Parameters for Ti:sapphire crystals

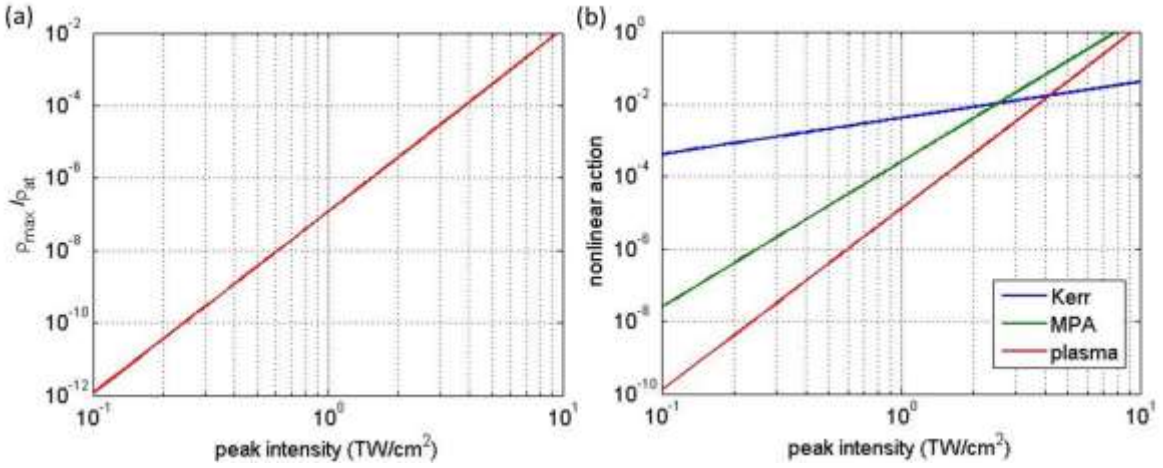

Fig. 4.1. (a) Maximum plasma density and (b) nonlinear action contributed by Kerr effect (blue), MPA (green), and plasma effects (red) as functions of peak intensity generated from 10 fs pulses, according to the parameters listed in Table 4.1.

4.2.2 **Optical Resonators**

In each round-trip, the pulse experiences nonlinear evolution when passing through the gain or Kerr medium, which dynamically reshapes its spatial and temporal profile. For the rest of the path, the pulse experiences linear propagation according to the spatial arrangement as well as the dispersion of the intracavity components.

Self-consistent q-parameter in ring cavity oscillators

Propagating Gaussian beam under paraxial approximation, the *q* parameter is very useful for describing the beam evolution through lenses, mirrors, and tilted plates, as well as optical systems, such as a laser cavity with a series of optical components. The effect of an optical system on a Gaussian beam can be determined by a bilinear transformation of *q* using the ABCD matrix approaches. The generalized ABCD matrices describing propagation, refraction, and reflection of Gaussian beams are shown in Table 4.2.

	$\begin{bmatrix} A & B \\ C & D \end{bmatrix}$	
	Sagittal	Tangential
Propagation in a medium with an optical path length d	$\begin{bmatrix} 1 & d \\ 0 & 1 \end{bmatrix}$	
Refraction at a curved interface	$\begin{bmatrix} 1 & 0 \\ \dfrac{cos\theta_i - \sqrt{{n_r}^2 - sin^2\theta_i}}{Rn_r} & \dfrac{1}{n_r} \end{bmatrix}$	$\begin{bmatrix} \dfrac{\sqrt{{n_r}^2 - sin^2\theta_i}}{n_r cos\theta_i} & 0 \\ \dfrac{cos\theta_i - \sqrt{{n_r}^2 - sin^2\theta_i}}{Rcos\theta_i\sqrt{{n_r}^2 - sin^2\theta_i}} & \dfrac{cos\theta_i}{\sqrt{{n_r}^2 - sin^2\theta_i}} \end{bmatrix}$
Reflection at a curved interface	$\begin{bmatrix} 1 & 0 \\ \dfrac{-2}{Rcos\theta_i} & 1 \end{bmatrix}$	$\begin{bmatrix} 1 & 0 \\ \dfrac{-2cos\theta_i}{R} & 1 \end{bmatrix}$

Table 4.2. ABCD matrices for beam propagation, refraction, and reflection at the sagittal/tangential plane. , θ_i is the angle of incidence; R is the radius of curvature of the interface. n_r is the medium index ratio of the output port to the input port.

To solve the resonant modes supported by a laser cavity, one can calculate the overall ABCD matrix by multiplying the matrix of each individual component in one round-trip. The ABCD matrix is calculated from an arbitrary plane of interest (*i.e.*, a reference plane). For a stable operation, the transverse mode must reproduce itself after every round-trip, *i.e.*,

$$q = \frac{Aq+B}{Cq+D}. \tag{4.8}$$

Without loss and gain during the ray transfer (*i.e.*, $AD - BC = 1$), the self-consistent *q* parameter is then given by

$$q = \frac{A-D}{2C} + j\frac{1}{|C|}\sqrt{1-(\frac{A+D}{2})}. \quad (4.9)$$

The stable cavity configuration is obtained by requiring that q must have nonzero imaginary part, *i.e.*,

$$-2 \le A + D \le 2. \quad (4.10)$$

Once the q parameter on a reference plane is found, the structure and the round-trip Gouy phase shift of the resonator mode across the entire cavity are obtained. The beam waist radius w_o and the waist position x with respect to the reference plane can be obtained from the Eigen-q-parameter according to:

$$x = -Re\{q\}, \quad (4.11)$$

$$w_o = \sqrt{\lambda/\pi Im\{q\}}. \quad (4.12)$$

The numerical model is tested on a four-mirror ring cavity. The scheme of the ring cavity, as well as the denoted distance between each optical element and tilted angle, is as shown in Fig. 4.2. The cavity consists of one pair of flat mirrors and one pair of curved mirrors with a radius of curvature (R) of 2.5 cm. The gain crystal is typically placed at Brewster angle in order to reduce the Fresnel reflection loss. During the cavity alignment, there are many practical issues related to the cavity stability and further the maximization of mode-locking strength. In the stability region, a standing wave can be formed in the cavity. Mathematically, it is judged by whether a self-consistent q parameter (see Eq. 4.9) exists or not. Moreover, in order to compensate the astigmatism induced from the tilted crystal, θ_1 and θ_2, as well as L_1 and L_2, should be optimized in order to overlap the cavity stability region between the tangential and sagittal plane.

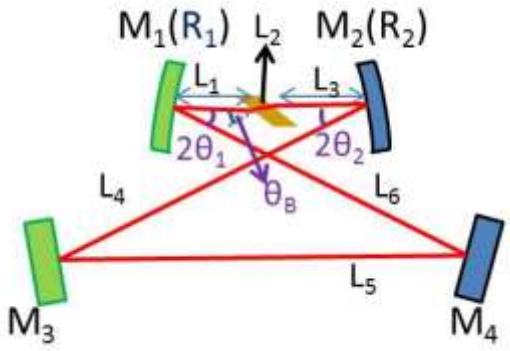

Fig. 4.2. Schematic of the typical ring cavities used for KLM oscillators. The curved mirrors M_1 and M_2 are tilted with θ_1 and θ_2, respectively, to compensate the astigmatism, which is introduced by the crystal that is placed at Brewster angle θ_B.

R_1=R_2	L_2	L_1=L_3	$\theta_1 = \theta_2$	L_4+L_5+L_6
25mm	2mm	11.5mm-15.5mm	10.03°	120mm

Table 4.3. Ring resonator paremeters applied in Fig. 4.2.

In a simple case, one can choose an identical angle (*i.e.*, $\theta_1 = \theta_2$) and an identical distance (*i.e.*, $L_1 = L_3$) to compensate the crystal astigmatism. As the cavity geometry with the listed parameters in Table 4.3, the size of the beam waist inside the crystal can be obtained as a function of curve mirror spacing (*i.e.*, L_1+L_2+L_3): one stability region can be found in such ring cavity oscillators as shown in Fig. 4.3.

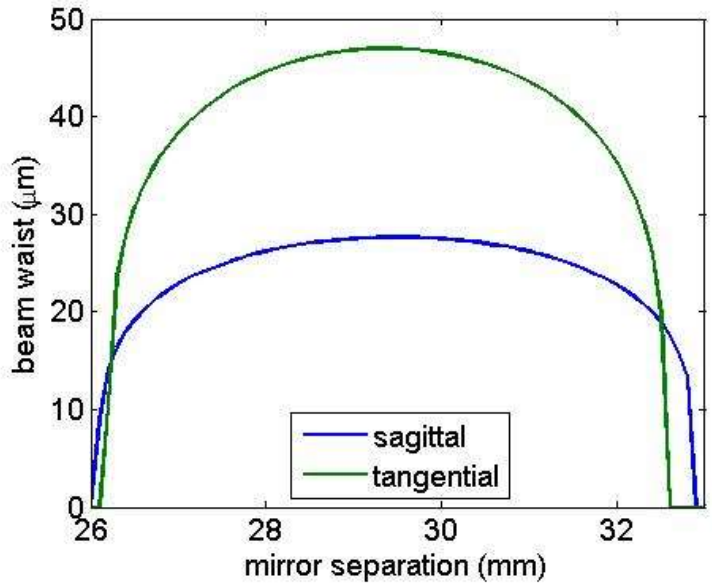

Fig. 4.3. Waist size vs. mirror spacing for astigmatism-free operation in sagittal (blue) and tangential (green) plane.

Transverse modes

Although the fundamental Gaussian beam is the most important spatial mode in ultrafast lasers, the existence of higher-order transverse modes cannot be ignored for understanding the solid-state mode-locking dynamics in the few-cycle regime. As discussed in many papers [4.15, 21], mode-locking of ultra-broadband lasers is usually accompanied by a wavelength-dependent beam profile. In a resonator (*i.e.*, with a self-consistent *q* parameter), these highly structured modes can be decomposed into a complete orthogonal basis set of Gaussian modes such as Hermite-Gaussian and Laguerre-Gaussian modes. In this work, we consider radially symmetry in the spatiotemporal simulations and use Laguerre-Gaussians as

the basic set in order to speed up the computation, although this is not true in reality due to the presence of tilted curved mirrors and Brewster plates. However, from a previous analysis, a radially symmetric cavity permits an effective resonator design and offers reliable guidelines for the final experimental optimization [4.28]. In this case, the mode field distribution with a radial index p and azimuthal index l is given by

$$u_{pl}(r,\varphi,z)\sim\frac{1}{w(z)}\left(\frac{\sqrt{2}r}{w(z)}\right)^{|l|}L_p^{|l|}(\frac{2r^2}{w^2(z)})e^{-\frac{r^2}{w^2(z)}}e^{-j\frac{kr^2}{2R(z)}}e^{il\varphi}e^{j(2p+|l|+1)\emptyset(z)}, \tag{4.13}$$

where $L_p^{|l|}$ are the generalized Laguerre polynomials. $w(z)$, $R(z)$, and $\emptyset(z)$ determined by the q parameter, are the beam radius, curvature of the waveform, and Gouy phase in fundamental Gaussian mode at position z, respectively. Aside from the more complex radial dependence, the experienced phase shift is greater than one in the fundamental mode by an amount that depends on the mode parameters. That is, the mode-dependent Guoy phase shift can be expressed as

$$\Delta\emptyset_{Guoy}(p,l)=(2p+|l|+1)\Delta\emptyset_{Guoy,fundamental}. \tag{4.14}$$

Typically, the fundamental mode sees more gain than the higher-order modes since it overlaps better with the pump laser. As a result, efficient oscillators are usually stably operated in the fundamental mode around their center wavelength. However, with a tightly focused beam inside the gain medium, the strong Kerr nonlinearity required for broadband operation induces higher-order transverse mode in the spectral wings. Therefore, in a broadband resonator, transverse-mode-dependent Guoy phase shift might lead to the coupling between longitudinal and transverse modes. As a result, especially in the wavelength regimes where the crystal provides nearly no gain (*e.g.* above 1.1 μm and below 0.6 μm for Ti:sapphire oscillators), these excited high-order modes could dominate the beam profile depending on the cavity loss and overall dispersion. The detailed phase-matching condition and resonances will be discussed in the following section.

4.3 Cavity simulation and dynamic analysis

4.3.1 Cavity setup

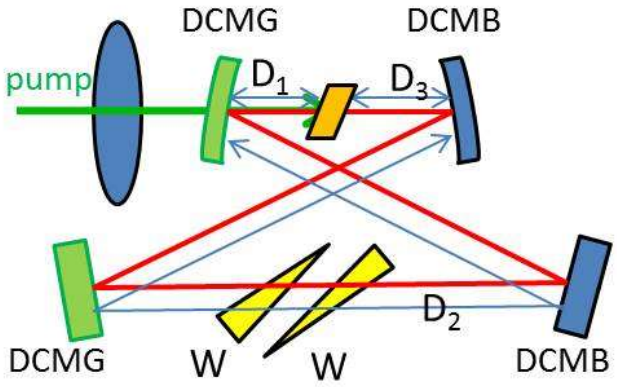

Fig. 4.4. Setup of four-mirror ring cavities of few-cycle Ti:sapphire oscillators.

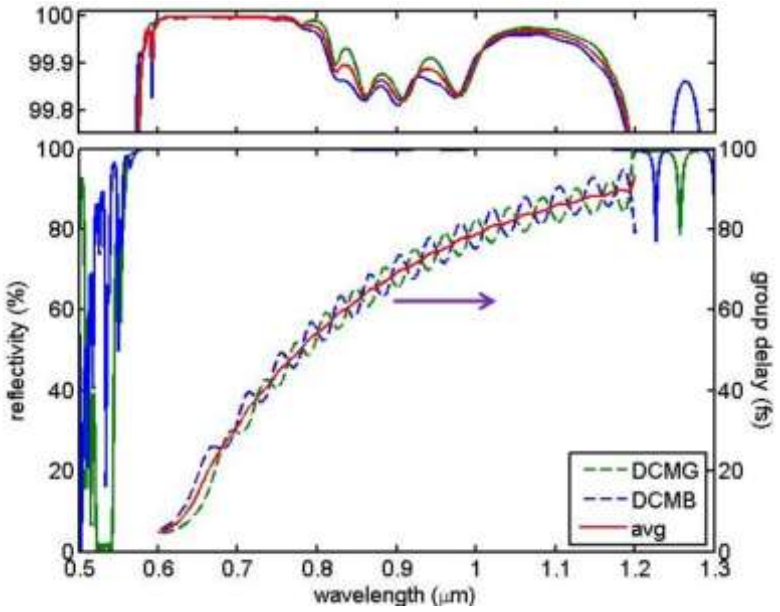

Fig. 4.5. Reflectivity and group delay for a typical double-chirped mirror pair used in the octave-spanning Ti:Sapphire laser, which comprises DCMG and DCMB. The high reflectivity window, as well as the designed GD behaviors, is well-controlled in the whole operating regime of 0.6 μm – 1.2 μm. DCMB also features an extreme-low reflection region near 532 nm which allows the transmission of the pump beam.

The laser dynamics is simulated with a four-mirror cavity as plotted in Fig. 4.4. The cavity comprises 2-mm Ti:sapphire crystal, one pair of flat mirrors, and one pair of curved mirrors with a radius of curvature of 25 mm, as well as a pair of wedges to fine tune cavity

dispersion. DCM pairs are employed as both flat and curved mirror pairs in order to compensate cavity dispersion with an octave-spanning bandwidth (*i.e.*, 0.6 μm – 1.2 μm). Fig. 4.5 shows the typical performance of a DCM pair that can support octave-spanning operation from the Ti:sapphire oscillators. The dispersion of the mirror pairs is carefully designed and fabricated to compensate the material dispersion, even considering the air dispersion, inside the laser cavity over the whole operating range.

In order to precisely control the size and the relative position of the cw laser mode and pump mode inside the crystal, we numerically adjust the position and the angle of the curved mirrors based on the analysis of cavity stability region as described in Subsection 4.2.2. In experiments, the dispersion of the crystal is usually overcompensated by the double-chirped mirror pairs and then precisely adjusted by inserting additional dispersion compensating wedges made of, for example, BaF_2 or fused silica. To simplify the numerical study and to explain the spatiotemporal mode-locking dynamics, we first test an ideal cavity with a constant loss and phase for all wavelengths, while varying a net GDD after a round-trip pass in order to simulate the dispersion fine-tuning. The dependence of important cavity parameters will be studied. Finally, the reflectivity and dispersion from the DCMs as well as the output coupler calculated from the real mirror designs will be used to simulate the practical cavity. In our simulation, we use a 300×1024 matrix to describe the field with a spatial and time resolution of 0.5 μm and 1.2 fs, respectively.

4.3.2 **Efficient beam propagation**

In the split-step method for efficient computation, some steps, especially the linear propagation, is usually calculated in frequency domain (for both time and space) instead of solving the equation directly in the real space. The frequency-domain field can be calculated by Hankel transform (HT) in the cylindrical coordinates in space and Fourier transform (FT):

$$\boldsymbol{A}(v, z, \Omega) = \boldsymbol{FT}\{\boldsymbol{HT}\{A(r, z, \tau)\}\}. \tag{4.15}$$

A is the complex envelop function with its amplitude normalized to the intensity I (*i.e.*, $|A|^2=I$). The physical meaning is also easier to understand when the beam is viewed as a superposition of many frequency components representing different longitudinal and transverse modes. After a fine propagation distance Δz, a linear propagation phase shift is added to each mode, *i.e.*,

$$\boldsymbol{A}(v, z+\Delta z, \Omega) = exp\left\{j\left[\left(1+\frac{\Omega}{\omega_0}\right)^{-1}\frac{2\pi^2 v^2}{n_0 k_0} - k(\Omega)\right]\Delta z\right\}\boldsymbol{A}(v, z, \Omega), \tag{4.16}$$

where the transverse Laplacian operator and the differentiation in time (∂_τ) are avoided and replaced by $-4\pi^2 v^2$ and $j\Omega$, respectively. Outside the gain crystal, the pulse experiences linear propagation according to cavity geometry and the dispersion of the intracavity components. For efficient computation, an equivalent optical system with two effective lenses, which is separated by an effective distance, can be found. In a ring cavity, Fig. 4.6 shows the unfolded schematic of a typical cavity path outside the crystal and the corresponding equivalent system. To find the equivalent system, an overall ABCD matrix describing all the components in the real path is calculated. The beginning and ending reference planes are both chosen inside the crystal. n_r is the refractive index ratio between crystal and free space; θ_B and $\theta_B{}'$ are the Brewster angle of the interfaces; θ_1 and θ_2 are the incident angles on the focusing mirrors used for astigmatism compensation.

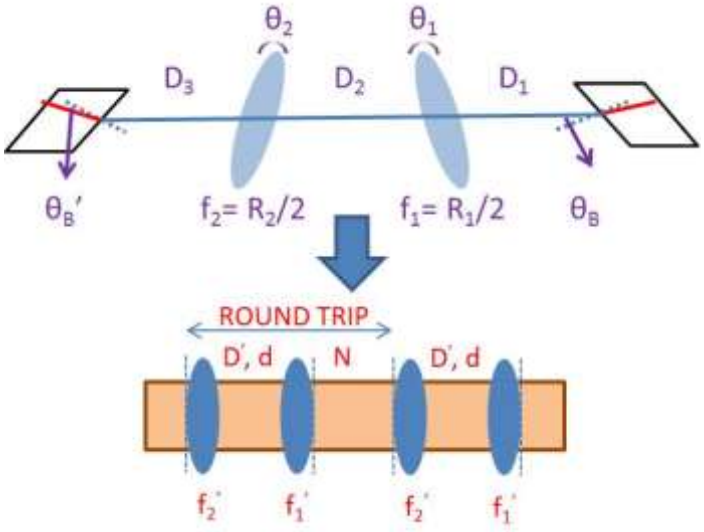

Fig. 4.6. Schematic of a typical unfolded ring cavity (top) with reference planes inside the interfaces of the gain medium, and its equivalent system (bottom) for efficient computation of the beam propagation outside the gain crystal. f', efficient focal length; D', effective spacing; d, cavity dispersion during linear pulse propagation outside the crystal; N, nonlinear pulse propagation in the crystal.

After calculating the overall ABCD matrix between the two reference planes, the efficient focal length (f_1' and f_2') and spacing (D') in the equivalent system [4.29] can be computed by

$$D' = B \tag{4.17}$$

$$f_1' = \frac{B}{1-A} \tag{4.18}$$

$$f_2' = \frac{B}{1-D} \tag{4.19}$$

With the equivalent system and Fourier optics, the propagation outside the gain crystal can be simplified with a series of transformation, from the end surface of the crystal at $z = L$ to the front surface at $z = 0$ in the next round trip:

$$\boldsymbol{A_{i+1}}(r,\Omega)|_{z=0} = \boldsymbol{d} \times \boldsymbol{F_2'} \times \boldsymbol{IHT}\{\boldsymbol{L} \times \boldsymbol{HT}\{\boldsymbol{F_1'} \times \boldsymbol{A_i}(r,\Omega)|_{z=L}\}\} \tag{4.20}$$

where $\boldsymbol{F}'_{1,2}$ are the matrices for the lens transformation $f'_{1,2}$ in space domain; $\boldsymbol{L}$ is the matrix for beam propagation with a distance D'in spatial frequency domain; $\boldsymbol{d}$ accounts for overall cavity dispersion excluding the crystal. These three matrices can be pre-computed with below forms:

$$\boldsymbol{F}'_{1,2}\,(r,\Omega) = exp[j(1+\frac{\Omega}{\omega_0})\frac{n_0 k_0 r^2}{2f'_{1,2}}] \tag{4.21}$$

$$\boldsymbol{L}(v,\Omega) = exp[j\left(1+\frac{\Omega}{\omega_0}\right)^{-1}\frac{2\pi^2 v^2}{n_0 k_0}D'] \tag{4.22}$$

$$\boldsymbol{d}\,(r,\Omega) = \exp[-jk_{all}(\Omega)] \tag{4.23}$$

Same approach can be applied to both linear and ring cavities for efficient computation of beam propagation outside the crystal. However, it should be noted that, in the linear cavity, the beam propagates through the crystal twice: two separated series have to be prepared and applied in two arms for one round-trip, as described in Subsection 5.2.1.

4.3.3 **Local error between round trip**

With the developed spatiotemporal model, the pulse dynamics in a round trip is simulated by considering the linear and nonlinear pulse evolution inside the crystal, and then the linear propagation of other elements inside the cavity with matrix transformations of an equivalent cavity system described in Subsection 4.3.2. In order to study the mode-locking dynamics, the simulation is performed by calculating the pulse evolutions during many round trips before it reaches steady state (*i.e.*, the pulse repeats itself after each round-trip iteration).

To check whether the laser cavity can support a stable pulse, we calculate the local error between round-trips using the following formula:

$$\varepsilon_A = \frac{||A_{i+1}|-|A_i||}{|A_i|} \tag{4.24}$$

When the pulse approaches steady state, the error ε_A gets closer to zero. In the simulation, round-trip iterations repeat until the local error converges and reaches 10^{-4}.

4.4 **Mode-locking Dynamics**

In order to initiate mode-locking in solid-state lasers, a proper trigger is required to stimulate longitudinal mode beating, which is typically obtained by inducing a small mechanical vibration of an intracavity element. As the preliminary test of the model and a reference point of operation used for later comparisons, we create an ideal cavity by assuming that the crystal dispersion is completely compensated by other dispersive components (*e.g.* mirrors and materials other than the crystal) inside the cavity, while providing extra net GDD to shape mode-locking. The cavity is numerically aligned to support a cold-cavity transverse mode (continuous wave mode) with a beam waist of 23 μm at the center of the crystal. The pump beam is also focused onto the same location with a waist size of 10 μm. A constant 3% output coupling is employed over the whole spectral range.

4.4.1 **Transient dynamics: from temporal spikes to stable few-cycle pulses**

Theoretically, mode-locking starts from mode beating, which generates several longitudinal modes simultaneously as temporal spikes. To simulate this phenomenon, a 5 nJ, 200 fs Gaussian pulse is used to trigger the mode-locking. With a net -2 fs^2 GDD cavity, the pulse characteristics (temporal evolution, peak intensity, beam waist, and the total pulse energy) when passing through the Ti:sapphire crystal from the initial condition to the steady-state are shown in Fig. 4.7, as well as the corresponding spectra in Fig. 4.8. The whole dynamics can roughly be described into 3 phases dominating by different pulse-shaping processes.

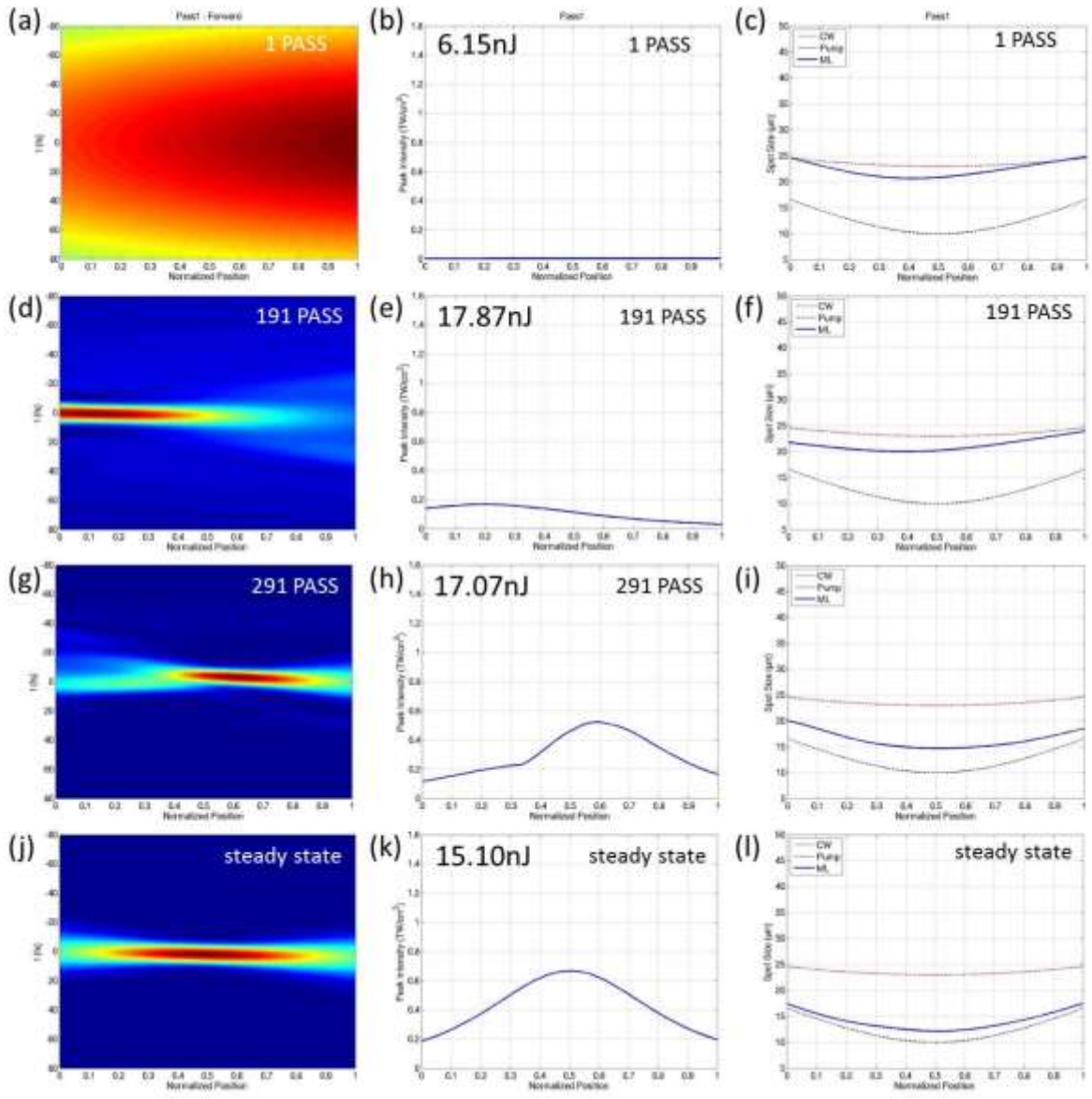

Fig. 4.7. Mode-locking dynamics inside the crystal from a 200-fs initial pulse to the steady state. (a-c), (d-f), (g-i), and (j-l) show the pulse characteristics (temporal evolutions (left), peak intensities (middle), and beam waists (right)) between different phases (1^{st}-191^{th} pass, 191^{th}-291^{th} pass, and 291^{th} pass to the steady state). The cw mode, pump beam, and pulse beam profile are plotted as the red dashed curves, black dashed curves, and blue curves in the right figures. A critical peak intensity (~0.2 TW/cm^2 in this case) as shown in (e) should be reached in order to induce enough SAM, by decreasing the beam size of the main pulse. Shorter pulse is thus favored with the peak intensity above 0.2 TW/cm^2, and the pulse evolution eventually shapes to the steady state. The horizon axes in all the figures are normalized to the crystal length.

Phase I (1^{st} – 191^{th} pass)

In the first phase, along with the growth of the pulse energy, new frequencies are generated due to SPM, and the initial 200 fs pulse is compressed by the cavity elements outside the crystal. As the peak intensity grows, the interplay among gain-guiding, diffraction, and self-focusing effects triggers the oscillation of the laser beam size. Meanwhile, the main

pulse shapes itself by radiating energy in the time domain, resulting in long pulse pedestals or satellite pulses.

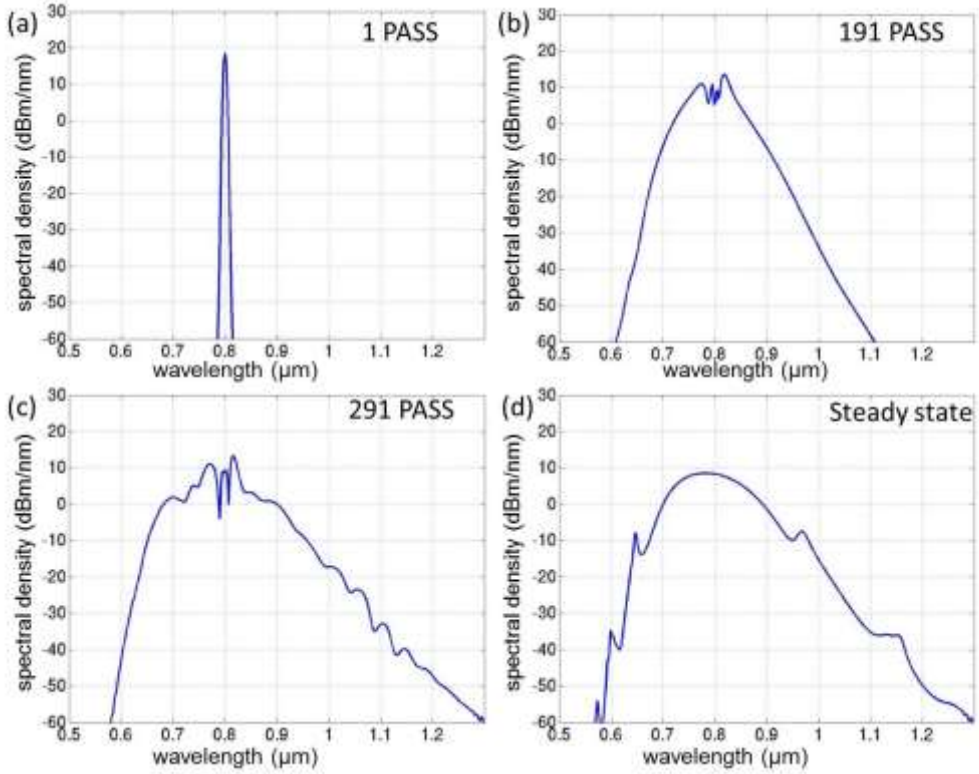

Fig. 4.8. Spectra between different phases (1st-191th pass, 191th-291th pass, and 291th pass to the steady state). In Phase I, the spectra are dominated by SPM. The broadest spectrum typically is obtained in the end of Phase II (291th pass), and shaped by gain bandwidth filtering. The steady-state spectrum eventually is reached and modified along with the cavity resonances.

Phase II (191^{th} – 291^{th} pass)

Once the increasing peak intensity is above a critical value (*e.g.*, ~0.2 TW/cm^2 in this case), the main pulse experiences more gain than the longer satellite pulses or continuous wave via self-amplitude modulation (SAM). SAM is induced by intensity-dependent beam profile: stronger peak intensity leads to stronger self-focusing forming a smaller beam inside the crystal. As a result, the main pulse and the other transients will overlap with the pump beam differently. If the cavity is aligned properly, the beam size of the main pulse has a better overlap with the pump as shown in Fig. 4.7. Otherwise, when propagating with the cold-cavity beam size without a strong-enough SAM inside the crystal, the main pulse, which has higher peak intensity with a broader spectrum, will obtain less gain than other pulse

transients or continuous wave due to gain bandwidth filtering. Although the main pulse still shapes itself in the time domain, the radiating long pulses can be eliminated after several round trips due to less gain. Eventually, the temporal evolution is cleaned up. A broader spectrum than the steady state is obtained via SPM along with gain bandwidth filtering.

Phase III (291^{th} pass to steady state)

After the elimination of pulse transients, the pulse obtains more gain and better beam overlap with the pump. Therefore, the peak intensity is increased, and the spectrum is further shaped by gain bandwidth filtering. The pulse is also modified and cleaned by the resonance cavity until reaching the steady state. For example, spectral spikes in the steady state are observed as shown in Fig. 4.8, which will be explained in Section 4.6.

4.4.2 Mode-locking dynamics with different net cavity dispersions

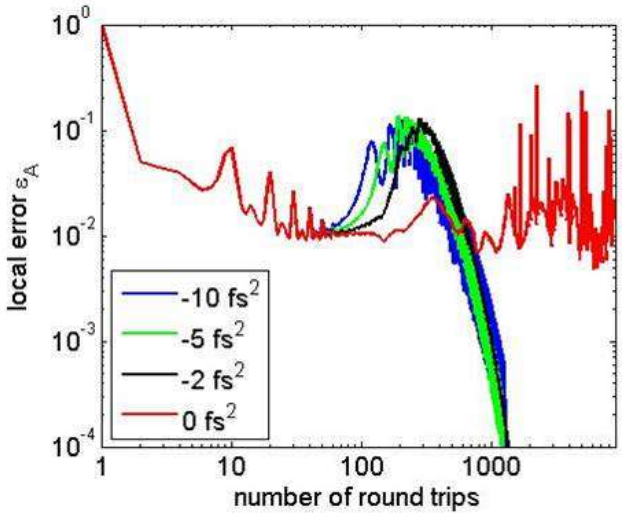

Fig. 4.9. Local errors ε_A from 200fs initial pulses to the steady states with different cavity dispersions.

In experiments, slightly negative dispersion in the cavity is typically employed to access working points of stable mode-locking. In order to simulate the process, we employ cavities with different net GDDs and study the mode-locking dynamics. Fig. 4.9 shows the comparison of local errors ε_A from 5 nJ, 200 fs initial pulses to the steady states with different cavity dispersion.

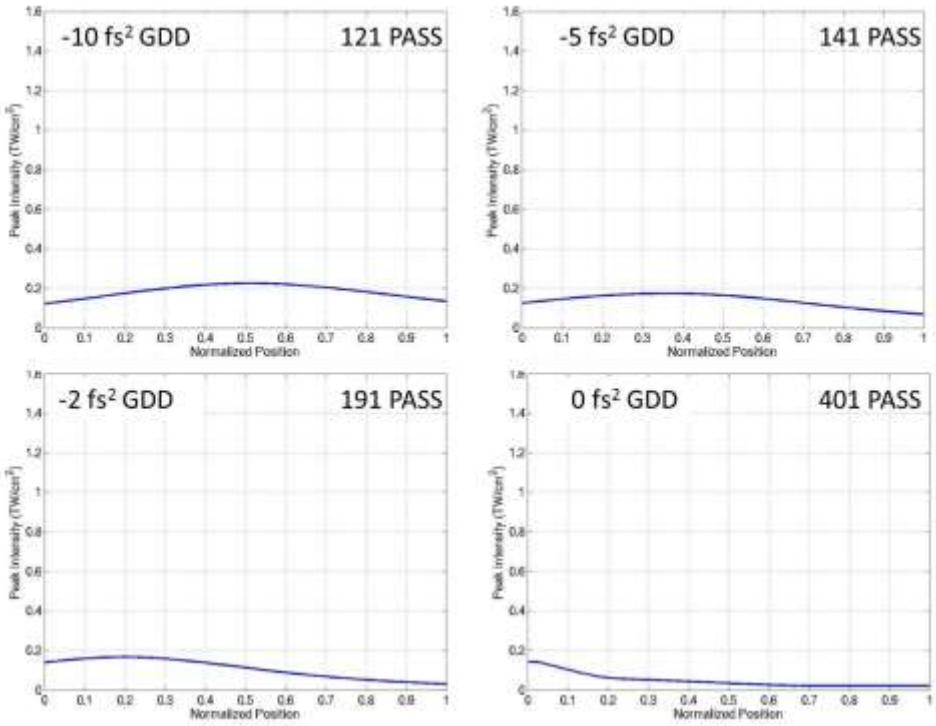

Fig. 4.10. Peak intensities inside the crystal with different cavity dispersion, (a-c) when the critical value (~0.2 TW/cm^2) is obtained, or (d) when the peak intensity reaches its maximum. The cavity dispersion and the corresponding round trip are indicated in the figure. The horizon axes in all the figures are normalized to the crystal length.

In contrast to the negative dispersion cases, the steady state cannot be obtained in the dispersion-free cavity even after more than 9000 round trips. The whole mode locking dynamics can be well-explained. Within ~60 round trips, all the local errors in Fig. 4.9 share the same behavior: the pulse energies are increased, trying to reach the balance between gain and loss. The local error is increased afterward due to the gain competition between the main pulse and its radiated light transients. In this stage, Kerr effect plays a more important role, and a net negative GDD inside the cavity will assist to balance the nonlinear phase induced by SPM. Therefore, the critical peak intensity (0.2 TW/cm^2), as shown in Fig. 4.10, is easier to be obtained along with a slightly negative dispersion within fewer round trips: the pulse can be compressed in a more efficient way. The corresponding evolution of pulse durations inside the crystal, when the critical peak intensity is reached, is also shown in Fig. 4.11. The cleanup of the pulse transients occurs afterwards in the negative dispersion cavities, and the laser dynamics converging to the steady state. However, in a dispersion-free cavity, the critical peak intensity cannot be reached, and the main pulse cannot experience enough gain while competing with the other transients during the whole process:

the temporal evolution and the beam profile inside the crystal in the dispersion-free case after ~9000 round trips are shown in Fig. 4.12.

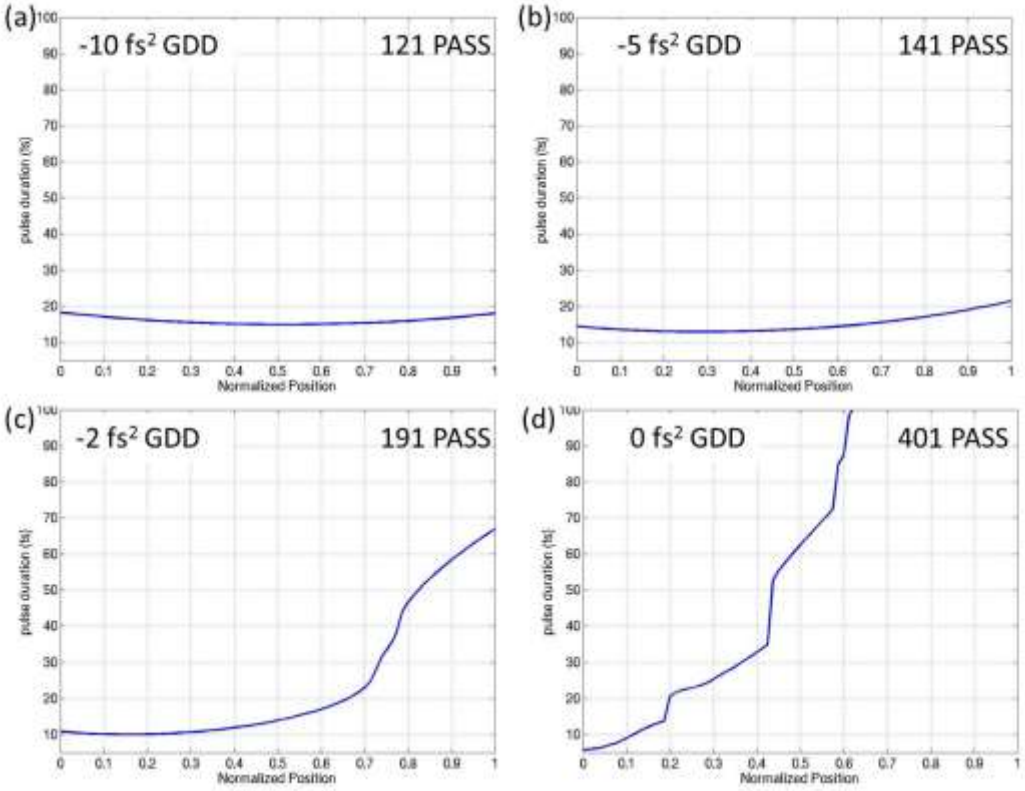

Fig. 4.11. FWHM pulse duration inside the crystal, (a-c) when the critical value (0.2 TW/cm^2) is obtained, or (d) when the peak intensity reaches its maximum. The cavity dispersion and the corresponding round trip are indicated in each figure. The horizon axes in all the figures are normalized to the crystal length.

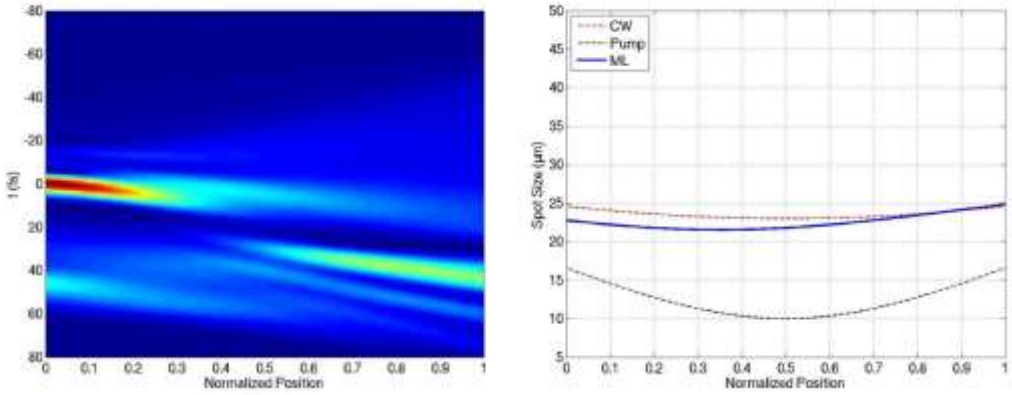

Fig. 4.12. Temporal evolution and the corresponding beam radius inside the crystal in the dispersion-free cavity after ~9000 round trips. The horizon axes in all the figures are normalized to the crystal length.

Although the mode-locking process is easier to be obtained with a negative cavity GDD, the broadest achievable spectrum in the steady state is typically generated with less net negative dispersion, even from the slightly-positive-dispersion cavity. The steady-state spectra with different cavity dispersion are shown in Fig. 4.13 and Fig. 4.14, respectively. However, it is difficult to initiate mode locking directly from such cavities since the critical peak intensity is hardly reached. Fig. 4. 15 shows the local errors using the dispersion-free cavity with different initial pulse durations. With a shorter initial pulse, the peak intensity is easier to reach the critical value, and the pulse transient is harder to be amplified in the crystal. As a result, one should first try to obtain a stable femtosecond generation with a negative cavity dispersion, and then carefully tuning the dispersion (*e.g.*, inserting more BaF_2 or fused silica) to acquire broader spectrum.

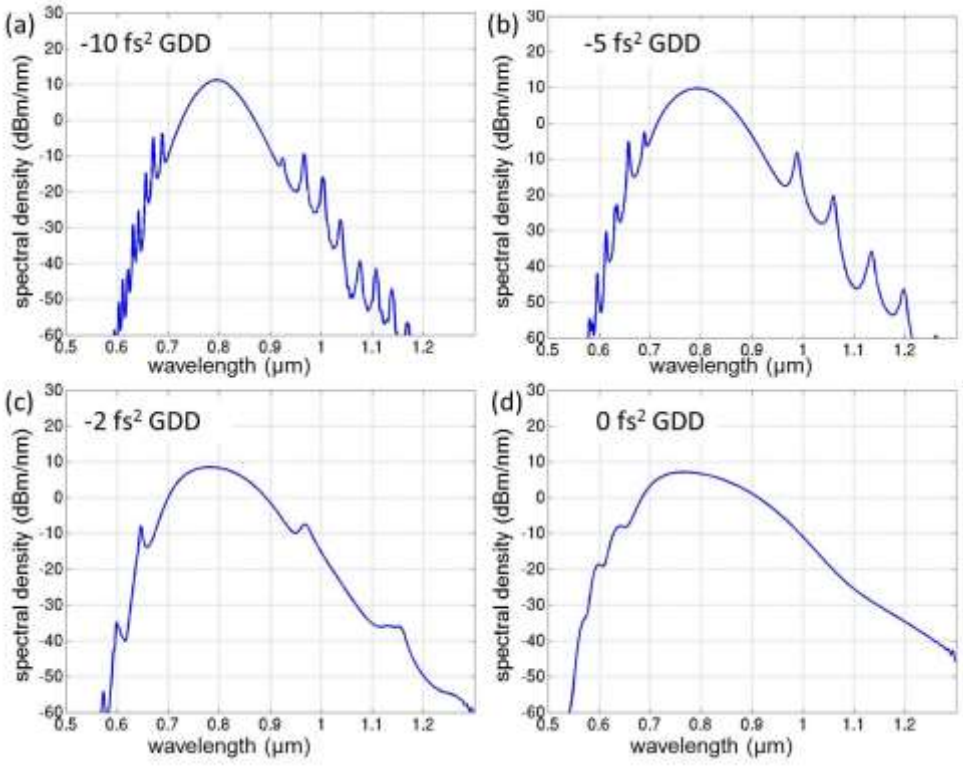

Fig. 4.13. The steady-state spectra with (a) -10fs² GDD, (b) -5fs² GDD, (c) -2fs² GDD, and (d) 0fs² GDD of net cavity dispersion. The corresponding transform-limited pulse width are 10.8 fs, 8.9 fs, 7.8 fs, and 6.2 fs from (a) to (d), accordingly.

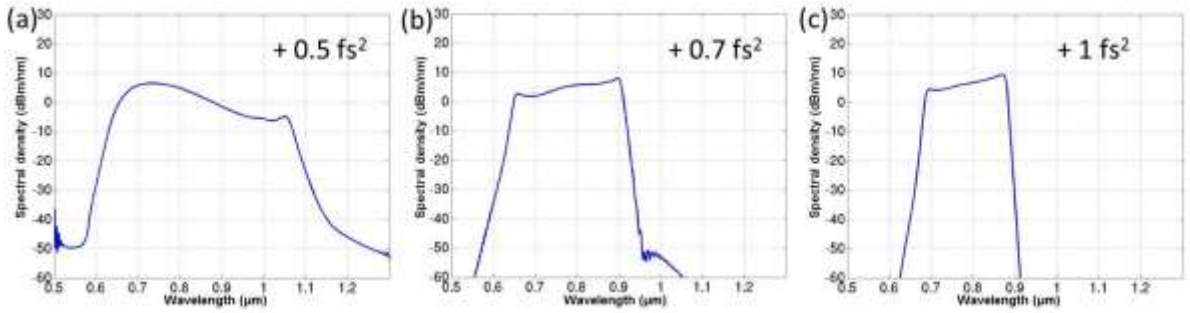

Fig. 4.14 Steady-state spectra with (a) +0.5 fs², (b) +0.7 fs², and (c) +1 fs² GDD of net cavity dispersion. The shortest transform-limited pulse width can be obtained with (a), 5.7 fs.

In order to compare the steady-state performance, Fig. 4.16 shows the simulated transform-limited pulse width and intracavity pulse energy supported by the cavity with different net dispersion. As shown in Fig. 4.16, the spectrum is broader with less pulse energy as the net cavity GDD changes from negative to slightly positive. These phenomena agree with the theory of dispersion-managed soliton mode-locking. When the GDD becomes more positive, a flattop spectrum forms with two steep edges. When the net GDD is closer to zero, the peaks become less dense. In the past, researchers attributed these peaks to phase-matching resonances, but unfortunately the phase-matching condition was not yet found. In fact, these spectral features often come with highly-structured beam profiles in the spectral wings. For example, Fig. 4.17 shows the simulated wavelength-dependent laser beam profiles for a net cavity GDD of -5, -2, 0, and +0.5 fs^2. As a result, one can obtain the broader spectrum, as well as the finer beam profile in the spectral wings, with a slightly positive dispersion. However, the corresponding pulse energy is the lower due to the soliton formation and gain bandwidth filtering.

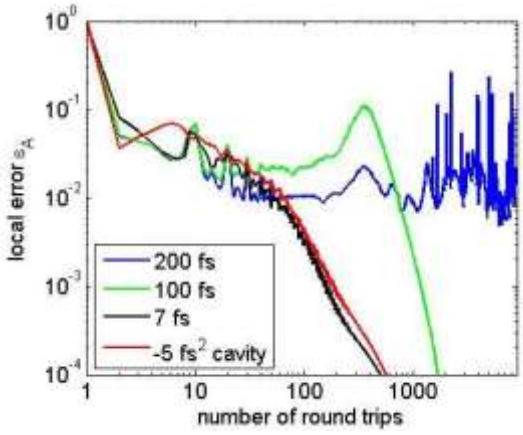

Fig. 4. 15. local errors using a dispersion-free cavity with different initial pulse durations, as well as triggering with the steady-state pulse from a -5 fs² cavity (red).

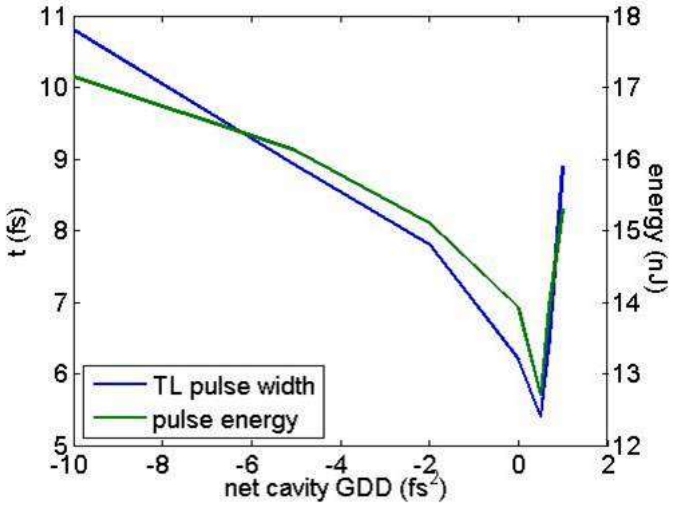

Fig. 4.16. Transform-limited pulse width and intracavity pulse energy vs. net cavity GDD.

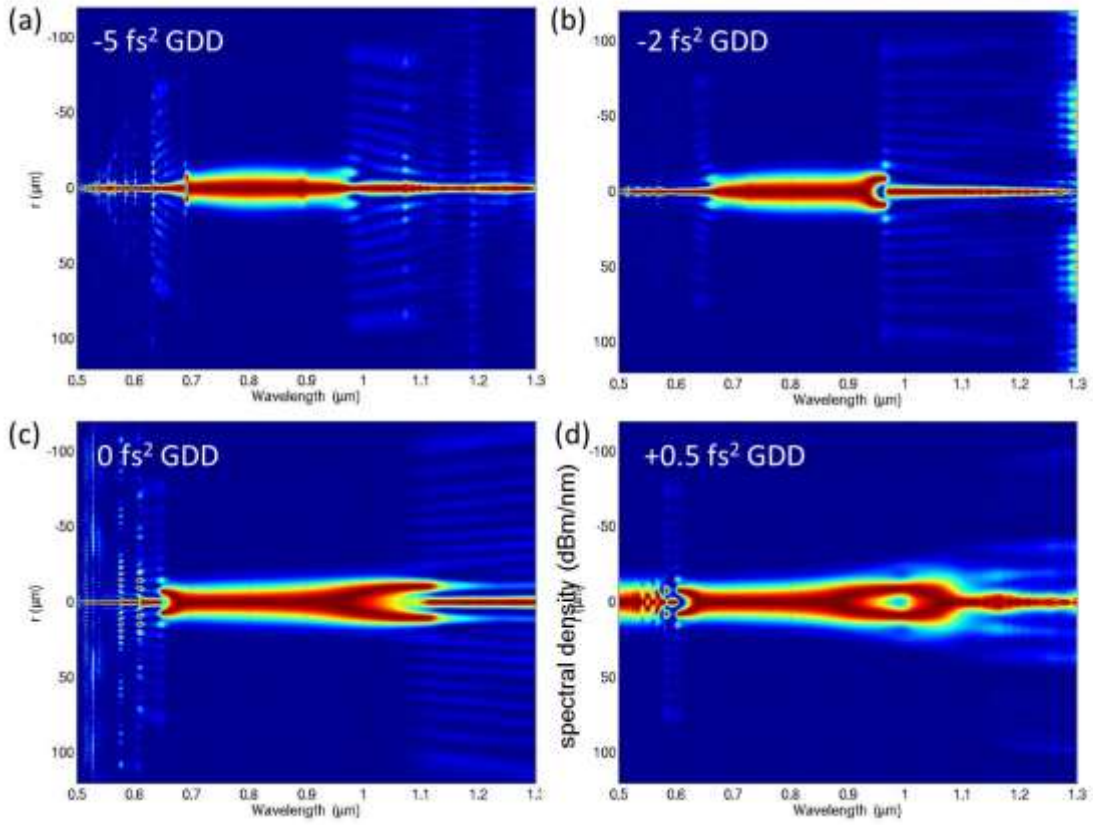

Fig. 4.17. Wavelength-dependent beam profile of a mode-locked beam from a cavity with a net GDD of -5, -2, 0, and +0.5 fs^2.

4.5 **Operating points and performance optimizations**

Looking for an operating point to obtain broadband spectrum with a high output power is an important issue in the construction of KLM oscillators. Even though the result from a pure temporal laser model has shown that octave-spanning spectra can be generated with careful dispersion management, the model fails to figure out the strength of the effective saturable absorption and its connection to the cavity alignment [4.20]. To study the dependence of laser performance on the operating point, a spatiotemporal model must be employed.

In order to optimize the laser performance in terms of the broadband operation with a high pulse energy, one can try to decrease the beam waist of the cavity by varying the mirror spacing between the curved mirrors or increasing the pumping. To illustrate the influences, we simulated the effect of decreasing the mirror spacing on the shorter edge of the stability region from a cw waist size of 23 μm (see Fig. 4.18).

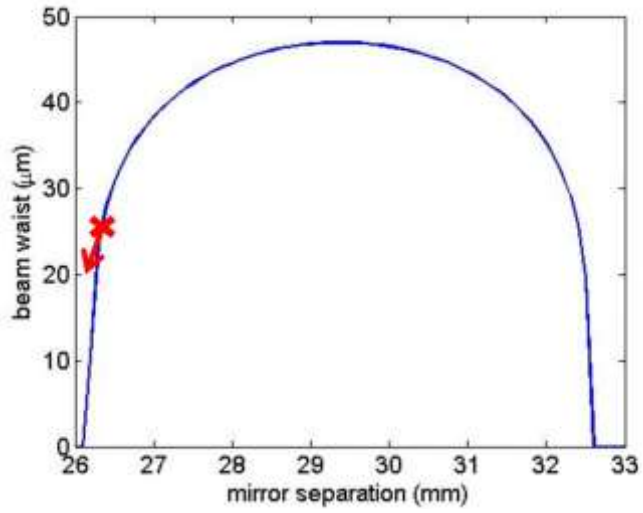

Fig. 4.18. Cold cavity waist size vs. the mirror spacing between the two curve mirrors. An operating point and the direction toward optimization are marked as the red cross and arrow, respectively.

In this set of experiments, instead of controlling mirror spacing, all the cavity parameters are the same as the previous setup with a dispersion-free cavity. The initial pulse duration is 7 fs, by assuming that one has already obtained stable mode-locking with a slightly narrower spectrum. With a smaller cold cavity beam waist, the mode-locked beam is focused to a smaller spot, and the operating point is closer to the edge of the stability region.

As shown in Fig. 4.19(a), the maximum pulse intensity could be as high as >1 TW/cm^2 for the 20 μm case. As a result, the spectrum is broader (see Fig. 4.19(b)) due to stronger SPM when an operating point closer to the edge of stability region is used. However, the pulse energy is decreased since broader spectrum experiences stronger gain bandwidth filtering. Furthermore, the laser might enter an unstable zone if the beam is too tightly focused. When closer to the edge of the stability region (*i.e.*, with a smaller cw beam waist), the pulse transients live longer and further show no sign of convergence with 20 μm of the cw beam waist, as shown in Fig. 4.20.

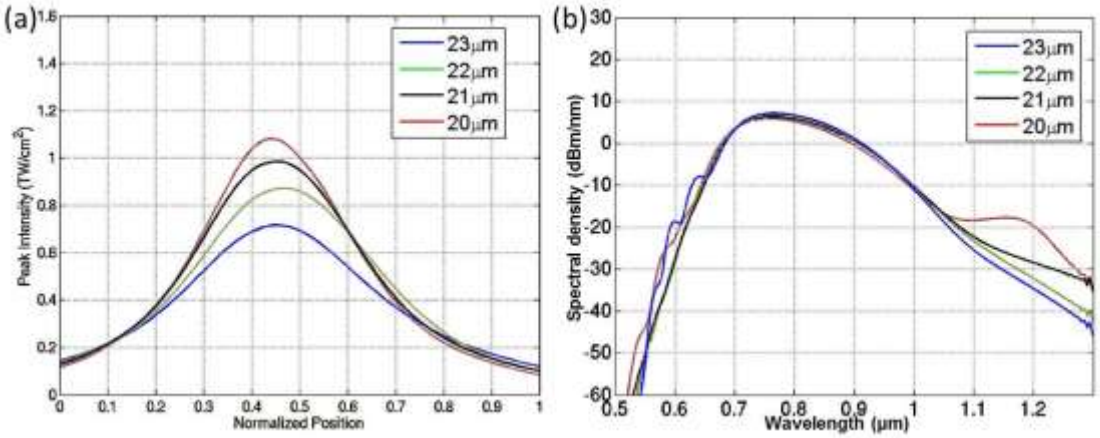

Fig. 4.19. (a) peak intensities and (b) spectra with different operating points, which vary the cold cavity waist sizes as indicated in the legend. The horizon axis in (a) is normalized to the crystal length.

The estimated intensity threshold for the unstable zone is ~1.1 TW/cm^2 in the 2-GHz cavity. This is also the level where a significant multi-photon (MP) effect could be induced. In order to investigate the role of higher-order optical nonlinearities, we numerically switch off the MP operator which is described in Section 4.2. In Fig. 4.21, there are almost no differences in the beam waists, peak intensities, and spectra between the two cases (*i.e.*, with MP and without MP) with ~3000 round trip. Fig. 4.22 also shows the round-trip errors in the two cases, which share very similar behaviors implying the same mode-locking dynamics. As a result, although the peak intensity is as high as ~1.1 TW/cm^2, the mode-locking dynamics is still ruled by the interplay between cavity setup (*e.g.*, geometry and dispersion), gain saturation, and optical Kerr effect inside the crystal.

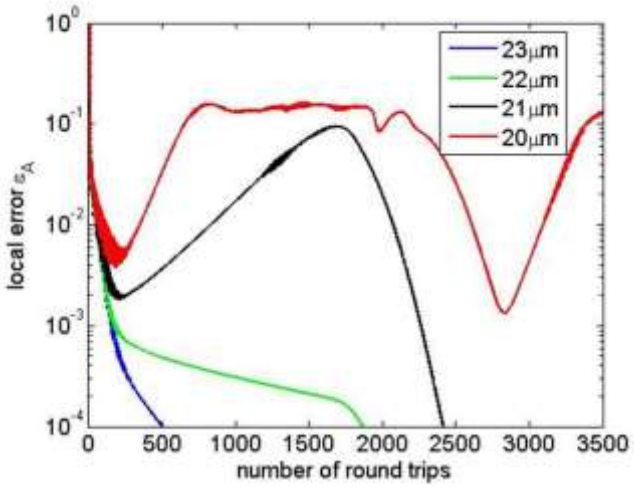

Fig. 4.20. Local errors with different operating points, which vary the cold cavity waist sizes as indicated in the legend. A cavity with <20 μm of the cw waist size inside the crystal cannot reaches a steady state within 3500 round-trips, even using an initial pulse as short as 7fs.

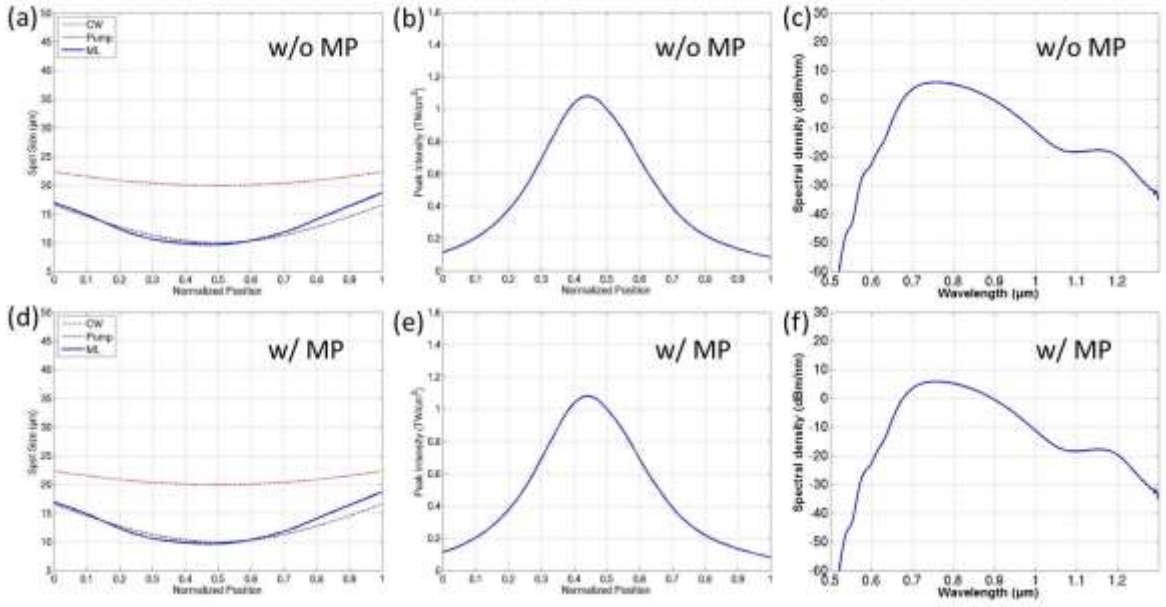

Fig. 4.21. Comparison of (a,d) the beam sizes, (b,e) peak intensities, and (c,f) spectra between two simulation cavity (a-c) including, or (d-f) excluding multiphoton effects, when the oscillator is in the margin of stability region. w/o MP, without multiphoton effects; w/ MP, with multiphoton effects.

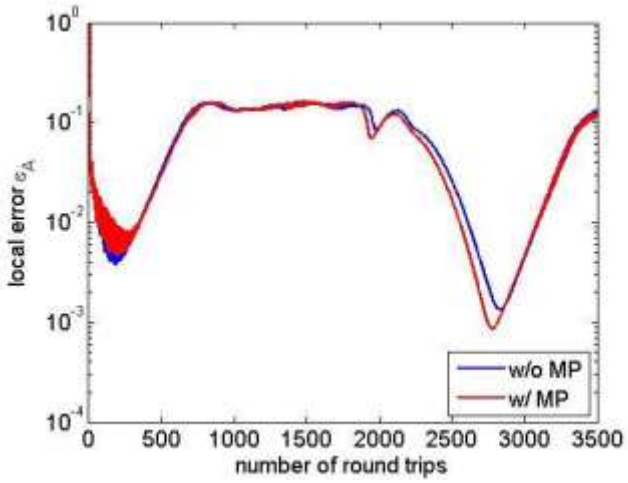

Fig. 4.22. Comparison between local-error dynamics with/without multiphoton effects using a cavity supporting a peak intensity as high as ~1.1 TW/cm^2.

In order to optimize the output power while maintaining the spectral bandwidth, one could try to increase the pumping with a larger cavity waist size. With a higher pump power, the peak intensity becomes larger since the pulse energy also increases. By optimizing the pump power with different cw beam sizes, Fig. 4.23 shows the maximal-obtainable peak intensities as well as the corresponding pulse energies and spectra. The pulse energy decreases when a smaller cw laser waist is employed with a fixed pump power, which agrees with our experimental observations. The result suggests that, in order to maximize the output power from a few-cycle laser, a large cw laser beam waist should be used. Ideally, one can still acquire similar amount of nonlinear phase by increasing the pump power. Practically, the beam distortion caused by the thermal lensing effect might become a severe problem when the pump power is too high.

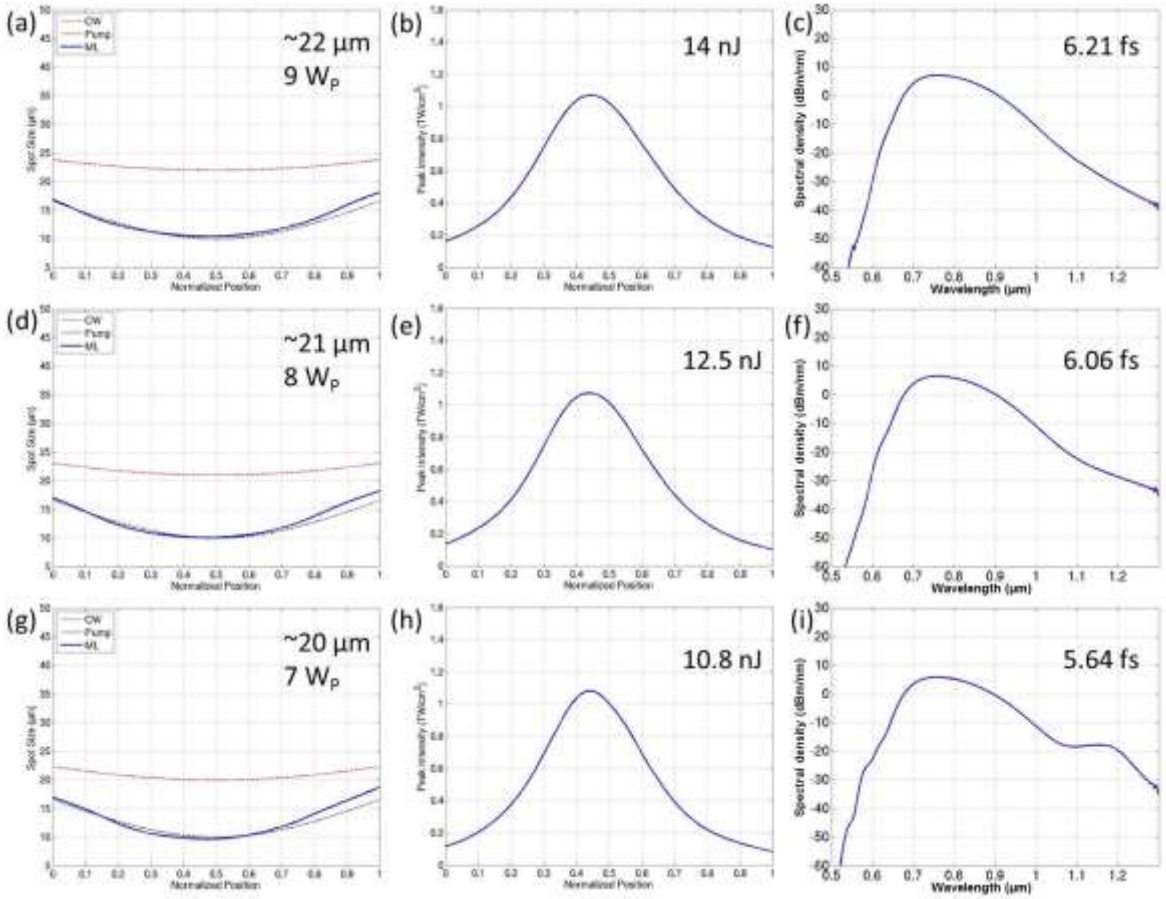

Fig. 4.23. With (a-c) 22 µm, (d-f) 21 µm , and (g-i) 20 µm of cw beam waists, the optimized beam profile (left), peak intensity (middle), and spectrum (right) by applying maximal pump power (indicated in the left figures). The corresponding intracavity pulse energy, and transform-limited pulse width are also shown in the middle and left figures, respectively.

4.6 From ideal cases to practical designs: intracavity spatiotemporal phase matching

After the studies of mode-locking dynamics and optimization of operating points from ideal cavities, some questions of the steady-state behaviors still remain such as the spectral resonances when varying the cavity dispersion (see Fig. 4.13 and Fig. 4.14). Furthermore, in practical cases, DCM pairs and a designed output coupler are used to control the bandwidth of cavity dispersion and round-trip reflectivity. As a result, the cavity dispersion has a certain compensating bandwidth with GD oscillations from DCM, instead of a smooth GD over the whole operation spectral range. Moreover, the output coupling window is usually smaller than the bandwidth of intracavity spectrum, in order to deliver more output from the spectral wings. With the octave-spanning spatiotemporal model, the DCM-based cavity can be numerically set up according to the experimental condition. Fig. 4.24 shows the overall DCM reflectivity and output coupling window in a ring cavity oscillator as well as the round-trip residual phase. All the reflectivity and dispersion of DCMs are calculated from the real mirror designs using in the experiment. The residual phase is obtained by integrating the net cavity GD over frequency. Fig. 4.25 shows a simulated output spectrum. Comparing with an ideal spectrum (see Fig. 4.13(d)) with a flat phase and reflectivity over the whole spectral range, multiple resonance peaks are found around 0.65 μm and 1.1 μm, which can be explained by intracavity spatiotemporal phase-matching.

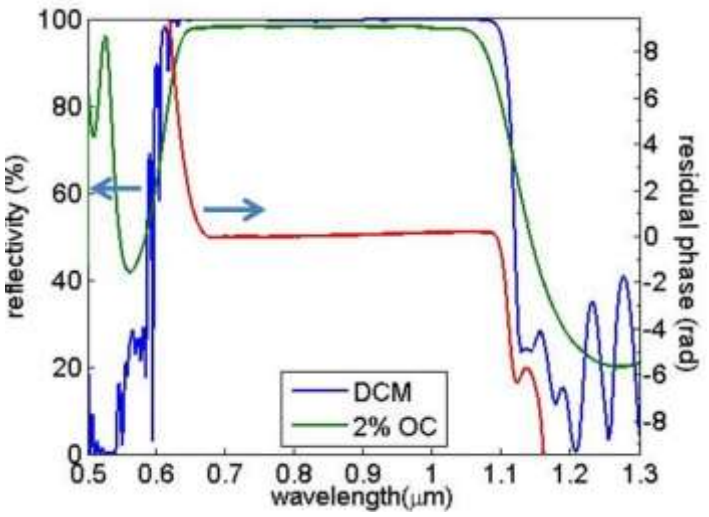

Fig. 4.24. Overall DCM reflectivity (blue) and output coupling window (green) in a DCM-based ring cavity oscillator, as well as the designed round-trip residual phase (red).

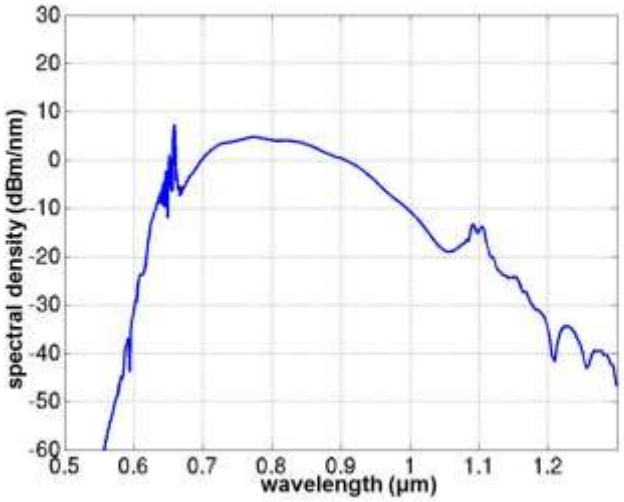

Fig. 4.25. Simulated spectrum from a DCM-based ring cavity.

4.6.1 **Intracavity spatiotemporal phase matching**

In the spectral domain, KLM Ti:sapphire lasers are considered as a dispersion-managed soliton that maintains its shape by the interplay of SPM and cavity dispersion [4.30]. The practical variations apart from ideal cases can be treated and explained as the perturbations to dispersion-managed soliton.

Assuming a lossless cavity without gain and higher-order dispersion, the dispersion-managed SPM associated with dispersive elements inside the cavity (*e.g.*, Ti:sapphire crystals and DCMs) can be balanced, supporting stable few-cycle pulses between round-trip evolutions. Dispersion-managed soliton is thus obtained, and the circulating pulse evolution only gains a fixed amount of nonlinear phase while remaining its shape after every round-trip. However, in addition to SPM and dispersion, the soliton-like mode-locked pulse experiences loss and gain during the propagation. Since the loss, gain, and higher-order dispersion per round-trip are usually small in the steady solid-state oscillators, they can be treated as perturbations to a dispersion-managed soliton whose dynamics is still dominated only by the SPM and GDD. These perturbations lead to radiation of dispersive waves. The low intensity dispersive wave propagates around the cavity with only linear effects like dispersion and diffraction. When the phase contributed by the linear effects equals the nonlinear phase experienced by the soliton wave, the newly generated and existing dispersive waves will coherently add up, resulting in resonantly enhanced peaks in the spectrum. The phase-matching process described here is similar to Kelly sideband generation

[4.31], high-order-dispersion-induced resonance [4.32, 33], and fiber-optic Cherenkov radiation [4.34].

In a solid-state oscillator, the Kerr effect not only induces coupling between longitudinal modes via SPM but also transverse modes via self-focusing. In the spatial domain, the dispersive wave at each wavelength from soliton perturbation can be viewed as a superposition of the transverse modes. As described in Subsection 4.2.2, the higher-order transverse modes experience more Gouy phase than the lower-order modes, which leads to a mode-dependent phase-matching condition. Here we assume that the dispersion-managed soliton is mainly in the fundamental transverse mode due to the mode matching with the pump beam. Therefore, the phase-matching condition is satisfied when the phase of the soliton-like wave equals the phase of the linear dispersive wave per round trip:

$$\emptyset_{Soliton,RT} + 2m\pi = \emptyset_{dispersive,RT} \tag{4.25}$$

That is, by requiring that the nonlinear phase $\emptyset_{NL}$ is matched to the linear phase contributed by the cavity dispersion $\emptyset_D$ and the mode-dependent round-trip Gouy phase $(2p + 1)\emptyset_{Guoy,RT}$, one can write a general phase-matching condition for Laguerre-Gaussian beam assuming radial symmetry with radial index p:

$$\emptyset_{NL} + \emptyset_{Guoy,RT} + 2m\pi = \emptyset_D + (2p + 1)\emptyset_{Guoy,RT}. \tag{4.26}$$

As a result, a transverse mode is enhanced, when the cavity dispersion satisfying the spatiotemporal phase-matching. Within the high reflectivity window of the cavity (*i.e.*, 0.65 µm -1.1 µm, see Fig. 4.24), pulse evolution is shaped by the cavity resonance, as the cases with different net cavity dispersions in Figs. 4.13-14. In addition, when applying the real DCM designs, the cavity dispersion varies rapidly away from a flat round-trip residual phase around the edge of high reflectivity region, which also leads to spectral resonances.

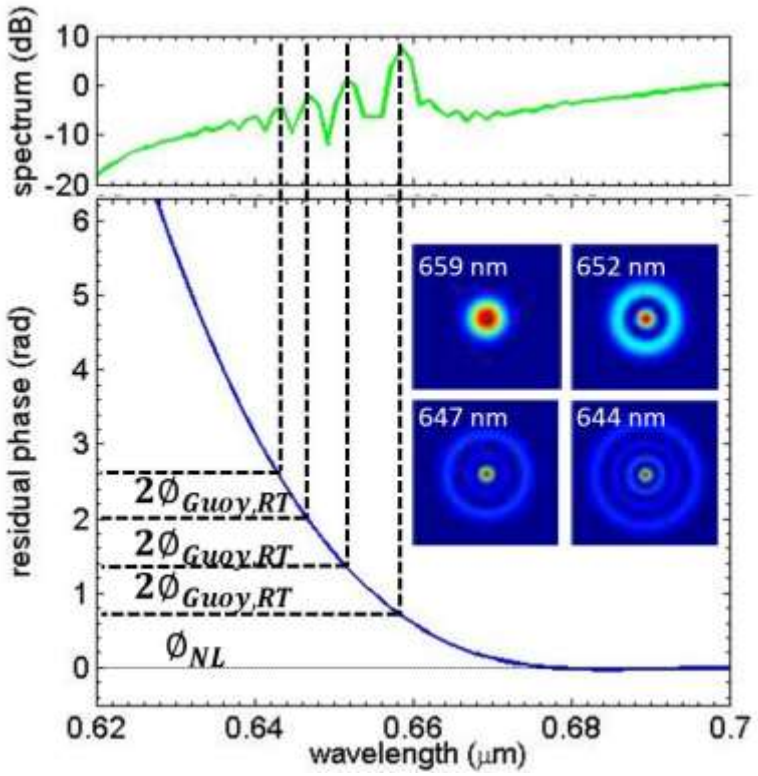

Fig. 4.26. (upper) The resonant peaks near 650 nm of the simulated spectrum, as shown in Fig. 4.25. (bottom) Corresponding round-trip residual phase $\emptyset_D$ due to cavity dispersion. The inset color plots show the phase-matched beam profiles around the specified wavelengths.

In the modeling, the round-trip Guoy phase in the fundamental Gaussian mode, -3.44 rad, is calculated by circulating the supported beam in a cold cavity; the round-trip phase of the dispersion-managed soliton (*i.e.*, $\emptyset_{NL} + \emptyset_{Guoy,RT}$) is around -2.88 rad. The residual phase difference between the wavelengths of adjacent resonant peaks, as shown in Fig. 4.26, is ~0.6 rad, which is consistent with Eq. 4.26 (*i.e.*, twice of Guoy phase shift in the cavity, $|2\emptyset_{Guoy,RT}+2\pi|$). As a result, the position of the phase-matching peaks, as well as the corresponding transverse modes, becomes predictable.

4.6.2 **The role of residual phase oscillations from DCMs**

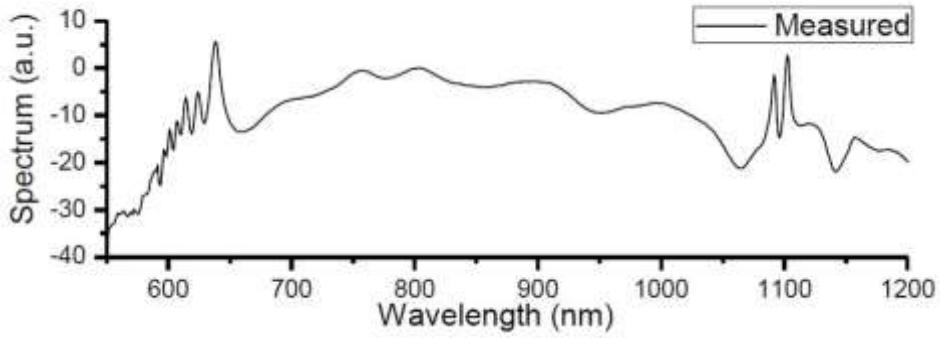

Fig. 4.27. Experimental spectrum from a DCM-based ring cavity [4.9].

Despite of the success in depicting mode-locking dynamics and phase-matching enhancement, detailed comparisons of experimental and theoretical results would help to further optimize the output performance. An experimental spectrum is shown in Fig. 4.27 [4.9], which shares the common behavior of multiple spectral peaks near 0.65 μm and 1.1 μm. However, in the experiment, spectral ripples around the center wavelength are typically observed, instead of a relatively smooth spectrum from simulation shown in Fig. 4.25. The possible reason behind the spectral ripples is residual phase errors from fabricated chirped mirrors. Apart from the design phase, slight fabrication variations of the elaborate mirror structures lead to unwanted GD oscillations. To study the influence of residual phase ripples, we implant phase oscillations in a dispersion-free cavity, as shown in Fig. 4.28(a), which has the same cavity setup as described in Subsection 4.4.2.

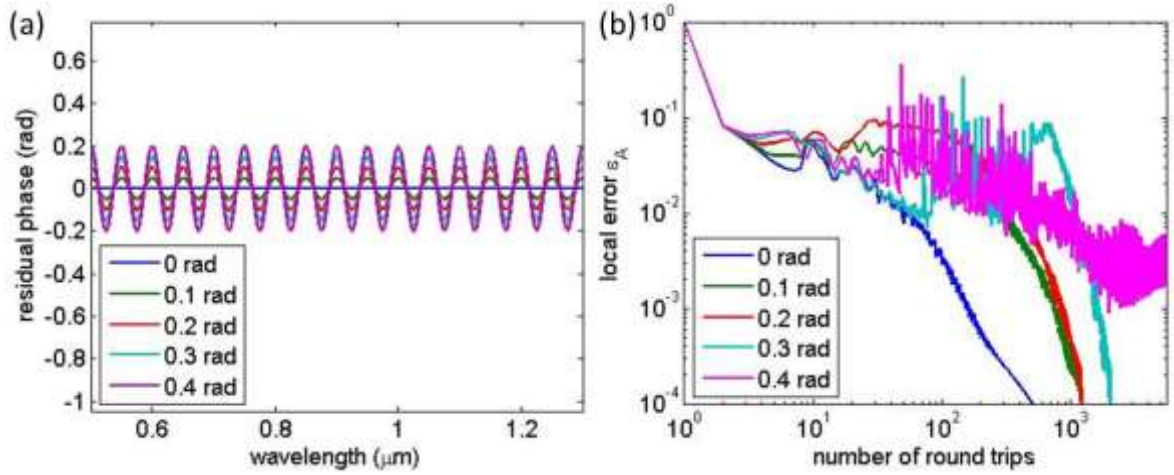

Fig. 4.28. (a) Simulated round-trip phases and (b) corresponding local-error dynamics, which characterize the effects of the sinusoidal phase oscillations with specified peak-to-peak values, in order to evaluate the role of residual phase errors from fabricated chirped mirrors.

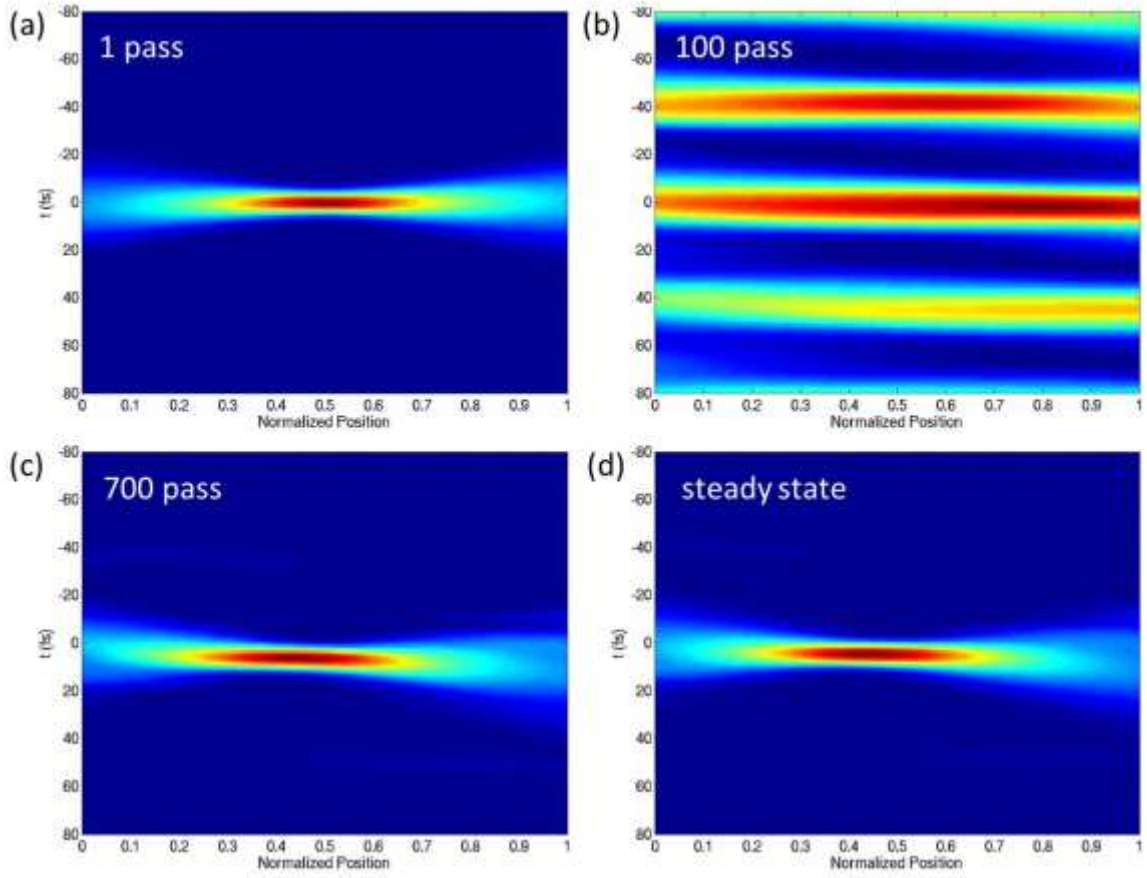

Fig. 4.29. Temporal evolution after specified round trips inside the crystal, using a cavity with a residual phase which has a peak-to-peak oscillation of 0.3 rad and a 7 fs initial pulse.

With specified phase oscillations shown in Fig. 4.28(a), the local-error dynamics is shown in Fig. 4.28(b), using a 7 fs initial pulse. With a stronger phase oscillation, the onset of stable mode-locking becomes more difficult; eventually a stable operation cannot be supported (the 0.4-rad case). The reason is that phase oscillations generate satellite pulses. When a pulse experiences larger phase oscillations induced by mirrors, stronger satellite pulses are obtained with larger time delays away from the main pulse. In the crystal, both the main pulse and the satellite pulses will compete for the gain, resulting in cavity instability. Fig. 4.29 shows the temporal evolution inside the crystal of the 0.3-rad case as shown in Fig. 4.28. In Fig. 4.29, an initial 7 fs pulse is separated into several pulses after 100 round trips, mainly due to the phase oscillation. Fortunately, a pulse is favored in the cavity after 700 passes (*i.e.*, the local maximum of the local-error dynamic as the cyan curve in Fig. 4.28(b)).

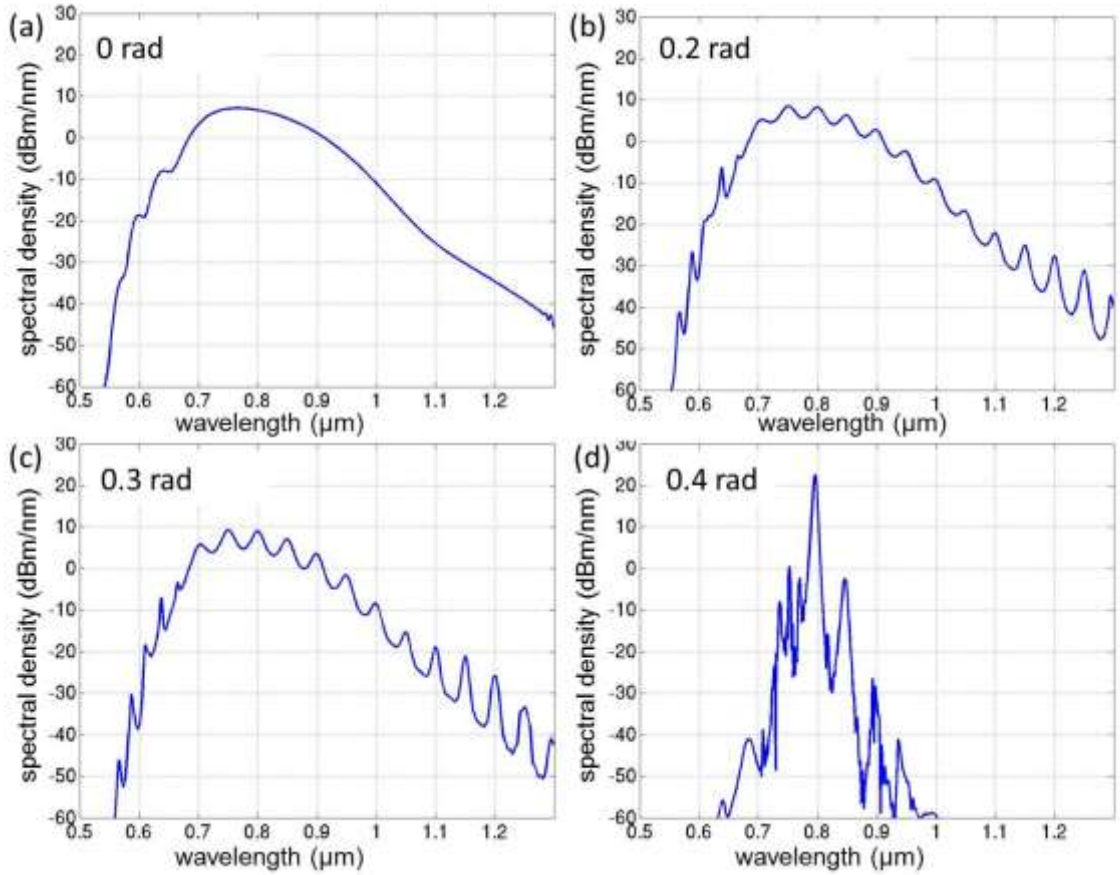

Fig. 4.30. Corresponding spectra from cavities with indicated phase oscillations. Steady-state spectra are obtained in (a-c) with tolerable phase modulations. The ripples on the spectra are consistent with the residual phases shown in shown in Fig. 4.28(a).

The corresponding output spectra are shown in Fig. 4.30, and the wavelength-dependent beam profiles are provided in Fig. 4.31. A larger phase oscillation leads to stronger modulation in both spectrum and beam profile, and the ripples on the spectra are compatible with the residual phases. According to the phase-matching theory, the maxima of phase oscillations are more close to cavity nonlinear phase (~0.6 rad). As a result, the phase maxima thus enhance the power spectral density with a fundamental beam profile at the corresponding wavelengths, resulting in local maxima in the spectra. <5 dB of spectral modulation around the center wavelength is observed from simulation, which is consistent with the experimental result (see Fig. 4.27).

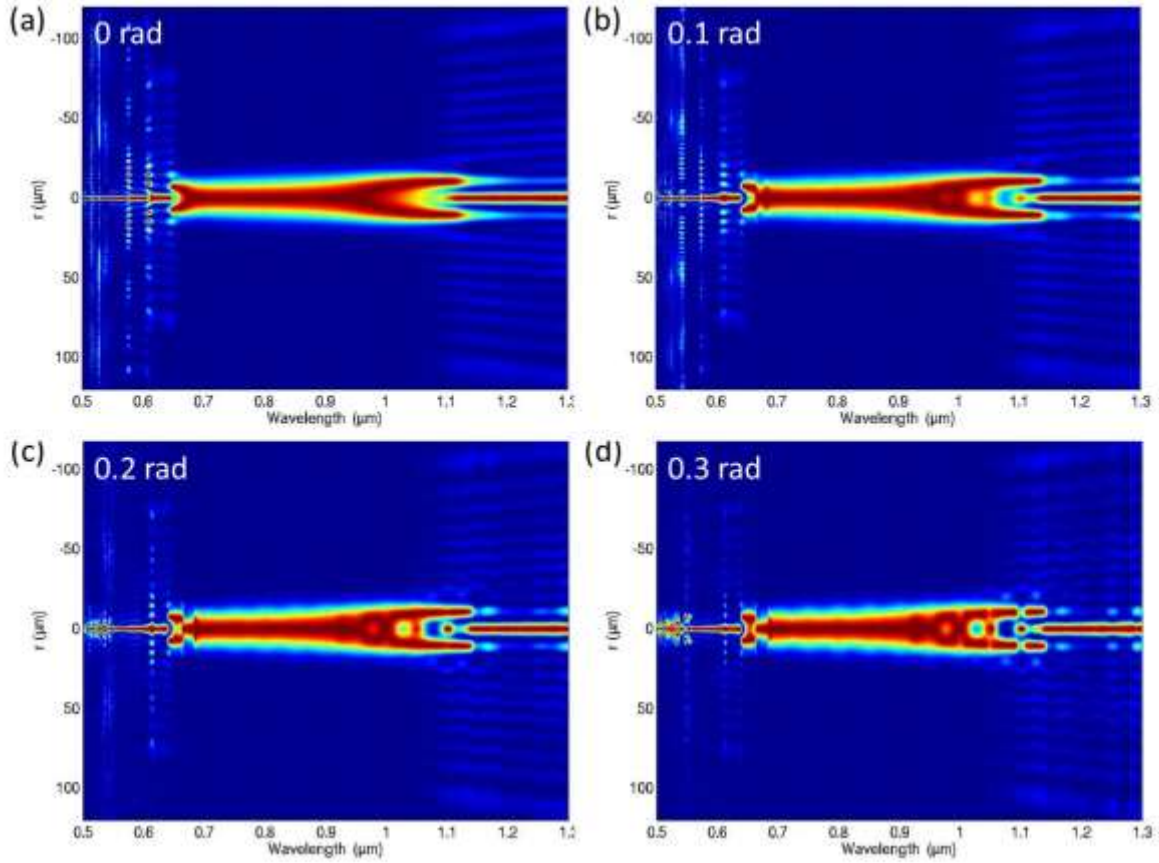

Fig. 4.31. Corresponding wavelength-dependent beam profiles from cavities with indicated phase oscillations. Stronger beam profile modulation can be found with larger phase oscillation, especially in the spectral regime away from the center wavelength.

4.7 **Toward broader spectrum with a better beam profile**

In order to optimize the output spectrum, an output coupler is typically designed to couple out the spectral wings outside the gain bandwidth. These spectral wings are generated via SPM of the intracavity dispersion-managed soliton. However, in this case, the beam profiles in the spectral wings are typically worse due to the interplay between wavelength-dependent diffraction and self-focusing, instead of mode-shaping from cavity resonances. As a result, a poor beam profile limits its capabilities when applying these beams for further applications, such as f-2f self-referencing [4.9, 11, 22, 35] and seeding of optical amplifiers [4.36].

One can also optimize the output spectrum via cavity enhancement. According to the proposed spatiotemporal phase-matching, a broader spectrum is obtained with slightly positive cavity dispersion, as shown in Fig. 4.14(a). When the round-trip residual phase matches with the nonlinear phase of the dispersion-managed soliton, the spectral density is enhanced with a fundamental beam profile. To compare the effects of the two cases (*i.e.*, coupling out the spectral wings without resonances and cavity enhancement via phase-matching), numerical experiments are conducted: (1) a dispersion-free cavity has a resonance window only within the gain bandwidth, 0.65 μm – 1.05 μm, and (2) phase-matched cavities have a uniform output coupling window. For the stability analysis, two optimized phase profiles are employed with 0.5 fs^2 of GDD or linear phase ramps on both spectral sides. The total reflectivity of the dispersion-free cavity and the round-trip phases of the phase-optimized cases are shown in Fig. 4.32.

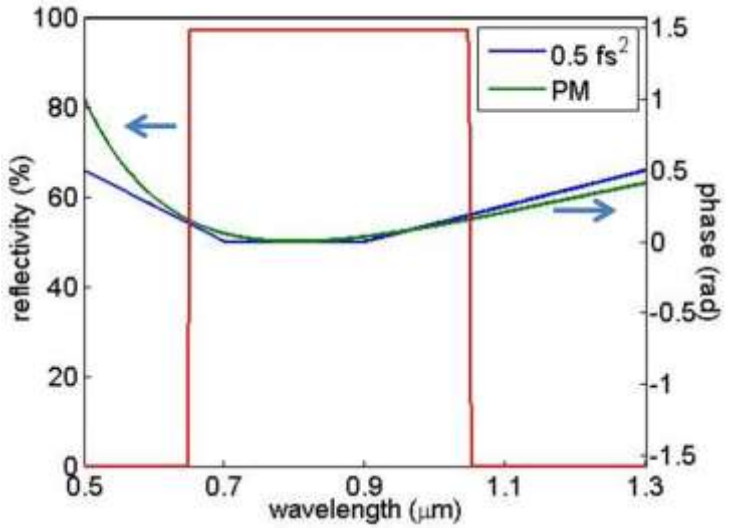

Fig. 4.32. A cavity reflection window (red) with a high reflection from 0.65 μm – 1.05 μm, the gain bandwidth of Ti:sapphire crystals; the round-trip phase profiles with 0.5 fs^2 of GDD (blue) or linear phase-matching ramps (green) below 0.7 μm and above 0.9 μm.

The intracavity and output spectra are shown in Fig. 4.33, as well as the wavelength-dependent beam profiles in Fig. 4.34. With optimized residual phases, the intracavity spectra can constructively be built up in the spectral wings, leading to broader spectra comparing with the dispersion-free case. Although the phase-matching concept leads to broader spectra, the spectral enhancements can be reached only around the matched wavelengths. As a result, more output beyond the matched wavelength, around 1.08 μm, can be found in the dispersion-free case. However, outside the reflectivity window of the dispersion-free cavity, nonlinear x-wave [4.37] is generated from single-pass nonlinear beam propagation in the crystal, showing conical emission at angles that enlarge when increasing detuning from the center frequency as shown in Fig. 4.34. In the phase-matched cases, instead of the conical emission without the cavity mode shaping, the constructive interferences in the fundamental transverse mode results in a good beam quality, not only in the center regime but also around the matched wavelength.

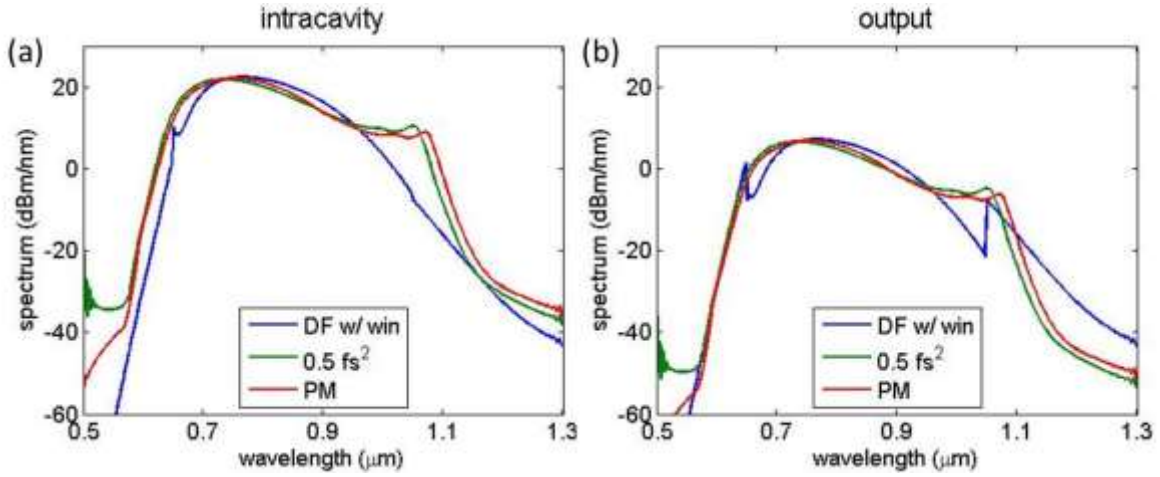

Fig. 4.33. (a) Intracavity and (b) output spectra of different cavities featuring different optimization strategies. DF w/ win, a dispersion-free cavity coupling out all the light outside the gain bandwidth, 0.65 μm – 1.05 μm; 0.5 fs^2, a cavity with a net round-trip dispersion of 0.5 fs^2 GDD and a constant output coupling; PM, a cavity with an optimized phase ramps, as the green curve in Fig. 4.32, and a constant output coupling.

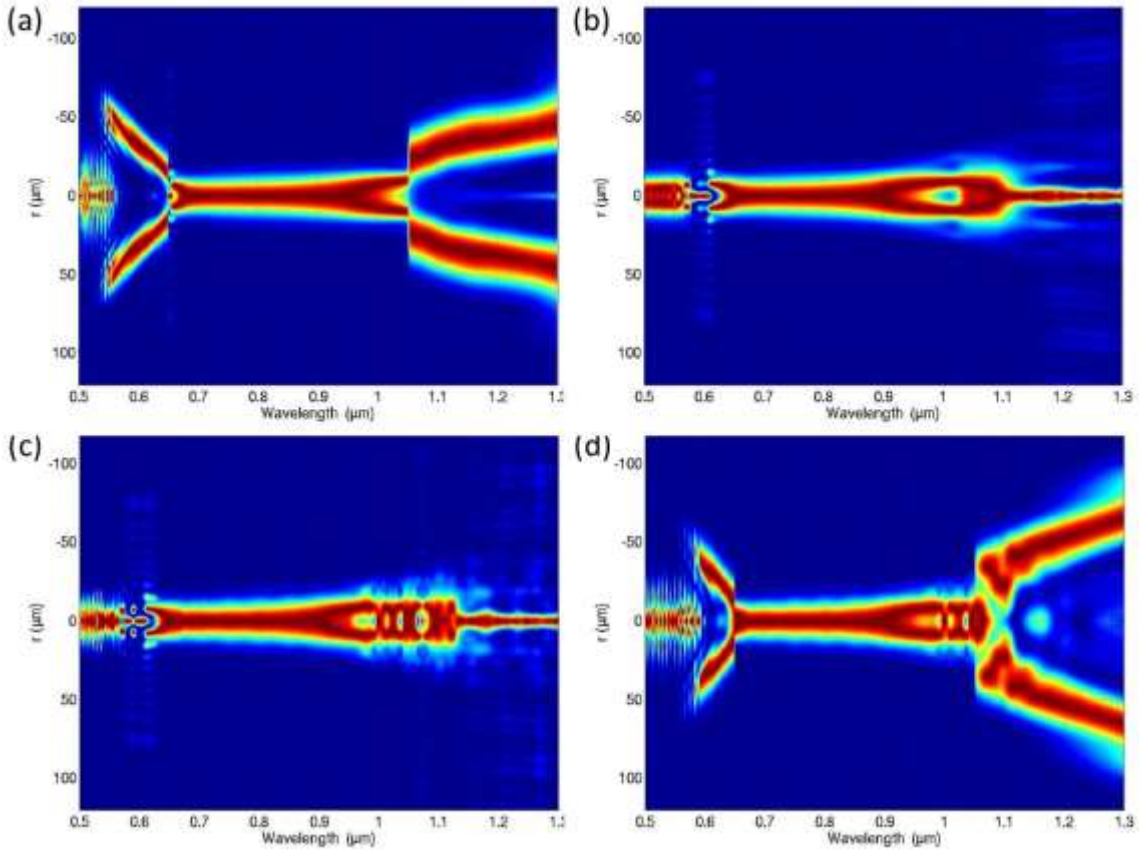

Fig. 4.34. Wavelength-dependent beam profiles using (a) a dispersion-free cavity coupling out all the light outside the gain bandwidth, (b) a cavity with an optimized phase ramps, as the green curve in Fig. 4.32, and a constant output coupling, (c) a cavity with the same features in (b) and a 0.2 rad of peak-to-peak phase oscillation, and (d) a cavity with the same configurations in (c) and coupling out all the light outside the gain bandwidth.

As discussed in Subsection. 4.6.2, the phase oscillations should be included when considering practical variations from DCMs. A 0.2 radian of peak-to-peak phase oscillation is introduced, and a reflection window (see Fig. 4.32) can be also applied to further optimize the output. Fig. 4.35 compares the local-error dynamics between cases with two kinds of optimized round-trip phases (see Fig. 4.32), as well as a the dispersion-free cavity case as a reference. The cavity with both 0.5 fs^2 of GDD and phase oscillations shows no sign of convergence after 6000 passes, while the case with linear phase-matching ramps reaches a steady state within 2000 passes: the positive dispersion, accompanied by the phase oscillation, around the center wavelength results in stronger perturbation to the stable soliton formation. As a result, the phase feature with a linear ramp is more robust when introducing phase-matching concept in reality. The corresponding output spectra with linear phase-matching ramps are shown in Fig. 4.36. For the bandwidth optimization of the laser output, one can apply both the phase-matching concept and a high output coupling in the spectral wings, as shown by the green and cyan curves in Fig. 4.36.

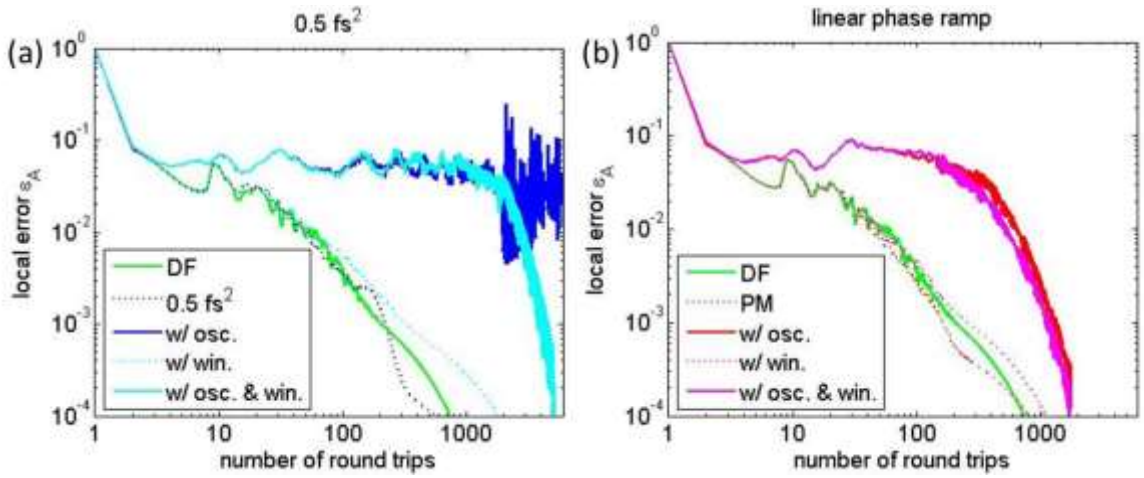

Fig. 4.35. Local-error dynamics using phase-matched cavities, with (a) 0.5 fs^2 of GDD and (b) linear phase-ramps. Several features are included accompanying with the specified phase profile. DF, a dispersion-free cavity as a reference; 0.5 fs^2 and PM, cavities with specified phase profile and a uniform output coupling; w/ osc., cavities with 0.2 rad of phase oscillation; w/ win., cavities with a high reflection window that couples out all the light outside the gain bandwidth; w/ osc. & win., cavities with both phase oscillations and a high reflection window.

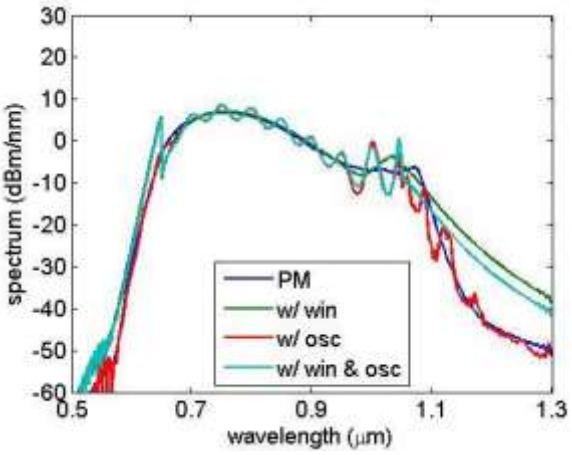

Fig. 4.36. Output spectra with optimized phase ramps, as the green curve Fig. 4.32. PM, a cavity with specified phase profile and a uniform output coupling; w/ osc., a cavity with 0.2 rad of phase oscillation; w/ win., a cavity with a high reflection window that couples out all the light outside the gain bandwidth; w/ win. & osc., a cavity with both phase oscillations and a high reflection window.

References

[4.1] S. A. Diddams, D. J. Jones, J. Ye, S. T. Cundiff, J. L. Hall, J. K. Ranka, *et al.*, "Direct link between microwave and optical frequencies with a 300 THz femtosecond laser comb," *Physical Review Letters,* vol. 84, p. 5102, 2000.

[4.2] D. J. Jones, S. A. Diddams, J. K. Ranka, A. Stentz, R. S. Windeler, J. L. Hall, *et al.*, "Carrier-envelope phase control of femtosecond mode-locked lasers and direct optical frequency synthesis," *Science,* vol. 288, pp. 635-639, 2000.

[4.3] T. Udem, R. Holzwarth, and T. W. Hansch, "Optical frequency metrology," *Nature,* vol. 416, pp. 233-237, Mar 14 2002.

[4.4] A. H. Zewail, *Femtochemistry: Atomic-Scale Dynamics of the Chemical Bond Using Ultrafast Lasers (Nobel Lecture)*: Wiley Online Library, 2001.

[4.5] W. Denk, J. H. Strickler, and W. W. Webb, "Two-photon laser scanning fluorescence microscopy," *Science,* vol. 248, pp. 73-76, 1990.

[4.6] C. Grienberger and A. Konnerth, "Imaging calcium in neurons," *Neuron,* vol. 73, pp. 862-885, 2012.

[4.7] N. G. Horton, K. Wang, D. Kobat, C. G. Clark, F. W. Wise, C. B. Schaffer, *et al.*, "In vivo three-photon microscopy of subcortical structures within an intact mouse brain," *Nature photonics,* vol. 7, pp. 205-209, 2013.

[4.8] D. E. Spence, P. N. Kean, and W. Sibbett, "60-fsec pulse generation from a self-mode-locked Ti: sapphire laser," *Optics letters,* vol. 16, pp. 42-44, 1991.

[4.9] L.-J. Chen, A. J. Benedick, J. R. Birge, M. Y. Sander, and F. Kärtner, "Octave-spanning, dual-output 2.166 GHz Ti: sapphire laser," *Optics express,* vol. 16, pp. 20699-20705, 2008.

[4.10] R. Ell, U. Morgner, F. Kärtner, J. G. Fujimoto, E. P. Ippen, V. Scheuer, *et al.*, "Generation of 5-fs pulses and octave-spanning spectra directly from a Ti: sapphire laser," *Optics letters,* vol. 26, pp. 373-375, 2001.

[4.11] L. Matos, D. Kleppner, O. Kuzucu, T. Schibli, J. Kim, E. Ippen, *et al.*, "Direct frequency comb generation from an octave-spanning, prismless Ti: sapphire laser," *Optics letters,* vol. 29, pp. 1683-1685, 2004.

[4.12] C. Chudoba, J. Fujimoto, E. Ippen, H. Haus, U. Morgner, F. Kärtner, *et al.*, "All-solid-state Cr: forsterite laser generating 14-fs pulses at 1.3 μm," *Optics letters,* vol. 26, pp. 292-294, 2001.

[4.13] D. Ripin, C. Chudoba, J. Gopinath, J. Fujimoto, E. Ippen, U. Morgner, *et al.*, "Generation of 20-fs pulses by a prismless Cr 4+: YAG laser," *Optics letters,* vol. 27, pp. 61-63, 2002.

[4.14] J. Herrmann, "Theory of Kerr-lens mode locking: role of self-focusing and radially varying gain," *JOSA B,* vol. 11, pp. 498-512, 1994.

[4.15] V. Kalosha, M. Müller, J. Herrmann, and S. Gatz, "Spatiotemporal model of femtosecond pulse generation in Kerr-lens mode-locked solid-state lasers," *JOSA B,* vol. 15, pp. 535-550, 1998.

[4.16] I. P. Christov, H. C. Kapteyn, M. M. Murnane, C.-P. Huang, and J. Zhou, "Space–time focusing of femtosecond pulses in a Ti: sapphire laser," *Optics letters,* vol. 20, pp. 309-311, 1995.

[4.17] I. P. Christov, M. M. Murnane, H. C. Kapteyn, and V. D. Stoev, "Mode locking with a compensated space–time astigmatism," *Optics letters,* vol. 20, pp. 2111-2113, 1995.

[4.18] I. P. Christov and V. D. Stoev, "Kerr-lens mode-locked laser model: role of space time effects," *JOSA B,* vol. 15, pp. 1960-1966, 1998.

[4.19] I. P. Christov, V. D. Stoev, M. M. Murnane, and H. C. Kapteyn, "Absorber-assisted Kerr-lens mode locking," *JOSA B,* vol. 15, pp. 2631-2633, 1998.

[4.20] M. Y. Sander, J. Birge, A. Benedick, H. M. Crespo, and F. X. Kärtner, "Dynamics of dispersion managed octave-spanning titanium: sapphire lasers," *JOSA B,* vol. 26, pp. 743-749, 2009.

[4.21] S. Cundiff, E. Ippen, H. Haus, and W. Knox, "Frequency-dependent mode size in broadband Kerr-lens mode locking," *Optics letters,* vol. 21, pp. 662-664, 1996.

[4.22] T. M. Fortier, A. Bartels, and S. A. Diddams, "Octave-spanning Ti: sapphire laser with a repetition rate> 1 GHz for optical frequency measurements and comparisons," *Optics Letters,* vol. 31, pp. 1011-1013, 2006.

[4.23] T. Brabec and F. Krausz, "Nonlinear optical pulse propagation in the single-cycle regime," *Physical Review Letters,* vol. 78, p. 3282, 1997.

[4.24] P. F. Moulton, "Spectroscopic and laser characteristics of Ti: Al 2 O 3," *JOSA B,* vol. 3, pp. 125-133, 1986.

[4.25] S. Tzortzakis, L. Sudrie, M. Franco, B. Prade, A. Mysyrowicz, A. Couairon, *et al.*, "Self-guided propagation of ultrashort IR laser pulses in fused silica," *Physical review letters,* vol. 87, p. 213902, 2001.

[4.26] J. Philip, C. D'Amico, G. Cheriaux, A. Couairon, B. Prade, and A. Mysyrowicz, "Amplification of femtosecond laser filaments in Ti: Sapphire," *Physical review letters,* vol. 95, p. 163901, 2005.
[4.27] A. Couairon and A. Mysyrowicz, "Self-focusing and filamentation of femtosecond pulses in air and condensed matter: simulations and experiments," in *Self-focusing: Past and Present*, ed: Springer, 2009, pp. 297-322.
[4.28] G. Cerullo, S. De Silvestri, V. Magni, and L. Pallaro, "Resonators for Kerr-lens mode-locked femtosecond Ti:sapphire lasers," *Optics Letters,* vol. 19, pp. 807-809, 1994.
[4.29] L.-J. Chen, "Design, optimization, and applications of few-cycle Ti: Sapphire lasers," Massachusetts Institute of Technology, 2012.
[4.30] Y. Chen, F. Kärtner, U. Morgner, S. Cho, H. Haus, E. Ippen*, et al.*, "Dispersion-managed mode locking," *JOSA B,* vol. 16, 1999.
[4.31] S. Kelly, "Characteristic sideband instability of periodically amplified average soliton," *Electronics Letters,* vol. 28, pp. 806-807, 1992.
[4.32] P. Curley, C. Spielmann, T. Brabec, F. Krausz, E. Wintner, and A. Schmidt, "Operation of a femtosecond Ti: sapphire solitary laser in the vicinity of zero group-delay dispersion," *Optics letters,* vol. 18, pp. 54-56, 1993.
[4.33] Q. Lin and I. Sorokina, "High-order dispersion effects in solitary mode-locked lasers: side-band generation," *Optics communications,* vol. 153, pp. 285-288, 1998.
[4.34] G. Chang, L.-J. Chen, and F. X. Kärtner, "Fiber-optic Cherenkov radiation in the few-cycle regime," *Optics express,* vol. 19, pp. 6635-6647, 2011.
[4.35] O. Mücke, R. Ell, A. Winter, J.-W. Kim, J. Birge, L. Matos*, et al.*, "Self-referenced 200 MHz octave-spanning Ti: sapphire laser with 50 attosecond carrier-envelope phase jitter," *Optics express,* vol. 13, pp. 5163-5169, 2005.
[4.36] S.-W. Huang, G. Cirmi, J. Moses, K.-H. Hong, S. Bhardwaj, J. R. Birge*, et al.*, "High-energy pulse synthesis with sub-cycle waveform control for strong-field physics," *Nature photonics,* vol. 5, pp. 475-479, 2011.
[4.37] C. Conti, S. Trillo, P. Di Trapani, G. Valiulis, A. Piskarskas, O. Jedrkiewicz*, et al.*, "Nonlinear electromagnetic X waves," *Physical review letters,* vol. 90, p. 170406, 2003.

Chapter 5

Broadband continuum generation in mode-locked cavities with phase-matched output couplers

5.1 Introduction

Passively mode-locked lasers assisted by the Kerr nonlinearity are widely employed in various broadband systems [5.1, 2] and continue to make tremendous impact in science and technology. Moreover, self-phase modulation (SPM) occurring in intracavity materials and its interplay with cavity dispersion engineered by dispersion-compensating mirrors (*e.g.*, double-chirped mirrors (DCMs)) make it possible to obtain laser output spectra even broader than the bandwidth of the gain medium [5.3-13]. For example, octave-spanning spectra have been achieved from mode-locked Ti:sapphire lasers incorporating both DCM pairs [5.5] and suitable output couplers (OCs) in the cavities [5.4, 6, 9, 12, 13]. The resulting spectral wings outside the gain bandwidth manifested as broadband continuum are of particular importance for frequency-comb applications [5.8-12] and generation of sub-two-cycle optical pulses [5.12] directly from the oscillator, and thus benefit many applications such as optical frequency metrology and seeding of optical parametric amplifiers [5.14-18] for attosecond science [5.19].

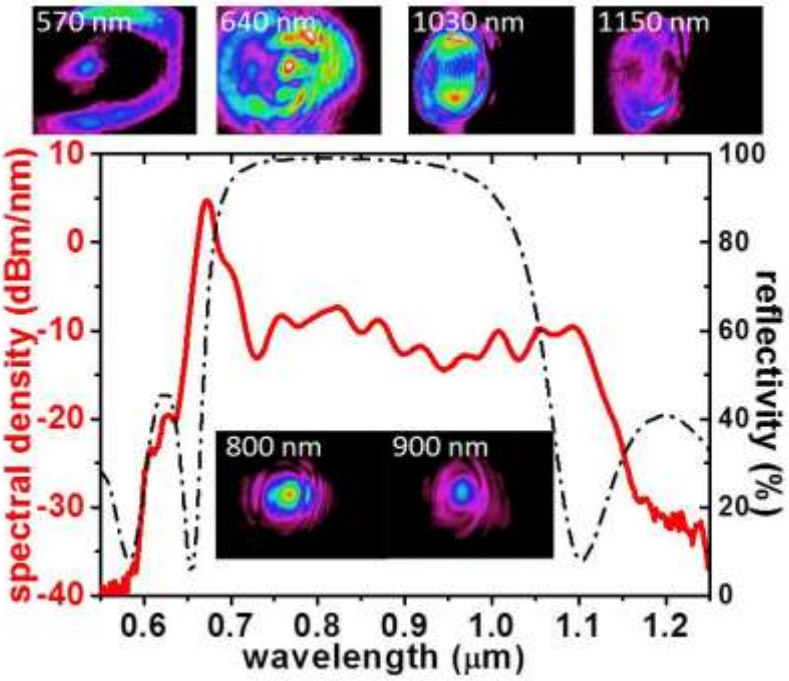

Fig. 5.1. Ti:sapphire output spectrum (red) with a 1% ZnSe/MgF_2 output-coupling window (dashed curve) covering the gain bandwidth (650 nm - 1100 nm), as well as the beam profiles at the specified wavelengths (1) within cavity resonance (*e.g.*, 800 nm and 900 nm), and (2) out of a cavity (*e.g.*, 570 nm, 640 nm, 1030 nm, and 1150 nm).

In the state-of-the-art broadband oscillators, low output coupling covering the gain bandwidth and high transmission in the spectral wings—as achieved with a 1% ZnSe/MgF_2 OC in a Ti:sapphire oscillator [5.4, 5, 9, 10]—has been regarded as the optimum for maximizing the intracavity SPM to obtain the utmost output power in the wings. Fig. 5.1 shows a state-of-the-art output spectrum, as well as the output coupling window. In our previous study, a gain-matched OC was also proposed to flatten the net gain and to reduce the required nonlinearity for broadband mode locking [5.13]. Following the discussion in Section 4.7, spectral wings, which are out of cavity resonance, with poor beam qualities are typically observed, as shown in Fig. 5.1. These spectral wings are mainly generated by single-pass nonlinear beam propagation inside the Ti:sapphire crystal and considered as non-resonant waves which cannot be well controlled [5.8, 11, 20].

However, in order to obtain broader spectra, the practical implementation of spatiotemporal phase-matching concept, as discussed in Section 4.7, should be addressed. The phase-matching process is similar to other well-known phenomena, such as Kelly sideband generation [5.21], high-order-dispersion-induced resonance [5.22, 23], and fiber-optic Cherenkov radiation [5.24]. However, unlike Kelly sidebands and high-order-dispersion-

induced resonances, which are typically regarded as adverse effects inducing mode-locking instabilities, the phase-matched dispersive wave described here well perturbs the dispersion-managed soliton [5.25] in order to enhance broadband continuum generation in a mode-locked laser. Following the guidelines from the developed spatiotemporal model, we propose and apply the cavity-enhancement concept to design a phase-tailored cavity for few-cycle Ti:sapphire oscillators. In particular, the implementation of phase-tailored OCs, in the following called phase-matched OCs (PMOCs), realizes the precise control of both the output-coupling window and the required phase-matching feature without changing other intracavity materials: PMOCs are designed to enhance cavity resonances and optimize output spectrum in terms of both spectral density and beam quality. The experimental results are in a great agreement with the simulation results.

5.2 Linear cavity dynamics

5.2.1 Cavity setup

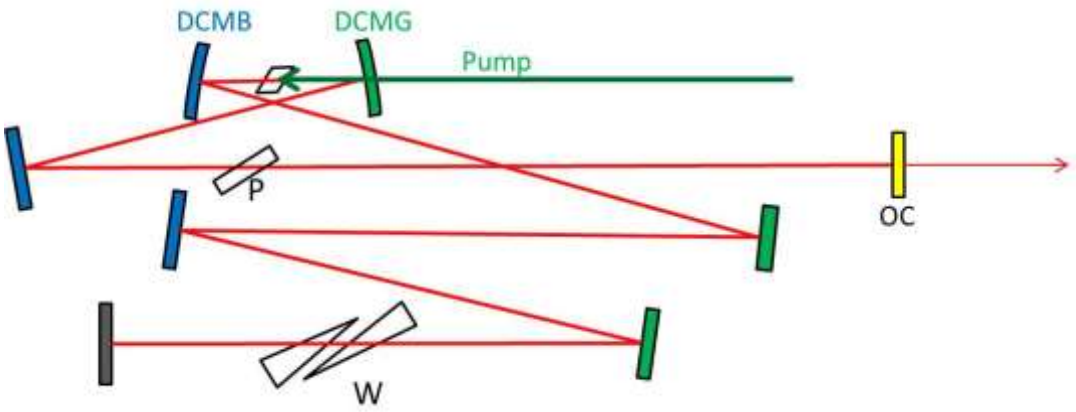

Fig. 5.2. Schematic of typical linear resonators used for DCM-based KLM lasers. DCM pairs (*i.e.*, DCMG and DCMB, green and blue mirrors) are typically employed for octave-spanning dispersion control. P and W are dispersive plates and wedges, respectively, for dispersion fine-tuning on two cavity arms. A silver mirror (gray mirror) and an output coupler (OC, the yellow mirrors) are used at the end of two arms.

Linear cavity Ti:sapphire oscillators operated at a repetition rate of ~80MHz are commonly used in many ultrafast applications. A robust design using a prism-less cavity is shown in Fig. 5.2. Different from a ring cavity, the circulating pulses pass the crystal twice in a round-trip, and the beam propagation outside the crystal is separated into two arms. Fig. 5.3 shows a simplified cavity setup and the equivalent system for modeling spatiotemporal dynamics,

which is similar to the equivalent system as described in Subsection 4.3.2. D denotes the path length, and d specifies the dispersion during beam propagation. Two separated series are prepared and applied in two arms for one round-trip. The Kerr-lens sensitivity in the linear laser cavity has been investigated by modeling self-focusing as a nonlinear lens [5.26]: A specific cavity using sophisticated calculation is usually performed in order to provide a guideline for cavity alignments. In experiments, one can find the operation points by continuously varying the positions of intracavity elements, and simultaneously observing the mode beating via an optical spectrum analyzer. However, it is hard to fine tune all the intracavity components in simulations. As a result, to release the demanding conditions of operating points in linear cavity, one would add an additional fast saturate absorber to suppress light transients. Typically, an asymmetric cavity (*i.e.*, $D_2+D_3 \neq D_1+D_4$) is more suitable to initiate a stable operation, and the focused beam waist is located closer to the front surface instead of the center of the crystal (*i.e.*, $D_1 > D_2$).

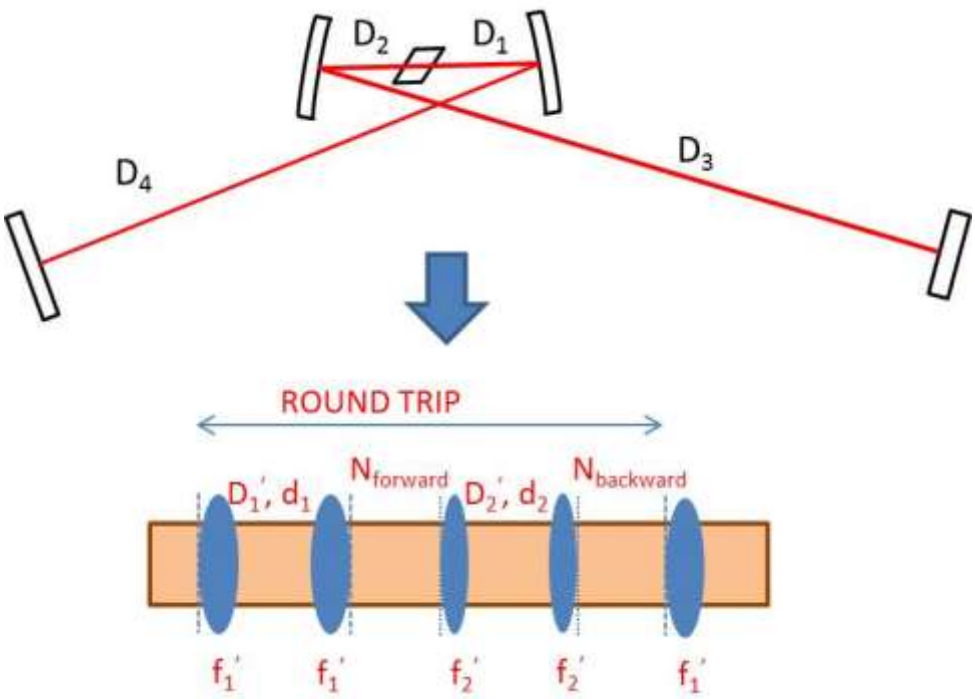

Fig. 5.3. Schematic of a linear cavity, and its equivalent system (bottom) for efficient computation of the beam propagation. f', efficient focal length; D', effective spacing; d, cavity dispersion during linear pulse propagation outside the crystal; N, nonlinear pulse propagation in the crystal. The subscripts in the equivalent system denote the equivalent elements on the two arms.

5.2.2 **Dispersion balancing**

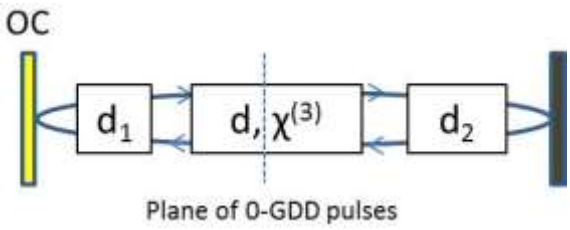

Fig. 5.4. Dispersion map in a linear cavity, according to Fig. 5.2. The position of the 0-gdd plane inside the crystal is determined by the dispersion distribution (*i.e.*, d_1 and d_2). d, crystal dispersion.

Fig. 5.4 shows the dispersion map in a linear cavity. Apart from ring cavity dynamics, the dispersion distribution between two arms (*i.e.*, d_1:d_2) is also crucial for obtaining broadband spectrum and stable operation. With octave-spanning pulses, the temporal evolutions inside the crystal can largely vary from ~50 fs to a compressed 5fs pulse using a 2-mm-long crystal. With a proper dispersion distribution, both the forward- and backward-propagating pulses are compressed inside the crystal per round trip, which exploits the KLM action twice per round trip [5.25]. Thus an optimized dispersion distribution leads to a stronger SAM and generation of shorter pulses.

In order to achieve stable dispersion-managed mode-locking, the dispersion distribution on two arms affects the position with zero-GDD pulses inside the crystal. With different dispersion distribution ratios in Fig. 5.5 (left: d1:d2=1:2; middle: d1:d2=1:1; right: d1:d2=2:1), the positions of zero-GDD plane can be visualized in the temporal evolutions (see Fig. 5.5(a-c)), where the pulses are compressed with minimum pulse widths. With a smaller ratio of the dispersion distribution, the zero-GDD plane is closer to the front surface inside the crystal.

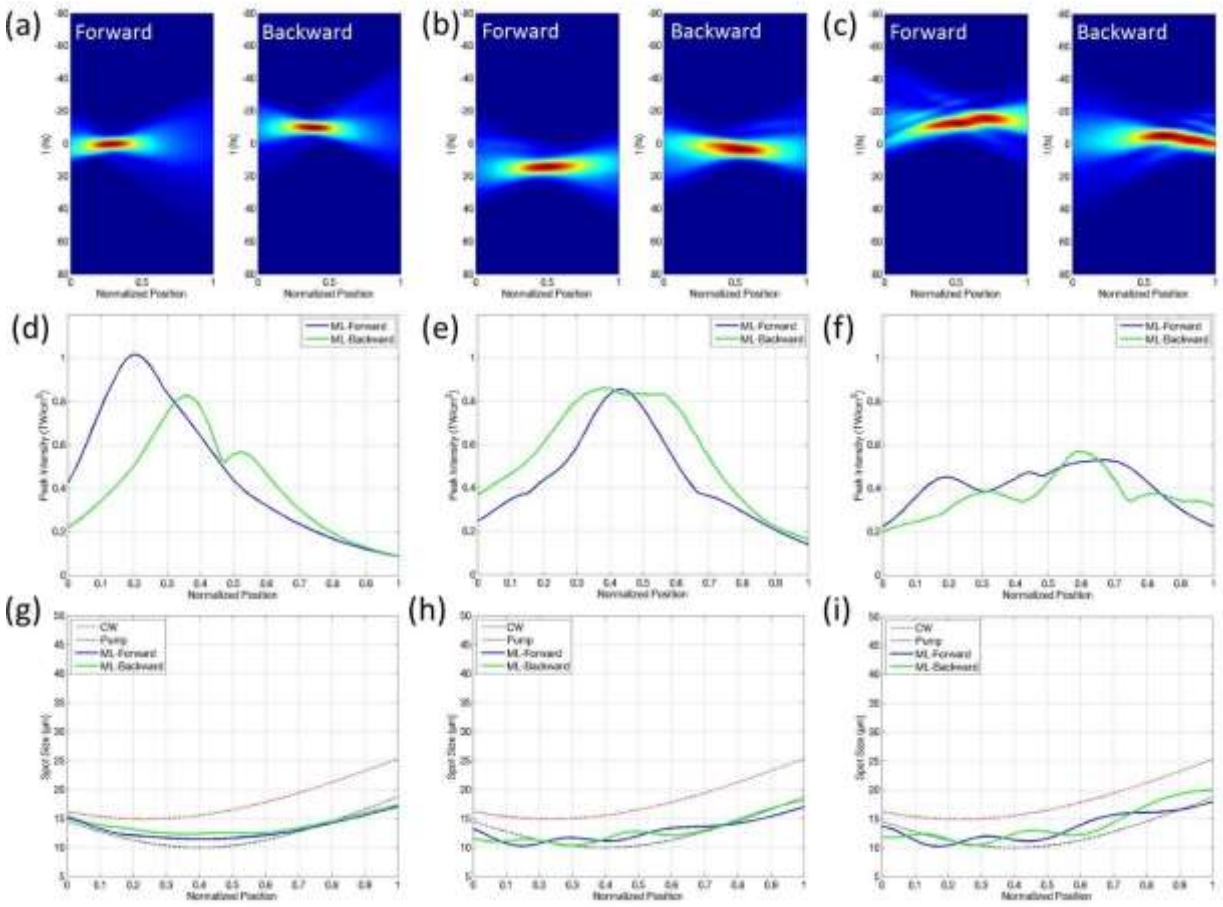

Fig. 5.5. Examples of pulse behaviors ((a-c) temporal evolutions, (d-f) peak intensities, and (g-i) beam profiles) with different dispersion distributions (left, d_1:d_2=1:2; middle, d_1:d_2=1:1; right, d_1:d_2=2:1) in a dispersion-free cavity (*i.e.*, $d_1+d_2+d=0$). Blue curves in (d-i), forward-propagating pulse; green curves in (d-i), backward-propagating pulse. The horizon axes in all the figures are normalized to the crystal length.

Higher peak intensity, which is required for the optimization of SAM and broadband spectra, is obtained when the 0-gdd plane is around the beam waist of the pulse. In order to obtain a stable mode-locking with strong Kerr-lens sensitivity, the location of cold cavity beam waist is usually close to the front surface inside the crystal, as the red dashed lines in Fig. 5.5(g-i). Therefore, <1 of the distribution ratio (see the left plots in Fig. 5.5) leads to an optimized peak intensity (~1 TW/cm^2) and shorter pulses: broader spectrum is obtained with 0.5 of the distribution ratio, supporting a 5.04 fs transform-limited (TL) pulse, comparing with the case with a symmetric distribution, 5.64 fs TL pulse.

5.2.3 **Phase-matching enhancement**

In a solid-state oscillator, the Kerr effect results in coupling among longitudinal modes via SPM and transverse modes via self-focusing. The dispersive wave originating from soliton perturbations at each wavelength can be viewed as a superposition of transverse modes. At the wavelength, where the dispersive wave and the soliton-like intracavity pulse have the same phase, the newly generated and existing dispersive waves will coherently add up, resulting in a resonant enhancement in both longitudinal and transverse modes. As a result, the phase-matching condition for the fundamental beam profile is satisfied if the phase contributed by the cold-cavity dispersion is equal to the nonlinear phase experienced by the soliton-like pulse. In principle, the phase-matched peaks can be tuned by varying the insertion of the intracavity dispersion-controlling material (*e.g.*, fused silica and barium fluoride wedges) to alter the cold-cavity dispersion. Normally a notable tuning requires a considerable amount of positive GDD, which may destabilize the mode locking and destroy the broadband spectrum, as discussed in Section. 4.7.

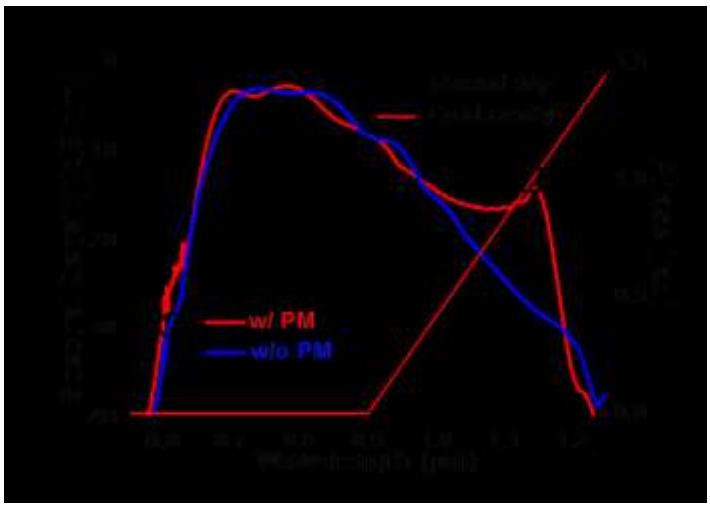

Fig. 5.6. The phase profile (red solid line) of the simulated phase-matched cavity, the nonlinear round-trip phase (black dashed line) of the soliton mode-locked laser, and the simulated output spectra with the phase-matched cavity (red) and with a dispersion-free cavity (blue). PM: phase matching.

To prove the concept in a linear cavity, we first simulate the laser dynamics with a constant 5% output coupling. We add an artificial phase profile to the intracavity round-trip phase in one cavity arm that provides phase matching at the wavelength around 1140 nm. The artificial phase acts as a perturbation to the intracavity soliton-like pulse whose center wavelength is around 800 nm. As shown in Fig. 5.6, the cold-cavity phase increases above

900 nm linearly and the dispersion is perfectly compensated for below 900 nm (red solid line), as well as the round-trip nonlinear phase (back dashed line). For the first demonstration, there is no additional phase feature to perturb the soliton-like pulse in the short-wavelength range. The phase ramp is started from the edge of the gain profile in order to optimize the phase-matched spectrum without compromising the laser stability. Furthermore, a linear phase ramp is created in order to not only provide the flexibility of varying the amount of the matched phase, but also realize the tunabilty of the spectral wing: The phase-matching wavelength can be linearly tuned by varying the insertion of the intracavity dispersion-controlling material. In addition to the spectrum generated within the gain bandwidth, spectral components around the phase-matched wavelength build up constructively via the interference between the already existing dispersive wave in the cavity and the newly generated dispersive wave in each round trip. As a result, the output spectrum shows a significant enhancement as high as 15 dB around the phase-matched wavelength (red curve) when compared with the case of a zero cold-cavity phase over the whole wavelength range (blue curve). The spectrum with an enhanced long-wavelength wing results in a 4.6-fs transform-limited (TL) pulse, which is even shorter than the dispersion-free spectrum supporting a 5.5-fs TL pulse.

5.3 **Experimental demonstrations**

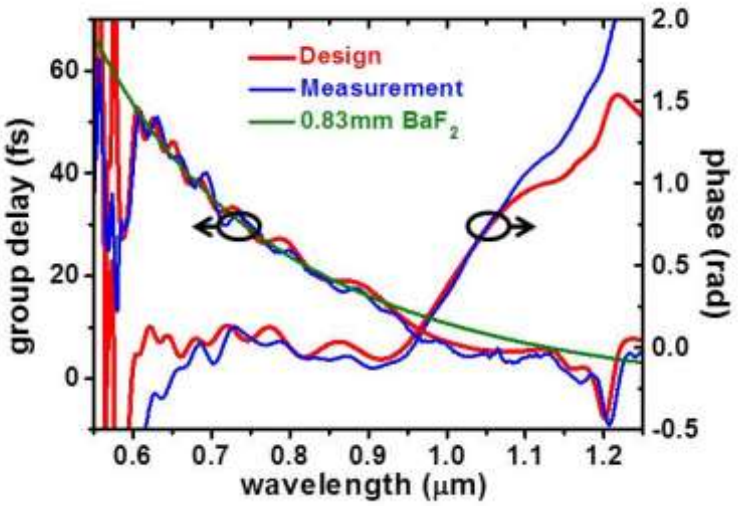

Fig. 5.7. The designed (red) and measured (blue) GD of the PMOC and the GD of 0.83 mm BaF_2 (green), as well as the corresponding designed and measured phases with both the PMOC and 0.83 mm BaF_2.

To experimentally demonstrate the spectral enhancement, we designed and fabricated the 5% PMOC based on multilayer Nb_2O_5/SiO_2 dielectric coatings. Multilayer dielectric coatings which allow for a large design freedom can be easily implemented in mode-locked lasers with various gain media [5.3, 7]. To minimize the uncompensated dispersion from the OC, we design the coatings with a dispersive behavior compensating for the dispersion of a BaF_2 plate with a certain thickness. The red curves in Fig. 5.7 show the calculated group delay (GD) and the net phase of the 5% PMOC. By decreasing the cavity dispersion with the equivalent of 0.83-mm optical path length of BaF_2 (green curve), the design phase can be achieved resulting in a phase ramp from 900 nm to 1200 nm. The low output-coupling window is extended from 600 nm to 1140 nm in order to enhance the intracavity interference outside the gain bandwidth. The extended output-coupling window allows the desired phase matching between the intracavity soliton-like pulse and the continuum for controlled spectral enhancement. The GD and phase measured with a home-built white-light interferometer (blue curves) agree well with the design curves in Fig. 5.7.

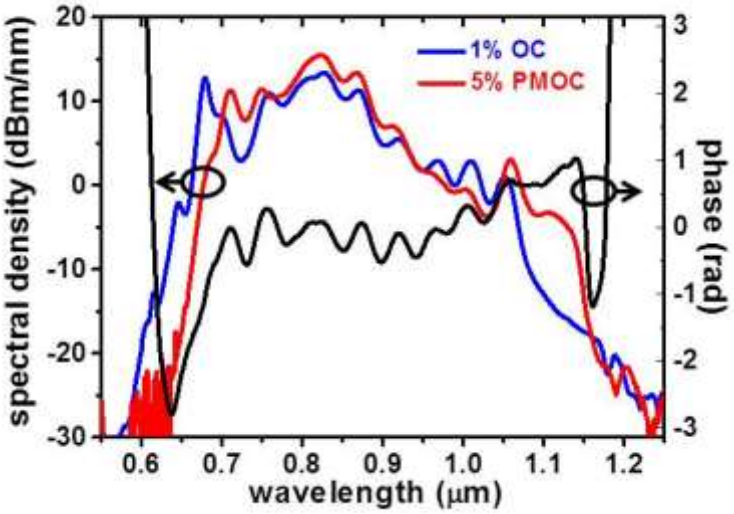

Fig. 5.8. Intracavity spectra with different OCs, a 5% Nb_2O_5/SiO_2 PMOC (red), a 1% ZnSe/MgF2 OC (blue), and the residual cold-cavity phase (black) of the laser with a 5% PMOC. The phase matching greatly enhances the long-wavelength wing up to 1150 nm even when compared with the spectrum achieved with the 1% OC.

The PMOC was tested in a 85-MHz ultrabroadband Ti:sapphire laser (Thorlabs Octavius-85M), where DCM pairs are used to compensate for the material dispersion including two adjustable wedges for dispersion fine tuning. The intracavity spectrum (red curve) and the cold-cavity residual phase (black curve) of the laser with the 5% PMOC and

DCM pairs are shown in Fig. 5.8; also plotted in the same figure is the intracavity spectrum with a 1% ZnSe/MgF_2 OC (blue curve). Applying the phase-matching concept using the 5% PMOC, the intracavity spectrum around 1140 nm is significantly enhanced by ~10 dB compared with the spectrum achieved with the 1% OC. In addition, the spectral ripples can precisely be predicted by the phase-matching condition. In Fig. 5.8, the amplitude of the cold-cavity phase ripples are close to the round-trip nonlinear phase of ~1 rad; the local maxima of the phase thus enhance the power density at the corresponding wavelengths and result in local maxima in the spectrum. Comparison of the cavity phase with the measured PMOC phase shown in Fig. 5.7 indicates that the oscillations are mainly due to the DCM pairs, which explain the consistent ripples on both spectra. On the other hand, the reduced negative residual phase below 700 nm mainly due to the DCM pairs explains the out-of-phase feature between the intracavity soliton-like pulse and the continuum in the short-wavelength range.

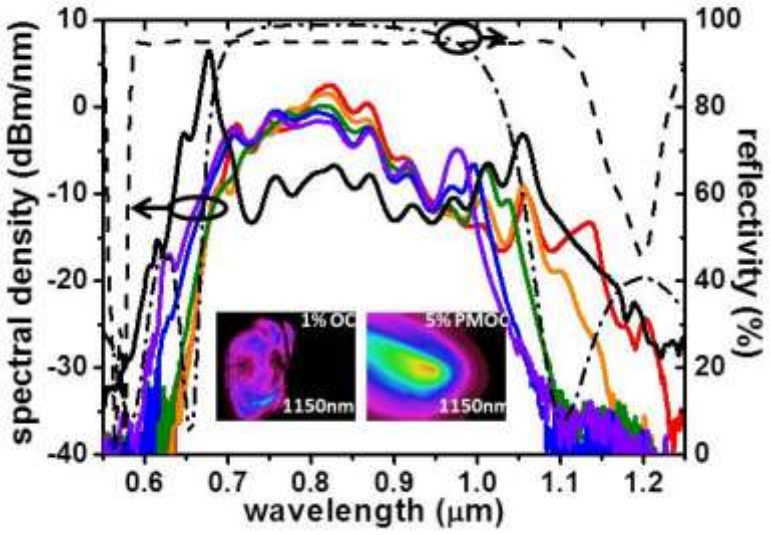

Fig. 5.9. Experimental output spectra using a 1% ZnSe/MgF_2 OC (black) and the 5% PMOC spectra with slightly different intracavity dispersions, as well as the output-coupling windows of the 1% ZnSe/MgF_2 OC (dash-dotted curve) and the 5% PMOC (dashed curve). The insets show the output beam profiles of the red and black spectrum at 1150 nm. The phase-matching concept improves the output spectrum around 1140 nm in terms of both the spectral density and beam quality. By increasing the insertion of BaF_2, the spectral peak around 1060 nm can continuously be tuned from the red, orange, green, and blue spectrum, accordingly, to 970 nm indicated as the purple one. The inserted extra optical path of BaF_2 in the purple spectrum is ~0.2 mm, corresponding to 7.6 fs^2 of intracavity GDD around 800 nm.

The output spectra and the output-coupling windows are shown in Fig. 5.9. The red spectrum in Fig. 5.9 shows only a 15 dB difference between the maximum spectral content

and the spectral wings around the wavelength of 1140 nm, much higher than the spectrum using a 1% OC of ~25 dB (black curve). The insets of Fig. 5.9 indicate that the output beam profile around the phase-matched wavelength is improved close to a fundamental Gaussian mode, instead of a less confined profile generated by a single pass through the laser using the 1% OC. Furthermore, the phase ramp with a nearly linear slope makes it possible to control the phase-matching wavelength by slightly changing the cavity dispersion. As Fig. 5.9 shows, varying the insertion of the BaF_2 wedge continuously tunes the phase-matching peak from 1060 nm to 970 nm. The optical path difference in BaF_2 corresponding to the red spectrum and the purple one is only ~0.2 mm, producing 7.6 fs^2 of GDD difference at 800 nm. This allows us to obtain stable mode locking without compromising the spectrum within the gain bandwidth—an ideal feature for optimizing the wavelength component around 1030 nm to seed ytterbium amplifiers for pumping optical parametric amplifiers [5.14-18] and frequency conversion of the Ti:sapphire spectrum [5.27].

Comparison between experiments and simulations

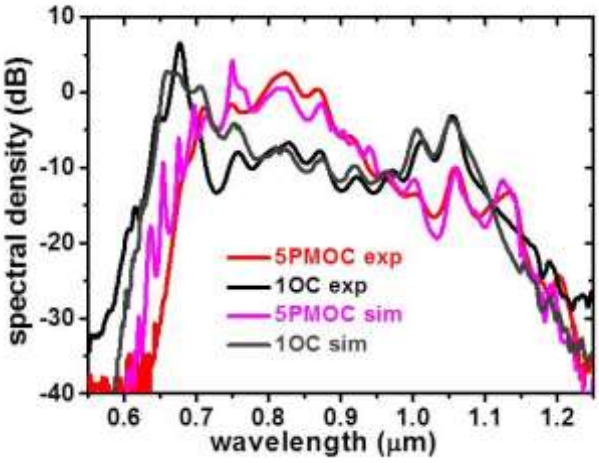

Fig. 5.10. Comparison of the simulated and measured output spectra.

Using the developed spatiotemporal model, the DCM-based cavity can be numerically set up according to the experimental conditions. All the reflectivity and dispersion of intracavity mirrors are characterized via photosepctrometer and a home-built white-light interferometer, respectively. Fig. 5.10 shows the comparison of output spectra between experiments and simulations. The simulated spectra quantitatively visualize not only the

spectral shapes on average, but also the positions and amplitudes of spectral substructures due to intracavity phase matching. However, in the short wavelength regime of the simulated spectra using 5% PMOC, spectral resonances appear in the simulation apart from the experiments. These resonances theoretically are generated from phase matching on higher order Gaussian modes, similar to the experimental result using a 2-GHz ring cavity oscillator shown in Fig. 4.25. Unfortunately, limited by the use of only 0.5-inch-diameter mirrors, these high order Gaussian modes, with spot sizes larger than the mirror apertures, cannot be supported in the 85-MHz linear oscillators, which have a ~1.7 m of cavity length. As a result, a narrower spectrum with a smooth fashion in short wavelength regime is experimentally observed. One can further improve the simulation precision by implementing aperture limitation during linear propagation in the numerical modeling.

5.4 **Tailoring broadband continuum from a mode-locked cavity**

With the developed spatiotemporal model, the laser dynamics and the output performances can be well characterized, leading to the possibilities of advanced cavity designs toward even broader spectrum. In order to obtain state-of-the-art performances, the laser operation is typically pushed to the very edge of the cavity stability region. However, as discussed in Subsection 4.6.2, the residual phase oscillations from DCM result in satellite pulses, which play an adverse role in the cavity stability. As a result, the overall residual phase ripples should be much smaller than the round-trip nonlinear phase, ~1 rad; it is a very demanding requirement after typical 12 bounces of DCMs inside the linear cavity.

In order to cancel out the phase ripples from intracavity DCMs, a phase-optimized end mirror (POEM) is designed and placed at the end of the other cavity arm. Fig. 5.11(a) shows the reflectivity and GD behavior of the POEM design. In chirped mirror designs with octave-spanning bandwidth, residual GD oscillation is typically unavoidable due to the interferences between layer structures inside the coatings, as discussed in Chapter 2. Therefore, with a dispersive behavior compensating 1.35 mm of BaF_2, the residual cavity dispersion from DCMs can be applied as the design goal. With the POEM, the oscillation amplitude of overall residual cavity phase can be controlled within 0.1 rad after 12 bounces of DCMs over the spectral range of 650 nm – 1150 nm, as shown in Fig. 5.11.

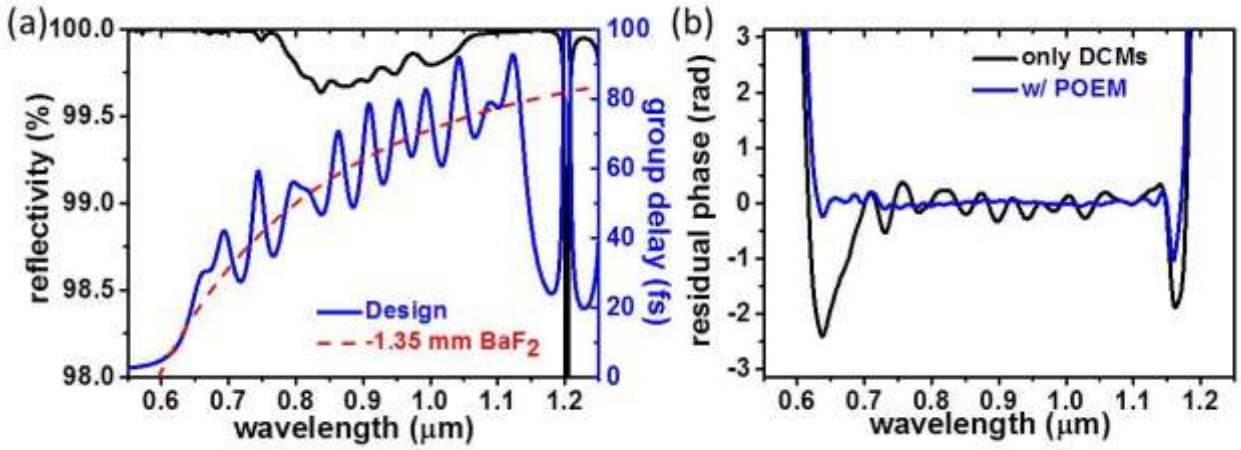

Fig. 5.11. (a) Reflectivity and group delay of a phase-optimized end mirror (POEM), in order to compensate the residual phase oscillations from intracavity DCMs. (b) The round-trip residual phase after 12 bounces of DCMs, (black) with a silver end mirror and (blue) with the POEM.

Since Ti:sapphire oscillators feature extremely low quantum noises, the broadband continuum generating from a mode-locked cavity has been applied to optical frequency metrology and seeding of optical parametric amplifiers [5.14-18] for attosecond science [5.19]. In optical frequency metrology, self-referenced carrier-envelope-phase (CEP) stabilization is achieved directly using the spectral components around 1140 nm for frequency doubling, and beating with the light around 570 nm. A stable frequency comb is thus established, and the laser output can be employed for precise spectroscopic applications or as a quiet seed for optical amplifiers, especially the light around 1030 nm for Yb-based sources. As a result, in the long spectral wing, the wavelength components around 1140 nm and 1030 nm are especially important, in terms of both spectral density and beam profile, for nonlinear conversion and further light amplification. On the other hand, the short spectral wing should be also broad enough to provide enough beating signals around 570 nm.

For these applications and exploring the cavity capability, new PMOCs are designed with 1% and 5% output coupling within the gain bandwidth. In order to enhance the longer wavelength, the phase-matching concept is applied by controlling the cavity reflectivity and providing a phase ramp feature. In the short wavelength, the light is almost coupled out, similar to the 1% ZnSe/MgF_2 OC, due to the design difficulty of precise control of both high reflectivity and cavity phase. With the use of POEM, Fig. 5.12(a) shows the simulated intracavity spectra and the mirror characteristics of the new designed 1% and 5% PMOC. Comparing with the spectra obtaining from 1% ZnSe/MgF_2 OC (see black curves in Fig. 5.12) and a silver end mirror, one can obtain much broader spectra in the long wavelengths due to cavity enhancements. The intracavity spectra share alike behavior even with different output coupling. That is, the loss perturbation from 1% to 5% output coupling doesn't affect the intracavity dispersion-managed soliton much. As a result, with a resembling phase ramp as shown in the inset of Fig. 5.12(a), one can obtain similar amount of the spectral components around 1140 nm.

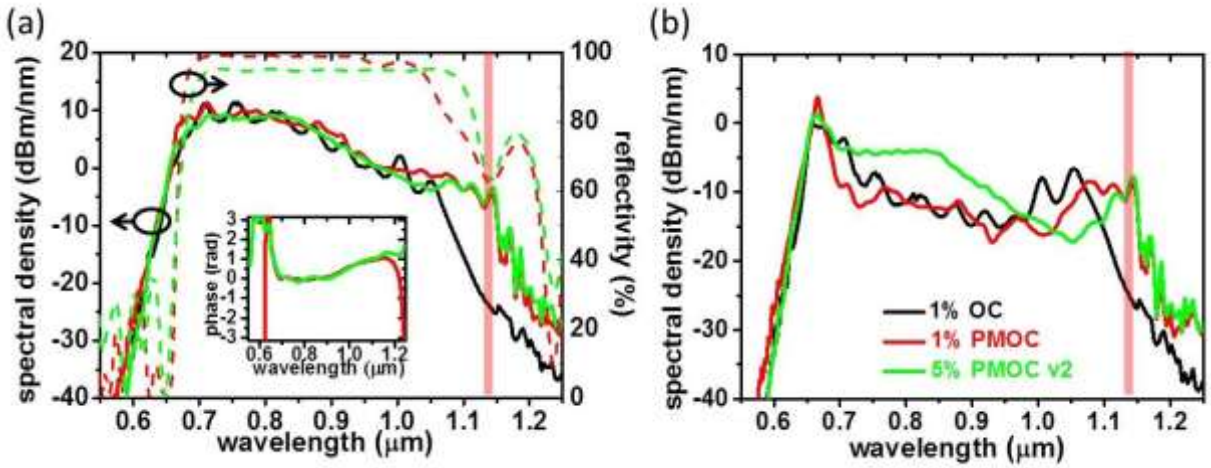

Fig. 5.12. (a) The simulated intracavity spectra, as well as the PMOC characteristics, and (b) the output spectra of the new designed 1% and 5% PMOC using POEM. The inset in (a) shows the residual phase from the PMOCs, similar to the red curve in Fig. 5.7. The red and green curves plot the corresponding outcomes from the 1% PMOC and 5% PMOC, respectively. The black curves are plotted as the references using 1% $ZnSe/MgF_2$ OC and a silver end mirror.

The output spectra are shown in Fig. 5.12(b). Comparing the two 1% output-coupling results, ~10% shorter TL pulse width can be obtained using the PMOC design. It implies that even shorter TL pulses are possible than the state-of-the-art TL pulse width, 3.5 fs, toward single-optical-cycle pulses, 2.7 fs from a single Ti:sapphire oscillator. Using the new 5% PMOC, >1mW of the output power around 1140 nm with a 10 nm bandwidth can be obtained, matching the 1% PMOC result, while the main output around the center wavelength is ~5 times larger.

Despite >1 mW of 1140nm components achievable from the mentioned PMOC designs, it is hard to optimize both wavelength components around 1030nm and 1140 nm. Fortunately, it can be well-controlled by precise tailoring the cavity output coupling in the range of 1000 nm to 1140 nm. Slightly increasing the output coupling around 1030 nm, more light around 1030 nm is obtained, at the expense of less light around 1140 nm from weakening cavity resonances. Fig. 5.13 shows the output spectra from different 5% PMOC designs, as well as the corresponding reflectivity and residual phase. With different output coupling windows, the weighting between 1030 nm and 1140 nm is varied, implying a controllable manner of the oscillator output aiming for different applications.

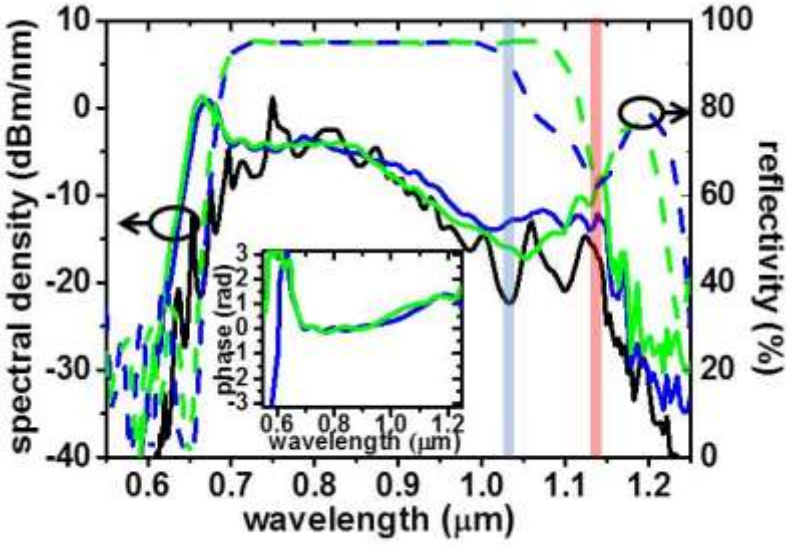

Fig. 5.13. The simulated output spectra, as well as the corresponding 5% PMOC characteristics, using different 5% PMOC designs and POEM. The inset shows the residual phases from the new designed 5% PMOCs. The green and blue curves plot the corresponding behaviors with different 5% PMOCs. The black curve provides references using the 5% PMOC described in Section. 5.3 with a silver end mirror.

References

[5.1] H. A. Haus, J. G. Fujimoto, and E. P. Ippen, "Structures for additive pulse mode locking," *JOSA B,* vol. 8, pp. 2068-2076, 1991.

[5.2] D. E. Spence, P. N. Kean, and W. Sibbett, "60-fsec pulse generation from a self-mode-locked Ti:sapphire laser," *Optics Letters,* vol. 16, pp. 42-44, 1991/01/01 1991.

[5.3] C. Chudoba, J. G. Fujimoto, E. P. Ippen, H. A. Haus, U. Morgner, F. X. Kärtner*, et al.*, "All-solid-state Cr:forsterite laser generating 14-fs pulses at 1.3 μm," *Optics Letters,* vol. 26, pp. 292-294, 2001/03/01 2001.

[5.4] R. Ell, U. Morgner, F. X. Kärtner, J. G. Fujimoto, E. P. Ippen, V. Scheuer*, et al.*, "Generation of 5-fs pulses and octave-spanning spectra directly from a Ti:sapphire laser," *Optics Letters,* vol. 26, pp. 373-375, 2001/03/15 2001.

[5.5] F. X. Kärtner, U. Morgner, R. Ell, T. Schibli, J. G. Fujimoto, E. P. Ippen*, et al.*, "Ultrabroadband double-chirped mirror pairs for generation of octave spectra," *Journal of the Optical Society of America B,* vol. 18, pp. 882-885, 2001/06/01 2001.

[5.6] A. Bartels and H. Kurz, "Generation of a broadband continuum by a Ti:sapphire femtosecond oscillator with a 1-GHz repetition rate," *Optics Letters,* vol. 27, pp. 1839-1841, 2002/10/15 2002.

[5.7] D. J. Ripin, C. Chudoba, J. T. Gopinath, J. G. Fujimoto, E. P. Ippen, U. Morgner*, et al.*, "Generation of 20-fs pulses by a prismless Cr4+:YAG laser," *Optics Letters,* vol. 27, pp. 61-63, 2002/01/01 2002.

[5.8] T. M. Fortier, D. J. Jones, and S. T. Cundiff, "Phase stabilization of an octave-spanning Ti:sapphire laser," *Optics Letters,* vol. 28, pp. 2198-2200, 2003/11/15 2003.

[5.9] L. Matos, D. Kleppner, O. Kuzucu, T. R. Schibli, J. Kim, E. P. Ippen*, et al.*, "Direct frequency comb generation from an octave-spanning, prismless Ti:sapphire laser," *Optics Letters,* vol. 29, pp. 1683-1685, 2004/07/15 2004.

[5.10] O. Mücke, R. Ell, A. Winter, J.-W. Kim, J. Birge, L. Matos*, et al.*, "Self-Referenced 200 MHz Octave-Spanning Ti:Sapphire Laser with 50 Attosecond Carrier-Envelope Phase Jitter," *Optics Express,* vol. 13, pp. 5163-5169, 2005/06/27 2005.

[5.11] T. M. Fortier, A. Bartels, and S. A. Diddams, "Octave-spanning Ti:sapphire laser with a repetition rate >1 GHz for optical frequency measurements and comparisons," *Optics Letters,* vol. 31, pp. 1011-1013, 2006/04/01 2006.

[5.12] H. M. Crespo, J. R. Birge, E. L. Falcão-Filho, M. Y. Sander, A. Benedick, and F. X. Kärtner, "Nonintrusive phase stabilization of sub-two-cycle pulses from a prismless octave-spanning Ti:sapphire laser," *Optics Letters,* vol. 33, pp. 833-835, 2008/04/15 2008.

[5.13] L.-J. Chen, M. Y. Sander, and F. X. Kärtner, "Kerr-lens mode locking with minimum nonlinearity using gain-matched output couplers," *Optics Letters,* vol. 35, pp. 2916-2918, 2010/09/01 2010.

[5.14] J. Moses, S. W. Huang, K. H. Hong, O. D. Mücke, E. L. Falcão-Filho, A. Benedick*, et al.*, "Highly stable ultrabroadband mid-IR optical parametric chirped-pulse amplifier optimized for superfluorescence suppression," *Optics Letters,* vol. 34, pp. 1639-1641, 2009/06/01 2009.

[5.15] M. Schultze, T. Binhammer, G. Palmer, M. Emons, T. Lang, and U. Morgner, "Multi-μJ, CEP-stabilized, two-cycle pulses from an OPCPA system with up to 500 kHz repetition rate," *Optics Express,* vol. 18, pp. 27291-27297, 2010/12/20 2010.

[5.16] M. Schultze, T. Binhammer, A. Steinmann, G. Palmer, M. Emons, and U. Morgner, "Few-cycle OPCPA system at 143 kHz with more than 1 μJ of pulse energy," *Optics Express,* vol. 18, pp. 2836-2841, 2010/02/01 2010.
[5.17] S.-W. Huang, G. Cirmi, J. Moses, K.-H. Hong, S. Bhardwaj, J. R. Birge*, et al.*, "High-energy pulse synthesis with sub-cycle waveform control for strong-field physics," *Nat Photon,* vol. 5, pp. 475-479, 08//print 2011.
[5.18] A. Harth, M. Schultze, T. Lang, T. Binhammer, S. Rausch, and U. Morgner, "Two-color pumped OPCPA system emitting spectra spanning 1.5 octaves from VIS to NIR," *Optics Express,* vol. 20, pp. 3076-3081, 2012/01/30 2012.
[5.19] F. Krausz and M. Ivanov, "Attosecond physics," *Reviews of Modern Physics,* vol. 81, pp. 163-234, 02/02/ 2009.
[5.20] S. Cundiff, E. Ippen, H. Haus, and W. Knox, "Frequency-dependent mode size in broadband Kerr-lens mode locking," *Optics letters,* vol. 21, pp. 662-664, 1996.
[5.21] S. Kelly, "Characteristic sideband instability of periodically amplified average soliton," *Electronics Letters,* vol. 28, pp. 806-807, 1992.
[5.22] P. Curley, C. Spielmann, T. Brabec, F. Krausz, E. Wintner, and A. Schmidt, "Operation of a femtosecond Ti: sapphire solitary laser in the vicinity of zero group-delay dispersion," *Optics letters,* vol. 18, pp. 54-56, 1993.
[5.23] Q. Lin and I. Sorokina, "High-order dispersion effects in solitary mode-locked lasers: side-band generation," *Optics communications,* vol. 153, pp. 285-288, 1998.
[5.24] G. Chang, L.-J. Chen, and F. X. Kärtner, "Fiber-optic Cherenkov radiation in the few-cycle regime," *Optics express,* vol. 19, pp. 6635-6647, 2011.
[5.25] Y. Chen, F. Kärtner, U. Morgner, S. Cho, H. Haus, E. Ippen*, et al.*, "Dispersion-managed mode locking," *JOSA B,* vol. 16, 1999.
[5.26] V. Magni, G. Cerullo, S. D. Silvestri, and A. Monguzzi, "Astigmatism in Gaussian-beam self-focusing and in resonators for Kerr-lens mode locking," *JOSA B,* vol. 12, pp. 476-485, 1995.
[5.27] J. Moses, H. Suchowski, and F. X. Kärtner, "Fully efficient adiabatic frequency conversion of broadband Ti: sapphire oscillator pulses," *Optics letters,* vol. 37, pp. 1589-1591, 2012.

Chapter 6

RF-modulated nonlinear light microscope

6.1 Introduction

Nonlinear light microscope has been regarded as one of the most important applications in ultrafast optics [6.1-7]. Ultrashort pulse trains from mode-locked lasers feature intense peak intensity with low average power: detectable nonlinear light signals are generated due to the high peak intensity, while the possible damage is reduced from thermal heating. Based on different nonlinear processes, sample fingerprints can be captured via various imaging contrast agents (for example, multiphoton fluorescence excited by labeled fluorophores [6.1, 5, 8], optical harmonics followed by the sample morphology [6.3, 4, 9], and Raman scattering signals sensitive to the molecule vibration modes [6.6, 7]). Since the nonlinear light is generated only around the focal region (*i.e.*, with strong-enough peak intensity), intrinsic optical sectioning capability is achieved without the use of spatial pinhole in confocal microscopes. Furthermore, thanks to the advance on ultrashort laser technology, near-infrared driving pulses are employed to reach a deep penetration [6.8]. As a result, nonlinear light microscope features deep penetration depth and intrinsic optical sectioning capability, opening up several promising possibilities for biological and medical applications.

For example, second harmonic generation (SHG) microscopy is a promising candidate for the preliminary observation of chiral crystals, so called second-order nonlinear optical imaging of chiral crystals (SONICC) [6.9]. Proteins perform various functions in bio-activities, which can be disclosed by its structure and ligand binding locations. Protein crystallization is typically demanded for the structural analysis via X-ray diffraction. Crystallizing proteins,

however, is often extremely difficult and requiring carefully screening and monitoring the trial processes. Imaging approaches to characterize crystallization processes are thus required. Via the SHG imaging contrast, the presence of protein crystals can be visualized with good sensitivity and background suppression: coherent SHG signals only arise from non-centrosymmetric structures, and it can be enhanced with certain classes of ordered systems. In addition, because of energy conservation, harmonic generation (HG) process leaves no energy deposition to the interacted specimens and thus can provide a least invasive imaging contrast mechanism compared with other electron-transition based nonlinear processes. Therefore, nucleation and growth kinetics of the crystals could be selectively observed in a least invasive fashion from high resolution SONICC imaging.

The technical feasibility of nonlinear light microscopy strongly depends on the availability of robust and easily-operated sources. Ultrafast fiber lasers are regarded as promising candidates due to the potential of compact sizes, simple maintenances, and relatively low costs [6.10]. Compared with other solid-state lasers requiring precise alignments, light guided by optical fibers can be bent around the path as desired. Furthermore, ultrafast fiber lasers can operate outside optical laboratories without additional efforts on environmental isolation, such as the control of temperature and humidity, and the use of optical tables. Moreover, with a long interaction length in optical fiber, both strong gain and potent Kerr nonlinearity can be provided in a round-trip: optical elements with relatively high losses (*e.g.*, Faraday isolators and grating pairs) can be applied in the cavity, and one can easily obtain femtosecond operation employing instantaneous nonlinear effects to provide a fast intensity-dependent saturable action, such as using nonlinear polarization evolution (NPE) [6.11] or nonlinear fiber loop mirror [6.12]. Therefore, advances on ultrafast fiber lasers play important roles in the developments of state-of-the-art nonlinear microscope systems. However, tasks with ultrafast fiber lasers are still remained, such as the excess of high-frequency relative intensity noise (RIN) and mode-locking stability.

To generate sufficient nonlinear signals, scanning microscope systems typically are employed, and the detected signal is sequentially mapped for image acquisition. Therefore, the advance on nonlinear light microscopy relies on high speed electronics. On one hand, the development of high frame rate imaging is driven by the desire of real-time observations of

fast biological or chemical dynamics [6.5]. Above-MHz level of data acquisition rate is thus required. On the other hand, modulated signals along with lock-in detection allows signal subtraction from its background: a radio-frequency (RF)-modulated Stokes pulses has been employed in stimulated Raman scattering (SRS) microscope recently [6.13]. Modulated signals in RF range can thus be separated with the DC background from pump pulses.

In this chapter, a state-of-the-art ultrafast fiber laser is built, delivering 3-nJ pulses with a shot-noise-limited RIN (*i.e.*, relative intensity noise) above MHz frequency range. A RF-modulated nonlinear light microscope is also demonstrated. The excitation pulses are modulated with a RF frequency via an electro-optic modulator (EOM). With the modulated excitation pulses, video-rate two-photon fluorescence imaging is obtained free from the low-frequency noise. The whole setup will be implemented for video-rate SONNIC imaging. Novel methods based on RF-modulated nonlinear light microscope are also proposed.

6.2 Development of low-noise sources

6.2.1 Ultrafast Yb-fiber laser with nonlinear polarization evolution

Yb-doped fiber lasers attract strong attention due to the high efficiency and ease of direct diode pumping [6.10, 14]. Moreover, compared with other fiber lasers operating in typically anomalous dispersion regime above 1.5 μm, cavity dispersion of Yb-fiber lasers, with a center wavelength of 1.03 μm, can be easily managed along with negative-dispersion elements (*e.g.*, prism pairs). The ease of intracavity dispersion management benefits the energy scalability of Yb-fiber laser oscillators as well as the spectral pulse shaping.

A saturate absorber is required for femtosecond generation in a cavity. In ultrafast fiber oscillators, nonlinear polarization evolution (NPE) is most commonly employed due to the ease of implementation and essentially instantaneous response [6.11]. Considering intense optical pulses in an optical fiber, Kerr nonlinearity impacts on not only spectral-broadening but also an intensity-dependent variation in the polarization state. The physical cause of these effects is related to self-phase modulation and cross-phase modulation (XPM). SPM- and XPM-induced phase shifts imposed on the orthogonally polarized components

leads to non-uniform polarization evolution across the pulse. As a result, NPE changes a linear polarization to an intensity-dependent elliptical polarization state. An artificial saturable absorber can be introduced when the pulses then pass through a polarization beam splitter (PBS), providing an intensity-dependent loss. A typical configuration contains fiber polarization controllers or waveplates, which can be adjusted such that the maximum transmission (minimum loss) at the polarizer occurs for the highest possible optical intensity. The feasibility of fast response and adjustable saturable strength (*i.e.*, by adjusting the polarization controller) makes mode locking with nonlinear polarization rotation a powerful technique.

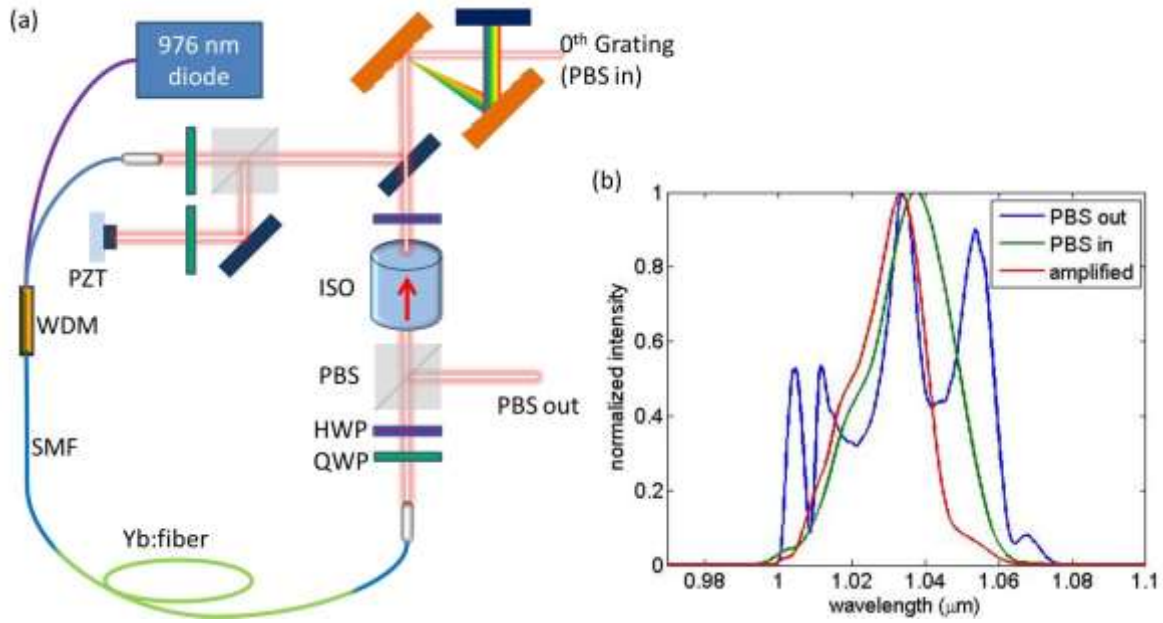

Fig. 6. 1(a) Cavity setup of an ultrafast Yb-fiber oscillator; (b) spectra from the main output (blue), zero-order reflection from the grating (green), and the amplified output (red). WDM, Wavelength-division multiplexer; SMF, single mode fiber, QWP, quarter-wave plate; HWP, half-wave plate; PBS, polarization beamsplitter; ISO, optical isolator.

The cavity setup (see Fig. 6. 1(a)) is similar to the scheme described in [6.15]. A bulk isolator imposes unidirectional operation. A pair of diffraction gratings (600 lines/mm, incidence angle of 45°) provides anomalous dispersion of adjustable magnitude. The gratings are of low quality with ~50% total transmittance. The laser repetition rate is 94MHz, and the cavity length can be active controlled by a PZT-mounted mirror for future repetition rate control. The Yb-fiber oscillator operates in the stretched-pulse mode-locking regime enabled by NPE, and the rejected light from PBS is extracted out of the cavity and used as the main output port. In addition, the zero-order reflection from the first grating is also monitored

and compared with the PBS output (see Fig. 6.1(a)): the laser stability is related to the saturatable strength of NPE, resulting in distinct spectral shape between the intracavity beam and PBS output. The ~0.5nJ main output from fiber oscillators is further amplified to ~4 nJ. The output spectra from the main output, zero-order reflection from the grating, and the amplified output are shown in Fig. 6.1(b).

6.2.2 **Relative intensity noise (RIN)**

In addition to output pulse energy and spectrum, the relative intensity noise (RIN) is of particular importance whether the femtosecond source is "quiet" enough for high sensitivity microscope applications. Noise is a physical quantity in time domain, while the noise source could have certain intrinsic frequency response. Therefore, in order to characterize noise in frequency domain, RIN can then be statistically described with a power spectral density (PSD):

$$S_P = \frac{2}{\bar{P}^2}\int_{-\infty}^{+\infty}\langle \Delta P(t)\Delta P(t+\tau)\rangle\, e^{i2\pi f\tau}d\tau \qquad (6.1)$$

where $\bar{P}$ and $\Delta P(t)$ stand for the mean value and fluctuating noise of the measured quantity, depending on the noise frequency f. A root mean square (rms) value of intensity noise can be also obtained by integrating over an interval [f_1, f_2] of RIN PSD.

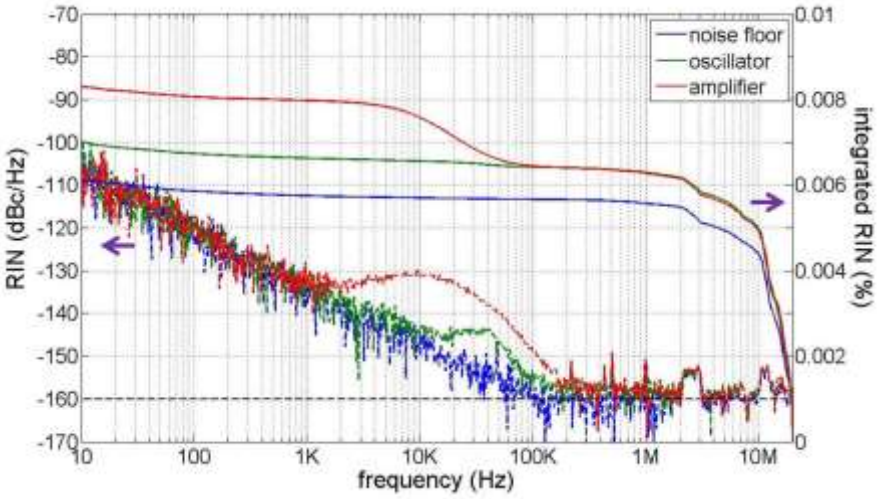

Fig. 6.2. Relative intensity noise of Yb:fiber lasers in terms of power spectral density (dashed lines) and integrated noise from 20MHz (solid lines) to 10 Hz. Blue, instrument noise floor; green, oscillator noise; red, amplifier noise.

In our setup, the mode-locking state and net cavity-dispersion are optimized in order to minimize the RIN, which is shown as the green curve in Fig. 6.2. A low-noise detector (DET 36A, Thorlabs) is employed with a rising time of 14 ns. Before saturating the detector, ~3mW of optical average power is shined on the detector. The shot-noise level of the 3-mW light is ~160 dBc/Hz, which is collided with the instrument noise floor. Our oscillator exhibits an integrated RIN of 0.007% from 10 Hz to 20 MHz, including 0.006% of the integrated noise from instrument noise floor (see the blue curve in Fig. 6.2). The Yb-fiber amplifier is optimized as well such that it only slightly degrades the RIN of the amplified pulses (red curve in Fig. 6.2). The measured RIN, as shown in the dashed curves in Fig 6.2, in the frequency range of 10 Hz to 1 kHz is buried under the instrument noise floor implying reduced technical noise, such as noise from pump and mechanical vibrations of the laser resonator. The excess noise in kHz range could be originated from relaxation oscillation in the cavity. The noise in this range can be reduced by fine-tuning the intracavity waveplates. Above 100 KHz, the intensity noise of both oscillator and amplifier output rolls off quickly to the shot-noise limited detection floor, -160dBc/Hz. The overlapping of the integrated RIN above 100 KHz from the oscillator and amplifier indicates that no noise is introduced in high frequency range.

6.3 **RF-modulated nonlinear light microscope**

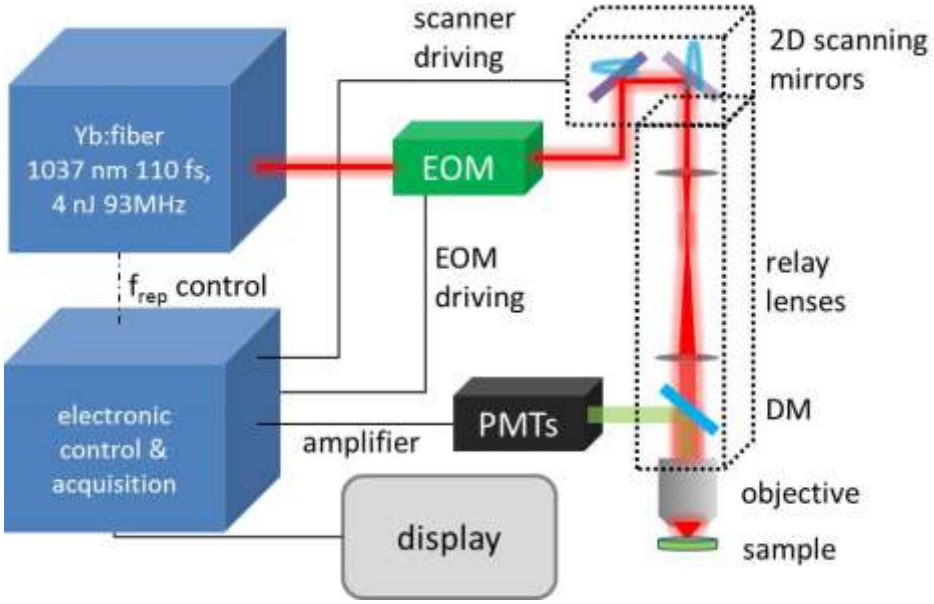

Fig. 6.3. System setup of the RF-modulated nonlinear light microscope. EOM, electro-optic modulator; DM, dichroic mirror; PMT, photomultiplier tube.

The system setup of the scanning nonlinear light microscope is illustrated in Fig. 6.3. The laser output is modulated by an electro-optic modulator (EOM) and then directed into the microscope. In the microscope, the incident beam is deflected by a resonant mirror and a galvanometer mirror, enabling two-dimension raster scanning of the laser beam. A tube lens pair, a 4-*f* system, projects the scanning beam on the back aperture of a high-NA water-immersion objective lens (Nikon CFI APO 60X) with a 1.0 of numerical aperture (NA), while expanding the beam size to overfill the objective back aperture in order to tightly focus the beam into the specimen. The excited nonlinear signals are backward collected by the same objective, and then reflected by a dichroic beam splitter. The signal is collected on photomultiplier tubes (Hamamatsu H7422-40) for sequential detection. Nonlinear light images are mapped out in a computer via a data acquisition system with proper electronic controls.

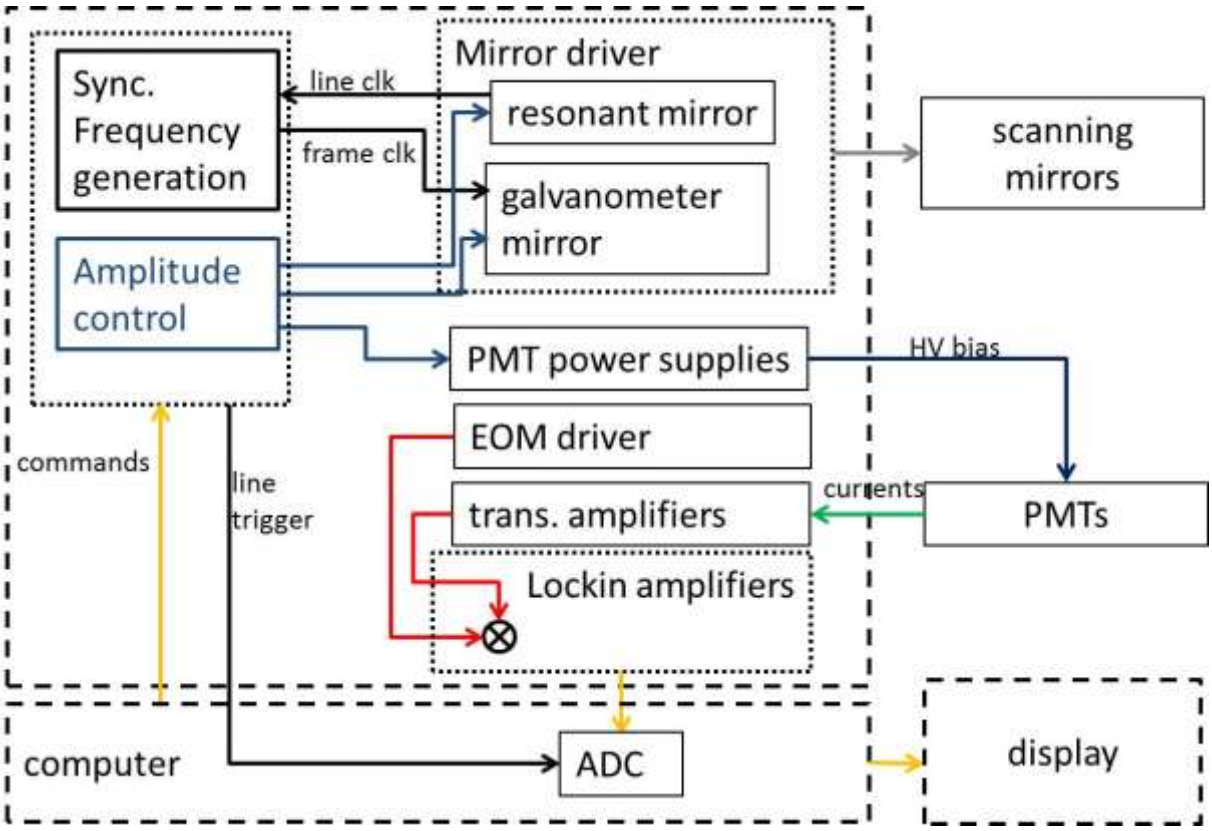

Fig. 6.4. Scheme for electronic signal generation and control

Depending on the sample condition, the excited nonlinear signal can be forward/backward collected. Typically, forward detection, employing a condenser to collect signal after the sample, requires thin or transparent samples, so that the weak nonlinear signal possibly propagates through the sample. On the other hand, backward detection, as

shown in Fig.6.3, is suitable for thick samples, especially strong scattering medium. For the imaging contrasts involving coherent nonlinear processes such as harmonic generations, imaging with different detection schemes might prevail different phase-matching enhancements: the phase mismatch in forward and backward generation are different, and backward detection is more sensitive to tiny structures due to much small coherent length (*i.e.*, larger phase mismatch) [6.16].

The electronic scheme for imaging acquisition/control is shown in Fig. 6.4. The scanning frequency of the fast axis (~8 KHz) is determined by the mirror resonance (*i.e.*, a resonant mirror); the frequency of the slow axis, synchronized to the fast scanning frequency, can be controlled as imaging frame rate (*e.g.*, 28Hz). The scanning amplitude of both axes can be commanded to vary the deflecting angle of the beam, as well as the imaging field of view. With synchronized scanning on the two axes, the position of the focused spot on the specimen can be traced to map images in the computer. The detected signal has a modulated signature due to the EOM-modulated excitation source. Therefore, the signal generated from the excitation source can thus be separated from background noise via signal demodulation. A data acquisition card (AlazarTech ATS9400), which is triggered by the synchronized scanning rates to form two-dimensional images, digitizes the detected signals with a sampling rate of 125 MHz.

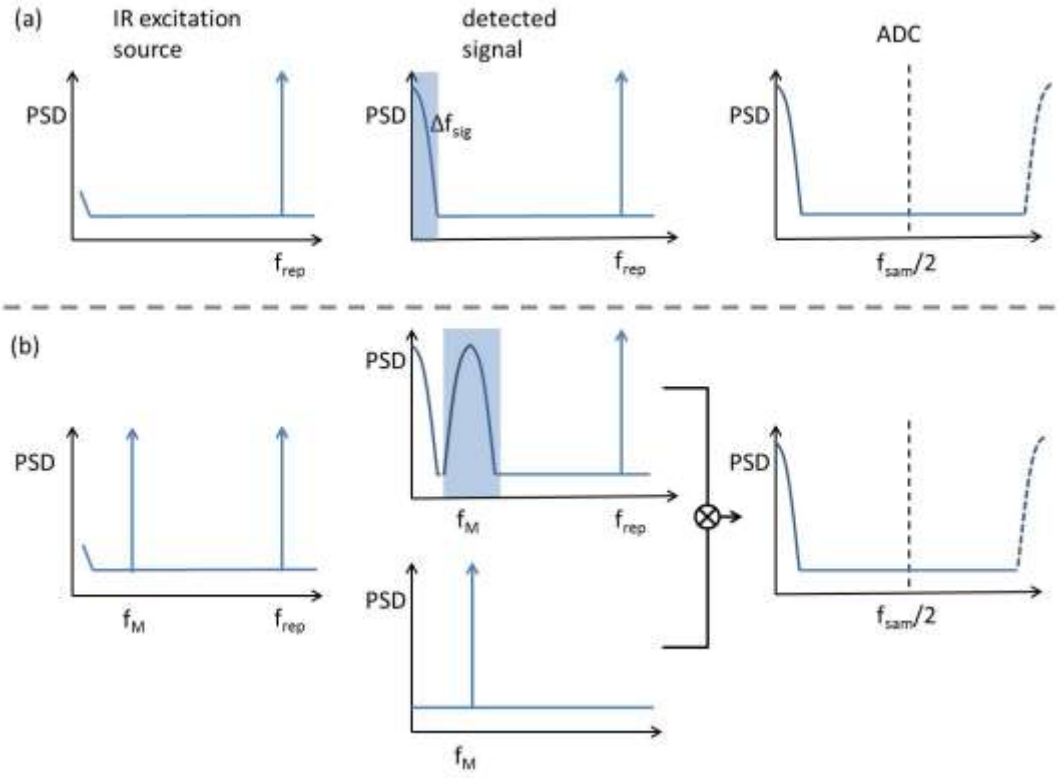

Fig. 6.5. The RF spectra of optical pulses/electronic signals (a) without/ (b) with a modulated excitation source. f_M, modulation frequency; Δf_{sig}, signal bandwidth after beam scanning on the sample; the detected signal from PMTs filtered with a low-pass filter in (a) and a bandpass filter in (b), as shown in the shallowed areas in the middle. In (b), the detected signal is mixed with a synchronized frequency from EOM. f_{sam}, sampling rate of the analog-to-digital converter (ADC). The sampling bandwidth is half of the sampling rate.

To describe the signal processing in detail, I illustrate the RF spectra of optical pulses/electronic signals in Fig. 6.5. The IR excitation pulse train exhibits a strong peak in its repetition rate. In a conventional scheme without additional source modulation (see Fig. 6.5(a)), the low frequency part of the detected signal reveals the nonlinear light contrast from different area of the specimen. Therefore, the bandwidth, Δf_{sig}, depends on not only the scanning speed but also the optical resolution limit. That is,

$$\Delta f_{sig} \sim f_{fast} \frac{l_{fast}}{d_r} \tag{6.2}$$

f_{fast} and l_{fast} are the scanning frequency and field of view on the fast axis, respectively, and d_r is the optical resolution limit. For example using a 60X 1.0NA objective LENS (*e.g.*, Nikon CFI APO 60X), Δf_{sig} is ~4 MHz with f_{fast} of 8KHz, l_{fast} of 250 µm, and ~0.5 µm optical resolution limit. The detected signal passes through a low-pass filter before sent to the data acquisition card, since the laser repetition rate and other high frequency noise could cause

aliasing due to undersampling according to Nyquist–Shannon sampling theorem. On the other hand with a modulated excitation sources (see Fig. 6.5(b)), the detected sample signature appears at the lower frequency as well as generates a duplicate centered at the modulation frequency. The modulated duplicate is filtered out by a bandpass filter, and then mixed with a pure sinusoidal signal from the EOM driver. The scheme is similar to lock-in detection but with a broad bandwidth (~8 MHz) for video-rate imaging, and the detuned signal is used for digital data acquisition.

Since the generated signals are quite weak, the detection sensitivities should be explored especially for high speed imaging acquisition. The detection limit is determined by both electronic and optical noise. To avoid stray light from environmental light sources (*e.g.*, screen or device control panels), the detection setup has to be completely sealed. With our modulated scheme, the sealing requirement can be relaxed since the environmental background, featuring lower frequency responses less than 1 MHz, does not contribute to the detected signal.

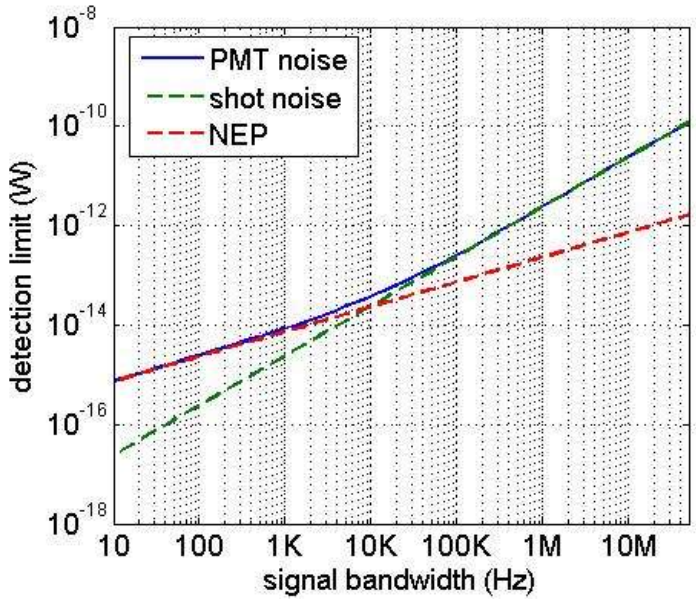

Fig. 6.6. Detection limit (*i.e.*, SNR=1) from the PMT (blue) at different detection bandwidths. Shot noise limit, green dashed line; noise equivalent power from the dark current, red dashed line.

Even with a perfect isolation from the environment noise, the fundamental detection limit is hampered by the dark current of the device and shot noise from the signal. The dark current noise is commonly expressed in terms of the NEP (noise equivalent power), which is

defined as the value of incident light flux required to produce an output current equal to the noise current. Using PMTs without considering noise current from amplifier circuit, the NEP and shot noise comes from the amplified anode dark current and signal current, respectively. As a result, the signal-to-noise ratio (SNR) can be expressed as

$$SNR = \frac{I_p}{\sqrt{2e(I_p+2I_d)FB}} \tag{6.3}$$

where I_p and I_d are the cathode signal and dark current, respectively. e is the elementary charge, F the secondary emission ratio, and B the signal bandwidth. Detection limits (*i.e.*, SNR=1) at different detection bandwidths are calculated as plotted in Fig. 6.6, followed by the data sheet of the PMT. The NEP plays a more important role with a narrower acquisition bandwidth. With a broader bandwidth, the minimum detectable signal increases, and the shot noise eventually dominates the PMT performance. As a result, the improving of SNR can be achieved by using higher quantum efficiency PMT (*i.e.*, increasing I_p), especially for broadband acquisition. Moreover, using cooling housing helps decrease the dark current, which is important for a lower imaging acquisition rate.

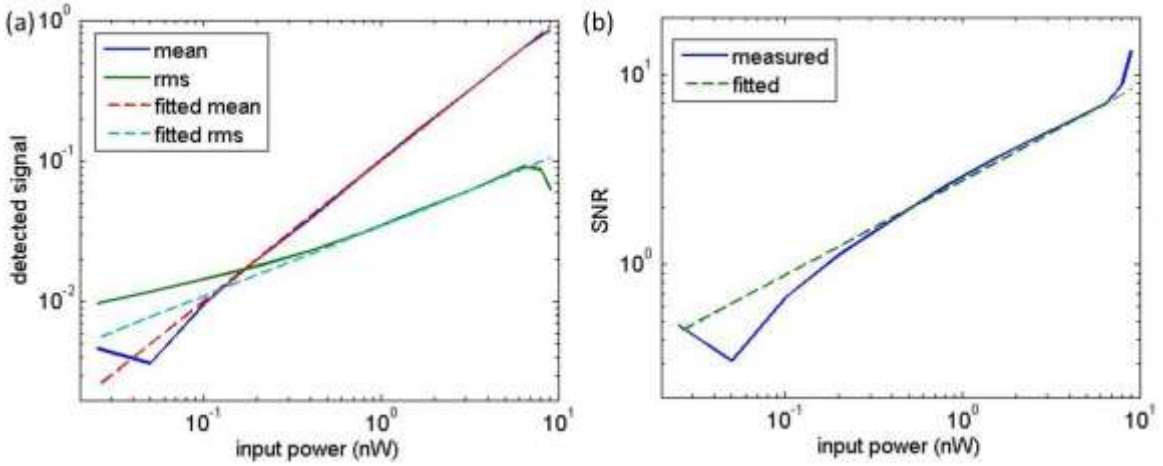

Fig. 6.7. Power-dependent characteristic of the detected signals from the PMT with a 5 MHz of signal bandwidth: (a) the mean values and rms fluctuations and (b) signal-to-noise ratio, as well as the fitting lines corresponding to shot-noise detection.

In order to experimentally demonstrate the SNR in our setup, we performed a power-dependent measurement without beam scanning to evaluate the detected electric signal and its rms fluctuation (see Fig. 6.7). SHG signals are measured with a 5 MHz of signal bandwidth; the rms values (*i.e.*, noise) are calculated with a bandwidth range from 25Hz to 5MHz, roughly corresponding to the noise response in one frame of the video-rate imaging

(*e.g.*, 28Hz in our case). In order to calibrate the input SHG power, a power meter with a μW level of sensitivity is employed before an OD 4 neutral density filter and the PMT. In the input range of 0.1 nW - 10 nW (see Fig. 6.7(a)), the mean and rms values of the PMT output are linearly proportional to the input powers and its square root, respectively. Below 0.1 nW, the excess noise floor apart from fitted shot noise could contribute from the amplification noise of electronic devices. Therefore, a shot-noise-limited detection can be achieved in the input range of 0.1 nW -10 nW with a few MHz of detection bandwidth. The SNR are plotted in Fig. 6.7(b), as well as a fitted line exhibiting a shot-noise-limited detection.

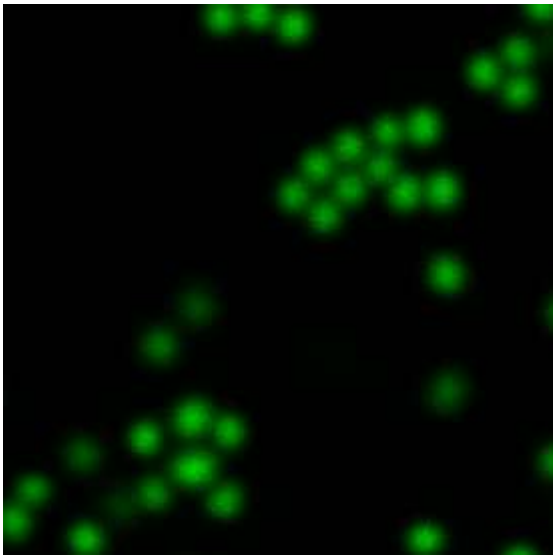

Fig. 6.8. Two-photon fluorescence (2PF) imaging of 1 μm beads with a 0.35 ms of exposure time (28 Hz of frame rate).

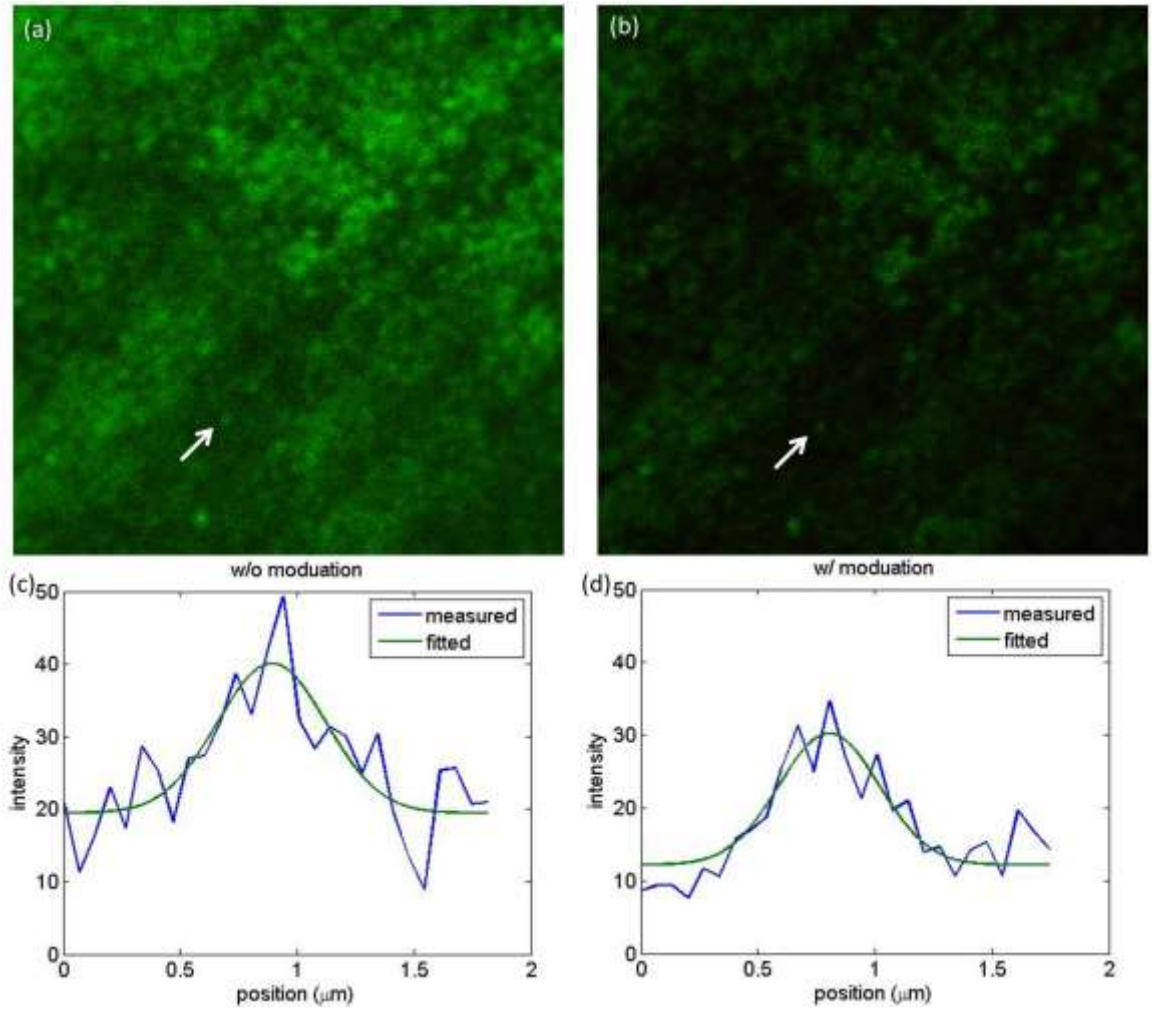

Fig. 6.9. (a-b) 2PF images of 0.1-μm-diameter beads (a) without/ (b) with a modulated excitation beam. (c-d) the corresponding profiles of the point spread functions obtained from the indicated bead pointed by arrows in (a-b), respectively. Blue, the measured profile; green, the fitted Gaussian profile with a FWHM of ~0.5 μm on both cases.

Before SHG visualization of chiral crystals, two-photon fluorescence (2PF) imaging of 1 μm beads (FluoSpheres F8820) is obtained with a ~0.35 ms of imaging acquisition time, as shown in Fig. 6.8. The microscope system provides the feasibility of sub-micron video-rate imaging. In order to evaluate the system performance, 0.1-μm-diameter beads (FluoSpheres F8800) is imaged via 2PF process, as shown in Fig. 6.9(a-b). The image using a modulated excitation source (Fig. 6.9(b)) is compared with the one (Fig. 6.9(a)) without EOM modulation. For a fair comparison, the input power is adjusted to deliver 10 mW after the objective lens for both cases. With 0.1-μm-diameter beads, the point spread function of the 2PF imaging is visualized since the bead diameter is much smaller than the focused spot size on the sample. The profiles of the indicated bead pointed by arrows in Fig. 6.9(a-b) are plotted in Fig. 6.9(c-d), respectively. ~0.5 μm FWHM of Gaussian fitted curves are obtained

in both cases, indicating the 2PF resolution of ~0.5 μm in our system. In addition, the adjusted R squares in Fig. 6.9(c-d), calculated with the fitted Gaussian profile, are 0.63 and 0.76, respectively. A better adjusted R square is obtained from the modulated setup.

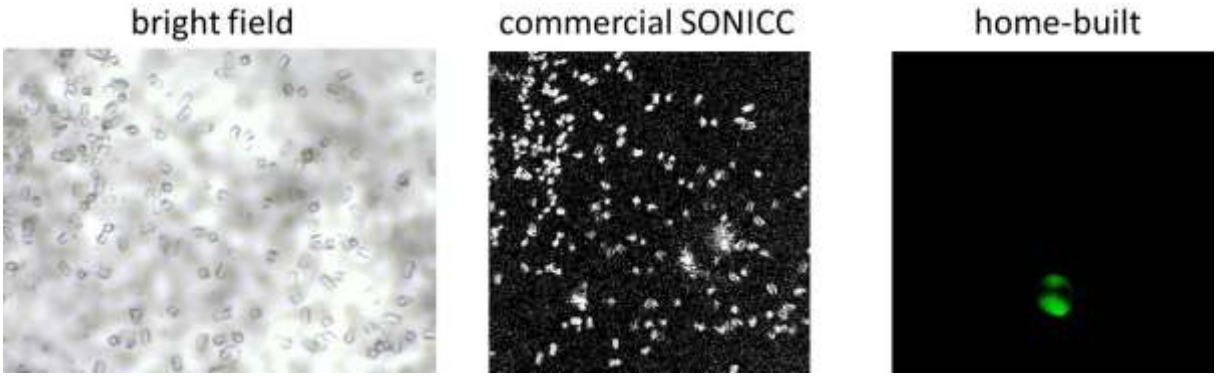

Fig. 6.10. ~10-μm-diameter lysozyme crystals from a bright field imaging, the commercial SONICC system, and the home-built microscope.

	commercial SONICC	home-built
objective lens	20X 0.45 NA	60X 1.0 NA
exposure time	3 s	0.035 s
image size	681 μm x 681 μm	113 μm x 113 μm
excitation wavelength	1064 nm	1037 nm
excitation power	273 mW	25 mW

Table 6.1. Comparison between the commercial SONICC system and home-built microscope.

A preliminary test is conducted to compare the system capability with a commercial SONICC microscope (Formulatrix SONICC Benchtop). ~10 μm-diameter lysozyme crystals are examined from a bright field microscope, the commercial SONICC system, and the home-built modulated-based microscope, as shown in Fig. 6.10. The experimental conditions of the imaging system are listed in Table 6.1. Despite of a smaller field of view mainly limited by magnification power of the objective lens, the image can be obtained with 10 times lower illumination power and 100 times shorter exposure time using the home-built system comparing with the commercial one. Video-rate SONICC images with sub-micron resolution can be achieved with a minimum illumination, which will benefit future implementation for monitoring crystal growing and delivering.

6.4 **Future works**

Heterodyne detection for coherent signals

Nonlinear light microscopy usually employs PMTs to detect extremely weak signals because they feature high sensitivity and large bandwidth (*e.g.*, >50 MHz). However, PMTs have disadvantages of large size (compared with *e.g.* photodiodes), higher cost, and requirement for a high-voltage supply (*e.g.*, >1 kV).

For coherent processes such as harmonics generation, coherent gating can be applied such as heterodyne detection: the generated signal is modulated, inherent from a modulated pump as our setup in Section 6.3, and detected along with a reference beam with another modulation RF frequency, Ω_{ref}. The detected light can be expressed in the following equation:

$$\begin{aligned} I_{det} &= \left|E_{sig}\cos\left(\Omega_{sig}t+\theta_{sig}\right)+E_{ref}\cos\left(\Omega_{ref}t\right)\right|^2 \\ &= \left|E_{sig}\right|^2+\left|E_{ref}\right|^2+2E_{sig}E_{ref}\cos\left(\Omega_{sig}t+\theta_{sig}\right)\cos\left(\Omega_{ref}t\right) \end{aligned} \quad (6.4)$$

where E_{sig} and E_{ref} are the electric field of the signal and reference, respectively. With a fixed E_{ref} and Ω_{ref}, the last term in Eqn. 6.4 includes the signal information (both amplitude and phase, E_{sig} and θ_{sig}, respectively), which can be measured by mixing down the detected signal with the heterodyne frequency (*i.e.*, $\Omega_{sig}-\Omega_{ref}$).

If the amplitude of the reference beam is much larger than the signal, which is quite weak from a nonlinear light microscope, the amplitude of the heterodyne detected signal is "amplified" (*i.e.*, $E_{sig}E_{ref} \gg \left|E_{sig}\right|^2$) without introducing additional noise; shot-noise detection of the quite weak signal can be achieved even using a photodiode instead of a PMT. Employing photodiodes and fiber laser systems, harmonic generation microscope (*e.g.*, SONICC system) can be built in a more compact and economic way.

Modulated stimulated emission depletion microscope

Due to optical diffraction, the resolution of conventional light microscopy is limited roughly by the full width at half maximum (FWHM) of the point spread function (*i.e.*, submicron range using a high NA objective lens and visible light). Super-resolution techniques provide images with a higher resolution than the diffraction limit, which can be obtained by

capturing the light containing higher spatial frequency (*e.g.*, detecting the evanescent waves or using structured illumination [6.17-19]), or by precise photo-switching/depleting the electron transition (*e.g.*, stimulated emission depletion and stochastic functional techniques) [6.20-22]. Comparing with other methods, STED microscopy [6.20, 23, 24] has been regarded as a powerful tool to achieve super-resolution imaging due to the feasibility of fast imaging acquisition (*e.g.*, video rate) and ultrafine resolution (>10 fold better resolution than the diffraction limit in the far field).

Using the modulation technique, the detected signals carried by different modulation frequencies can be separated in the RF frequency domain even sharing the same color. As a result, signals originating from different mechanisms can be well separated via modulation-based excitation. Here, a novel method is proposed to achieve super-resolution stimulated emission depletion (STED) imaging with a simpler setup.

In order to achieve super-resolution imaging, the point spread function of STED microscopy is modified by using another beam to nonlinearly deplete the fluorescent states of the fluorophores. Along with the excitation source, a doughnut-shaped red-shifted pulse, termed the STED beam, is applied to achieve instantaneously stimulated emission. Upon interaction of the STED photon and the excited fluorophore, the fluorophore molecule is returned to the ground state through stimulated emission before spontaneous fluorescence emission. By properly superimposing the STED and excitation beam, only molecules dwelling in the center of the STED beam (*i.e.*, where the STED beam with a zero intensity) are able to emit fluorescence, thus effectively narrowing the point spread function. As a result, even though both STED and excitation pulses are diffraction-limited, the narrowed point spread function ultimately improves imaging resolution beyond the diffraction limit. In the conventional setup, the choice of the fluorophores is quite important: the factor of the resolution improvement depends on the ratio between the power of STED beam and the saturation peak power ($P_{sat} = \hbar\omega_0/\sigma_L\tau_L$, with a cross-section σ_L and the upper-state lifetime τ_L, similar to the stimulated behavior described in Subsection 4.2.1) of the stimulated emission. As a result, P_{sat} should be small than the sample damage threshold. Moreover, photobleaching due to excitation into an even higher excited state or excitation in the triplet state should be avoided.

Since a dichroic mirror is typically employed to separate the spontaneous fluorescence from the STED beam in detection, the STED wavelength has to be at the edge of the whole emission spectrum. However, use of longer STED wavelength at the emission edge along with dichroic mirrors leads to a trade-off between the detected spontaneous fluorescence and the required STED power for stimulated emission depletion, which is determined by the saturation peak power P_{sat}. Larger fluorescence signal can be obtained when the STED wavelength is located at the emission edge. However, the emission cross section at the edge is quite small, demanding a larger saturation peak power. By properly modulating the excitation and STED beam at different frequencies, the fluorescence signals carried by the excitation modulation will be detected, while the excitation modulation signature is depleted by the STED beam. As a result, modulated STED microscope can be achieved with relaxed constraints on the dye selection and reduced STED power.

6.5 **Summary**

Our approach to setup a nonlinear light microscope system is also described based on femtosecond fiber lasers and high speed electronics. The ultrafast fiber laser system, including a nonlinear-polarization-evolution mode-locked Yb:fiber oscillator and an amplifier is constructed to deliver ~110-fs pulses with ~3 nJ of pulse energy featuring low relative intensity noise (RIN). The schemes of electronic control and optical setup of the microscope systems are provided. With the demonstrated nonlinear light microscope, we obtained sub-μm resolution imaging with a video imaging rate at a reduced excitation power compared with the commercial SONICC systems, as the comparisons listed in Table 6.1. With the developed ultrafast fiber laser technology and optimized electronic control, a more compact nonlinear light microscope can be constructed to monitor nucleation and growth kinetics of protein crystals.

References

[6.1] W. Denk, J. H. Strickler, and W. W. Webb, "Two-photon laser scanning fluorescence microscopy," *Science,* vol. 248, pp. 73-76, 1990.

[6.2] C. Xu, W. Zipfel, J. B. Shear, R. M. Williams, and W. W. Webb, "Multiphoton fluorescence excitation: new spectral windows for biological nonlinear microscopy," *Proceedings of the National Academy of Sciences,* vol. 93, pp. 10763-10768, 1996.

[6.3] Y. Barad, H. Eisenberg, M. Horowitz, and Y. Silberberg, "Nonlinear scanning laser microscopy by third harmonic generation," *Applied Physics Letters,* vol. 70, pp. 922-924, 1997.

[6.4] S.-W. Chu, S.-Y. Chen, T.-H. Tsai, T.-M. Liu, C.-Y. Lin, H.-J. Tsai*, et al.*, "In vivo developmental biology study using noninvasive multi-harmonic generation microscopy," *Optics Express,* vol. 11, pp. 3093-3099, 2003.

[6.5] W. R. Zipfel, R. M. Williams, and W. W. Webb, "Nonlinear magic: multiphoton microscopy in the biosciences," *Nature biotechnology,* vol. 21, pp. 1369-1377, 2003.

[6.6] C. L. Evans, E. O. Potma, M. Puoris' haag, D. Côté, C. P. Lin, and X. S. Xie, "Chemical imaging of tissue in vivo with video-rate coherent anti-Stokes Raman scattering microscopy," *Proceedings of the National Academy of Sciences of the United States of America,* vol. 102, pp. 16807-16812, 2005.

[6.7] C. W. Freudiger, W. Min, B. G. Saar, S. Lu, G. R. Holtom, C. He*, et al.*, "Label-free biomedical imaging with high sensitivity by stimulated Raman scattering microscopy," *Science,* vol. 322, pp. 1857-1861, 2008.

[6.8] N. G. Horton, K. Wang, D. Kobat, C. G. Clark, F. W. Wise, C. B. Schaffer*, et al.*, "In vivo three-photon microscopy of subcortical structures within an intact mouse brain," *Nature photonics,* vol. 7, pp. 205-209, 2013.

[6.9] R. D. Wampler, D. J. Kissick, C. J. Dehen, E. J. Gualtieri, J. L. Grey, H.-F. Wang*, et al.*, "Selective detection of protein crystals by second harmonic microscopy," *Journal of the American Chemical Society,* vol. 130, pp. 14076-14077, 2008.

[6.10] M. E. Fermann and I. Hartl, "Ultrafast fibre lasers," *Nature photonics,* vol. 7, pp. 868-874, 2013.

[6.11] M. E. Fermann, M. L. Stock, M. J. Andrejco, and Y. Silberberg, "Passive mode locking by using nonlinear polarization evolution in a polarization-maintaining erbium-doped fiber," *Optics Letters,* vol. 18, pp. 894-896, 1993/06/01 1993.

[6.12] N. Doran and D. Wood, "Nonlinear-optical loop mirror," *Optics Letters,* vol. 13, pp. 56-58, 1988.

[6.13] B. G. Saar, C. W. Freudiger, J. Reichman, C. M. Stanley, G. R. Holtom, and X. S. Xie, "Video-rate molecular imaging in vivo with stimulated Raman scattering," *Science,* vol. 330, pp. 1368-1370, 2010.

[6.14] V. Cautaerts, D. J. Richardson, R. Paschotta, and D. C. Hanna, "Stretched pulse Yb3+:silica fiber laser," *Optics Letters,* vol. 22, pp. 316-318, 1997/03/01 1997.

[6.15] H. Lim, F. Ö. Ilday, and F. W. Wise, "Generation of 2-nJ pulses from a femtosecond ytterbium fiber laser," *Optics Letters,* vol. 28, pp. 660-662, 2003/04/15 2003.

[6.16] D. Débarre, N. Olivier, and E. Beaurepaire, "Signal epidetection in third-harmonic generation microscopy of turbid media," *Optics Express,* vol. 15, pp. 8913-8924, 2007/07/09 2007.

[6.17] E. Betzig and J. K. Trautman, "Near-field optics: microscopy, spectroscopy, and surface modification beyond the diffraction limit," *Science,* vol. 257, pp. 189-195, 1992.

[6.18] M. G. Gustafsson, "Surpassing the lateral resolution limit by a factor of two using structured illumination microscopy," *Journal of microscopy,* vol. 198, pp. 82-87, 2000.

[6.19] M. G. Gustafsson, "Nonlinear structured-illumination microscopy: wide-field fluorescence imaging with theoretically unlimited resolution," *Proceedings of the National Academy of Sciences of the United States of America,* vol. 102, pp. 13081-13086, 2005.
[6.20] S. W. Hell and J. Wichmann, "Breaking the diffraction resolution limit by stimulated emission: stimulated-emission-depletion fluorescence microscopy," *Optics letters,* vol. 19, pp. 780-782, 1994.
[6.21] E. Betzig, G. H. Patterson, R. Sougrat, O. W. Lindwasser, S. Olenych, J. S. Bonifacino, *et al.*, "Imaging intracellular fluorescent proteins at nanometer resolution," *Science,* vol. 313, pp. 1642-1645, 2006.
[6.22] M. J. Rust, M. Bates, and X. Zhuang, "Sub-diffraction-limit imaging by stochastic optical reconstruction microscopy (STORM)," *Nature methods,* vol. 3, pp. 793-796, 2006.
[6.23] T. A. Klar, S. Jakobs, M. Dyba, A. Egner, and S. W. Hell, "Fluorescence microscopy with diffraction resolution barrier broken by stimulated emission," *Proceedings of the National Academy of Sciences,* vol. 97, pp. 8206-8210, 2000.
[6.24] B. Harke, J. Keller, C. K. Ullal, V. Westphal, A. Schönle, and S. W. Hell, "Resolution scaling in STED microscopy," *Optics express,* vol. 16, pp. 4154-4162, 2008.

Chapter 7

Summary and future work

The explorations of research frontiers in ultrafast science require the generation and control of octave-spanning optical sources. On the one hand, the generation of isolated attosecond XUV pulses and the investigations of attosecond physics critically rely on the feasibility of intense phase-controlled sub-cycle optical waveforms. On the other hand, optical pulse trains, which are obtained from femtosecond mode-locked oscillators, with a high repetition rate (*e.g.*, in RF frequency) can be used as optical flywheels providing a very precise timing reference, opening up several interesting research fields such as frequency metrology, optical clocks, and timing links for the next generation of X-ray free-electron lasers (FELs). In this dissertation, I present the enabling technology for the fully control of octave-spanning optical sources based on dielectric chirped mirrors. Moreover, nonlinear light microscopy with various imaging contrast mechanisms has been regarded as a powerful tool for molecular imaging, clinical applications, and chiral crystal examinations. The feasibility of nonlinear light microscope depends on the availability of robust femtosecond sources and reliable electronic control. During my PhD studies, a nonlinear light microscope system is also constructed based on a robust femtosecond fiber laser and high speed electronics, which is capable of observing nucleation and growth kinetics of protein nanocrystals.

Regarding dispersion management using dielectric chirped mirror designs, >2-octave-spanning chirped dichroic mirrors and high-reflection chirped mirrors are demonstrated based on analytically analyzing a novel mirror design, dual-adiabatic-matching (DAM) structures. The design limitations, in terms of the handling bandwidth, the magnitude of dispersion, and the damage threshold, are discussed: (1) the bandwidth capabilities of dielectric chirped mirrors depend on different incident angles and polarizations. With a larger angle of incidence in s-polarization, a larger covering bandwidth can be obtained with a more pronounced residual GD variations. (2) A trade-off is found between the amount of compensating dispersion and the design bandwidth. With a fixed total layer number, the

design bandwidth is compromised when one trying to increase the amount of compensating dispersion. (3) Although the repetition rate, pulse duration, and center wavelength of the optical source, as well as the coating structures of the DCMs would also affect the breakdown fluence, sub-cycle optical pulses supporting up to several tens of mJ pulse energy with a >1 cm^2 beam size should be possible based on the multilayer chirped mirrors. With a typical <10 μm of total coating thickness, ~1 TW/cm^2 of the peak intensity should be tolerable with <1 rad of nonlinear phase shift (*i.e.*, B-integral).

The demonstrated broadband mirrors are employed as a two-octave-spanning dispersion-controlled scheme in sub-cycle optical waveform synthesizers, providing a new enabling technology for pulse-energy and bandwidth scaling. Super-octave-wide waveform synthesizers delivering multi-mJ pulse energy are introduced based on the advanced chirped mirror technology: 3-channel parametric synthesizers with 3 amplification stages are discussed. These novel designs provide custom-tailored dispersion and reflectivity over more than two octaves of bandwidth ranging from 0.49 μm - 2.3 μm, supporting 1.9-fs-short sub-optical-cycle pulses. In addition, different channels of femtosecond optical parametric amplifiers operate at different wavelength regimes, and the material dispersion shows distinct behaviors in each channel. A dispersion distribution scheme is designed in order to provide a guideline for experimental constructions. The FROG measurements of the second stage results of different channels, as well as the characterization of the passive timing jitter, demonstrate the feasibility of sub-cycle optical waveform synthesizers.

Regarding spatiotemporal dynamics of octave-spanning oscillators, we analyzed the full spatiotemporal features of few-cycle Ti:sapphire oscillators to better understand the laser dynamics for advanced optimization and applications. Different laser conditions numerically are examined and analyzed to optimize the experiment-obtainable working points of octave-spanning oscillators, by means of fine-tuning cavity dispersion, cavity geometry, and pump power. In addition, we explained the detailed features of the experimental demonstrations by considering the intracavity residual phases and the output coupling as the perturbation to dispersion-managed soliton mode-locking. The advanced studies are focused on the intracavity spatiotemporal phase-matching based on the perturbation of dispersion-managed solitons. With a proper intracavity phase-matching, the wavelength components in the spectral wings (*e.g.*, ~1.14 μm for the direct generation of

frequency combs and ~1.03 μm for seeding of Yb amplifiers for further parametric amplification) can be greatly enhanced while maintaining a fundamental beam shape. The phase-matching concept is demonstrated experimentally in a linear Ti:sapphire oscillator, providing a >10 dB enhancement around 1140 nm with a good beam quality. The advanced improvement requires a more precise intracavity dispersion control: a phase-optimized end-mirror is designed and fabricated to compensate the residual dispersion errors in the cavity. 12 bounces of chirped mirrors and one bounce of the phase-optimized end-mirror may result in <0.1 rad of intracavity residual phase over the whole operating bandwidth of 0.65 μm – 1.14 μm. With different output coupling window, the weighting between 1030 nm and 1140 nm is varied, implying a controllable manner of the oscillator output aiming for different applications. The whole simulation environments describing octave-spanning spatiotemporal dynamics will be implemented for optimizing advanced ultrafast sources, such as hollow-core fiber/ waveguide compressors and parametric synthesizers.

Our approach to setup a nonlinear light microscope system is also described based on femtosecond fiber lasers and high speed electronics. The ultrafast fiber laser system, including a nonlinear-polarization-evolution mode-locked Yb:fiber oscillator and an amplifier is constructed to deliver ~110-fs pulses with ~3 nJ of pulse energy featuring low relative intensity noise (RIN). The schemes of electronic control and optical setup of the microscope systems are provided. With the demonstrated nonlinear light microscope, we obtained sub-μm resolution imaging with a video imaging rate at a reduced excitation power compared with the commercial SONICC systems. With the developed ultrafast fiber laser technology and optimized electronic control, a more compact nonlinear light microscope will be constructed to monitor the nucleation and growth kinetics of protein crystals.